ALMA MATER STUDIORUM
UNIVERSITÀ DI BOLOGNA

DOTTORATO DI RICERCA IN

MECCANICA E SCIENZE AVANZATE DELL'INGEGNERIA

Ciclo 38

Settore Concorsuale: 09/C2 - FISICA TECNICA E INGEGNERIA NUCLEARE

Settore Scientifico Disciplinare: ING-IND/11 - FISICA TECNICA AMBIENTALE

FROM ACCESSIBLE MUSICAL INSTRUMENTS PLATES CHARACTERIZATION TOWARDS AN ANALYSIS FRAMEWORK FOR THE CONSERVATION OF HISTORICAL MUSICAL INSTRUMENTS.

Presentata da: Sebastian Duran

Coordinatore Dottorato

Lorenzo Donati

Supervisore

Michele Ducceschi

Co-supervisore

Ludovico Ausiello
Henna Tahvanainen

Esame finale anno 2026

Abstract

Over the past decades, research on the vibroacoustic analysis and modeling of musical instruments has gained increasing attention, both for virtual prototyping and for creative applications. Within the framework of the NEMUS project, this thesis focuses on the experimental vibroacoustics analysis of musical instruments plates. Specifically, this research aims to validate experimental protocols and techniques for characterizing the mechanical and material properties of string-based musical instrument soundboards, which play a crucial role in efficiently radiating sound generated by the strings. The work begins with a comprehensive literature review outlining the historical developments and the state-of-the-art concerning experimental and numerical approaches used to study the dynamical behavior of musical instruments. An inverse parameter estimation method is introduced to enable the characterization of the elastic constants of instrument plates. This approach supports the development of physics-based models within the NEMUS project and offers a practical tool for luthiers and restorers to obtain accurate material property data. The methodology is complemented by the validation of a more accessible experimental modal analysis ecosystem, designed to facilitate the acquisition of modal properties via a cost-effective approach. Several application scenarios are presented to demonstrate the accuracy and reliability of the proposed analysis methods. Two case studies illustrate the application of these techniques and address the uncertainties involved in estimating the elastic features of string-based musical instruments. A non-dimensional numerical modal analysis framework based on the Finite Element Method is developed, highlighting the limitations of conventional assumptions typically adopted in the modeling orthotropic plates. Finally, the thesis explores the impact of uncertainty in material characterization through a pilot study on an ancient Arpicordo in non-playable condition. The results show how different characterization approaches influence the structural robustness of the instrument under static loading conditions, as assessed through numerical modeling. The study ultimately advocates for the integration of uncertainty and robustness analyses within a comprehensive reverse engineering protocol, supporting restorers and instrument makers in making informed decisions when dealing with these fragile and historically valuable structures.

Acknowledgements

First, I want to thank my supervisor, Michele Ducceschi, for the precious guidance, inspiration, and trust during these three years. The journey has been as challenging as it has been stimulating, and it would not have been the same without him and the rest of the inspiring team he created. I am also thankful to Ric, Matt, Craig, and Henna for their collaboration and for contributing to a constructive and inspiring team atmosphere. I am grateful to all the students, researchers, and colleagues I had the opportunity to meet during this path, Alexis, Damian, Maria, Philemon, and Pierre, for the fruitful exchanges and the pleasant working environment we shared. Being able to learn, work, and contribute to a project like NEMUS definitely represented a milestone in my personal and professional growth.

Thanks to my co-supervisor, Ludovico Ausiello, for yet another effort in supervising my work. His encouragement and inspiration were fundamental in motivating me to pursue a PhD in musical acoustics. I also wish to thank Henna Tahvanainen for her co-supervision and for her valuable suggestions and support during the development of this thesis.

A big thanks to Romain Viala, Scott Cogan, and Alicia Deseille for the supervision and great hospitality during my months in France. I am grateful for the incredible chance to deepen my knowledge of musical instrument making at the unique ITEMM centre, as well as to conduct a completely new and yet extremely intriguing research line for me at FEMTO. I would also like to thank all the lab mates I met during my stay—Thibaud, Vini, Liam, Leonardo, Alexandre, Wajih, Arthur, Grégoire, Israà, Adam, Tsilat, and the entire DMA group—for making this experience truly memorable. A special thanks to Maxence for being a one-of-a-kind flatmate during my time in Besançon.

I am deeply grateful to my colleagues from the acoustics UniBo group, Giulia Fratoni, Domenico De Salvio, Gioia Fusaro, Vincenzo Pettoni Possetti, Matteo Cingolani, Matteo Spinelli, Virginia Tardini and Alessia Nora, for being such a cohesive and supportive group! I would also like to thank Tommaso Paolo Emiliano Randazzo for being both a wonderful lab neighbor and a dear friend.

I am very grateful to the reviewers of my thesis, Giacomo Squicciarini and Kerem Ege, for their valuable and insightful comments and suggestions, which helped improve the quality of my work. Their feedback will undoubtedly have a lasting impact on my future research.

Thanks to my partner, Marta, for the long-lasting support during the tough moments of this journey. Thanks to Alex, Alice, Diamante, and the many friends I met during these years for the moments shared beyond research. I dedicate this work to my mother, Maddalena, for the encouragement, support, and faith, and to my late grandfather, Cesare - I wouldn’t have achieved any of this without you.

Table of contents

List of figures

List of tables

Chapter 1

Introduction and context

The conservation of historical musical instruments typically follows two distinct approaches: restoration and preservation [47]. Restoration seeks to return an ancient instrument to playing condition, making it possible to explore the intangible heritage embedded in its original sound and function [137]. Preservation, on the other hand, emphasises the protection of the object and the related craftsmanship by avoiding intrusive interventions that could compromise its historical integrity [110]. Historical musical instruments do not only represent precious archaeological pieces, but they also incorporate a unique intangible cultural heritage, and recently, the need for a more holistic approach in their conservation has been advocated [265]. Such an approach would allow not only to preserve the mere historical object but also the music played by it, the associated musical genres and playing techniques, and so a broader cultural meaning [137]. Within this context, the presented thesis fits into the NEMUS project, which is dedicated to the numerical restoration of plucked string-based historical instruments. Specifically, this work focuses on the experimental vibrational analysis of orthotropic soundboards.

While it is well established that structural modifications play a dominant role in shaping a musical instrument's vibrational behavior [269], precise material characterization remains crucial in restoration practices. This is important both to define and preserve the correct mechanical features of an instrument, supporting potential interventions [47, 165], and to also inform accurate physical models of musical instruments [59]. The latter is of primary interest to the NEMUS project. This need is particularly critical when considering the significant variability observed even within the same wood species, which is further influenced by environmental aspects [275, 270, 187]. Accurate material characterization thus becomes important to reduce the inherent uncertainty associated with historical musical instruments [271]. While nondestructive methods have been developed for this purpose [251, 46], many recent experimental approaches still require costly equipment and, as will be discussed in the following sections, several of the available techniques present practical limitations. Accordingly, the purpose of this thesis is twofold:

- Investigate accessible techniques and user-friendly methods for accurately estimating both the physical and mechanical properties of musical instrument plates.
- Address material properties uncertainty to support the conservation of historical musical instruments.

1.1 Role and design of soundboards

Soundboards are of main interest across chordophones as they allow the instruments to radiate sound efficiently, thanks to their plate-like structures, and their design directly influences the perceived vibroacoustics signature [150]. Recent studies have particularly discussed the critical role of soundboard dynamics on string vibrations in pianos [190]. Their design has continuously evolved over history and each structural change encompasses information on the music played and the related technological, economic and scientific advancements. The violin family expanded as a technical necessity imposed by baroque music, whilst firstly being used for chamber music and handcrafted by recognized masters as Antonio Stradivari and Giuseppe Guarnieri del Gesú, the instruments underwent structural design alterations to play in larger concert halls [47, 104]. The six-string classical guitar we know today is also a consequence of important design interventions from the original classical guitar introduced in the Renaissance. The design introduced in the 19th century by the luthier Antonio de Torres enlarged the body size and established the use of fan-shaped bracing style in the top plate, enhancing the instrument's perceived loudness and vibroacoustics signature [104, 47, 236]. Additional soundboard bracing patterns were also introduced, influencing and shaping the structural and mechanical behavior of the full instrument. An example is the lattice bracing introduced by the luthier Greg Smallman [47, 105], which enabled the guitar to be suited in larger concert halls by enhancing its loudness and sound projection capabilities [142, 242]. Parallel to the classical guitar, the steel-string acoustic guitar also evolved, and a specific bracing pattern like the X-Bracing introduced by Martin addressed structural challenges imposed by the higher string tension, which was later refined by the falcate bracing proposed by Trevor Gore [105, 118]. Before the transition to the piano in the 18th century introduced by Bartolomeo Cristofori, the harpsichord family already showed important differences among various national making schools. Italian harpsichords were characterised by a thinner and smaller soundboard, making them more suitable for accompanying music [261]. Conversely, Flemish harpsichords featured a substantially larger body and soundboard size, which gave them a more pronounced bass response [156]. Other prominent harpsichord traditions from the 16th to the 18th centuries include the French and German schools, which introduced distinct soundboard geometries and varying dimensions [60, 61], thus giving rise to a diverse array of historical models. In the recent years, while wood has historically been the main construction material used for string-based musical instruments, alternative solutions such as composites or 3D printing materials have recently been investigated and used in traditional musical instrument making of chordophones [50, 84, 274, 71]. Within this context, the NEMUS project is closely connected to the work of luthiers and instrument restorers, the methodological advancements proposed in this thesis are designed to be implemented by such professionals. In doing so, the research extends beyond an exclusive focus on fragile historical artefacts, opening up approaches that are also relevant to contemporary instrument-making practice.

A detailed outline of this work is given in Section 1.6. In the next paragraphs, a literature review is presented concerning the state of the art in experimental and numerical methods used to characterize the vibroacoustic behavior of musical instrument soundboards and estimate their mechanical properties.

1.2 Material characterization of musical instruments plates

The identification methods for the characterization of material properties can be divided into destructive and nondestructive approaches. Destructive techniques provide a direct identification of material properties by allowing standardized mechanical testing on isolated samples. In contrast, nondestructive methods generally rely on indirect (i.e., inverse) estimation based on the global vibrational response of the mechanical structure under test [251]. Destructive methods have the advantage of enabling the direct assessment of key elastic material properties, including Young's moduli, shear moduli, and yield stresses, through standardized tensile, compression, bending, and torsional test procedures [109, 233]. However, nondestructive techniques have gained popularity as they avoid damaging the structure under test and are essential for the material characterization of ancient and fragile musical instruments [46, 165]. Nondestructive testing (NDT) methods are principally classified into numerical or experimental approaches and aim to estimate the elastic features of the sample under test based on its modal parameters — namely, natural frequencies, mode shapes, and modal damping [251, 268, 169]. With regards to musical instrument plates, the advancements in materials property estimation encouraged more studies to investigate the correlation between physical and mechanical material properties and the grading or selection of wood for musical instrument making. In 2007, Buksnowitz et al. reported that mechanical and acoustical properties of wooden plates could not be directly linked to luthiers' subjective preferences and selection criteria. However, these properties can still be useful for objectively informing decisions in the building process, and dedicated tools would be needed to predict them [49]. Objective criteria incorporating key physical and mechanical features have also been proposed to support the grading of wood used for musical instruments making processes (i.e. tonewood)[288], hence encouraging further investigations into material properties of tonewoods, aiming to establish more objective criteria for their selection and classification. In the following sections, the historical advances in NDT methods with specific regards to applications involving musical instruments plates are presented and grouped relatively to the main approaches identified in the avaiable literature.

1.2.1 Semi-analytical methods

In 1984, the work by Caldersmith and Rossing [54] investigated modal coupling effects due to the Poisson ratio occurring at specific aspect ratios in isotropic and orthotropic (wooden) plates, introducing simple formulas to predict Poisson values for rectangular plates. In the same period, further work conducted by Caldersmith, as well as parallel research published by Woodhouse and McIntyre, led to the development of formulas enabling the estimation of Young's moduli in the longitudinal and radial directions and the shear modulus in the longitudinal–radial plane, based on a comparison between experimentally obtained natural frequencies and approximated analytic solutions using the Rayleigh-Ritz method [55, 184, 183]. A practical demonstration of this approach was later provided by Caldersmith and Freeman in 1990 [53].

This method has gained significant popularity over the decades due to its simplicity and low cost, as no specialized equipment is needed when using plates with a square aspect ratio and uniform thickness. Today, it is still used by researchers and instrument makers for quickly estimating material properties from small, available wooden samples [221, 220, 173, 116, 95].

However, the method has limited flexibility in its use, as it is strictly valid only under the assumption of fully free boundary conditions (BCs). Moreover, while the two Young's moduli are estimated with good accuracy, the shear modulus is generally less reliably determined, as will be discussed later in this work (see Section 3.5). Moreover, when different plate aspect ratios are used, the method may lead to inaccurate estimations due to modal crossings or degeneracies, which can result in altered mode shapes and thus hinder the proper identification of the material's elastic properties. In these cases, measurements on the sample under test are still required to identify the correct operational deflection shapes (ODSs).

In 1999, the approach undertaken by Gaul, Willner, and Hurlebaus [108] used electronic speckle pattern interferometry (ESPI) and took advantage of the formulas derived by Caldersmith [55]. In 1994, Urgela and Saldner [264] presented an application of the method introduced a decade earlier by McIntyre and Woodhouse [184], adapting it to violin tonewood halves before any shaping or carving steps in the instrument-making process. The study confirmed the effectiveness of the estimation approach in identifying the Young's moduli and the shear modulus of the samples. However, it also discussed how limitations arising from larger thickness and non-homogeneous geometry might lead to modal distortion in the observed patterns, thus increasing the error in the estimation of material properties.

1.2.2 Numerical methods

In the late 1980s and throughout the 1990s, iterative techniques employing computational methods became increasingly popular. In 1987, Fällström and Molin showed how the finite element method (FEM) can be exploited to iteratively estimate the elastic constants of thin composite plates under fully free BCs [100] . In their study, they employed ESPI to enable real-time visualization of the vibration pattern and used a FEM model of the plates under test. The parameters were retrieved by updating the simulated elastic constants until a good agreement was found between measured and simulated data. They observed that this iterative method could provide more reliable results, being less sensitive to defects in the samples and to the experimental BCs of the bars. The study further confirmed that each of the first three vibration modes in rectangular orthotropic plates exhibits strong dependence on only one material parameter, thereby enabling the identification of the main elastic constants. The method was later refined through an updated phase-stepped ESPI method [101].

De Wilde and Sol described a method to estimate the elastic constants of composite material plates by matching experimental frequencies with a FEM model of the same plate. Similarly, in 1992, Pedersen and Frederiksen combined standard experimental modal analysis (EMA) techniques with a numerical model based on the Rayleigh–Ritz method, minimizing the error between experimental and numerical data to retrieve accurate estimations for orthotropic rectangular plates under free boundary conditions [207]. Similar inverse estimation routines were developed during the same years [16, 73], and this approach proved reliable even when dealing with noisy data [160]. Several studies have particularly focused on orthotropic thin plates — that is, plates for which transverse shear deformation is considered negligible and which are therefore described by the Kirchhoff-Love model (see Section 2.4 for a detailed discussion of orthotropic plate modeling). In 1993, Lai and Lau estimated the elastic constants of orthotropic thin plates under free BCs by combining EMA and the Rayleigh–Ritz method to implement the corresponding numerical models [161]. The study showed that good accuracy between experimental and simulated frequencies can be achieved (i.e., $\leq 5\%$). Nonetheless, while good consistency was observed in the estimated Young's moduli in the longitudinal and transverse directions, larger discrepancies were spotted when comparing the estimated shear modulus and Poisson's ratio values with reference data obtained via tensile tests.

De Visscher, Sol, and De Wilde illustrated a mixed experimental–numerical iterative routine to estimate the elastic constants of thin plates [72]. As in previous studies, the identification process relied on experimental measurement of the resonance frequencies of a plate under free BCs, while the elastic constants were iteratively updated within a Rayleigh–Ritz numerical model based on Love–Kirchhoff thin plate theory. Although a good match between simulated and experimental data could be achieved, the authors highlighted several important sources of uncertainty, primarily related to the assumptions underlying the numerical model. If the thin plate assumption is violated—for example, due to excessive thickness—the model may yield inaccurate estimates, leading to a misrepresentation of the actual physical and mechanical properties of the plate.

A refined method using a numerical model that includes transverse shear deformation was proposed by Ayorinde [15], allowing for a rapid estimation of the elastic constants of thick composite plates via a least-squares optimization matching experimental and predicted frequencies. In 1997, Larsson [163] used an iterative finite element model updating (FEMU) inverse method to identify the orthotropic elastic constants of spruce plates using experimental modal data. The method relied on minimizing the error between simulated and measured frequencies of the thin plate under test. As with previous methods, the estimation procedure was tailored for plates under free BCs.

In 2011, Pérez Martinez, Poletti, and Gil Espert assessed the impact of moisture content on the estimated in-plane elastic constants of thin wooden plates used in instrument making [179]. As in earlier studies, a FEMU routine was implemented to minimize the difference between numerical eigenfrequencies and experimental data.

In the past decade, several studies have focused on developing new methods and tools to estimate the elastic constants of wood for musical instrument making. Zhou et al. conducted a comparative study on measuring the elastic constants of wooden plates using modal testing under three BCs: all sides free (FFFF), one side simply supported (SFFF), and two opposite sides simply supported (SFSF) [290]. They first obtained estimates of the main thin plate elastic constants using closed-form equations from the Rayleigh method, and then applied the FEMU technique to refine those estimates. A sensitivity analysis was also carried out to determine which vibration modes were most influenced by each elastic constant, enabling targeted frequency selection for inverse calculation. The results demonstrated that appropriate BCs and mode selection are critical for accurate non-destructive estimation of elastic properties.

In 2018, inverse methodologies were further refined by Viala, Placet, and Cogan, who proposed an updated version of the FEMU approach named FUM-3DVF [274]. This version combined 3D laser vibrometry experimental data with FEM modeling to estimate the elastic constants and damping properties of complex-shaped geometries (e.g., violin top plates), with errors confined between 5.9 % and 8.5 % for the two Young's moduli in the longitudinal and transverse directions and the longitudinal-to-transverse shear modulus. The method was subsequently applied to investigate the natural variability of mechanical properties in different wood species for instrument making [275].

From a different perspective, Igea and Cicirello recently proposed an estimation routine [138, 140] inspired by the earlier work of Woodhouse and Caldersmith [183, 53]. Starting from closed-form equations derived via the Rayleigh method and using EMA combined with Chladni pattern techniques [64], an initial guess of the Young's moduli, shear modulus, and Poisson's ratio is obtained. This is then refined through an iterative optimization process involving comparison between experimental data and a numerical model based on either a Rayleigh–Ritz or FEM approach. Despite requiring only low-cost equipment, the method might still demands extra sample preparation to estimate all elastic constants.

1.2.3 Standard defined methods

Roohnia et al. assessed the elastic features of Arizona cypress logs to determine the impact of growth rings on their suitability for instrument making [231]. To do so, they estimated the longitudinal Young's modulus based on the ASTM C1548-02 standard. However, it has to be noted how since this standard assumes perfectly isotropic samples, it cannot be used for accurate estimation of all the wood elastic constants.

Other research has adapted similar resonance-based techniques to account for wood's orthotropy. Among these, the flexural vibration method has been employed to estimate both the longitudinal Young's modulus and the longitudinal-transverse shear modulus for freely supported wooden samples [286]. This approach has been standardised for wood-based materials in ASTM D6874-12 and additional studies have explored the use of flexural vibration tests to estimate the Young's modulus values of solid wood specimens[287, 219]. Although the method offers a convenient and practical way for estimating the main elastic properties of wooden samples, its applicability is limited to specific BCs. Furthermore, additional sample preparation may be required when elastic constants in different directions are needed.

1.2.4 Other experimental methods

In addition to the approaches described above, several further techniques have been proposed in the literature and are worth mentioning here for completeness. In 1984, Bucur and Archer explored the use of ultrasound-based techniques [45]. The study demonstrated the feasibility of retrieving the full orthotropic elastic tensor from wave velocity measurements in small wood samples. The estimation is performed by conducting as many velocity measurements across different fiber directions as the number of independent wood elastic constants (i.e., nine). While good accuracy is observed in the estimation of Young's and shear moduli, Poisson's ratios proved more error-prone in this method, as their calculation relies on off-axis measurements, which are strongly affected by scattering and attenuation effects caused by wood inhomogeneity.

A decade later, the work published by Kahle and Woodhouse [148] proposed a model based on a microscopic geometrical analysis of softwoods, leveraging a pre-existing honeycomb model [6] that assumes literature-based cell-wall elastic properties. The study highlighted the impact of assumed cell-wall properties on the resulting estimated elastic constants, ultimately suggesting adjustments to the values reported in the literature to improve agreement with experimental data.

In 2001, Urgela proposed a nondestructive tool combining earlier advancements in the use of ESPI for EMA with colorimetric testing of the wood surface to characterize different wood types [263].

Static tests were also used in a nondestructive manner on spruce samples for guitar soundboards [86]. The study proposed relationships among mechanical properties of thin plates used in instrument making, thus allowing luthiers and manufacturers to reduce time and cost while aiming for acoustically consistent instruments. Despite being nondestructive, the method still depends on tensile and three-point bending tests that require specialized lab equipment, which may be expensive, difficult to access, and not ideally suited for users without technical expertise.

Recent studies have also explored the use of neural networks (NNs) to accelerate inverse estimation routines that traditionally rely on finite element method (FEM) simulations [18, 17]. In this framework, NNs are trained on large datasets generated via FEM simulations, where material and geometrical parameters are independently sampled from Gaussian distributions. In the optimization phase, a cost function is minimized to match the measured and NN-predicted modal features. While this approach significantly reduces computational demands compared to full FEM-based model updating, it requires generating new FEM datasets and retraining the networks when different geometries or material classes are considered.

Overall, the estimation methods developed over the last decades have primarily focused on improving either result accuracy, cost-effectiveness, or computational efficiency. However, most approaches tend to emphasize one of these criteria at the expense of the others. As a result, many estimation routines rely on high-end equipment and costly experimental setups, limiting their accessibility. At the same time, a significant number of techniques are restricted to rectangular plate samples under idealized free boundary conditions, which might constrain their applicability when dealing with different practical contexts. A summary of the gathered data is presented in 1.1.

Method used	**Number of collected studies**	**References**
Semi-analytical	12	[53, 54, 55, 116, 95, 108, 173, 183, 184, 220, 221]
Numerical	16	[15, 16, 72, 73, 100, 101, 138, 139, 161, 160, 163, 179, 207, 268, 275, 290]
Standard	3	[230, 285, 286, 219]
Other	6	[17, 18, 45, 86, 148, 263]

Table 1.1 Summary of collected studies on elastic constants estimation for wood plates and musical instrument plates, grouped per method used.

1.3 Modal Analysis of musical instrument plates

As highlighted in the previous section, modal parameters are crucial in order to characterise the material properties of musical instruments' soundboards and plates. Accordingly, vibroacoustics analysis is instrumental when investigating the mechanical and acoustical properties of historical instruments [97, 29] or when evaluating the impact of design changes on their acoustical signature [42, 117, 92]. The following sections will provide a general overview of current research and findings, and highlight the need for future research to be conducted.

Vibrating structures such as musical instruments are characterized by specific modes of vibrations [123]. Accordingly, as these structural vibrations can be considered to be linear, modal analysis techniques allow for the investigation of their natural frequencies, modal damping and mode shapes [123, 234]. By providing a more detailed examination of the characterization techniques introduced earlier, the following literature review explores the experimental setups, measurement equipment, and numerical techniques commonly employed to extract modal parameters from musical instruments' soundboards.

1.3.1 EMA of soundboards and musical instrument plates

Traditionally, when performing modal analysis measurements, the interested structure is excited by a defined force whose response is measured and analysed as a frequency response function (FRF) [234], defining the relationship in the frequency domain between an input and an output signal of an assumed linear and time-invariant system. In order to generate and capture the FRF, sound sources and receivers must be defined.

Excitation techniques

Common excitation approaches for modal analysis include impulsive (i.e., impact hammer) and shaker-based setups [234, 98, 14, 260]. Both have been widely applied to string-based musical instruments [242, 32, 67, 93, 176, 175, 224, 282, 289, 19]. Impact testing with a hammer requires multiple impulse responses to be measured and averaged to improve measurement reliability. However, human error can often lead to inconsistencies, such as double hits on the structure under test. In a study on violins, Duerinck et al. [85] stressed that, beyond the risk of damaging historical instruments, the reliability of impact hammer testing heavily depends on the operator's skill, reducing the repeatability of the procedure. To overcome these issues, automated impact hammer systems have been developed, including linear actuators, beam-bending systems, and rotating mechanisms [171, 23, 34, 196, 144].

Leveraging this approach, several studies have aimed to implement low-cost experimental setups for EMA on string instruments. Singh and Moore [240] proposed a low-cost automated hammer using affordable automation equipment. However, a commercial impact hammer was still used as the sensor, only partially reducing overall setup costs. Focusing on musical instruments, Curtin developed a dedicated rig for violin sound radiation measurements using a swinging hammer mechanism [69], later refined and standardized for consistent sound radiation testing [146, 70]. Rau introduced a cost-effective 3D-printed setup for modal analysis of soundboards, utilizing a piezo sensor to capture the impact force [225]. Low-cost impact techniques have also been explored for tonewood analysis. Rau built a device with two piezo sensors—one for input and one for output—to estimate sound speed based on time-of-flight between the signals [225]. Similarly, Jost compared a simple longitudinal standing wave measurement setup using a hammer to the commercial Lucchi Meter device for estimating sound speed and Young's modulus [147], finding good agreement, though sample preparation was more demanding in the low-cost method. Despite its popularity, the impact hammer method poses risks for historical or fragile instruments. Soft covers can be used to prevent damage but reduce the frequency range of the excitation [98]. To minimize such compromises, alternative experimental techniques have been explored. Le Moyne, Le Conte, and Ollivier performed modal analysis on a fragile historical harpsichord using a single impact recorded via a large microphone array [165].

Another well-established excitation method in EMA is the use of shakers—classified into mechanical, electromagnetic, and electrohydraulic types [98]. While offering more controlled excitation, shakers can affect structural dynamics through the added mass and stiffness of their stingers [14]. Pyrkosz and Van Karsen [217] observed that using a shaker on a violin soundboard led to higher detected frequencies than with an impact hammer, due to stiffening effects. Duerinck [85] reported similar discrepancies between shaker and hammer results for the main signature modes of a violin. To lower costs, Ausiello proposed using a budget-friendly electromagnetic exciter with the exponential sine sweep (ESS) method developed by Farina [103, 102], applying it to modal testing on string instruments [10, 12]. A less traditional method is the acoustic excitation via a speaker. Among different excitation methods, Duerinck identified the speaker as the most safer and faster reliable alternative when performing modal analysis measurements on musical instruments under laboaratory settings [85]. Several researches have adopted the acoustic excitation for EMA purposes [90, 172, 203].

However, results can be sensitive to speaker placement, requiring multiple excitation points for thorough modal identification [84]. Moreover, although ideally conducted in an anechoic environment to reduce acoustic reflections [91, 90], the unknown input force limits its use for full modal parameter identification [85]. Finally, high sound pressure levels (SPLs) may be needed to sufficiently excite the structure [172].

Acquisition techniques

Regarding the acquisition system, accelerometers represent the most traditional method for capturing output signals and have been widely used in EMA measurements on various chordophones [229, 68, 92, 200, 168, 36, 188]. Like shakers, accelerometers add mass to the structure, which can significantly affect the experimental data, as confirmed by several studies [33, 85, 7]. Therefore, a balance must be struck between measurement accuracy, precision, and practicality [22]. Alternatively, low-cost sensors have been proposed as replacements for expensive commercial accelerometers [225, 147].

The Laser Doppler Vibrometer (LDV) is a widely adopted non-contact measurement device used to acquire vibroacoustic properties of musical instruments via surface velocity measurements, without introducing mass loading or damage to the instrument [175, 203, 172, 41, 270, 31]. A comparison between LDV and traditional accelerometers conducted by Mansour, Scavone, and Freour [174] revealed that accelerometers significantly influenced the detection of natural frequencies and modal shapes, reinforcing the benefits of LDV systems. However, LDVs and scanning LDVs (SLDV) remain costly and are limited by their line-of-sight requirements and susceptibility to speckle noise [98, 178, 145].

Microphones offer a more affordable and non-contact alternative for acquisition [90, 229, 200, 262, 188, 10, 12], and have been used in estimating material properties of wooden samples [135, 177, 256, 147]. Nonetheless, these approaches often lack rigorous validation against standard EMA setups. In other cases, microphones have been combined with accelerometers on the instrument soundboard to evaluate sound radiation and radiation efficiency [69, 221, 222, 259, 246, 112, 261]. A notable microphone-based acquisition technique is the INAH method proposed by Le Moyne, Le Conte, Ollivier, Frelat, Battault, and Vaiedelich [165] Le Moyne et al. [165], adapted from nearfield acoustic holography (NAH) [201, 281, 280, 181, 267] to accommodate impulsive excitation. This approach reconstructs the normal velocity field of a vibrating surface from near-field acoustic pressure measurements taken over a planar grid. A similar method, Statistically Optimized Nearfield Acoustical Holography (SONAH), demonstrated good agreement with standard EMA setups [35]. As this type of acquisition does not directly capture the structural vibration of the surface, modes with low radiation efficiency may not be detected [35]. Furthermore, while semi- or fully anechoic conditions are ideal for preserving signal-to-noise ratio, the use of large microphone arrays can make the setup costly and logistically challenging. In general, while these studies underline the importance of non-destructive methods for safeguarding fragile historical artefacts, they also open the possibility of adapting such techniques to controlled experimental settings, an idea further developed in the context of this thesis.

1.3.2 Numerical modal analysis of musical instruments soundboards

In the last two decades, researchers have extensively applied numerical modeling to the modal analysis of soundboards in stringed musical instruments. Computational simulations have complemented experimental approaches, either by enabling model-based updating estimation methods for material characterization or by offering insights into how design changes could affect vibrational and structural behavior [113, 274].

For this purpose, finite element methods (FEM), boundary element methods (BEM), and finite difference methods (FDM) have been employed [150, 30, 191, 279]. While BEM focuses only on the boundaries of the modeled domains, making it more suitable for sound radiation modeling [150, 249, 248], FDM has traditionally been applied to simpler geometries that can be easily discretized on structured grids [150] and in sound synthesis applications [30, 278, 212, 82].

On the other hand, despite its higher computational cost, FEM has become the predominant numerical technique for analyzing and extracting modal parameters from musical instruments, thanks to its flexibility in handling complex geometries [285, 65, 221, 186, 117, 122, 121, 176, 208, 141, 190]. This approach has proven especially valuable in restoration studies as it allows to investigate] the effects of structural modifications on historical and fragile instruments [211, 226] without affecting their integrity. Le Conte et al. [165] implemented a FEM model of an ancient harpsichord to predict the impact of restoration interventions. Their work showed how FEM can be used to optimize restoration choices, ensuring low shear stress gradients while preserving the soundboard's modal behavior. Konopka, Ehricht, and Kaliske [154] demonstrated how a FEM model of a clavichord can accurately simulate hygromechanical loading, reinforcing FEM's role in supporting conservation efforts. Almanza et al. [3] combined experimental and numerical studies using an uncalibrated FEM model of an ancient lute to assess the effects of assembly and gluing processes. The study validated the predictive capability of FEM in modeling modal trends due to assembly procedures.

More recently, several studies have combined imaging-based nondestructive testing (NDT) techniques with FEM modeling to analyze structural and modal behavior and support restoration efforts. These methods are particularly relevant for historical instruments, as they provide otherwise inaccessible geometrical details. For example, Coaldrake [65] created a FEM model of a Japanese Koto using computed tomography (CT) scans, achieving good agreement between experimental and simulated vibrational behavior. Similarly, Plath and Kirsch [151] outlined a workflow using open-source software to create a FEM model of an ancient violin from CT data, although no FEM analysis was included in that study. Carvalho, Debut, and Antunes [59] presented a step-by-step workflow for physical modeling and sound synthesis of historical bells, using structured-light scanning to generate a FEM model for modal analysis, which was validated through EMA and used for time-domain modal synthesis.

Finally, Viala et al. [271] derived a FEM based model of an ancient damaged cello by Pietro Guarnieri (1734) from 3D radiographies. However, for the purpose of the study, the identified internal damage caused by an insect gallery is simplified as a circular material removal, and a surrogate model is used to perform a static analysis. In all the mentioned case studies, precise material properties and the model's geometry are crucial to ensure accurate and reliable values. While data collected from experimental measurements can be used to validate computer-based simulations [42, 272, 13], the anisotropic (mainly orthotropic) properties of wood used in instrument soundboards have an impact on the validity of mathematical simulations. Their influence was discussed in [13, 285, 284, 198].The difficulty in accurately defining wood properties is particularly relevant for ancient instruments, whose mechanical properties are difficult to determine, either experimentally or numerically. To address this uncertainty, Viala et al. [271] proposed an info-gap-based static analysis framework. This is a non-probabilistic decision-making approach designed to evaluate system performance under conditions of severe uncertainty, especially when precise probabilistic information is unavailable. Such an investigation can serve as a powerful tool for supporting restoration decision-making when high uncertainty in material properties is present.

1.4 Literature summary and discussions

From the brief literature reviews presented, several research trends can be observed. First, recent advancements in the characterization of the mechanical and physical properties of musical instrument plates or tonewoods have increasingly relied on combined numerical and experimental approaches. These often include iterative procedures aimed at minimizing discrepancies between experimental modal parameters and simulated data to refine the estimation of the main elastic constants of plate-like components. However, most of these estimation techniques have been validated primarily on rectangular samples under fully free boundary conditions. Thus, there is a clear need for more flexible methods that can take into account different sample geometries and various boundary conditions. Such adaptability would be particularly valuable in experimental scenarios where conventional setups may not be feasible—especially in instrument-making processes or restoration interventions with limited accessibility.

With respect to modal analysis techniques used to retrieve the necessary modal parameters, non-contact methods are generally preferred. These minimize the influence of added mass and reduce the risk of damaging fragile structures. Among these, impact hammer excitation is widely used as a practical method that avoids altering the mass of the structure. While potentially invasive for delicate components, previous studies have shown that the number of impacts can be minimized to limit the risk of damage [165, 261]. Acoustic excitation, on the other hand, offers a safer alternative for historical instruments but requires semi-anechoic or fully anechoic environments and high sound pressure levels (SPLs) to adequately excite the soundboard over a wide frequency range—conditions that may be difficult to achieve in practice. Laser Doppler Vibrometry (LDV) and Scanning LDV (SLDV) systems, though widely used for their precision and non-contact nature, are costly and may not be accessible as practical tools for restorers or instrument makers. Microphones offer a more affordable and non-invasive acquisition solution but are sensitive to the surrounding acoustical environment and may not effectively capture the actual vibrational response of the soundboard. Although recent signal processing advancements using large microphone arrays show promise, these methods still involve substantial costs and setups that may not be practical for non-specialist users. Overall, it is clear that despite the importance of non-contact techniques for the study of fragile historical instruments, their direct implementation often remains impractical. However, as anticipated in Section 1, the present thesis focuses on the development of experimental techniques tailored to the context of instrument making and digital conservation. Within the NEMUS project, this is pursued through collaborations with luthiers and restorers, where accurate replicas provide a safe and flexible ground for testing. This perspective emphasizes that the experimental methods developed here are not conceived solely as tools for heritage conservation, but as user-friendly and workshop-oriented procedures designed to directly support instrument makers and restorers. Within this context, although they entail computational and financial demands, FEM has proven to be the most widely used and effective approach for predicting the modal behavior of musical instrument soundboards. FEM-based virtual prototyping has been especially valuable as a decision-making tool in restoration efforts and in assessing the impact of structural design changes [249, 3, 165]. Finally, it is important to highlight how in the last decade, several studies attempted to establish an analysis framework for the structural and acoustical behavior of ancient musical instruments, starting from a geometrical non-invasive scanning to the implementation of a FEM model for either sound synthesis or restoration purposes. Nonetheless, various 3D scanning techniques exist, each with its own limitations and intended applications [218]. As a result, different instruments and case scenarios may present distinct challenges, requiring tailored frameworks for the specific needs of individual musical instruments.

1.5 Thesis objectives

This thesis will therefore address multiple objectives:

- **Propose and validate an inverse parameter estimation method for the elastic constants of musical instruments plates.** The method will rely on the plate modal data and explicitly designed to handle arbitrary BCs, ensuring a reliable applicability in realistic, workshop-related scenarios where varying experimental setups may be required.
- **Validate an open-source software tool to support the estimation routine.** This tool will make the estimation method accessible by avoiding the need for commercial software.
- **Validate a user-friendly and cost-effective framework for wideband modal analysis.** The framework will enable reliable broadband experimental measurements of vibroacoustic properties using simple setups, eliminating the need for high-end specialized equipment. Wideband capability is particularly relevant in this context, as higher frequencies become increasingly important when smaller samples are tested, or when a full-spectrum analysis of an instrument or component is required. By making such measurements accessible, the method lowers barriers for both instrument makers and restorers, supporting workshop-related practices.
- **Propose a practical framework that integrates available numerical and experimental tools to assist restorers and instrument makers in addressing restoration and conservation challenges.** This framework considers both methodological reliability and the practical constraints of heritage conservation scenarios. It will integrate exist-

ing advancements within a broader workflow while also expanding the methodology to new use cases and ensuring that it can be replicated and applied consistently.

- **Lay the foundations for a conservation and restoration framework for historical musical instruments.** The proposed framework will integrate the outcomes of this research with established diagnostic methods, such as computed tomography (CT) data, offering a practical basis for informed decision-making process in the conservation and restoration of historical instruments.

1.6 Thesis Outline

The thesis is divided into five chapters. The core research objectives introduced in 1.5 are presented and discussed in chapters 3, 4, 5 and 6.

Chapter 2 introduces the necessary theoretical background related to the elastic behavior and mechanical variability of tonewoods. The main dynamic plate models are presented, introducing the relevant thin and thick plate models. Finally, the essential concepts of Experimental Modal Analysis (EMA) are outlined, along with the basic principles of the Finite Element Method (FEM).

Chapter 3 introduces an inverse method for estimating the main thin-plate elastic constants. The method is benchmarked numerically using commercial FEM-based software and experimentally validated on a tonewood sample. A first case study is also reported, exploiting the method to compare the elastic constants of aged and non-aged tonewood samples.

Chapter 4 discusses the implementation and validation of a resource- and cost-efficient measurement ecosystem for the material characterization of musical instrument plates. An application to real instrument plates is provided, along with a discussion on the reliability of estimated data from tonewood samples for predicting the modal behavior of worked plates.

Chapter 5 presents an analysis framework to distinguish between thin and thick plate regimes in the modal domain, supporting the validity of elastic constant estimations. A numerical case scenario is also given to show the applicability of the framework.

Chapter 6 focuses on evaluating the influence of material property uncertainty on the structural behavior of a full soundboard model of a historical musical instrument. It examines the influence of different assumed material values, derived both from literature and experimental data. The chapter presents results from both deterministic and info-gap analysis approaches, inspired by recent research, and discusses their implications for conservation strategies. Finally, the chapter aims to lay out the foundations for a comprehensive reverse engineering protocol for decision-making processes in the restoration of historical musical instruments.

Chapter 7 provides a summary of the main research outcomes achieved from this thesis and suggests future research perspectives.

Chapter 2

Material properties and modeling of musical instruments plates

In this section, the necessary theoretical background is presented to provide the reader with the fundamental terminology and standard definitions relevant to the context of this work. The aim is to outline the essential concepts required to understand the research conducted in the following chapters. First, a concise overview of the structure of wood and its main mechanical and physical properties is given. Then, the core modal properties considered and evaluated throughout this thesis are described. Finally, the two plate models considered in this work are introduced and discussed, together with a brief conceptual presentation of the numerical techniques adopted in the subsequent chapters.

2.1 Brief anatomy of wood

Wood is a complex biological material with a hierarchical structure spanning multiple length scales [115]. Representation of its structure is given in Figure 2.1. An understanding of wood's anatomy is essential before delving into its material properties, as many chordophones (e.g., violins, pianos, guitars) rely on specific woods whose acoustic and mechanical behavior are direct outcomes of their anatomical features [46, 47, 48].

Macroscopic view

Figure 2.2 illustrates a macroscopical view of a trunk of a tree. The main elements, including the outer bark (ob) and inner bark (ib), the vascular cambium (vc), the sapwood, and the heartwood, can be observed. At this scale, wood is recognizable by its annual growth rings,

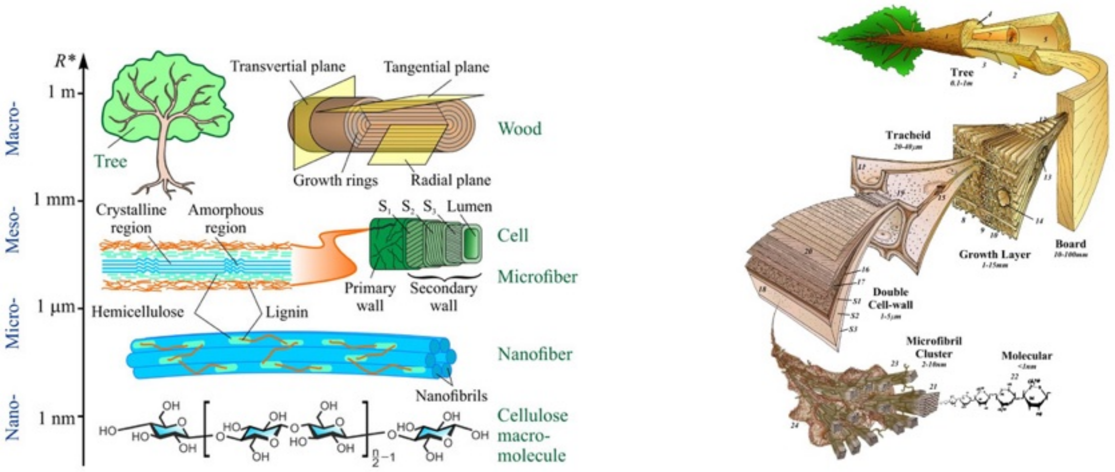

(a) From [115].

(b) From [133].

Fig. 2.1 Illustrations of wood's hierarchical structure.

color variations (e.g., sapwood vs. heartwood), and grain patterns. Growth rings (or annual rings) are concentric layers of wood produced by a tree in each growing season. Each growth ring consists of an inner zone called earlywood (formed at the start of the growing season) and an outer zone of latewood (formed later in the season). Earlywood is characterized by cells with larger diameters and thinner walls, giving it a lighter color and lower density, whereas latewood cells have smaller diameters and thicker walls, appearing darker and denser [237, 233]. Density variations at the macroscopic scale are largely tied to the proportion of latewood versus earlywood in each annual ring and the presence of different tissue types. These structural non-uniformities play a significant role in the vibroacoustics behavior of soundboards. This will be discussed in the following sections.

Woods are traditionally classified into "softwoods" and "hardwoods", which mainly differ in the types of cells and so in their appearance [237] as it is reported in the data from Table 2.1. However, these terms are associated with two different botanical groups, namely gymnosperms and angiosperms, rather than their inherent hardness [233].Table 2.2 reports density and Longitudinal Young modulus literature values of common examples for hardwoods and softwoods. The data shows how differences between hardwood species can be larger than those between hardwoods and softwoods. Material and physical properties will be introduced and discussed in more detail in the following Sections.

The term "grain" refers to the directionality and alignment of wood fibers. Wood is considered an orthotropic material, meaning its mechanical behavior differs along three principal axes relative to the grain orientation. Wood for musical instruments, such as

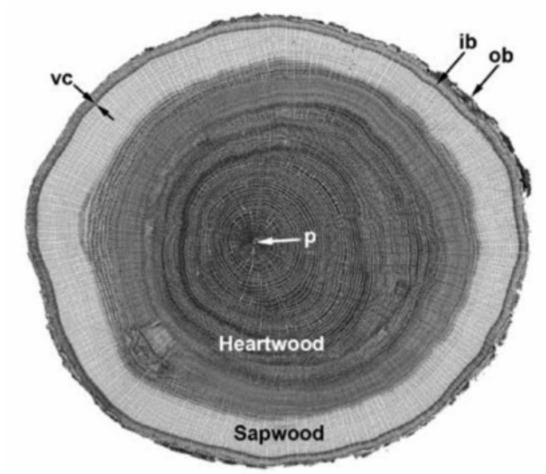

Fig. 2.2 Macrospcopical view from [233].

soundboards and plates, is generally referred to as quarter-sawn wood, meaning that the blanks are radially cut from the logs. A comparison between quarter sawn cutting and the standard plain sawn cutting is shown in Fig. 2.3. Despite most of string based musical instruments (e.g guitar, violin, piano, kantele, harpsichord) are generally built from quarter sawn wood [232], plain or flat sawn wood has been reported in the construction of the main components (e.g. soundboards, top and back plates, bridges) of different chordophones including the Koto or the Hammered Dulcimer [276, 210]. Overall, wood used for making musical instruments is generally referred to as tonewood.

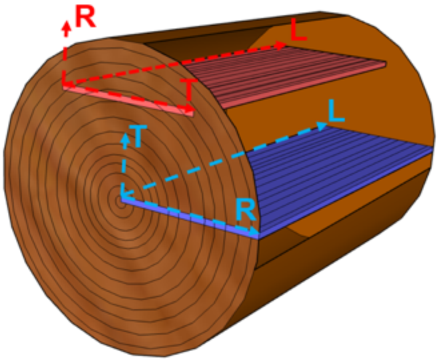

Fig. 2.3 Comparison of blanks cutting techniques. Quarter sawn (in blue) against plain sawn (in red) cutting. L,R,T respectively denote the longitudinal, radial and tangential directions relative to the fiber orientation.

Parameters values for different species			
Softwoods	**Abies alba**	**Picea abies**	**Pinus sylvestris**
Density (kg/m^3)	410	430	490
Cell dimensions: tracheids			
Length (mm)	4.3	2.9	3.1
Diameter (µm)	50	30	30
Cell percentage			
Tracheids	90	95	93
Parenchyma	Scarce	1.4–5.8	1.4–5.8
Rays	9.6	4.7	5.5
Hardwoods	**Fagus sylvatica**	**Quercus robur**	**Populus spp.**
Density (kg/m^3)	680	650	400
Cell dimensions: vessels			
Length (mm)	3–7	1–4	5–20
Diameter (µm)	5–100	10–400	20–150
Cell percentage			
Fibers	37	43–58	62
Vessels	31	24	27
Parenchyma	4.6	4.9	0
Rays	27	16–29	11

Table 2.1 Comparison of averaged cell dimensions values for some hardwoods and softwoods wood species from [46, p.2].

Microscopic view

Softwoods generally have a simpler microstructure, with only a couple of cell types dominating: tracheids and parenchyma cells. The first are long cells arranged in a longitudinal direction. These occupy most of the wood volume and are constituted by a primary and a secondary layer. The second layer is made of an additional three sublayers. While tracheids provide mechanical support and conduct water through the pits connecting the adjacent tracheids, their ordering significantly influence the wood mechanical properties [233, 270]. Ray parenchyma cells constitute only 5 to 10% of wood volume in softwoods. These are usually narrower in softwoods than in hardwoods, and they form the rays transverse to the annual rings. Axial parenchyma are also sometimes present in softwoods, but these are arranged as vertical strings of cells within the axial system [233]. In contrast, hardwoods are characterized by a much more complex structure, including characteristic parenchyma

Species	Density (kg/m^3)	Longitudinal Young Modulus (GPa)	Classification
Oak	660	5.3	Hardwoods
Beech	750	13.7	Hardwoods
Spruce	440	15.9	Softwood
Fir	450	12.7	Softwood
Scotch pine	550	16.3	Softwood

Table 2.2 Density and longitudinal Young's moduli of various wood species. Values taken from [46, p.46].

patterns, several fibers, tracheids, and vessels. Fibers provide the mechanical support, while vessels are responsible for water conduction [233, 243, 46]. An illustration of the structural complexity in the arrangement of hardwood cells compared to softwood is given in Figure 2.4.

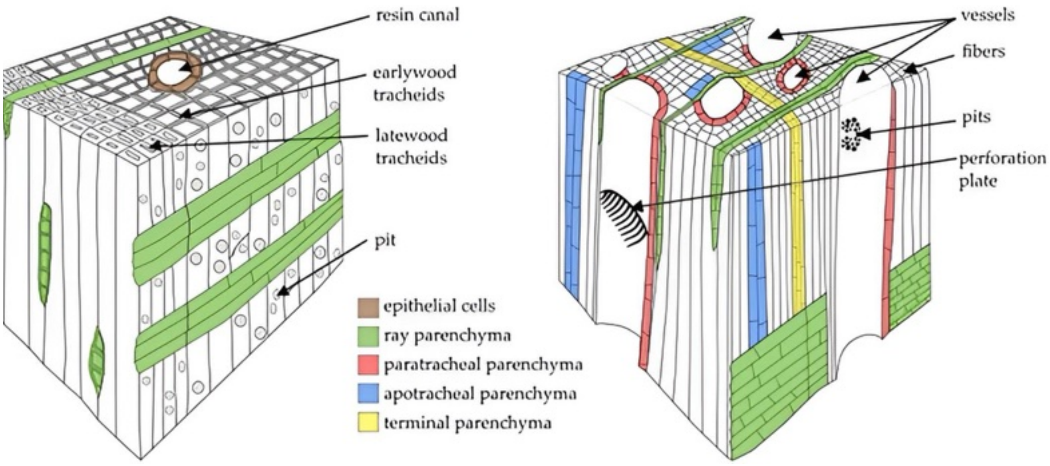

Fig. 2.4 Comparison between softwood (left) and hardwood (right) cells arrangement (left) reported in [243].

The material properties of the cell walls, together with their geometrical configuration, govern the macroscopic elastic behavior of wood [148]. At the scale of interest considered in this work, wood can be represented as an orthotropic continuum, as will be illustrated in the following sections.

2.2 Elastic and physical properties of tonewoods

Understanding the elastic behavior of wood is fundamental for analyzing the mechanical response and vibroacoustic performance of string-based musical instruments. This section introduces the elastic behavior of tonewood together with the main physical properties traditionally used to grade and quantify its acoustic performance. A discussion on the natural elastic properties variability in tonewoods and the main sources of uncertainties affecting their mechanical features is also given.

2.2.1 Wood elastic behavior

Stress and Strain

Elasticity describes a material's ability to return to its original shape after being deformed by an external force. Stress σ_{ij} is defined as the internal force per unit area acting within a material, while strain ε_{ij} represents the relative deformation of the material. Considering a given surface with orientation defined by axes i and j, the cross-sectional area is denoted as A_{ij} and the stress component is defined as:

$$\sigma_{ij} = \frac{F_j}{A_i} \tag{2.1}$$

The indices i and j represent directions within a three-dimensional Cartesian coordinate system and are chosen from the three orthogonal axes, conventionally labeled as $\{x, y, z\}$ (or equivalently $\{1, 2, 3\}$). F_j is the force component acting in the j direction and A_i is the area of the face normal to the i axis. If $i = j$ the corresponding stress component is normal to the surface. Conversely, if $i \neq j$ it represents a shear stress component.

In the context of an infinitesimal volume element, ε_{ij} defines the local displacement u in the i and j directions under deformation:

$$\varepsilon_{ij} = \left(\frac{\partial u_i}{\partial x_j} + \frac{\partial u_j}{\partial x_i} \right) \tag{2.2}$$

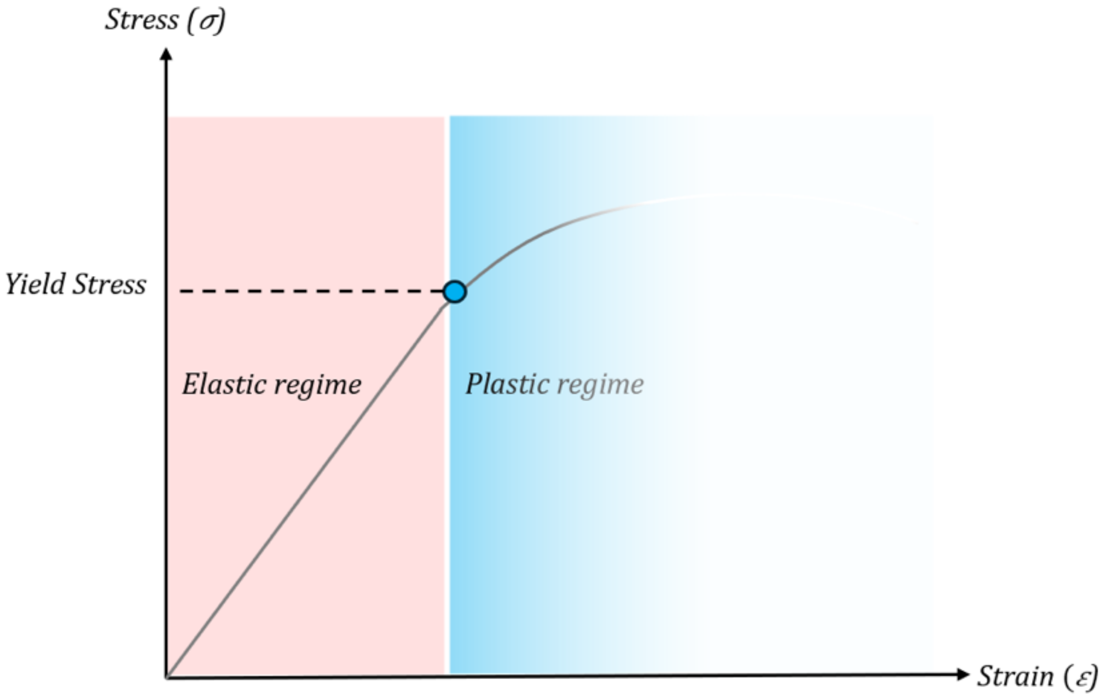

Fig. 2.5 Simplified visual representation of a stress-strain curve. The yield stress point marks the onset of plastic deformation. A more comprehensive explanation is offered in the relevant literature [194, 232].

As per the stress components, if $i = j$ the force is applied to the face normal to the i axis, resulting in axial deformation. On the other hand, if $i \neq j$, the force is applied transversely to the surface, causing shear strain. It is also worth noticing how the stress and strain tensors are considered symmetric, meaning that $\sigma_{ij} = \sigma_{ji}$ as well as $\varepsilon_{ij} = \varepsilon_{ji}$.

The relationship between stress and strain are crucial to characterize the elastic behavior of wood material properties. This is observed by the so called stress-strain curve. This is generally obtained by applying a fixed load to the specimen while measuring the deformation. From the curve, different material properties can be estimated, and the elastic regime can be identified. Within this region, stress and strain remain proportional and reversible. However, beyond a certain threshold, known as the yield point or stress, this proportionality breaks down. The corresponding stress value is called the yield stress (or yield strength), and it marks the onset of permanent, plastic deformation [194, 232]. An illustration of the yield stress point from the stress-strain curve is given in Figure 2.5. For wood and other orthotropic materials, this threshold is not uniform across all directions due to their orthotropic structure. Materials also exhibit a yield shear stress (or shear yield strength), which characterizes the material's resistance to permanent deformation under shear loading. Both yield stress and shear yield stress are essential in defining the design limits of wooden components under mechanical loading. They help establish failure criteria, thus guiding safety factors in structural applications, as it will be discussed in Chapter 6.

2.2.2 Mechanical properties

Young Modulus

The Young's Modulus, also known as the Modulus of Elasticity, is a measure of stiffness for an elastic material before plastic deformation occurs, i.e., until a proportional ratio can be maintained between stress and strain. Assuming uniaxial stress along the i component and strain components, it can be calculated by Hooke's law:

$$\sigma_{ii} = E_i \varepsilon_{ii} \tag{2.3}$$

Where E_i is the uniaxial Young modulus in the i direction. E_i is measured in Pascal (Pa).

Shear modulus

The shear modulus G_{ij} or modulus of rigidity quantifies a material's resistance to deformation under shear stress. It is measured in Pa and defined as:

$$\sigma_{ij} = G_{ij} \varepsilon_{ij} \tag{2.4}$$

Poisson's ratio

The Poisson ratio defines the transversal to the normal strain ratio, measuring the deformation of a solid body perpendicular to the loading direction, defined as:

$$\nu_{ij} = -\frac{\varepsilon_{ij}}{\varepsilon_{ii}} \tag{2.5}$$

Where the minus sign ensures that ν_{ij} remains positive. Accordingly, when $\varepsilon_{ii} > 0$ (axial elongation), $\varepsilon_{ij} < 0$ (transverse contraction), leading to a positive value for ν_{ij}.

When a full 3D deformation is considered, under the hypothesis of orthogonal anisotropy, the elasticity equations are described compactly as:

$$\begin{bmatrix} \varepsilon_{xx} \\ \varepsilon_{yy} \\ \varepsilon_{zz} \\ \varepsilon_{yz} \\ \varepsilon_{xz} \\ \varepsilon_{xy} \end{bmatrix} = \mathbf{S} \begin{bmatrix} \sigma_{xx} \\ \sigma_{yy} \\ \sigma_{zz} \\ \sigma_{yz} \\ \sigma_{xz} \\ \sigma_{xy} \end{bmatrix} \tag{2.6}$$

Where **S** contains the elastic constants:

$$\mathbf{S} = \begin{bmatrix} \frac{1}{E_x} & -\frac{\nu_{yx}}{E_y} & -\frac{\nu_{zx}}{E_z} & 0 & 0 & 0 \\ -\frac{\nu_{xy}}{E_x} & \frac{1}{E_y} & -\frac{\nu_{zy}}{E_z} & 0 & 0 & 0 \\ -\frac{\nu_{xz}}{E_x} & -\frac{\nu_{yz}}{E_y} & \frac{1}{E_z} & 0 & 0 & 0 \\ 0 & 0 & 0 & \frac{1}{G_{yz}} & 0 & 0 \\ 0 & 0 & 0 & 0 & \frac{1}{G_{zx}} & 0 \\ 0 & 0 & 0 & 0 & 0 & \frac{1}{G_{xy}} \end{bmatrix} \tag{2.7}$$

Because of the material symmetry, the following relations exist:

$$\frac{\nu_{ij}}{E_i} = \frac{\nu_{ji}}{E_j}, \quad \forall i, j \tag{2.8}$$

Thus, only three Poisson's ratios can be used and nine elastic constants are sufficient to fully characterize the material elastic behavior, namely $E_x, E_y, E_z, G_{xy}, G_{yz}, G_{zx}, \nu_{xy}, \nu_{yz}, \nu_{zx}$.

2.2.3 Physical properties

The above mentioned mechanical wood properties directly shape the corresponding acoustical features. In particular, the material density ρ, E_x and the internal damping have been identified as the key influencing material properties [288, 236, 277, 275]. The latter can be evaluated in terms of loss coefficient η, quality factor Q, logarithmic decrement δ or damping coefficient ξ [118, 209, 277, 220]. These are introduced in more detail in Section 2.3. Based on these material properties, a large variety of physical metrics have been established to classify tonewoods. Some of the main measures are reported in Table 2.3.

Parameter	Definition	Reference
$c = \sqrt{\frac{E}{\rho}}$	Speed of sound	[119]
$z = cp = \sqrt{E\rho}$	Material's impedance	[119]
$\delta = \log \frac{w(t)}{w(t+T)}$	Logarithmic decrement	[118, 225]
$Q = \frac{f_0}{f_2 - f_1}$	Quality factor	[118]
$\eta = \frac{1}{Q} = \frac{\delta}{\pi} = \tan\psi$	Loss coefficient	[277, 58]
$\frac{c}{\rho}$	Sound speed / density	[239]
$R = \frac{c}{\rho} = \sqrt{\frac{E}{\rho^3}}$	Sound radiation coefficient	[277]
$ACE = RQ = \sqrt{\frac{E}{\rho^3}}Q$	Acoustic conversion coefficient	[220, 288, 202]
$\frac{c}{\rho}$	Antivibration parameter	[288]
cQ	Transmission parameter	[288]
$\frac{E_L}{\rho}$	Specific modulus of elasticity in the longitudinal direction	[58, 275]
$\frac{E_R}{\rho}$	Specific modulus of elasticity in the radial direction	[275]
$\frac{G_{LR}}{\rho}$	Specific shear modulus in the longitudinal-radial plane	[275]

Table 2.3 Physical and Acoustical properties used to characterize tonewoods. Several of the reported parameters are described in detail in Section 2.3.

2.2.4 Impact of density variations, wood aging and wood moisture

Wood density ρ is primarily influenced by temperature, moisture content (MC), and the relative humidity (RH) of the surrounding air. In softwoods commonly used for musical instrument making, ρ typically ranges from 350 to 500 kg/m^3 [47]. This property has a significant impact on the mechanical rigidity of wood [270]. In general, a lower density is associated with higher values of Young's modulus E and, consequently, lower values of the damping factor η, which is generally desirable in tonewoods [277, 114, 49].

In tonewoods, ρ is closely linked to the distribution of annual growth rings, which results in local density variations within a single wood sample [187, 270]. These internal variations contribute to appreciable fluctuations in density even among pieces from the same wood species [275]. The overall wood structure, particularly the proportion of latewood to earlywood, has a significant impact on density. Latewood, being denser, increases ρ [233]. Therefore, tonewoods with minor density differences between earlywood and latewood are preferred to reduce scattering effects and improve uniformity [185, 275].

Generally, woods with high specific modulus (E/ρ) also tend to exhibit low internal damping [43]. This means that lightweight, stiff woods like resonance spruce lead to higher sound radiation coefficient R values but also exhibit moderate damping properties that are highly desirable for the soundboards of stringed musical instruments [231].

In addition to static mechanical properties, wood density significantly influences dynamic acoustic response parameters, including wave speed c, acoustic impedance z, and the sound radiation coefficient R. Specifically, a lower density enhances the R value. Wegst [277] highlighted that high R and low η are typical features of tonewoods, contributing to superior loudness and sound projection.

Wood aging also affects the density of tonewoods. One of the main consequences of long-term natural aging is altered moisture interaction: aged tonewoods typically become less hygroscopic, meaning they absorb and retain less water than fresh wood. Obataya (2017) demonstrated that aging leads to a lower equilibrium moisture content at any given RH, hence improving dimensional stability [199]. Structural changes due to aging restrict swelling under RH fluctuations—particularly relevant when analyzing historical instruments. As a result, aged wood often exhibits lower effective density compared to newer samples. This trend was experimentally confirmed in studies on naturally aged wood from historical buildings [257].

Accelerated aging through UV exposure has also been shown to reduce density significantly—by approximately 19% in spruce and 10% in maple—accompanied by corresponding changes in stiffness [129]. These reductions are more pronounced in softwoods such as spruce than in hardwoods like maple. Stoel and Borman [245] further observed that historical violins exhibited smaller density differences between earlywood and latewood than modern instruments, suggesting that natural aging may lead to a more uniform internal density.

However, aging also comes with drawbacks. Fracture resistance decreases, brittleness increases, and long-term durability may be compromised [157]. Noguchi et al. [195] noted that after approximately 121 years of natural aging, the longitudinal modulus E_L can begin to decline. Furthermore, aging and prolonged moisture exposure can foster conditions favorable to mold, blue stain fungi, and insect activity, all contributing to biodeterioration [47].

Wood is hygroscopic and naturally exchanges moisture with its environment. The moisture content (MC) significantly impacts its mechanical properties and is defined as the percentage of water relative to the dry mass:

$$MC = \frac{m_{wet} - m_{dry}}{m_{dry}} \times 100 \tag{2.9}$$

Here, m_{dry} is the oven-dry mass and m_{wet} is the mass at a given moisture content [233]. In freshly cut, or "green" wood, MC can range from 30% to over 200%, depending on the species. This is due to saturated cell walls and free water in the cell lumina [233]. Generally, it is recognized how relevant mechanical properties, such as the Young's modulus E, tend to decrease as MC increases [162, 219]. Borland [37] observed how the values of modal frequencies tend to drop at higher MC across guitar soundboards, while the same trend could not be identified for internal damping. The recent research conducted by Qiu et al. [219] on quarter-sawn spruce samples showed how the value of η tends to decrease for higher MC levels and the study highlighted how the loss factor also decreases as frequency increases. Korkmaz reported that each 1% increase in MC results in a 2.5% decrease in the bending modulus of elasticity [155]. Studies by Palka [204] and Guitard [128] showed that elastic constants (E_{ij}, G_{ij}, ν_{ij}) also vary with MC, with E_R and E_T more affected than E_L. Viala et al. [270] summarized that a maximum of 3% change in these moduli occurs per 1% increase in MC.

Typical MC values for string instruments under normal concert hall conditions range between 7% and 12% [47]. Borland [37] found that modal parameters of guitar soundboards (frequencies and damping) vary by no more than 2% within this range. Qiu et al. [219] investigated how MC from 2% to 12% affects quarter-sawn Sitka spruce and Indian rosewood tonewood samples. First-order resonance frequencies and amplitude ratios decreased by 6.67%–7.63% and 13.84%–31.43%, respectively. Longitudinal modulus E_L also decreased by 4.40%–6.38% at 12% MC. More significant variations were observed in derived properties: the specific modulus E_L/ρ dropped by 12.90%–14.66%, and the acoustic conversion efficiency (ACE) fell by over 40% across all samples.

Finally, changes in MC are directly linked to changes in wood density. The density at a given MC level, ρ_{wet}, can be estimated as [159]:

$$\rho_{wet} = \rho_{dry} \left(\frac{1 + MC}{1 + 0.84\, \rho_{dry}\, MC} \right) \tag{2.10}$$

where ρ_{dry} is the oven-dry density Qiu et al. [219] observed that increasing MC from 2% to 12% led to a ~10% increase in density in both spruce and rosewood. Viala, Placet, and Cogan also reported an approximate 1% increase in ρ for every 1% increase in MC [273]. From a psychoacoustics point of view, Borland [37] investigated in his work Just Noticeable Difference (JND) levels in MC to be perceptible by participants via listening tests. The results showed how a 0.7 % variation in MC could lead to a 1 % difference in the material's elastic properties and a perceived tonal difference in the proposed sound samples, thus highlighting the impact of MC. While this thesis does not address the matter of ageing wood in detail, a brief case study will be presented in Section 3.7 comparing the elastic properties of aged and not aged tonewoods. Nevertheless, it is relevant for the scope of this work to conceptually stress how wood ageing can indeed represent a source of uncertainty when characterizing material properties of historical artefacts.

2.3 Modal properties

While the above-mentioned mechanical features have been generally used to characterize and cluster different wood types or families [277], a frequency-dependent analysis is necessary to characterize the dynamical behavior of a musical instrument. Furthermore, as observed from the literature review in Section 1.2, modal parameters are fundamental in retrieving the material properties of a specific musical instrument component in a non-destructive manner through dynamical testing (see Section 1.3). Modal parameters are namely referred to as natural frequencies, modal damping, and modal shapes [98, 234]. Their definitions are provided in this section. By recalling the equation of motion for an n-degree-of-freedom (DOF) linear mechanical system:

$$\mathbf{M}\frac{\partial^2 \mathbf{w}}{\partial t^2} + \mathbf{C}\frac{\partial \mathbf{w}}{\partial t} + \mathbf{K}\mathbf{w} = \mathbf{F}(t) \tag{2.11}$$

Where $\mathbf{M}, \mathbf{C}$ and $\mathbf{K}$ are the mass, damping, and stiffness matrices, respectively, $\mathbf{w}$ is the displacement vector, and $\mathbf{F}(t)$ represents an external force. For an undamped and free vibration (i.e. $\mathbf{C} = 0, \mathbf{F}(t) = 0$), seeking harmonic solutions of the form:

$$\mathbf{w} = \phi e^{i\omega t} \tag{2.12}$$

And substituting (2.12) into (2.11), leads to the eigenvalue problem:

$$(\mathbf{K} - \omega^2 \mathbf{M})\phi = 0 \tag{2.13}$$

Which can then be solved for specific natural frequencies ω and associated mode shapes ϕ.

Natural frequency

From (2.13), each mode has a specific angular frequency ω_n expressed in radians per second (rad/s). This is a measure of the angular rate of vibration and it is related to the natural frequency f_n in Hertz by:

$$f_n = \frac{\omega_n}{2\pi}. \tag{2.14}$$

Mode damping

Modal damping assesses how quickly the vibrational energy of a mode is dissipated. Many metrics can be used to directly quantify damping, some of the mentioned parameters from the previous section (see Section 2.2.3) are here discussed in more detail.

The Quality factor Q is defined as :

$$Q = \frac{f_0}{f_2 \; - f_1} \tag{2.15}$$

which defines the ratio between the central frequency f_0 and the resonance width $f_2 - f_1$ (or Δf), where f_2 and f_1 are the values of the two frequencies whose vibrational amplitude drops to $1/\sqrt{2}$ of its maximum value.
The logarithmic decrement δ is defined as:

$$\delta = \log \frac{w(t)}{w(t+T)} \tag{2.16}$$

It quantifies damping from the temporal response of the system by taking the logarithm of the ratio of two amplitudes from consecutive peaks, denoted here as $w(t)$ and $w(t+T)$ where $T = 2pi/\omega$ is the period of oscillation. This parameter relates to the damping ratio ζ by:

$$\zeta = \frac{\delta}{\sqrt{4\pi^2 \; + \delta^2}} \tag{2.17}$$

Lastly, the decay time (or reverberation time) t_{60} defines the time required for a sound signal to decay by 60 decibels (dB), and it is also widely used in room and architectural acoustics [143]. It is expressed as:

$$t_{60} = 3\log(10)\tau \tag{2.18}$$

Where $\tau = 1/\zeta\omega_0$ denotes an exponential decay rate [225].

Mode shapes

Finally, the mode shape ϕ_n from (2.13) describes the deformation pattern of a structure at the same natural frequency f_n across multiple points on the system. Mode shapes are determined by the system's geometry, material properties, and BCs. Mode shapes may be expressed as single values when measured at one point on the structure, or as vectors containing complex amplitudes at multiple points, which can be further decomposed into magnitude and phase information, hence describing how different parts of the system move relative to each other [225, 270]. Mode shapes of musical instruments, plates, and soundboards can be experimentally determined through EMA measurement setups or analytically by utilizing numerical approximation techniques, which will be discussed in the following sections.

2.3.1 Frequency Response Function

An FRF describes the ratio between the output response of a structure under test and an applied input force in the frequency domain. In the context of this thesis, an FRF enables the acquisition of the modal behavior of a soundboard or musical instrument plates, specifically their natural frequencies, modal damping, and mode shapes.

For forced vibration response, the equation of motion can be solved to obtain a complete solution, denoted in the frequency domain as the frequency response matrix $H(\omega)$. Each $H_{jk}(\omega)$ represents the frequency response of the system at a DOF j as a consequence of an applied harmonic force $F_k(\omega)$ at a DOF k These FRFs are complex-valued functions encompassing both magnitude and phase. Using the system modal properties, each FRF is described as a sum of modal contributions [98]:

$$H_{jk}(\omega) = \sum_{r=1}^{N} \frac{A_{jk}^{r}}{\lambda_r^2 - \omega^2} \tag{2.19}$$

where λ_r represents the eigenvalue - containing both the natural frequencies and damping values - of the r^{th} mode while A_{jk}^{r} is the modal constant determined from the associated mode shapes. This modal constant is constructed from the r^{th} eigenvector $\{\boldsymbol{\phi}\}_r$ as

$$A_{jk}^{r} = \phi_{jr}\phi_{kr}, \tag{2.20}$$

with ϕ_{jr} denoting the j^{th} component of the r^{th} mode shape. This formulation offers a clear illustration relating all the modal properties of the system.

Experimentally, the FRF can be gathered by exciting the structure with a harmonic input force $F(t)$ and measuring the response signals. The FRF can then be expressed in the frequency domain as:

$$H_{jk}(\omega) = \frac{X_j(\omega)}{F_k(\omega)} \tag{2.21}$$

Where $X_j(\omega)$ and $F_k(\omega)$ denote the frequency spectra of the measured response and input forcing signals [98]. Depending on the transducers used to acquire the response signal, the FRF can be described as compliance (displacement / force), mobility (velocity/force), accelerance or inertance (acceleration/force), dynamic stiffness (1/compliance), impedance (1/mobility), or dynamic mass (1/accelerance) [235]. It is worth noting that, in practice, at each frequency peak observed in the FRF, a phase shift occurs, resulting in a phase decrease of 180°. Conversely, each frequency minimum (also known as anti-resonance) corresponds to a phase shift of 180° [14].

2.4 Plate models

When modeling the behavior of plate-like structures, the choice of model depends on the thickness. The following section introduces two classical plate theories: the KL model,and the Mindlin–Reissner (MR) model. The first is suitable for thin plates where transverse shear deflection can be neglected. While it represents a standard model choice thanks to its efficiency [30, 74, 123, 132, 258] it can lead to modeling errors as the plate thickness increases due to the presence of shear and rotary inertia effects [62]. On the other hand, the Mindlin-Reissner theory [228, 189] provides a more comprehensive model taking into account shear effects and rotary inertia in plates. Although the two mathematical models are laid out here, a more thorough and practical discussion is available in Chapter 5.4 where an example of dispersion relations is presented for an orthotropic rectangular plate in Figure 5.1 and a case study is considered (see section 5.7) highlighting the impact of different modelling assumptions on plate-like structures.

2.4.1 Kirchhoff-Love equation

The KL theory is the classical model for thin elastic plates, extending the Euler–Bernoulli beam assumptions to two dimensions. It assumes the plate's thickness is small compared to its planar dimensions. The key kinematic hypotheses imply that plane sections normal to the mid-surface remain plane and normal to the mid-surface during deformation. Transverse shear deformation is neglected meaning that a line initially perpendicular to the mid-plane does not rotate relative to the mid-surface as the plate bends. Let coordinates (x,y) define the mid-plane of the plate and z the thickness coordinate. The transverse deflection of the mid-surface is denoted by $w(x,y,t)$. Under KL assumptions, the displacement field is expressed as [89]:

$$u_x(x,y,z,t) = -z\frac{\partial w}{\partial x}, \quad u_y(x,y,z,t) = -z\frac{\partial w}{\partial y}, \quad u_z(x,y,z,t) = w(x,y,t).$$

Here u_x, u_y are the in-plane displacements and u_z is the transverse displacement.
Figure 2.6 illustrates the main KL assumptions for a plate section undergoing deformation, where the straight lines perpendicular to the mid-surface remain straight to it after deformation, implying that transverse shear deformation is neglected. Because the KL assumptions

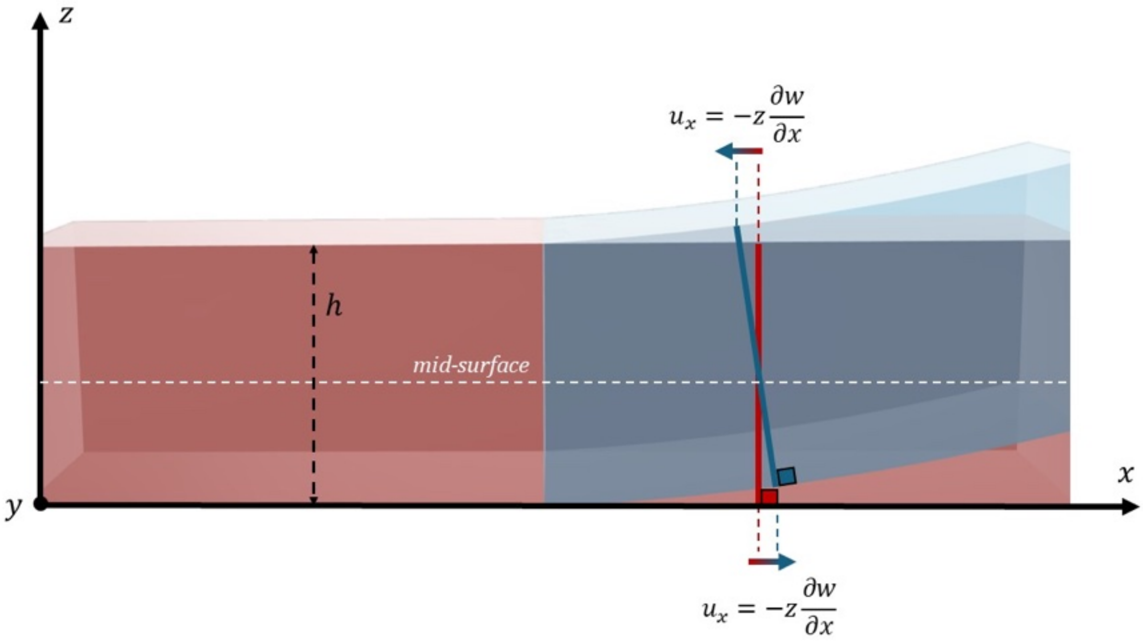

Fig. 2.6 Illustration of KL kinematic assumptions. The deformation is illustrated in light blue. The straight lines remain normal to the mid-surface after deformation. Figure inspired from [89].

state that straight lines initially normal to the mid-surface remain straight and normal to the mid-surface during deformation, the transverse shear strain vanishes:

$$\varepsilon_{xz} = \varepsilon_{yz} = 0. \tag{2.22}$$

Furthermore, the stress component normal to the mid-surface is neglected so that:

$$\sigma_{zz} = 0. \tag{2.23}$$

The only nonzero strains are the in-plane normal ($\varepsilon_{xx}, \varepsilon_{xx}$) and shear ($\varepsilon_{xy}, \varepsilon_{yx}$) strains due to bending curvatures. For small deflections, the strain-displacement relations yield :

$$\begin{aligned} \varepsilon_{xx} &= \frac{\partial u_x}{\partial x} = -z\frac{\partial^2 w}{\partial x^2}, \\ \varepsilon_{yy} &= \frac{\partial u_y}{\partial y} = -z\frac{\partial^2 w}{\partial y^2}, \\ \varepsilon_{xy} = \varepsilon_{yx} &= \frac{\partial u_x}{\partial y} + \frac{\partial u_y}{\partial x} = -2z\frac{\partial^2 w}{\partial x \partial y}. \end{aligned} \tag{2.24}$$

For a linearly elastic orthotropic plate under plane stress, Hooke's law reads:

$$\begin{bmatrix} \sigma_{xx} \\ \sigma_{yy} \\ \sigma_{xy} \end{bmatrix} = \begin{bmatrix} \frac{E_x}{1-\nu_{xy}\nu_{yx}} & \frac{\nu_{yx}E_x}{1-\nu_{xy}\nu_{yx}} & 0 \\ \frac{\nu_{xy}E_y}{1-\nu_{xy}\nu_{yx}} & \frac{E_y}{1-\nu_{xy}\nu_{yx}} & 0 \\ 0 & 0 & G_{xy} \end{bmatrix} \begin{bmatrix} \varepsilon_{xx} \\ \varepsilon_{yy} \\ \varepsilon_{xy} \end{bmatrix} \tag{2.25}$$

approximating 2.6 under KL assumptions. Here E_x, E_y are Young's moduli in x and y directions, ν_{xy}, ν_{yx} are Poisson's ratios, and G_{xy} is the in-plane shear modulus. Orthotropy symmetry implies $\nu_{xy}E_y = \nu_{yx}E_x$.

The linear stress distribution from (2.25) produces bending moments, obtained by integrating the stress components over the homogeneous thickness h:

$$\begin{aligned} M_x(x,y) &= \int_{-h/2}^{h/2} z\,\sigma_{xx}(x,y,z)\,dz, \\ M_y(x,y) &= \int_{-h/2}^{h/2} z\,\sigma_{yy}(x,y,z)\,dz, \\ M_{xy}(x,y) &= \int_{-h/2}^{h/2} z\,\sigma_{xy}(x,y,z)\,dz. \end{aligned} \tag{2.26}$$

Here, M_x is the bending moment per unit length acting on a section normal to x (curving the plate in the x-direction), M_y is the bending moment per unit length on a section normal to y, and M_{xy} is the twisting moment per unit length.

Substituting into (2.26) yields:

$$\begin{bmatrix} M_x \\ M_y \\ M_{xy} \end{bmatrix} = - \begin{bmatrix} D_x & \nu_{yx} D_x & 0 \\ \nu_{xy} D_y & D_y & 0 \\ 0 & 0 & D_s \end{bmatrix} \begin{bmatrix} \dfrac{\partial^2 w}{\partial x^2} \\ \dfrac{\partial^2 w}{\partial y^2} \\ \dfrac{\partial^2 w}{\partial x \partial y} \end{bmatrix} \tag{2.27}$$

where the bending rigidities are:

$$D_x = \frac{E_x h^3}{12\,(1 - \nu_{xy}\nu_{yx})}, \quad D_y = \frac{E_y h^3}{12\,(1 - \nu_{xy}\nu_{yx})}, \quad D_s = \frac{G_{xy} h^3}{3}. \tag{2.28}$$

These constants encompass the orthotropic elastic properties and the cubic dependence on thickness h typical of bending stiffness. In the KL assumptions, shear forces F_x and F_y follow from moment equilibrium of an infinitesimal plate element [134]:

$$F_x = -\frac{\partial M_x}{\partial x} - \frac{\partial M_{xy}}{\partial y}, \quad F_y = -\frac{\partial M_{xy}}{\partial x} - \frac{\partial M_y}{\partial y}. \tag{2.29}$$

The equilibrium in the transverse direction is expressed as:

$$\frac{\partial F_x}{\partial x} + \frac{\partial F_y}{\partial y} + \mathscr{F}(x,y,t) = \rho h \frac{\partial^2 w}{\partial t^2}, \tag{2.30}$$

where $\mathscr{F}$ is the distributed transverse load and ρh is the mass per unit area. Eliminating F_x and F_y from (2.30) using (2.29) gives:

$$\frac{\partial^2 M_x}{\partial x^2} + 2\frac{\partial^2 M_{xy}}{\partial x \partial y} + \frac{\partial^2 M_y}{\partial y^2} + \mathscr{F}(x,y,t) = \rho h \frac{\partial^2 w}{\partial t^2}. \tag{2.31}$$

Substituting the moment–curvature relations from Eq. (2.27):

$$
\begin{aligned}
M_x &= -D_x \frac{\partial^2 w}{\partial x^2} - \nu_{yx} D_x \frac{\partial^2 w}{\partial y^2}, \\
M_y &= -\nu_{xy} D_y \frac{\partial^2 w}{\partial x^2} - D_y \frac{\partial^2 w}{\partial y^2}, \\
M_{xy} &= -\frac{D_s}{2} \frac{\partial^2 w}{\partial x \partial y},
\end{aligned}
$$

into Eq. (2.31)yields the governing equation for a homogeneous orthotropic Kirchhoff–Love plate:

$$
D_x \frac{\partial^4 w}{\partial x^4} + (\nu_{yx} D_x + \nu_{yx} D_y + D_s) \frac{\partial^4 w}{\partial x^2 \partial y^2} + D_y \frac{\partial^4 w}{\partial y^4} + \mathscr{F}(x,y,t) = \rho h \frac{\partial^2 w}{\partial t^2}. \tag{2.32}
$$

Setting $\mathscr{F}(x,y,t) = 0$ for an unforced response, by rearranging and collecting terms, the system can be written as:

$$
\rho h \frac{\partial^2 w}{\partial t^2} = -\left(D_x \left(\frac{\partial^4 w}{\partial x^4} + \nu_{yx} \frac{\partial^4 w}{\partial x^2 \partial y^2} \right) + D_y \left(\frac{\partial^4 w}{\partial y^4} + \nu_{xy} \frac{\partial^4 w}{\partial x^2 \partial y^2} \right) + D_s \frac{\partial^4 w}{\partial x^2 \partial y^2} \right) w. \tag{2.33}
$$

For a unique solution, BCs are imposed along the plate's edges. Classic BCs are defined for the KL plate model as [80]:

$$
\begin{aligned}
\text{Free} : M_{nn} &= F_n = 0, \\
\text{Simply-Supported} : w &= M_{nn} = 0, \\
\text{Clamped} : w &= \frac{\partial w}{\partial n} = 0.
\end{aligned} \tag{2.34}
$$

Where $\hat{n}$ here represents the normal direction to the boundary.

Dispersion relation

Assuming an harmonic plane wave solution of the form

$$
w(x,y,t) = w_0 e^{j(\omega t - k_x x - k_y y)}, \tag{2.35}
$$

where w_0 is the (complex) amplitude, ω is the angular frequency, and k_x, k_y are the wavenumber components in the x- and y-directions, respectively.

Substituting (2.35) into Eq. (2.33) and applying these rules gives the dispersion relation for a homogeneous orthotropic Kirchhoff–Love plate:

$$\rho h\,\omega^2 = D_x(k_x^4 + \nu_{yx}k_x^2k_y^2) + D_y(k_y^4 + \nu_{xy}k_x^2k_y^2) + D_s k_x^2 k_y^2. \tag{2.36}$$

Equation (2.36) relates the angular frequency ω to the wavevector components (k_x, k_y), showing the dependence of the flexural wave speed on both direction and orthotropic stiffnesses.

2.4.2 Mindlin-Reissner model

The Mindlin-Reissner (MR) model generalizes the KL equation for thicker plates by:

- allowing cross sections initially assumed normal to the mid-surface of the plate to rotate during motion, thus
- accounting for transverse shear deformation and rotary inertia.

The displacements unknowns are here represented by the transverse deflection w and the two shear angles along the x and y axes, here denoted as ψ_x and ψ_y respectively.

For a homogeneous orthotropic plate, the MR equations can be written as a coupled system for (ψ_x, ψ_y, w).

For a free orthotropic plate, the Mindlin–Reissner equations used here are

$$\begin{aligned}
D_x\frac{\partial^2\psi_x}{\partial x^2} + \nu_{yx}D_x\frac{\partial^2\psi_y}{\partial x\partial y} + \frac{D_s}{2}\frac{\partial^2\psi_x}{\partial y^2} + \kappa^2 G_{xz}h\left(\psi_x + \frac{\partial w}{\partial x}\right) &= \frac{\rho h^3}{12}\frac{\partial^2\psi_x}{\partial t^2},\\
D_y\frac{\partial^2\psi_y}{\partial y^2} + \nu_{xy}Dy\frac{\partial^2\psi_x}{\partial x\partial y} + \frac{D_s}{2}\frac{\partial^2\psi_y}{\partial x^2} + \kappa^2 G_{yz}h\left(\psi_y + \frac{\partial w}{\partial y}\right) &= \frac{\rho h^3}{12}\frac{\partial^2\psi_y}{\partial t^2},\\
\kappa^2 G_{xz}h\left(\frac{\partial\psi_x}{\partial x} + \frac{\partial w}{\partial x}\right) + \kappa^2 G_{yz}h\left(\frac{\partial\psi_y}{\partial y} + \frac{\partial w}{\partial y}\right) &= \rho h\frac{\partial^2 w}{\partial t^2}.
\end{aligned} \tag{2.37}$$

G_{xz} and G_{yz} are the transverse shear moduli and κ is the shear correction factor, typically ≈ 0.9 [124].

The BCs for the MR model can be described as [4, 130]:

$$\begin{aligned}
\text{Free}: M_n = F_n = M_t &= 0,\\
\text{Simply-Supported}: w = M_n = \psi_t &= 0,\\
\text{Clamped}: w = \psi_n = \psi_t &= 0.
\end{aligned} \tag{2.38}$$

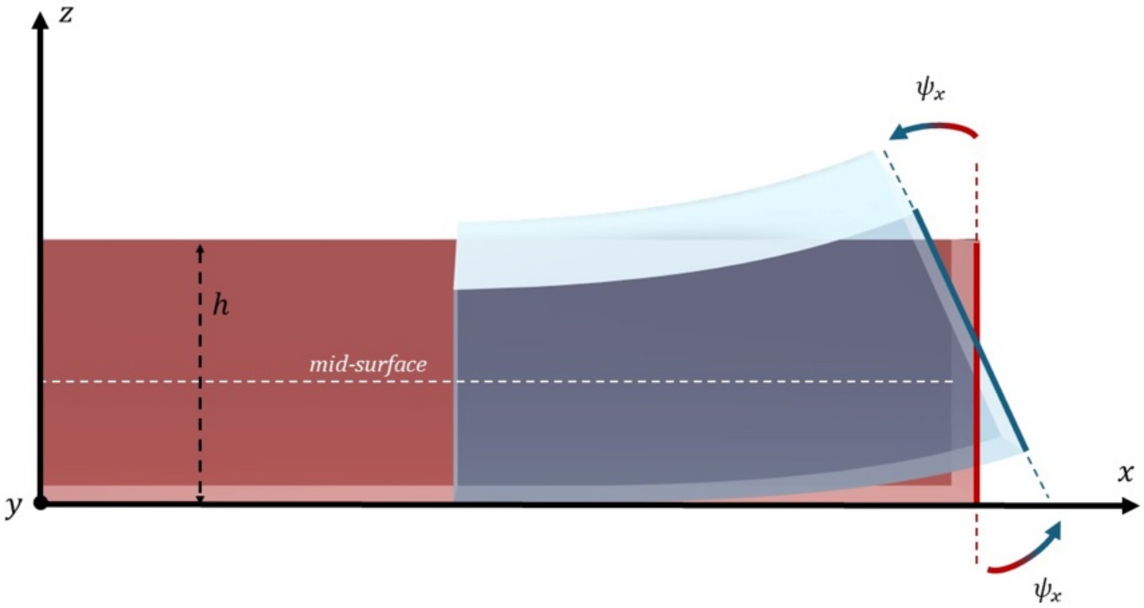

Fig. 2.7 Illustration of the shear angle ψ_x from the MR theory. The straight lines do not remain normal to the mid-surface after deformation. Figure inspired from [89].

As above, n represents the normal direction to the boundary while t represents the tangential direction to the boundary.

Dispersion relation

Considering harmonic plane waves solutions of the form:

$$\psi_x(x,y,t) = \psi_{x0} e^{j(\omega t - k_x x - k_y y)}, \quad \psi_y(x,y,t) = \psi_{y0} e^{j(\omega t - k_x x - k_y y)}, \quad w(x,y,t) = w_0 e^{j(\omega t - k_x x - k_y y)}, \tag{2.39}$$

It converts (2.37) into the algebraic system:

$$\left(K(k_x,k_y) - \omega^2 M\right)\mathbf{u} = 0, \qquad \mathbf{u} = [\psi_{x0}, \psi_{y0}, w_0]^T. \tag{2.40}$$

This can be solved for ω given input k_x, k_y. It is worth stressing how Equation (2.40) relates the angular frequency ω to the wavevector components (k_x, k_y) through the eigenvalues of the system matrix, yielding three dispersion branches corresponding to the coupled flexural–shear modes of the plate. An illustration of the three branches is provided in Section 5.

2.5 Numerical techniques for modal analysis

Numerical modeling provides a valuable tool for the modal analysis of orthotropic plate-like components, such as musical instrument soundboards. These methods allow for evaluating the impact of material properties, plate geometries, and boundary conditions in a fully contactless manner. As discussed in Section 1.3.2, FEM-based analysis offers high flexibility and capability to handle more complex geometries, thanks to its formulation based on shape functions, which enable the interpolation of displacement between nodal points within each subdomain, called an element [227, 150]. On the other hand, FDM approaches provide a simpler and more direct computational framework for structures with regular geometries. Specifically, the formulation on a uniform grid avoids the use of shape functions and element assembly, making them well-suited for efficient simulation of simplified plate models [30, 5].

2.5.1 Conceptual comparison of FEM and FDM

Both FEM and FDM are used to approximate the partial differential equations (PDEs) defined in (2.32) and (2.37), transforming them into systems of algebraic equations. In FDM, the domain is discretized into a regular grid, and the differential operators are replaced with finite difference stencils. Derivatives are approximated by computing differences between neighboring grid points [30], allowing for straightforward updates of nodal displacements using only local information. This approach applies the governing equations directly at discrete points.In FEM, the weak form of the PDEs is derived by multiplying by test functions and integrating over the domain. This leads to the assembly of a global system of equations discretizing the entire domain through elements, and the solution is approximated by a combination of shape functions [227, 250]. Overall, while FDM builds the solution through local operations at each grid point, FEM adopts a variational formulation that ensures the governing equations are satisfied over the entire domain. The two methods are therefore conceptually different: FDM performs local approximations at discrete nodes, whereas FEM constructs a global approximation over the domain [125]. An illustrated comparison of the two techniques is provided in Figure 2.8. An illustrated comparison of the two techniques is provided in Figure 2.8.

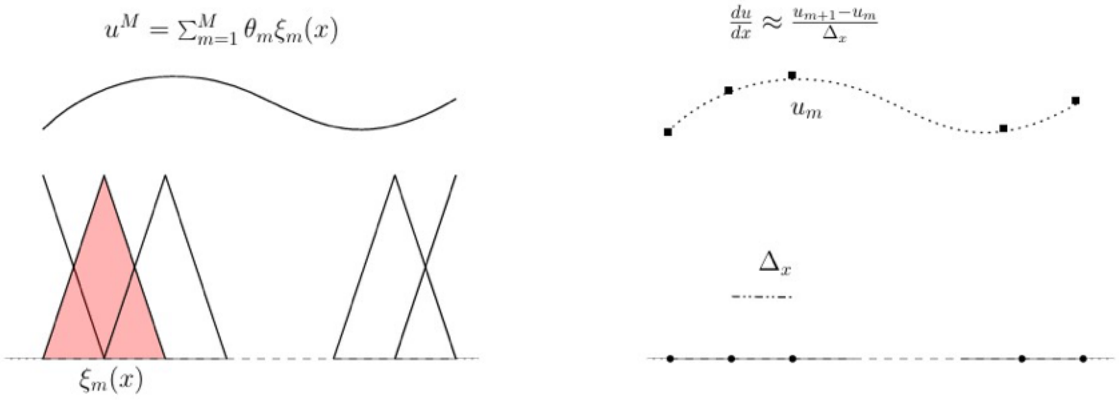

Fig. 2.8 Illustrated comparison between FEM (on the left) and FD (on the right) discretizations. While FEM approximates the solution via a finite sum of test functions over each element, FD discretizes the differential operators on a structured grid of nodal points. Figure taken from [81].

Both FEM and FDM ultimately discretize the PDEs into a second-order system of the form given in (2.41), where damping and forcing terms may be omitted in the case of undamped, free vibration, resulting in:

$$\mathbf{M}\frac{\partial^2 \mathbf{w}}{\partial t^2} + \mathbf{K}\mathbf{w} = 0 \tag{2.41}$$

Where damping can be later introduced through an additional matrix **C** if required.

Chapter 3

Elastic constants estimation via a least-squares

As discussed in Sections 1.2 and 1.3, a wide variety of techniques have been developed to retrieve the mechanical and physical properties of musical instrument plates. While traditional methods have proved accurate, their implementation often requires specialized equipment and controlled laboratory conditions, which can limit their accessibility in practical restoration and instrument-making contexts. This chapter introduces a flexible and resource-efficient methodology for estimating the orthotropic elastic constants of wooden plates. The goal is to offer a flexible and accurate estimation method applicable to tonewood samples as well as musical instruments' plate-like components. Sections 3.2 and 3.3 lay out the full process. Numerical benchmarking results are then provided in Section 3.4 together with a comparison with classical literature methods given in Section 3.5. Finally, a first experimental validation of the estimation procedure is presented in Section 3.6 and an applied case scenario is described in Section 3.7. The method introduced here has also been published and presented in the form of conference paper and journal article [88, 83].

3.1 Introduction

In the field of elastic property estimation, inverse parameter estimation encompasses a broad range of approaches in which unknown constants are inferred by comparing experimental observations with predictions obtained from numerical models [268, 140, 18]. The experimental procedure proposed here aims at delivering an accurate and reliable technique capable of quantifying the variability of elastic parameters among wood samples of the same type, thereby enabling more precise numerical material models. Building on the classical methods of McIntyre and Woodhouse [183], Caldersmith and Freeman [53], and subsequent developments such as Igea and Cicirello [140] discussed in Section 1.2, the present work introduces an extension overcoming existing limitations. Specifically, starting from the KL thin-plate assumptions, a linear dependence of the squared modal frequencies on the elastic constants is shown, and the linear coefficients are extracted from a set of numerical plates, here referred to as *training plates* sharing the same BCs and aspect ratios as the experimental plate under test. A least-square minimization is run to estimate the elastic constants. The method eliminates the exclusive reliance on free BCs or predetermined mode selections, thus offering greater flexibility. Moreover, by formulating the problem in a linear framework, the need for nonlinear optimization—where convergence and uniqueness are not always guaranteed [51]—is avoided. Consequently, the estimation only requires the knowledge of the experimental modal frequencies and their associated deformation patterns, encouraging the validation of more accessible measurement techniques in the experimental stage.

3.2 Non-dimensional model

From the governing equation for an orthotropic thin plate in Equation (2.33), one can acknowledge how several parameters are involved. Attempting to invert that system could be impractical considering the many unknowns and the risk of non-unique solutions. Even though for certain computational applications, such as in machine learning contexts, accuracy in the predicting features is prioritized over results interpretability [96], within this thesis a meaningful physical interpretation is required both to guarantee a plausible materials characterization of the numerical models as well as to support conservation decision making protocols. This can be achieved by reducing the amount of independent parameters and so simplifying the model through a scaling process [30]. To simplify the governing relation (2.33), both sides can be divided by ρh, and the term D_s is factored on the right-hand side, leading to the following expression:

$$\frac{\partial^2 w}{\partial t^2} = -\gamma^2 \Big(\frac{\partial^4 w}{\partial x^4} + \nu_{yx} \frac{\partial^4 w}{\partial x^2 \partial y^2} \Big) p + \Big(\frac{\partial^4 w}{\partial y^4} + \nu_{xy} \frac{\partial^4 w}{\partial x^2 \partial y^2} \Big) r + \frac{\partial^4 w}{\partial x^2 \partial y^2} \Big) w, \tag{3.1}$$

Where $\gamma^2 = \rho^{-1} h^{-1} D_s$, $p := D_s^{-1} D_x$, $q := D_s^{-1} D_y$. Then, dimensionless variables are introduced as:

$$w = A^{\frac{1}{2}}\, \bar{w},\ x = A^{\frac{1}{2}}\, \bar{x},\ y = A^{\frac{1}{2}}\, \bar{y},\ t = \gamma^{-1} A \bar{t}, \tag{3.2}$$

Where the non-dimensional variable is denoted by the overbar and $A = L_x L_y$ is the plate surface area. Substituting these into (3.1), it becomes:

$$\frac{\partial^2 \overline{w}}{\partial \overline{t}^2} = -\left(\left(\frac{\partial^4 \overline{w}}{\partial \overline{x}^4} + \nu_{yx}\frac{\partial^4 \overline{w}}{\partial \overline{x}^2 \partial \overline{y}^2}\right)p + \left(\frac{\partial^4 \overline{w}}{\partial \overline{y}^4} + \nu_{xy}\frac{\partial^4 \overline{w}}{\partial \overline{x}^2 \partial \overline{y}^2}\right)q + \frac{\partial^4 \overline{w}}{\partial \overline{x}^2 \partial \overline{y}^2}\right)\overline{w}, \tag{3.3}$$

defined over the non-dimensional domain $\bar{\mathscr{V}} = \{(\bar{x},\bar{y}) \,|\, 0 \leq \bar{x} \leq \alpha^{\frac{1}{2}}, 0 \leq \bar{y} \leq \alpha^{-\frac{1}{2}}\}$, with $\alpha := L_y^{-1} L_x$ denoting the aspect ratio of the plate. Equation (3.3) depends only on the two ratios p, q, as well as α. The dispersion relation for the non-dimensional orthotropic KL model then looks as:

$$\bar{\omega}^2 = (\bar{k}_{\bar{x}}^4 + \nu_{yx}\bar{k}_{\bar{x}}^2\bar{k}_{\bar{y}}^2)\,p + (\bar{k}_{\bar{y}}^4 + \nu_{xy}\bar{k}_{\bar{x}}^2\bar{k}_{\bar{y}}^2)\,q + \bar{k}_{\bar{x}}^2\bar{k}_{\bar{y}}^2, \tag{3.4}$$

If p and q are kept fixed, the scaling only depends on the BCs and α. Conversely, by fixing the set of BCs and α while varying the material elastic constants via p and q, a linear dependence is assumed as:

$$\bar{\omega}_{m,n}^2 = a_{m,n}\,p + b_{m,n}\,q + c_{m,n}, \tag{3.5}$$

Where $(a_{m,n}, b_{m,n}, c_{m,n}) \geq 0$ represent the modal dependent coefficients and $m,n \in \mathbb{N}$ denote a pair of indices associated to the nodal lines of each mode in the x and y directions on the surface of the plate. A similar relationship for the fundamental frequency of rectangular plates only was already shown by Leissa in [167] (Chapter 9). The dimensional frequencies can be obtained as:

$$\omega_{m,n}^2 := \gamma^2 A^{-2}\bar{\omega}_{m,n}^2 = D_s\,\rho^{-1} h^{-1} A^{-2}\bar{\omega}_{m,n}^2. \tag{3.6}$$

Finally, by substituting (3.5) into (3.6):

$$\omega_{m,n}^2 = \lambda\left(a_{m,n}D_x + b_{m,n}D_y + c_{m,n}D_s\right), \tag{3.7}$$

with $\lambda := \rho^{-1}h^{-1}A^{-2}$.

3.3 Least-Square problem formulation

The goal of the presented method is to estimate the unknown plate's rigidities D_x, D_y D_s. To this end, the trivial plate parameters (ρ, L_x, L_y, h) and the experimental BCs are assumed to be known. The estimation is then conducted by minimizing the error between the discrepancy between numerically computed eigenfrequencies $\omega_{m,n}$ and their experimentally measured counterparts $\hat{\omega}_{m,n}$. The minimization is performed with respect to the unknown rigidities, $\tilde{D}_x, \tilde{D}_y, \tilde{D}_s$ which represent estimates of the true parameters. To this end, the following variables are defined:

$$\boldsymbol{\vartheta} := \lambda^{-1}\hat{\boldsymbol{\omega}}^2, \quad \boldsymbol{\varphi}\left(\tilde{D}_x, \tilde{D}_y, \tilde{D}_s\right) := \begin{bmatrix}\mathbf{a}, \mathbf{b}, \mathbf{c}\end{bmatrix} \begin{bmatrix}\tilde{D}_x \\ \tilde{D}_y \\ \tilde{D}_s\end{bmatrix} := \mathbf{X}\,\mathbf{d}, \tag{3.8}$$

Where $\mathbf{X} = [\mathbf{a}, \mathbf{b}, \mathbf{c}]$ and $\mathbf{d} = [\tilde{D}_x, \tilde{D}_y, \tilde{D}_s]^T$. Each of the vectors $\mathbf{a}, \mathbf{b}, \mathbf{c}$ is assembled by stacking modal coefficients $a_{m,n},\ b_{m,n}, c_{m,n}$ over the selected modes. For instance, if the modes (0,1), (1,1) and (1,2) are considered then $\mathbf{a} = [a_{0,1},\ a_{1,1}, a_{1,2}]^T$. The error is defined as:

$$\mathscr{J}\left(\tilde{D}_x, \tilde{D}_y, \tilde{D}_s\right) := \frac{1}{2}\|\boldsymbol{\vartheta} - \boldsymbol{\varphi}\|_2^2, \tag{3.9}$$

which can be then minimized through a least-square minimization expressed as [39]:

$$\mathbf{d} = \arg\min \mathscr{J} = \left(\mathbf{X}^{\mathsf{T}}\mathbf{X}\right)^{-1}\left(\mathbf{X}^{\mathsf{T}}\boldsymbol{\vartheta}\right). \tag{3.10}$$

Finally, from the identified rigidities, the estimated elastic constants are obtained as:

$$\tilde{E}_x = \frac{12(1-\nu_{xy}\nu_{yx})\tilde{D}_x}{h^3}, \qquad \tilde{E}_y = \frac{12(1-\nu_{xy}\nu_{yx})\tilde{D}_y}{h^3}, \qquad \tilde{G}_{xy} = \frac{3\tilde{D}_s}{h^3}, \tag{3.11}$$

Where the values for ν_{xy} and ν_{yx} are assumed to be known a priori because of their low variability across specimens [47].

3.4 Numerical benchmarking

Before moving to the experimental setup required to extract the necessary modal parameters, the method is benchmarked through a series of numerical case studies.

It is worth pointing out here that in the following numerical validation of the presented method, the numerical eigenfrequencies are computed based on an FE model via commercial software. While FE models allow for a simpler modeling of non-trivial geometries, these are commonly based on the MR model. Therefore, while the unknown elastic parameters are defined starting from the KL equation, the numerical model might also account for additional phenomena such as transverse shear deformation and rotary inertia. Accordingly, the validity of the method and the reliability of its physical interpretation depend on the applicability of the thin-plate assumptions involved in the KL model for the plate under test. A systematic analysis on the influence of plate thickness on modelling assumptions is presented in Chapter 5.4. The method's effectiveness in extracting reliable rigidity constants from a collection of virtual rectangular test plates is evaluated. Three representative BCs sets are considered, namely cantilever $(BCs = \text{C-F-F-F})$, fixed $(BCs = \text{C-C-C-C})$ and free $(BCs = \text{F-F-F-F})$ configurations. Here, the focus is not to revisit well-established results but rather to illustrate that the proposed framework can extend those classical approaches to plate configurations that are less commonly treated. In particular, the clamped-edge case provides a stringent benchmark, since it is especially challenging to decouple the contributions of the different elastic constants. The intention is not to suggest that cantilever or clamped plates should become the standard experimental setup, but instead to show that accurate estimates of the elastic parameters can be achieved even for plates with fixed edges.

For the purpose of the benchmarking process, the FEM simulation software COMSOL Multiphysics [1] is used to implement a model of an orthotropic plate under the different BCs by using the *Plate* component.

3.4.1 Linear dependence of the non-dimensional frequencies on elastic constants

To illustrate the dependency of the squared non-dimensional frequencies $\bar{\omega}^2_{m,n}$ on the rigidity ratios p, q, a reference tonewood spruce rectangular sample is considered with $\alpha = 223/114$, $h = 3\,mm$, $\rho = 473.9$ $[kg/m^{-3}]$, for $BC = \text{C-F-F-F}$. Material properties representative of spruce wood are taken from literature [47]. These are reported in Table 3.1.

Data is generated by scaling E_x and E_y by factors $\mathbf{v} := [0.8, 0.9, 1.0, 1.1, 1.2]$, while keeping G_{xy} fixed, producing 25 cases with $4.3 < p < 6.6$ and $0.28 < q < 0.45$. These are obtained by varying the initial elastic constants E_x and E_y by $\pm 20\%$. It is worth stressing how this perturbation is purely arbitrary, the only purpose is to sample the p, q space to obtain the necessary *training plates*. While larger dataset could be considered, the twenty-five sampled combinations are sufficient to ensure accurate results, as it will be demonstrated in the following sections. Once collected, the first six modal frequencies from COMSOL corresponding to modes (1,0), (1,1), (2,0), (1,2), (2,1), (2,2) are sorted in the same order for each *training plate*. To guarantee the correct pairing between the modal frequency and the respective mode shape when exporting the data from COMSOL, the modal assurance criterion (MAC) is used. This is a standard metric used in modal analysis to compare the

Kirchhoff plate parameters

ρ	L_x	L_y	h	E_x^0	E_y^0	G_{xy}	ν_{xy}
473.9 $\mathrm{kg} \cdot \mathrm{m}^{-3}$	223 mm	114 mm	3 mm	10.7 GPa	716 MPa	500 MPa	0.51

Thick-plate parameters

E_z	G_{yz}	G_{xz}	ν_{yz}	ν_{xz}
0.39 GPa	0.023 GPa	0.62 GPa	0.45	0.50

Table 3.1 Input constants for the COMSOL simulations, inspired from the table in [47] (page 96). These constants are used to create a “training” set from which the modal coefficients $a_{m,n}$, $b_{m,n}, c_{m,n}$ are estimated. The plates included in the training set have material and geometrical constants as per the table, and where (E_x, E_y) are selected as the twenty-five possible combinations of the elements of the sets E_x, E_y, where $E_x = \mathbf{v}E_x^0$, $E_y = \mathbf{v}E_y^0$, with $\mathbf{v} := [0.8, 0.9, 1.0, 1.1, 1.2]$.

similarity between two modal shapes and it is defined as [205]:

$$\mathrm{MAC}(\mathbf{U}, \mathbf{U}') := \frac{|\mathbf{U}^\intercal \mathbf{U}'|^2}{||\mathbf{U}||^2 \, ||\mathbf{U}'||^2}. \tag{3.12}$$

Where $\mathbf{U}$ and $\mathbf{U}'$ are two column vectors containing the displacement values at each nodal point of the plate. Values close to 1 indicate an high correlation between the mode shapes. Here, this is applied to compare the sampled modal shapes exported from COMSOL against a reference set of eigenshapes. Examples of MAC plots are given in Figure 3.1. As it can be observed, while modal crossing occur, some of the reference modal shapes can not be recognized for some *training plates* because of modal distortion (i.e. where nodal lines get significantly bent with respect to the reference x and y axes.) At this stage, where a clear modal shape identification could not be obtained, the training data was discarded. Once the training data is sorted in the correct order and filtered in order to preserve an high correlation in the modal shapes, the modal coefficients $a_{m,n}, b_{m,n}$ and $c_{m,n}$ are estimated via a simple constrained linear fit in Matlab by forcing fitted coefficients to be ≥ 0, according to (3.5). The resulting fitting coefficients are reported in Table 3.2.

Notably, all the coefficients of determination R^2 are very close to 1, demonstrating how the linear dependence in (3.5) leads to a good prediction of the modal frequencies as a

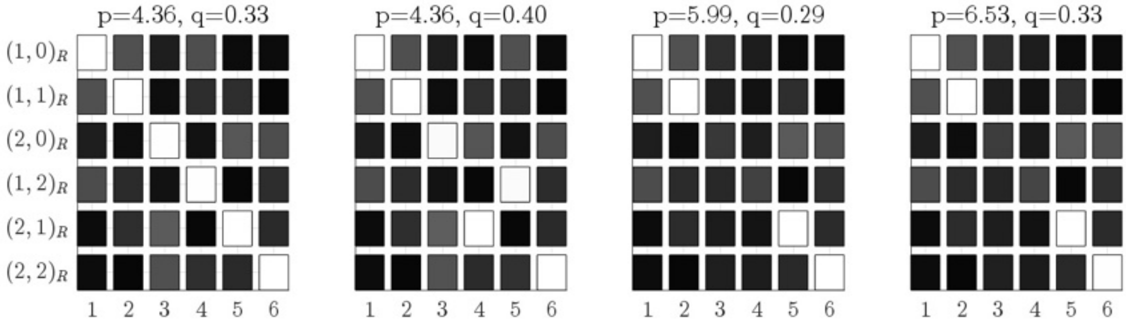

Fig. 3.1 Modal Assurance Criterion (MAC) matrices for the plate with $\alpha = 223/114$ and $BC = \{\text{C-F-F-F}\}$, evaluated across different values of the parameters p and q. White squares indicate strong agreement between the reference mode shapes (denoted by the subscript $_R$) and those from the batch set corresponding to the labeled p,q pair. Mode shapes are indexed in order of ascending frequency from 1 to 6. In some configurations, mode crossings occur (e.g. at $(p = 4.36, q = 0.40)$). Ambiguity in identifying specific modes (i.e. (2,0) and (1,2)) in the final two matrices, leads to their exclusion from the fitting process. The reference modal set corresponds to the configuration $p = 4.36, q = 0.29$.

	(1,0)	(1,1)	(2,0)	(1,2)	(2,1)	(2,2)
$a_{m,n}$	3.21	3.99	117.0	14.4	124	134
$b_{m,n}$	0.00	0.94	41.9	1720	15.6	1910
$c_{m,n}$	0.00	40.5	13.6	155	328	1260
R^2	1.00	1.00	0.999	0.999	1.00	1.00

Table 3.2 Linear fit data for a plate with $\alpha = 223/114$, and $BCs = \{\text{C-F-F-F}\}$ (where the plate is clamped along the radial direction). The coefficients of determination R^2 are also reported.

function of the material rigidities contained in p and q. This can also be observed from Figure 3.2 where a visual illustration is provided. Now, the collected modal coefficient can be used to perform the estimation step for the rigidity constants of the plate. This is done considering groups of plates sharing the same set of BCs and aspect ratio α. Numerical plates are used in the following sections to conveniently simulate the "experimental" plates, avoiding the uncertainty sources caused by laboratory setups as well as the uncertainty given by the natural variability of wood. "Experimental" plates considered in the benchmarking also include plates with p and q values outside the training ranges. This helps in assessing the efficiency and capabilities of the fit.

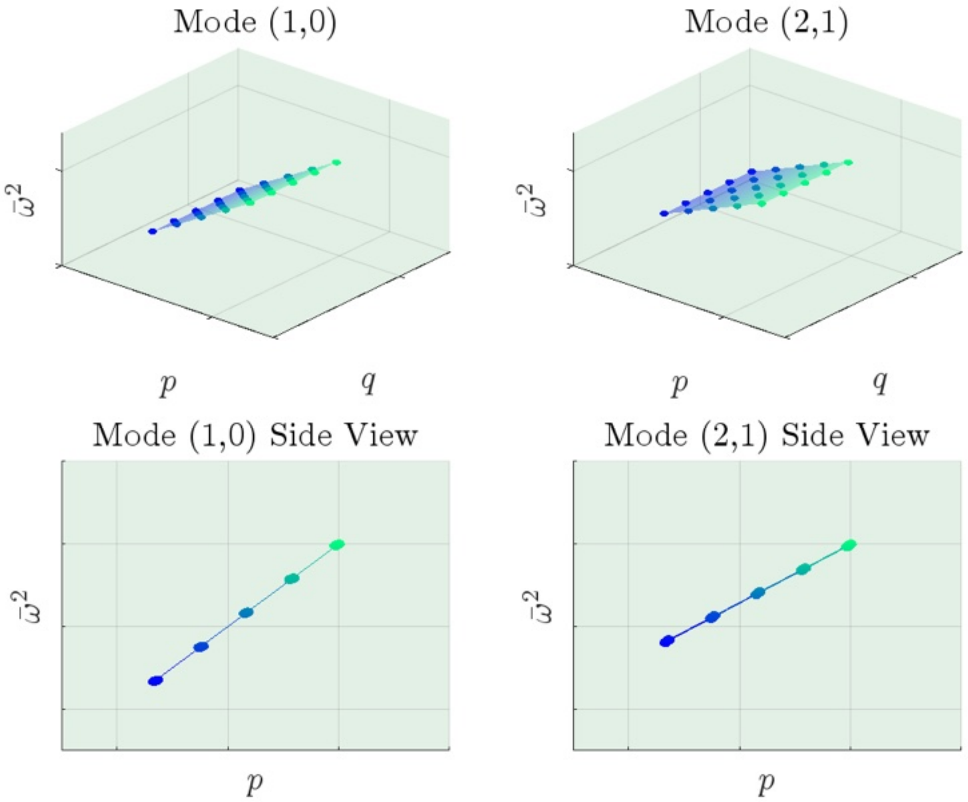

Fig. 3.2 Linear relationship between the non dimensional frequencies $\bar{\omega}^2_{m,n}$ and the elastic ratios p and q, for a plate with $\alpha = 223/114$ and $BCs = \{\text{C-F-F-F}\}$ (for a plate clamped along the radial direction. Dots denote computed frequency values, while the planes are obtained from (3.5) using the coefficients in Table 3.2.

3.4.2 Benchmarking for $BCs = \{\text{C-F-F-F}\}$

To evaluate the accuracy in the case of cantilever BCs, three "experimental" plates are assessed, sharing the same properties as per Table 3.1 except for E_x and E_y which are selected so that p and q fall inside and outside the training ranges. Table 3.4 reports the considered p and q values. The rigidities $\tilde{D}_x, \tilde{D}_y, \tilde{D}_s$ are estimated according to 3.10 and the modal coefficients in Table 3.2. Errors in the estimated values are shown in Table 3.4. These are computed as:

$$\text{err}_x = \frac{D_x - \tilde{D}_x}{D_x}, \quad \text{err}_y = \frac{D_y - \tilde{D}_y}{D_y}, \quad \text{err}_s = \frac{D_s - \tilde{D}_s}{D_s}. \tag{3.13}$$

Here, it is important to stress on the selection of modes used to obtain the modal coefficients. Despite more than three modes can be used, at least three of them should reveal independent modal coefficients. As an example, it can be observed from Table 3.2 how by using only modes (1,0), (1,1) and (2,1) would lead to an unreliable estimate for D_y and so for E_y as the $b_{m,n}$ coefficients are small or zero compared to the values for $a_{m,n}$ and $c_{m,n}$. This yields a poorly conditioned formulation of the matrix in (3.10). As an example, an estimate of Dx, Dy and Ds is performed using only modes (1,0), (1,1) and (2,1) and the results are compared from an estimation conducted using six modes for an "experimental" plate with p and q lying within the training set of plates. The comparison is given in Table 3.3.

Sets of modes	$\mathrm{err}_x(\%)$	$\mathrm{err}_y(\%)$	$\mathrm{err}_s(\%)$
Modes (1,0), (1,1), (2,1)	0.42	18.74	0.0
Modes (1,0),(1,1),(2,1),(2,2)	0.52	0.70	0.0

Table 3.3 Relative errors computed using (3.13) for the case $\alpha = 223/114$, $BCs = \{$C-F-F-F$\}$ using only modes (1,0), (1,1) and (2,1) and using modes (1,0),(1,1),(2,1),(2,2). The other plate parameters are as per Table 3.1. The training ranges are: $4.3 < p < 6.6$, $0.28 < q < 0.45$. Relative errors are computed using (3.13), and here the percentage values are reported. Modes (1,0),(1,1),(2,1),(2,2) are considered here. E_x^0 and E_y^0 values are reported in Table 3.1.

	E_x/E_x^0	E_y/E_y^0	p	q	$\mathrm{err}_x(\%)$	$\mathrm{err}_y(\%)$	$\mathrm{err}_s(\%)$
Plate 1	1.3	0.7	7.1	0.25	0.77	0.9	0.78
Plate 2	1.0	0.7	5.4	0.25	0.65	1.2	0.031
Plate 3	1.3	1.0	7.1	0.36	0.28	0.11	0.57

Table 3.4 Test plate materials parameters and discrepancies for the case $\alpha = 223/114$, $BCs = \{$C-F-F-F$\}$. The other plate parameters are as per Table 3.1. The training ranges are: $4.3 < p < 6.6$, $0.28 < q < 0.45$. Relative errors are computed using (3.13), and here the percentage values are reported. Modes (1,0),(1,1),(2,1),(2,2) are considered here. E_x^0 and E_y^0 values are reported in Table 3.1.

3.4.3 Sensitivity analysis for $BCs = \{$C-F-F-F$\}$

To emulate the error introduced from measurement uncertainty, the simulated eigenfrequencies are now randomly perturbed by ±2%, generating five new sets of "experimental" eigenfrequencies. The resulting errors in the estimation of D_x, D_y, D_s are reported in Table 3.5. As expected, higher errors occur. However, these are still within ranges reported by the FEMU-3DVF method [274].

	$\varepsilon_{(1,0)}$	$\varepsilon_{(1,1)}$	$\varepsilon_{(2,0)}$	$\varepsilon_{(1,2)}$	$\varepsilon_{(2,1)}$	$\varepsilon_{(2,2)}$	$\text{err}_x(\%)$	$\text{err}_y(\%)$	$\text{err}_s(\%)$
Test 1	1.8	-1.7	1.1	-0.73	1.6	0.95	-4.2	13.0	-3.8
Test 2	-1.6	0.76	1.6	-1.1	-1.4	-2.0	-3.5	7.2	11.0
Test 3	0.03	-0.1	1.6	-0.95	1.3	-1.4	-6.4	11.0	8.6
Test 4	0.76	0.89	0.66	0.79	1.7	1.6	-3.4	9.2	-6.0
Test 5	-0.94	-0.55	0.026	-0.35	0.15	-0.92	-2.4	9.1	4.3

Table 3.5 Sensitivity analysis for Plate 1 from Table 3.4, with $\alpha = 223/114$ and $BCs = \{\text{C-F-F-F}\}$. The perturbation parameter ε was randomly selected within $\pm 2\%$ of the corresponding exact modal eigenfrequency and is reported in the table as a percentage. The quantities err_x, err_y, and err_s are defined according to (3.13).

On the sensitivity to Poisson ratio

As for the proposed method, the Poisson ratio ν_{xy} is assumed to be known a priori, given its relatively low intra-specimen variability reported in the literature [47]. Nevertheless, to evaluate the sensitivity of the inverse estimation method to uncertainty in this parameter, a dedicated sensitivity analysis is performed for the case of cantilever BCs. An “experimental” plate with elastic constants ratios p and q lying within the training range is first considered, and the elastic constants are identified using the nominal value of ν_{xy}. Subsequently, based on reported intra-specimen variability, ν_{xy} is perturbed by $\pm 9.3\%$, leading to two additional “experimental” plates ("experimental" plate 1 and 2) with slightly modified p and q ratios, as reported in Table 3.6. As can be observed from the results, the inverse identification procedure maintains acceptable error levels even when ν_{xy} is perturbed to its extreme values.

	ν_{xy}	p	q	$\text{err}_x(\%)$	$\text{err}_y(\%)$	$\text{err}_s(\%)$
Reference "experimental" plate	0.51	6.5	0.43	0.52	0.70	0.0
"experimental" plate 1	0.46	6.5	0.43	0.42	0.12	0.2
"experimental" plate 2	0.56	6.6	0.44	0.62	1.28	0.4

Table 3.6 Sensitivity of the inverse identification to perturbations in the Poisson ratio ν_{xy} for cantilever boundary conditions ($BCs = \{\text{C}-\text{F}-\text{F}-\text{F}\}$, $\alpha = 223/114$). A reference “experimental” plate is first identified using the nominal value of ν_{xy}, and two additional plates are obtained by perturbing ν_{xy} by $\pm 9.3\%$, leading to slightly modified ratios p and q. The table reports the resulting discrepancies in the identified elastic constants. Relative errors are computed using (3.13) and expressed as percentages.

3.4.4 Benchmarking for $BCs = \{\text{C-C-C-C}\}$

For the fully clamped test case, a spruce rectangular tonewood with $\alpha = 150/103$ is considered as a reference. This is used to comply with the experimental validation that will be presented in Section 4.3. The modal coefficients are computed again in the same manner as described in 3.4.1 and reported in Table 3.7. As it can be seen, all the coefficients of determination are equal to 1.00 for the fully constrained plate. Therefore, the linear dependence in (3.5) appears to be particularly valid under this set of BCs. The considered modal shapes for this test case are illustrated in Figure 3.3 while Table 3.8 reports the estimation errors for the current case.

	(0,0)	(0,1)	(1,0)	(0,2)	(1,1)	(1,2)
$a_{m,n}$	236	237.5	1790	242	1792	1799
$b_{m,n}$	1214	8589	1652	31910	10180	35250
$c_{m,n}$	146.9	552.3	534.9	1196	2051	4469
R^2	1.00	1.00	1.00	1.00	1.00	1.00

Table 3.7 Linear fit data for a plate with $\alpha = 150/103$, and $BCs = \{\text{C-C-C-C}\}$. The coefficients of determination R^2 are reported in the bottom line.

3.4.5 Sensitivity analysis for $\mathscr{B} = \{\text{C-C-C-C}\}$

As for the case in 3.4.2, a sensitivity analysis is conducted. The results are shown in Table 3.9. While low errors are found for the D_x and D_y rigidity constants, D_s seems to be more sensitive, leading to higher errors when perturbing the eigenfrequencies within ±2%. A way to overcome this sensitivity is proposed via a statistical approach in Section 3.6.

	E_x/E_x^0	E_y/E_y^0	p	q	$\text{err}_x(\%)$	$\text{err}_y(\%)$	$\text{err}_s(\%)$
Plate 1	1.3	0.7	7.1	0.25	0.81	0.86	0.12
Plate 2	1.0	0.7	5.4	0.25	-0.28	-0.26	0.043
Plate 3	1.3	1.0	7.1	0.36	- 0.12	-0.12	0.036

Table 3.8 Parameters and error values for the test plate with $\alpha = 150/103$ $BCs = \{\text{C-C-C-C}\}$. The training intervals are $4.3 < p < 6.6$ and $0.28 < q < 0.45$. The errors are defined according to (3.13) and expressed as percentages. All six modes are included in this analysis.

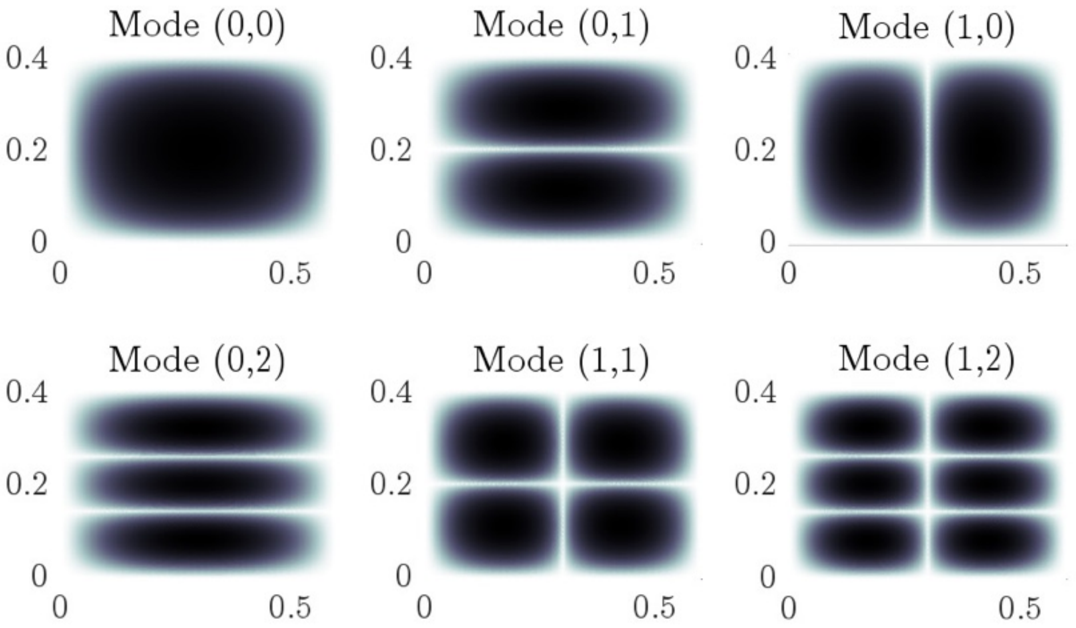

Fig. 3.3 Mode shapes corresponding to the plate with $\alpha = 150/103$, $BCs = \{\text{C-C-C-C}\}$, $p = 6.53$, and $q = 0.29$.

3.5 Comparison against standard literature methods for $\mathscr{B} = \{\textbf{F-F-F-F}\}$

A final benchmarking of the method is run considering the traditional case of fully free BCs. Besides testing the versatility of the method, this also helps to validate it against the widely used and established method introduced by McIntrye and Woodhouse [183] and by Caldersmith and Freeman [53]. As for the previous cases, all the "experimental" frequencies are here computed through COMSOL. These are reported in Table 3.10 together with the physical properties of the "experimental" plate. First, the modal coefficients are computed for the free BCs. These are given in Table 3.11. Also for this test case, high coefficients of determination are observed, highlighting the goodness of the linear dependence.

	$\varepsilon_{(0,0)}$	$\varepsilon_{(0,1)}$	$\varepsilon_{(1,0)}$	$\varepsilon_{(0,2)}$	$\varepsilon_{(1,1)}$	$\varepsilon_{(1,2)}$	$\text{err}_x(\%)$	$\text{err}_y(\%)$	$\text{err}_s(\%)$
Test 1	0.64	0.51	0.37	-1.0	1.6	-0.95	-2.5	3.7	10.6
Test 2	2.0	-1.0	-1.7	-0.86	-1.4	1.7	8.3	8.4	-52
Test 3	1.2	1.4	2.0	-1.9	-0.65	0.63	-1.1	5.7	-6.9
Test 4	-0.49	-1.2	-1.1	0.8	0.98	1.3	3.7	3.3	-30.0
Test 5	0.89	-0.95	-0.2	-1.9	0.75	-1.6	-1.1	5.4	11.0

Table 3.9 Sensitivity analysis for Plate 1 in Table 3.8, with $\alpha = 150/103$ and $BCs = \{\text{C-C-C-C}\}$. The perturbation ε was randomly chosen within ±2% of the corresponding exact modal eigenfrequency and is expressed in the table as a percentage. The errors err_x, err_y, and err_s are computed according to (3.13).

Kirchhoff plate parameters

ρ	L_x	L_y	h	E_x	E_y	G_{xy}	ν_{xy}
687 $\text{kg} \cdot \text{m}^{-3}$	204 mm	204 mm	1.18 mm	13 GPa	702 MPa	688 MPa	0.3

	(1,1)	(0,2)	(1,2)	(2,1)	(2,2)	(2,0)
COMSOL freqs. (Hz)	29.3	29.5	66	81.2	120	127

Table 3.10 Thin-plate elastic constants values used in COMSOL for the plate under fully free BCs and resulting modal frequencies.

	(1,1)	(0,2)	(1,2)	(2,1)	(2,0)	(2,2)
$a_{m,n}$	0.15	0.519	1.73	4.7	497	6.41
$b_{m,n}$	15.1	483	550	3620	0	3790
$c_{m,n}$	122	0.269	506	9.98	0	1140
R^2	0.996	1.00	1.00	1.00	1.00	1.00

Table 3.11 Linear fit data for a plate with $\alpha = 1$, and $BCs = \{\text{F-F-F-F}\}$.

Then, recalling the formulae by McIntyre and Woodhouse for the estimation of $\tilde{D}_x, \tilde{D}_y, \tilde{D}_s$ under free BCs:

$$\tilde{D}_x = 0.079\, f_{(2,0)}^2\, \rho A^2 h, \tag{3.14a}$$

$$\tilde{D}_y = 0.079\, f_{(0,2)}^2\, \rho A^2 h, \tag{3.14b}$$

$$\tilde{D}_s = 0.27\, f_{(1,1)}^2\, \rho A^2 h. \tag{3.14c}$$

and the ones proposed by Caldersmith and Freeman:

$$\tilde{D}_x = 0.08\, f_{(2,0)}^2\, \rho A^2 h, \tag{3.15a}$$

$$\tilde{D}_y = 0.08\, f_{(0,2)}^2\, \rho A^2 h, \tag{3.15b}$$

$$\tilde{D}_s = 0.40\, f_{(1,1)}^2\, \rho A^2 h. \tag{3.15c}$$

As both sets of formulae only take into account three modes, the same ones are used to perform the presented estimation routine. A comparison of the results is provided in Table 3.12. It can be noticed how, despite all the methods yield very accurate results for $\tilde{E}_x$ and $\tilde{E}_y$, larger discrepancies are found for $\tilde{G}_{xy}$ when applying the formulas from [183, 53]. Nonetheless, this can be explained when looking closer at the modal coefficients for mode (1,1) in Table 3.11. In fact, it is clear how, for this mode, E_y has a non-negligible effect. Therefore, it can not be assumed to be a pure "shear" mode, and the impact of E_y has to be taken into account. By combining the coefficients from Table 3.11 with the linear dependence expressed in (3.7), the following updated refined formulae are proposed:

	$\tilde{E}_x$ (GPa)	$\tilde{E}_y$ (MPa)	$\tilde{G}_{xy}$ (MPa)	$\mathrm{err}_x(\%)$	$\mathrm{err}_y(\%)$	$\mathrm{err}_s(\%)$
Ref. [183]	13.0	701	594	0.1	0.2	14
Ref. [53]	13.1	709	880	-1.1	-1.0	-28
Proposed	12.9	701	686	0.8	0.1	0.3

Table 3.12 Parameters and error values for the test plate with $\alpha = 1$ and $BCs = \{\text{F-F-F-F}\}$ using the proposed estimation routine introduced in Section 3.3 compared to classical formulae. Only the initial estimates of the elastic constants are considered for the methods presented in [183, 53], without further refinement. Improved estimates for G_{xy} can be obtained through the iterative procedure described in [183].

$$\tilde{D}_x = 0.079\, f_{(2,0)}^2\, \rho A^2 h, \tag{3.16a}$$

$$\tilde{D}_y = 0.079\, f_{(0,2)}^2\, \rho A^2 h, \tag{3.16b}$$

$$\tilde{D}_s = 0.32\, f_{(1,1)}^2\, \rho A^2 h - 0.1\, \tilde{D}_y. \tag{3.16c}$$

Using these formulae, the errors become $\mathrm{err}_x = 0.1\%$, $\mathrm{err}_y = 0.2\%$, $\mathrm{err}_s = 0.2\%$. It should be noted how the refined formula applies to the present case scenario and it is therefore relevant for the case of square orthotropic plates with α = 150/103, $BCs = \{\text{F-F-F-F}\}$ and elastic constants ratios $p = 4.8$ and $q = 0.3$.

3.6 Experimental validation on a kantele tonewood

A spruce tonewood specimen from Finland, provided by a master luthier, serves here to conduct a first preliminary experimental validation of the method. The piece was originally a leftover fragment from the production of a concert kantele, a traditional plucked string instrument of Finnish origin [247]. Its initial geometry measured $L_x^0 = 25.3$ cm in length, $L_y^0 = 11.4$ cm in width, and $h^0 = 5$ mm in thickness. Prior to experimentation, the thickness was carefully reduced to $h = 3$ mm using a belt sander. This reduction step was not strictly mandatory, since piano soundboards up to 8 mm thick exhibit only minor discrepancies between thin- and thick-plate approximations [89]. Nevertheless, it was applied here to improve accuracy, as preliminary simulations with standard spruce elastic constants from literature showed that thinning from 5 mm to 3 mm decreases the mismatch between the two plate models from about 6% to $\leq 2\%$ for the lowest six modes. The impact of plate thickness on the estimated elastic constant values will be discussed in more detail in Section 5.7. A dedicated clamping system was engineered to enforce the desired BCs, following the strategy outlined in [87]. The setup consisted of two angular iron bars, each weighing 1.8 kg, pressed together with six evenly distributed spring clamps. To achieve a more uniform pressure distribution in the y-direction, a supplementary flat iron plate (1.2 kg) was positioned between the wood and one angular bar. To safeguard the delicate spruce surface from over-compression, a thin protective rubber sheet was inserted at the contact interface. The final assembly is illustrated in Figure 3.4. As a consequence of the clamping, the plate contracted slightly along the x-axis, yielding an effective length of $L_x = 22.3$ cm. For all subsequent analysis, the effective geometry (L_x, L_y, h) and density ρ reported in Table 3.1 were used. The modal coefficients $a_{m,n}$, $b_{m,n}$, and $c_{m,n}$ derived from these conditions are given in Table 3.2. Excitation and response measurements were carried out using a PCB 086E80 miniature impact hammer, paired with a PCB 352A21 uniaxial accelerometer. To assure a consistent impact position over multiple hits, the hammer is fixed to a pendulum. After each impact, the hammer is stopped by hand by the user to preserve double hits. To avoid surface damage, the hammer's steel tip was covered with a vinyl cap, which at the same time attenuated high-frequency components in the excitation [98] while retaining sufficient bandwidth up to 1 kHz, as specified by the impulse hammer technical data illustrated in Figure 3.6 which is also experimentally verified when plotting the force spectrum of the hammer covered by the tip on the tonewood sample, as shown in Figure 3.7 . The experimental measurement setup is shown in Figure 3.8.

Fig. 3.4 Experimental setup for the tonewood sample with $BCs = \{\text{C-F-F-F}\}$ and $\alpha = 223/114$, whose modal coefficients are provided in Table 3.2. The impact hammer is mounted on a pendulum that halts after recoil to prevent multiple impacts. The protective rubber pad used in the clamping system is visible below.

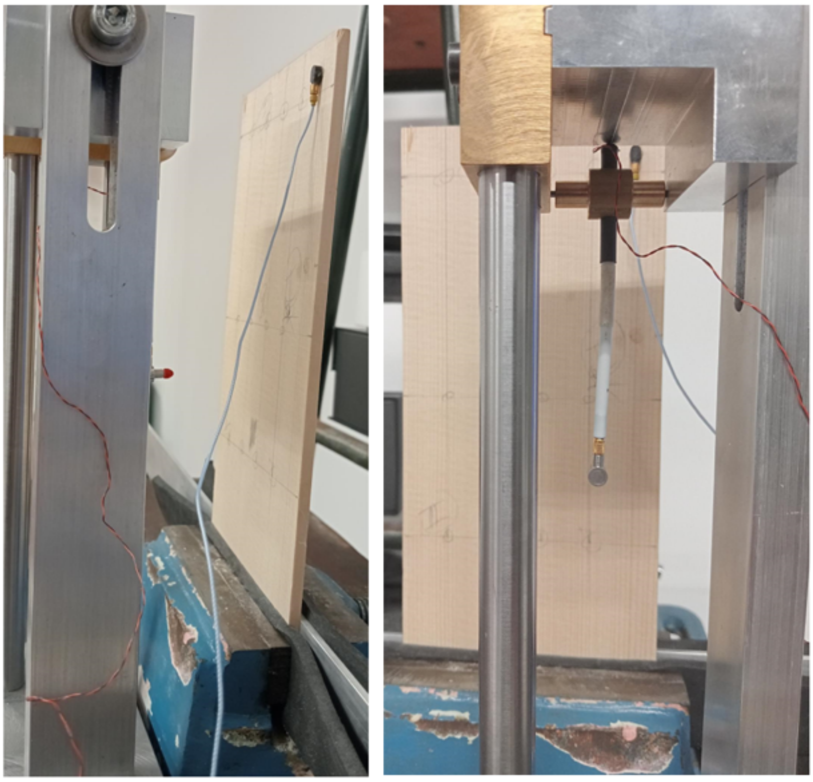

Fig. 3.5 Experimental measurement set-up.

	(1,0)	(1,1)	(2,0)	(1,2)	(2,1)	(2,2)
Measured freqs. (Hz)	52	98	310	337	398	637

Table 3.13 Spatially averaged experimental frequencies and identified mode shapes for the cantilever Finnish spruce tonewood.

Six evenly spaced excitation points were selected, with the accelerometer fixed at a single reference location. The distribution of these points was chosen to ensure observability of the first six vibrational modes, as will be discussed later. Each location was struck five times, and the responses were averaged to minimize uncertainties stemming from hammer-force variability [14]. The accelerometer was carefully positioned away from nodal lines to avoid missing modal contributions. Acquired signals were post-processed in Matlab to calculate the FRFs. The resulting spectra are presented in Figure 3.9, while the averaged experimental eigenfrequencies are summarized in Table 3.13. Resonances were extracted via peak-picking across the six excitation positions, then spatially averaged to improve reliability. As emphasized in Section 3.4.1, accurate identification of modal coefficients $a_{m,n}, b_{m,n}, c_{m,n}$ required determination of nodal lines in both fibre directions (x and y). Mode shapes were

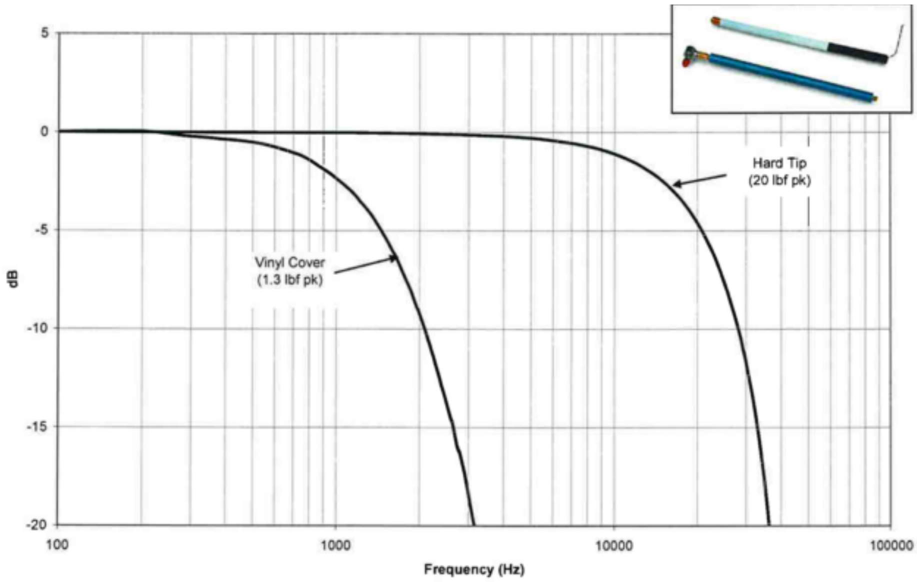

Fig. 3.6 Spectrum of the hammer input force provided in the technical datasheet of the PCB Piezotronics 086E80 [206]. It can be observed how the use of a vinyl cover limits the hammer's force bandwidth.

therefore visualized with the Chladni pattern technique [64], in accordance with previous research [140]. The plate was mounted horizontally and excited with a PCB 2004E miniature shaker fixed using beeswax. Pure sinusoidal signals were generated at the experimentally determined modal frequencies, while fine sand was scattered on the plate to reveal nodal regions. The experimental setup and representative Chladni figures are shown in Figure 3.10.

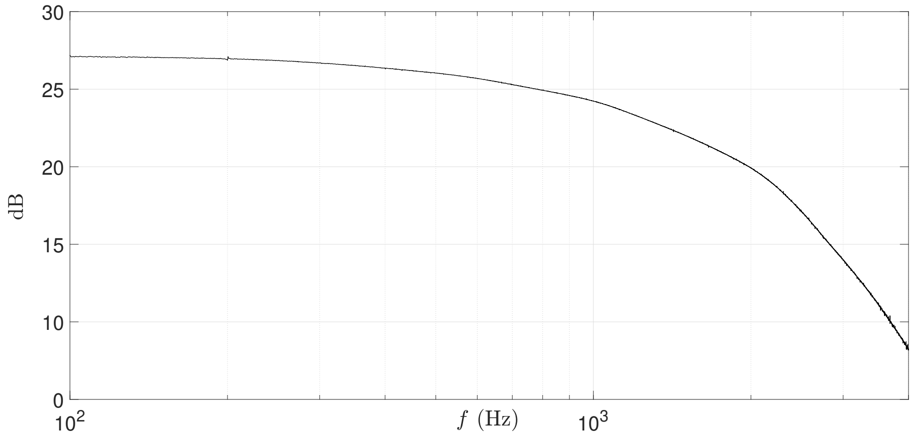

Fig. 3.7 Measured hammer input force spectrum with vinyl cover. A significant frequency roll-off can be observed above 1 kHz.

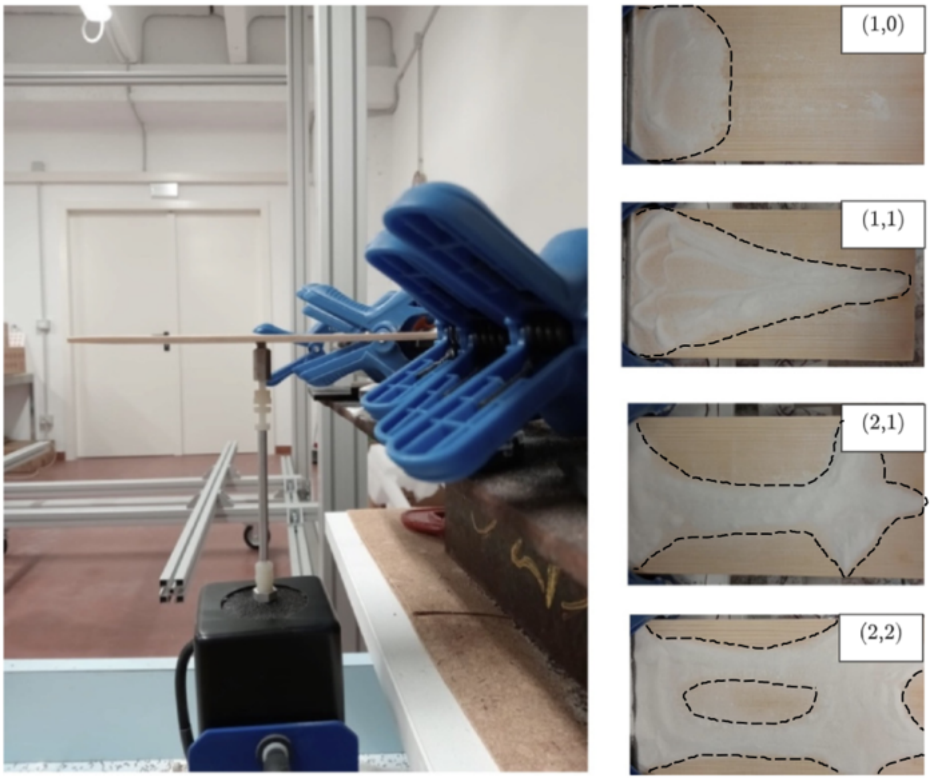

Fig. 3.10 Experimental setup showing the miniature shaker (left) and the resulting Chladni patterns (right) on the tonewood sample.

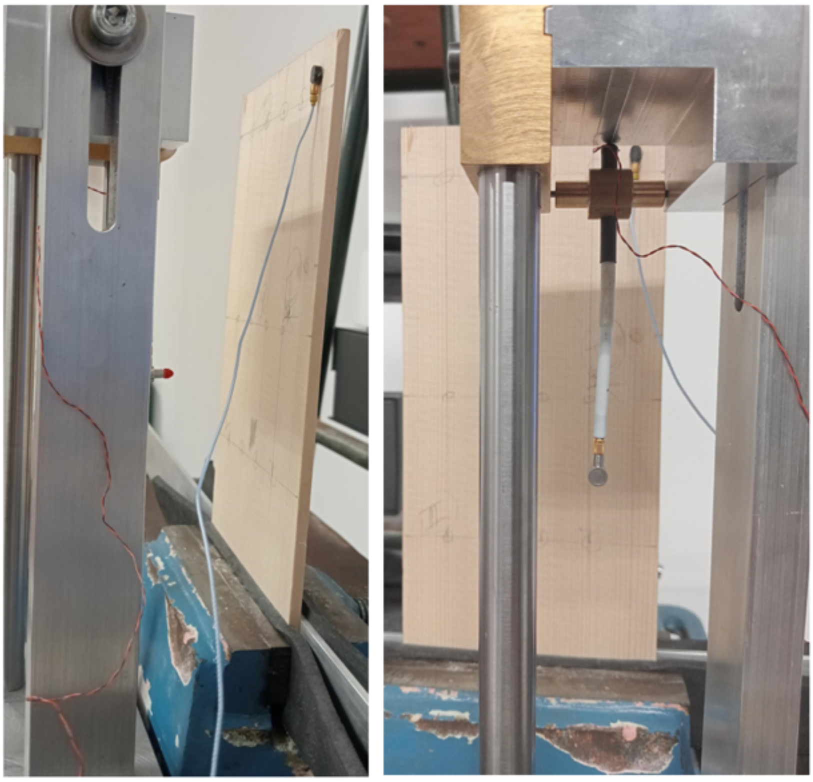

Fig. 3.8 Experimental measurement set-up.

3.6.1 Results

Elastic constants are retrieved using the experimental frequencies from Table 3.13, the modal coefficients from 3.2 and the equations 3.10 and 3.11. While all six modes could be used directly to get a single estimate, considering all possible subsets of three or more modes allows for a more robust statistical assessment of the estimated elastic constants. Accordingly, as six modes were successfully identified, a total of 42 different combinations of modes can be obtained, including at least three modes each, hence allowing for multiple estimates of elastic constants from which a mean value and standard deviation can be computed. To this end, spurious values are removed by excluding negative estimates from the statistics analysis. Then, outliers are also discarded. These are calculated based on the interquartile range (IQR) method so that an estimated value is evaluated as an outlier if falls outside of the range $[Q_1 - 1.5\,\mathrm{IQR}, Q_3 + 1.5\,\mathrm{IQR}]$, where $\mathrm{IQR} = Q_3 - Q_1$, and where Q_1, Q_3 are the first and third quartile, respectively [21]. Finally, mean and standard deviations are obtained, these are shown in Figure 3.11 and Table 3.14. Compared to available data, estimated mean values are within literature spruce values [47]. To further double check the accuracy of the estimate, the average values obtained can be inputted again in COMSOL and the resulting

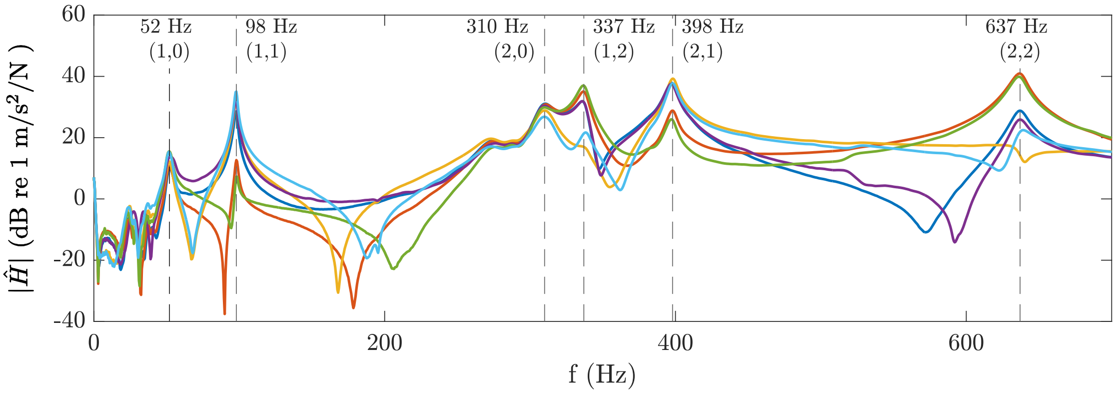

Fig. 3.9 Frequency spectra measured at six points on the spruce tonewood plate. The frequency range of interest extends up to 800 Hz. Dashed lines indicate the spatially averaged detected frequency peaks.

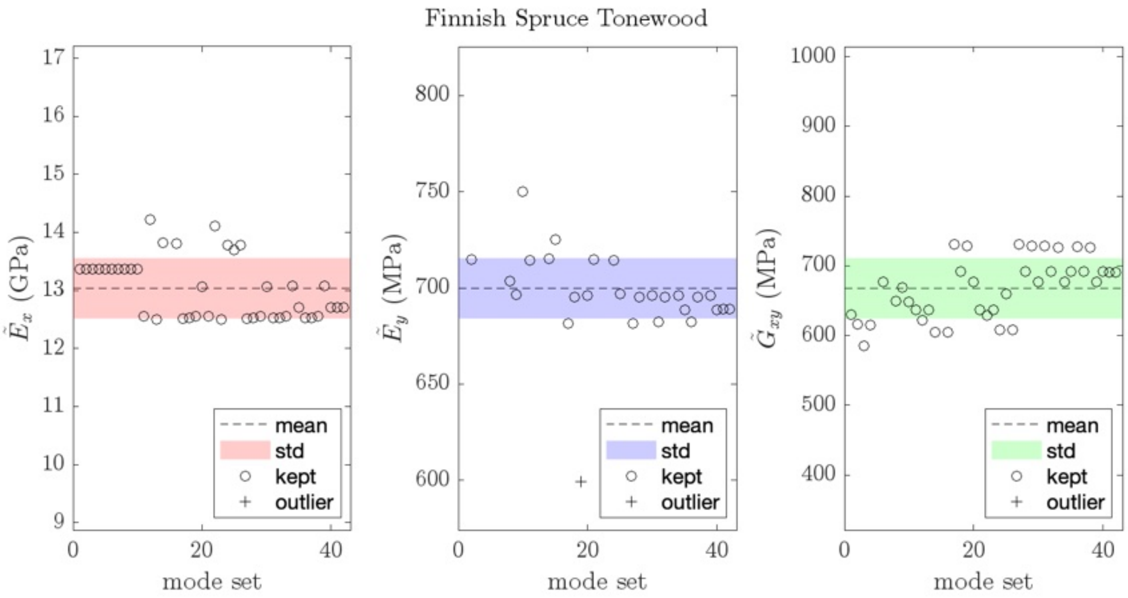

Fig. 3.11 Estimated elastic constants for the Finnish spruce tonewood. Forty-two mode sets are analyzed, corresponding to all possible combinations that include at least three of the six measured experimental modes. Mean values and standard deviations are represented by dashed lines and coloured bands, respectively. Outliers are identified using the interquartile range (IQR) method [21].

eigenfrequencies can be compared to the experimental ones. The comparison is reported in Table 3.15.

		$\tilde{E}_x$ (GPa)	$\tilde{E}_y$ (MPa)	$\tilde{G}_{xy}$ (MPa)
Finnish spruce (cantilever)	mean	13.0	700	668
	rel. std	4.0%	2.2%	6.5%

Table 3.14 Mean elastic constant values and corresponding relative standard deviations for the kantele spruce tonewood. The obtained values are consistent with previously reported data for spruce, as presented in [47, p.96].

	Meas. (Hz)	Num. (Hz)	Δf_n (Hz)	$\frac{\Delta f_n}{f_n}$ (%)	Δf_n (cent)
(1,0)	52	51	-1	-1.5	-25
(1,1)	98	100	2	1.9	32
(2,0)	311	315	4	1.3	22
(1,2)	337	335	-2	-0.6	-10
(2,1)	398	394	-4	-0.9	-16
(2,2)	637	629	-8	-1.2	-21

Table 3.15 Errors between experimentally measured and numerically computed eigenfrequencies for the Finnish spruce plate under cantilever BCs. The numerical frequencies were obtained in COMSOL using the mean elastic constant values reported in Table 3.14.

From the comparison, one can observe how errors are $\leq 2\%$, validating the accuracy of the presented methodology under experimental settings.

3.7 Case study 1: A comparison of normal and thermally-aged tonewood elastic properties

As mentioned in Section 2.2.4, the impact of wood aging represent a relevant source of uncertainty when trying to obtain a best estimate of the elastic constants of tonewood used to build musical instruments. Within this case study, the estimation routine presented and validated in the previous sections is now exploited to compare the elastic properties of aged tonewood and not-aged specimens. For this purpose, six Finnish tonewood samples used for kantele making available from a master luthier, are considered. Three out of the six samples were thermally aged to serve as a comparison. The trivial properties of the samples are reported in Figure 3.16. Generally, the thermally aging process for tonewoods requires different phases including the temperature increase, the heat treatment by keeping a fixed temperature and humidity and finally the cooling step. Overall, used temperature for thermally aged tonewoods range between ≈100°C and 180°C [149, 52]. The thermally aged tonewoods in this study were treated in a DIY oven owned by the luthier. An example of a similar oven kind can be found in [193]. The internal oven temperature was initially increased up to 170°C. This first stage took a total of between 3 and 4 hours. Simultaneously, steam is added until the internal tonewood temperature reaches 90°C. The temperature was then kept constant for 4 hours before switching it off. The tonewoods were then left in the oven until the day after, when the internal temperature decreased to 40°C. Overall, the entire aging procedure took about 24 hours.

Plate Number	L_x (m)	L_y (m)	h (m)	ρ (kg/m^3)
1	0.204	0.1	0.00482	400
2	0.224	0.099	0.00476	447
3	0.215	0.108	0.00461	439
4	0.144	0.107	0.00481	439
5	0.207	0.09	0.00476	490
6	0.211	0.105	0.00478	438

Table 3.16 Physical properties of the tonewoods. Colored plates denote thermally aged tonewoods

Elastic constants estimation

To estimate the elastic constants using the method laid out in Section 3.3, EMA measurement campaigns were performed on the specimens. To do this, the same experimental cantilever BCs used in 3.6 was implemented. The miniature impact hammer (PCB 086EB0) was used to excite the plates under test, while the monoaxial accelerometer (PCB 352A21) captures the impulse responses (IRs). The accelerometer remains fixed at a single location, whereas the hammer roved across three excitation positions. Source and receiver locations were chosen so as to avoid nodal lines of the modes of interest, which were identified beforehand using a COMSOL plate model of the tonewood. To reduce measurement uncertainty, the hammer was mounted on a steel frame to stabilize the impact point, and five IRs were acquired at each position to compensate for the low repeatability of the force signal. The signals were sampled at 44 kHz and subsequently processed in MATLAB to obtain the FRFs. The three FRFs from each plate were then averaged, and experimental modal frequencies were extracted via a peak-finding routine. These are illustrated in Figure 3.12.

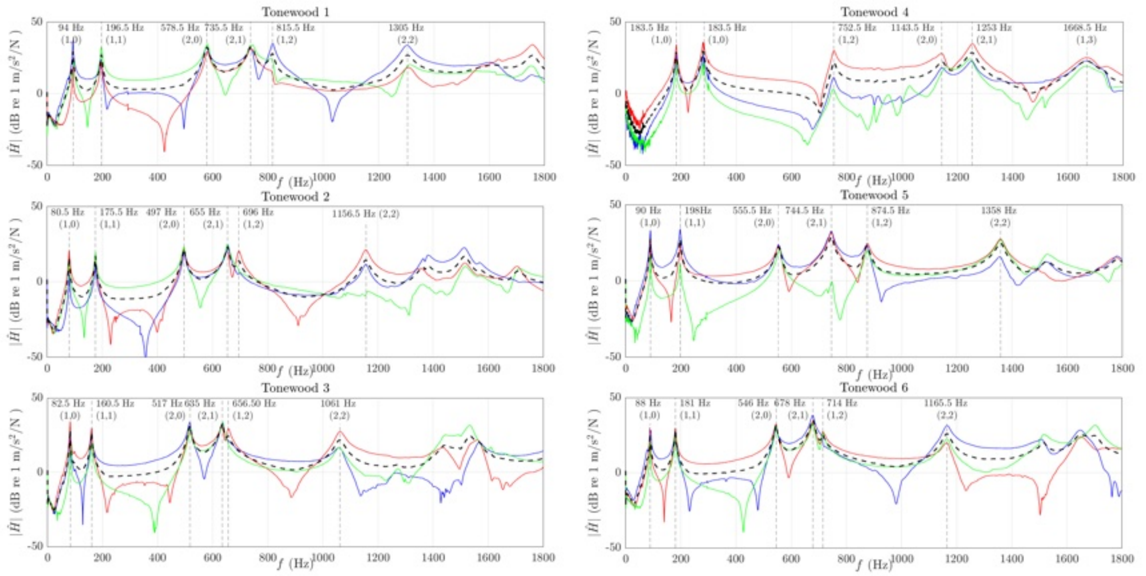

Fig. 3.12 Magnitude spectra of the FRFs for the six tonewood samples under study. Three excitation positions were evaluated for each plate. Dashed black lines indicate the averaged peak frequencies.

To validate the experimental measured data and the implemented BCs, a second measurement campaign was repeated on Tonewood 3, under the same setup after removing and mounting again the same specimen. The data from this repeated campaign, along with a comparison of the spatially averaged frequency spectra from the two campaigns, are shown in Figure 3.13. The identified frequency peaks differed by ≤ 3 % between the two datasets. As

Frequency (Hz)						
Dataset 1	82.5	160.5	517	635	656.5	1061
Dataset 2	81.0	157.0	507.5	629.5	668.0	1071
Error %	1.81	2.18	1.83	0.86	1.75	0.94

Table 3.17 Comparison of frequency peaks for Tonewood 3 between the two measurement campaigns. Errors are reported as percentage differences.

per the preliminary experimental validation of the inverse estimation method given in 3.6, the

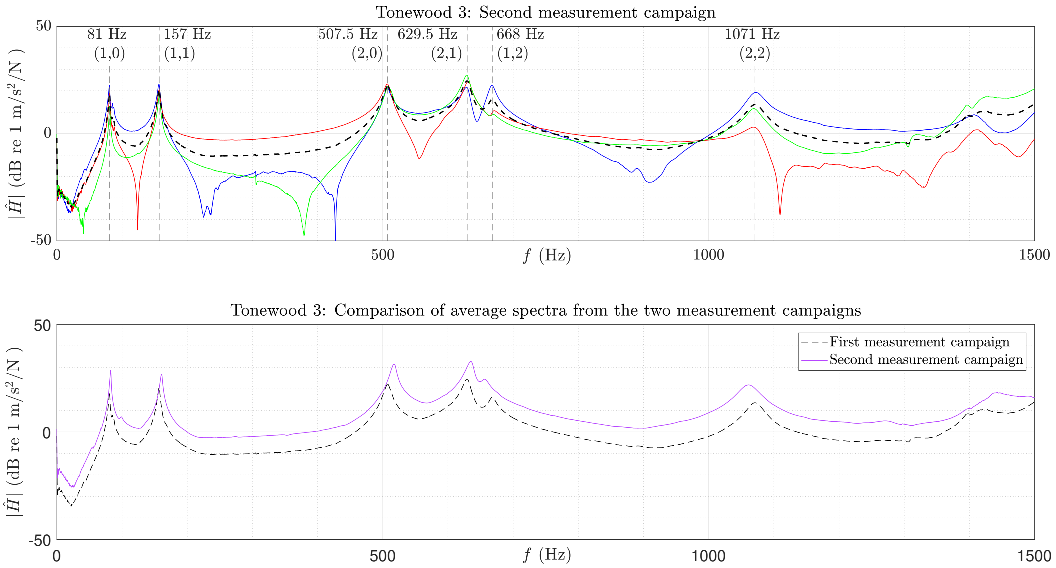

Fig. 3.13 Top: FRF spectra for Tonewood 3 at the three measurement positions from the second campaign. Bottom: comparison of the spatially averaged FRF spectra between the first and second campaigns. Note how the magnitude offset observed between the two spectra is due to a different input gain amplification used between the two measuremnents campaigns.

Chladni patterns tests were here used to identify the ODSs on the different tonewoods. This was done using the identical excitation setup from Section 3.6. The identified patterns are reported in Figure 3.14. As it can be seen from the ODSs, Tonewood 4 presents a different sequence of modal patterns due to the different α value. Finally, the training set of plates required to retrieve the necessary numerical data was computed in COMSOL as explained in Section 3.6, using the same set of elastic constants in Table 3.1.

Results

The resulting values are reported in Figure 3.15. From a first glance, it would seem that overall the values of the tonewood elastic constants tend to increase after aging. This observation appears to be in line with previous literature results on the impact of natural wood aging, which showed an increase in the elastic constants E_x and G_{xy} of akamatsu (red pine) after 8 years from the collection of the wood samples [195]. To assess the minimum observable differences between untreated and thermally aged tonewoods, Lehr's equation [166] was applied. This formula quantifies the required sample size n_{req} to detect a given

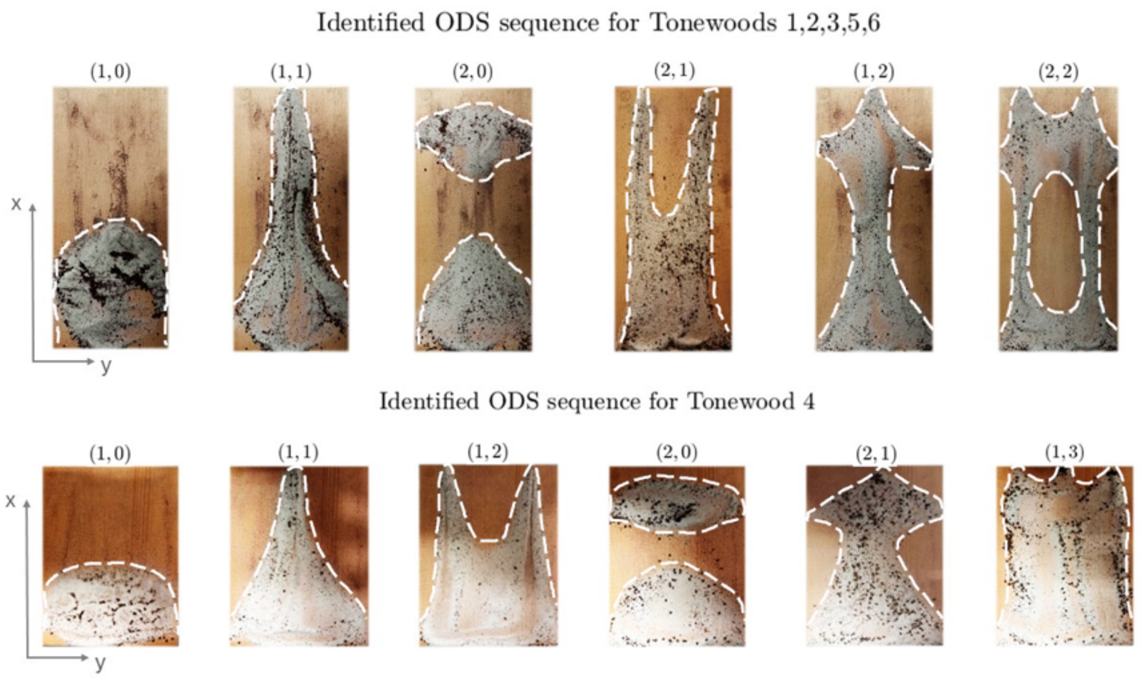

Fig. 3.14 Identified operational deflection shapes (ODS) sequences for the tonewoods under study. (a): ODS sequence for tonewoods 1,2,3,5,6 . Here, tonewood 1 was taken as an illustrative example for all the interested tonewoods (b): ODS for tonewood 4. Images brightness and contrast were modified only for illustrative purposes.

percentage change p between group means:

$$n_{req} = \frac{16\,cv^2}{p^2}, \tag{3.17}$$

where cv is the coefficient of variation, defined as

$$cv = \frac{100s}{\bar{x}}, \tag{3.18}$$

with s the sample standard deviation and $\bar{x}$ the sample mean. Rearranging 3.17 gives the minimum detectable difference:

$$p = \frac{4cv}{\sqrt{n_{req}}}. \tag{3.19}$$

The corresponding values for p are reported in Table 3.18, together with the absolute differences between the mean values of untreated and thermally aged samples. As shown, no statistically significant differences could be detected given the sample size of this study.

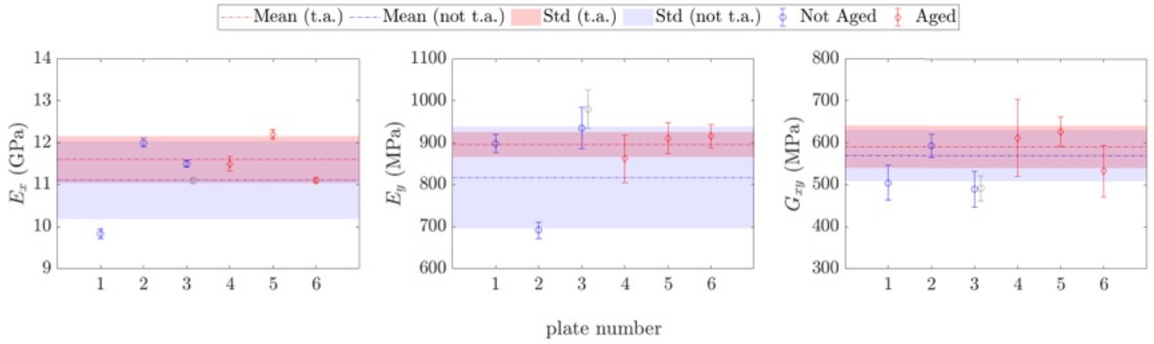

Fig. 3.15 Comparison of estimated values for the E_x, E_y and G_{xy} elastic constants for all the six tonewoods samples under study. In red are reported the values for the thermally aged (‘*t.a.*’) plates. In blue are reported the values for the not thermally aged (‘*not t.a.*’) plates.

Elastic constant	p (%)	$\lvert\mu_{n.t.a.} - \mu_{t.a.}\rvert$ (%)
E_x	12.1	4.4
E_y	16.1	9.6
G_{xy}	17.0	3.7

Table 3.18 Minimum detectable changes p for each elastic constant, compared to the absolute percentage difference between the mean values of thermally aged ($\mu_{t.a.}$) and untreated tonewoods ($\mu_{n.t.a.}$).

Decay times

T_{60} values were evaluated for all tonewoods, considering only the modes common to all plates. These were obtained from the relationship between the -3 dB bandwidth ($\Delta f_{-3\text{dB}}$) and the reverberation time [216]. The t_{60} were then estimated from 2.18. For a lightly damped system $\Delta f_{-3\text{dB}} = 2\zeta f_n$ [225]. Accordingly, the time constant and the -3 dB bandwidth are related by $\tau = 1/(\Delta f_{-3\text{dB}})$ so that:

$$t_{60} = \frac{3\log(10)}{\Delta f_{-3\text{dB}}}. \tag{3.20}$$

The -3 dB bandwidth values were estimated using a peak-finding routine in Matlab. As expected, t_{60} decreased with increasing frequency across all samples. Equation 3.19 was again used to determine the minimum detectable mean differences between thermally aged and untreated tonewoods. The mean values of the aged samples appeared lower than those of untreated tonewoods. Again, this would be in accordance with the decrease in internal damping found in naturally aged wood in [195]. However, the observed differences were smaller than the detectable thresholds as it can be seen from the minimum detectable differences reported in Table 3.19.

Mode index (x,y)	p (%)	$\lvert\mu_{n.t.a.} - \mu_{t.a.}\rvert$ (%)
(1,0)	44.1	27.9
(1,1)	29.4	9.3
(2,0)	29.7	7.6
(2,1)	22.8	19.5

Table 3.19 Minimum detectable differences p in t_{60} values for each modal shape, compared with the absolute percentage differences between mean values of thermally aged ($\mu_{t.a.}$) and untreated tonewoods ($\mu_{n.t.a.}$).

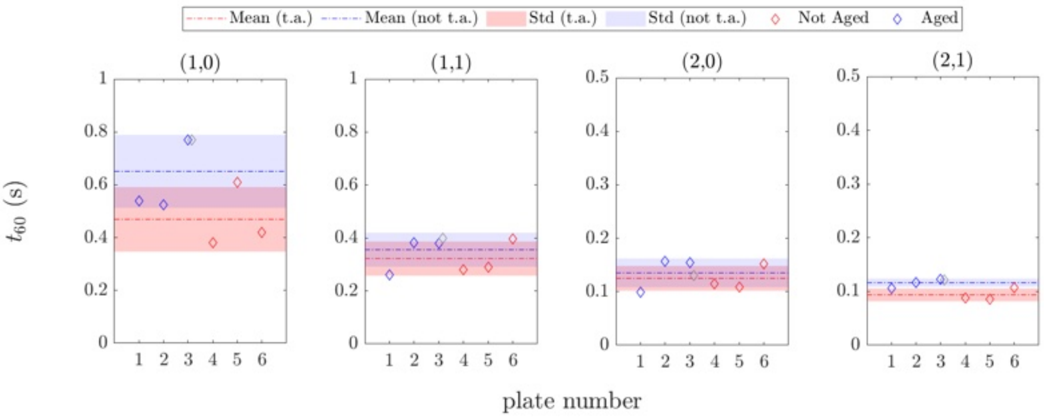

Fig. 3.16 Decay times (t_{60}) for the first four modes shared by all tonewoods.

Discussions

Overall, despite the limited sample size available for this study, no statistically significant differences were observed between the thermally aged and untreated tonewood specimens in terms of either elastic constants or modal decay times. While the results cannot be generalized beyond the specific materials and conditions tested here, they provide useful insights both for luthiers and instrument makers when dealing with new instruments or restoration interventions. In particular, they suggest that, under the specific thermal aging process adopted in this study, the mechanical and damping properties of Finnish tonewood may remain largely unaffected. However, further studies involving a larger number of samples and controlled aging conditions are needed to confirm these assumptions.

3.8 Summary

The Chapter introduced the first main research outcome from the work conducted within the PhD thesis. Specifically, by recalling the first research objective from Section 1.5, an inverse estimation method based on the least squares minimization between measured and numerically obtained eigenfrequencies is presented, enabling an estimate of the rigidity constants D_x, D_y, and D_s under arbitrary BCs. The method was numerically benchmarked using FE based models via COMSOL for three different configurations: cantilever, fully clamped, and free BCs. Accurate results are obtained for all the numerical test cases, with errors not exceeding bounds reported in previous established methods [268]. Compared to reference analytical estimation techniques [183, 53], the method allowed for a refinement to the estimate of the shear modulus in the closed-form formula for a rectangular plate under fully free BCs. The method is then validated experimentally, where the classical and well-established Chladni patterns technique [64] is exploited to identify the ODS. The low errors (i.e. ≤ 2 %) between measured and numerically computed eigenfrequencies retrieved by inputting average estimated elastic constants values in COMSOL confirmed the applicability of the method under a real case scenario. Lastly, a first case study is also presented, offering an example of a possible application of the method. Here, a comparison between thermally aged tonewoods and non-aged specimens is provided. Despite the low number of specimens, the results seem in line with previous research. For the presented experimental test cases, a standard excitation approach is used (i.e., impact hammer and shaker), as well as standard EMA practices. In the next Chapter, the focus is on the development and validation of a cost-effective and user-friendly experimental measurement chain.

Chapter 4

Towards a cost-effective experimental setup

In this section, an experimental validation is presented to support the development of a cost-effective measurement setup . The validation starts by assessing the use of electrodynamic transducers (exciters) for EMA purposes. Previous studies have already demonstrated their suitability in workshop scenarios, providing an accessible tool for luthiers and instrument makers while enabling wideband excitation signals [10, 12]. A major advantage of this approach is the ability to inject sufficient energy into the structure under test at higher frequencies, which is particularly relevant when working with musical instrument components that can vary significantly in size and, consequently, in their natural frequencies. The chapter proceeds by presenting a validation of a cost-effective measurement chain to define a reliable and accurate setup that can be implemented in workshop contexts to support modal analysis practices. This is followed by an additional experimental validation of the method introduced in Section 3 carried out on a real guitar plate, demonstrating the applicability of the proposed setup under realistic workshop conditions. Finally, the validation of a fully accessible framework that incorporates the open-source software MagPie to generate the numerical training data required by the method described in Section 3.3 is presented, thereby removing the need for commercial software on both the numerical and experimental sides of the estimation process.

4.1 Electro-dynamic transducers for modal analysis

The use of small electro-dynamic exciters combined with the use of the ESS technique [103, 102] has been recently introduced as a more accessible wideband excitation solution for modal analysis measurements on real musical instruments [10, 12]. Here, a comprehensive experimental validation is performed against standard EMA setups [57, 42], showing the application in practical case scenarios. Particularly, guidelines are given regarding the influence of exciter size and positioning on the boards under test, while the feasibility of continuous wideband excitation is exploited as a tool for real-time spectral analysis during instrument-making practices.

4.1.1 Validation against Impact hammers

As anticipated in Section 1.3, the impact hammer technique represents a widely adopted approach in EMA of musical instruments and related structures [111, 44, 92, 174]. The impulsive excitation provided by the impact hammer is intended to approximate a Dirac delta, though in practice the finite duration of the pulse leads to a progressive loss of energy at higher frequencies [131]. Furthermore, the stiffness of the hammer tip influences the usable range, which becomes particularly critical for softwoods such as spruce [69, 98]. On the other hand, the ESS technique offers a broadband continuous excitation approach, ensuring high measurements coherence and the advantage of separating nonlinear effects from the linear spectral response of the structure under test [103, 102, 127, 214, 107]. The use of exciters together with the ESS test signal was used to investigate subtle design interventions at different manufacturing stages on guitar soundboards, from varnishing to bracing design [9]. However, as pointed out in previous research, the additional mass added by the exciter can significantly impact the the measured vibroacoustics response of the instrument soundboard [174]. Hence, to conduct a thorough experimental validation, exciters of different mass are here assessed, ranging from 2.5 g up to 50 g. Table 4.1 reports the Thiele & Small parameters measured in free air via the "added-mass" method [215], indicating progressive increases in driving capability with size, at the cost of larger added mass. For the validation, a rectangular spruce plate was used with dimensions $L_x = 600\,mm$, $L_y = 210\,mm$ and $L_z = 40\,mm$. To

	Tot. Mass (g)	f_{md} (Hz)	R_e (Ω)	Q_{ms}	Q_{es}	Q_{ts}	C_{ms} (mm N^{-1})	M_{ms} (g)	R_{ms} (Ω)	BL (N A^{-1})	L_e (mH)
Exciter 1	2.5	1325	3.5	24.72	445.3	23.42	0.14	0.10	0.03	0.08	0.01
Exciter 2	6.5	483	7.0	12.43	111.9	6.09	0.20	0.52	0.13	0.97	0.04
Exciter 3	12.5	451	1.7	7.90	2.80	2.07	0.20	0.58	0.21	1.01	0.02
Exciter 4	50	333	4.0	8.60	1.44	1.24	0.21	1.06	0.26	2.48	0.04

Table 4.1 Physical and Electrical Parameters of Different EXC Models

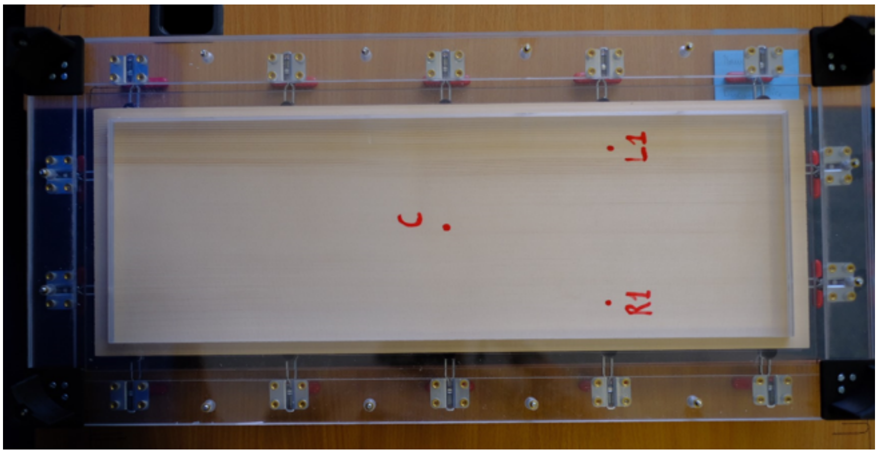

Fig. 4.1 Schematic representation of the measurement setup. The red dots **L1** and **C** indicate the excitation points, namely locations for either the impact hammer hits or the contact point for the exciters while performing the validation measurements, while **R1** indicates the position of the accelerometer.

practically perform the experimental measurements, the board was clamped along all its edges by using a dedicated heavy plexiglass frame, as shown in Figure 4.1. For the purpose of the validation, a PCB Piezotronics 352C23 accelerometer was used in this validation stage to maintain consistent measurement conditions and avoid additional sources of variability. Two excitation positions were explored: a lateral point (L1), chosen to minimize interference, and a central point (C), where modal nodes and antinodes alternate and where the presence of added mass is expected to have stronger consequences. For each exciter, four conditions were examined:

- **Impact hammer exciting the board.** This configuration provided a reference dynamic behavior of the board obtained using a standard EMA approach.
- **Impact hammer exciting the board with an equivalent exciter mass attached.** This configuration aimed to isolate the effect of an added equivalent attached mass on the board's frequency response.
- **Impact hammer exciting the board with the exciter attached but not powered.** This configuration allowed to assess the influence of the exciter's mechanical coupling on the board's dynamic behaviour while comparing it against the simpler attached mass test case.
- **ESS excitation of the board through the exciter.** Finally, this condition exploited the capability of the proposed measurement setup and was used to compare the result-

ing dynamic response with the reference EMA measurement obtained from the first configuration.

To provide an equivalent mass for the different exciters, coins of various sizes were used and attached to the board through the use of wax, providing the same equivalent mass of each exciter. These are shown in Figure 4.2. For the measurements with the impact hammer, five impacts were used to provide reliable data [111]. On the other hand, an ESS signal ranging from 45 Hz to 8 kHz and normalised at - 6 dBLUFS was generated with Adobe Audition 3.0 software using the Aurora plugins [56]. The ESS was outputted from a portable computer through a Focusrite Scarlet 2i2 audio interface and entering a 20 W linear amplifier. The linear amplifier respone can be appreciated in Figure 4.3 . This was measured using the ESS method by connecting the output terminals of one of the two channels to a 8 Ω dummy resistor (5 W power rating). The amplifier output was then calibrated to provide 1 W over 8 Ω, namely 2.83 V. For the measurements, the output voltage of each exciter was measured via a Fluke 177 multimeter and calibrated in order to consistently produce 0.25 W at 1 kHz. Finally, a zoom F8 audio interface was used to acquire the data which was then post processed in Matlab. The FRFs spectra are here reported in terms of mobility Y in dB. Note how for the case of the exciter, as no forcing signal is recorded during the sine sweep measurements, the excitation force F can be retrieved using the known measured Thiele and Small parameters as expressed by the Lorentz force [99]:

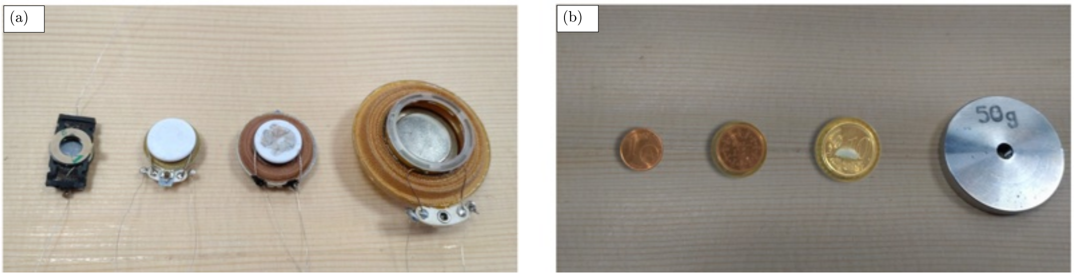

Fig. 4.2 (a): Electrodynamic exciters used in this study, ordered left to right: Exciters 1 through 4. (b): Corresponding equivalent masses: 2.5 g, 6.5 g, 12.5 g, and 50 g.

$$F = Bl \cdot I \tag{4.1}$$

Where $I = V_{exc}/Re$ and V_{exc} is the exciter output voltage. As it will be discussed in Section 4.1.3, F can indeed be assumed constant within the interested bandiwidth when locating the exciter in a suitable excitation point (i.e. a point where the response can be assumed to be unaffected by the coupling with the board under test.) The measurements comparison is

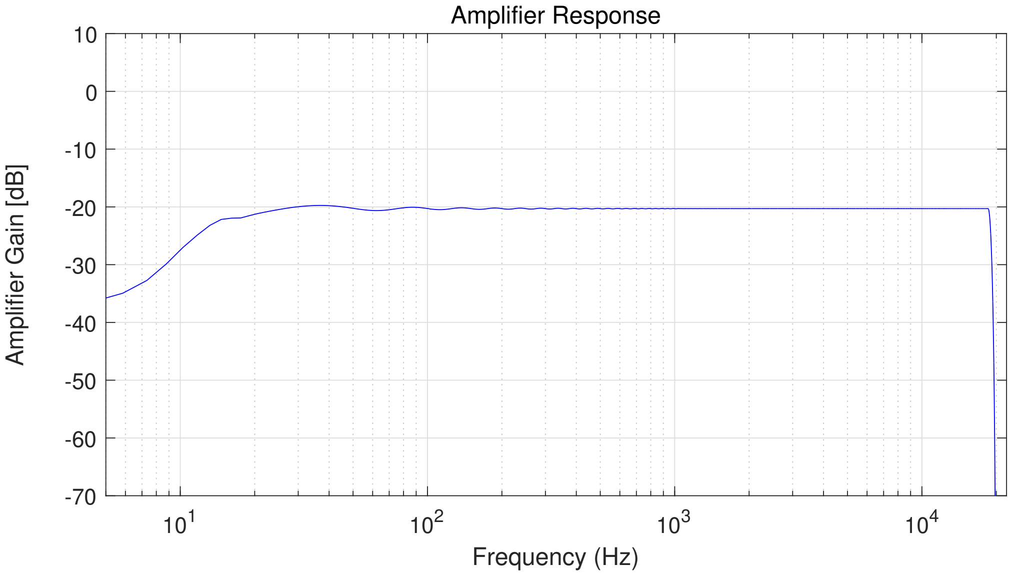

Fig. 4.3 Response of the 20W class D amplifier used for all the experiments.

reported in Figure 4.4 for the four configurations. In the plots, the reference FRFs from the impact hammer measurement setup are reported in blue, the measured data gathered from the exciter setup using the ESS signal is reported in black, and the measurements performed using the equivalent coin mass and the exciter mass are given in green and red. The results show how Exciter 1 could not provide enough energy at low frequencies to excite the first natural frequency of the board under test. Nonetheless, an overall good agreement is observed when comparing the impact hammer setup against the measurements carried out with the exciter mass and through the ESS signal driven by the exciters. Conversely, larger discrepancies are found when comparing the reference data to the resulted spectra in the equivalent coin mass configuration. Deviations in the first resonance frequency identified through the impact hammer against the exciter measurement setup at excitation point L1 are reported in Table 4.2. The validation was then conducted using C as the excitation point. This location was deliberately chosen to accentuate differences between measurement configurations, as it lies across regions of alternating nodes and antinodes in the modal shapes under fully clamped conditions. As per the previous excitation point, the resulting spectra are given in Figure 4.5. Evidently, the response at low frequencies is strongly affected by the presence of the transducers. However, clear discrepancies emerge between the coin-mass and exciter-mass cases. Specifically, the coin appears behaving as a simple added mass, producing a downward shift in resonance, whereas the exciters introduce an upward shift, indicating a more complex interaction.

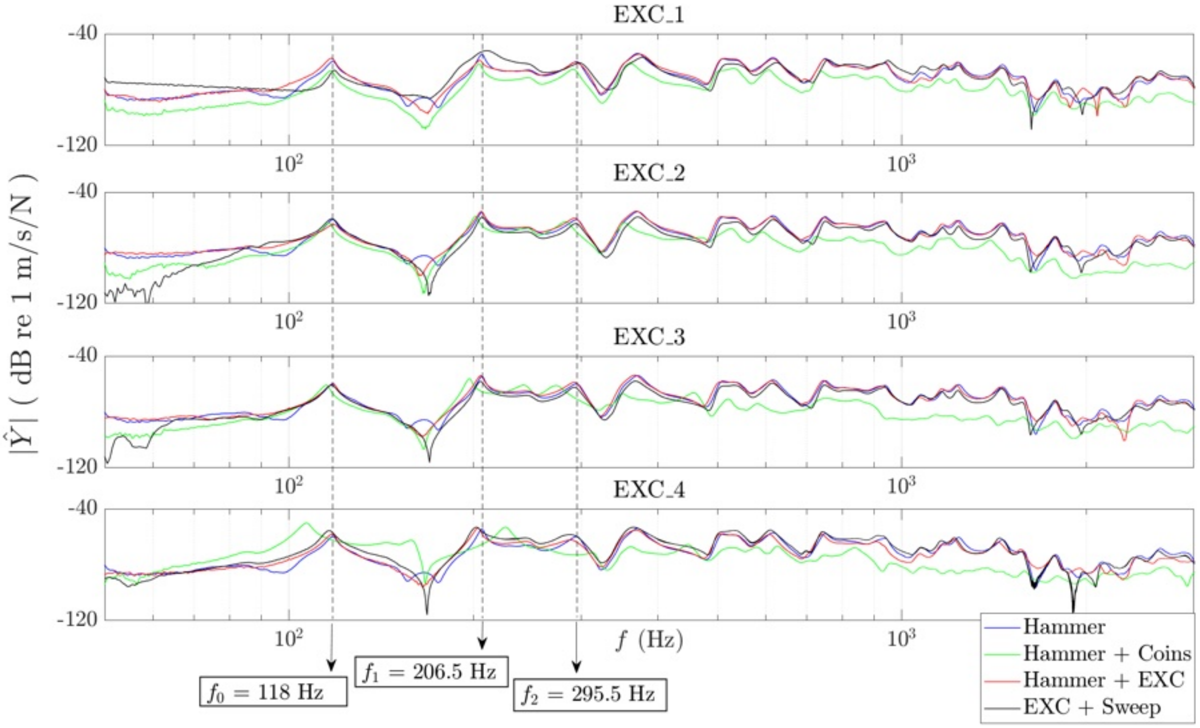

Fig. 4.4 Exciter validation comparison. In all plots, the FRF spectra are shown for the following cases: hammer excitation on the raw board (solid blue), hammer on the board with exciter attached (red), hammer on the board with an equivalent-mass coin (green), and sine sweep excitation via the exciter (black). Coin masses match those of the corresponding exciters, as listed in Table 4.1. Dashed black lines denote the first three reference experimental frequencies identified through the hammer measurements. Excitation is applied at point L1, and response is measured at R1 from 4.1.

		EXC_1	EXC_2	EXC_3	EXC_4
Hammer	f_0 (Hz)	118.5	117.5	117	116
$f_0 = 118$ Hz	dev. (%)	0.42	-0.43	-0.85	-1.72
	dev. (cent)	7	-7	-14	-29

Table 4.2 Fundamental frequency f_0 and associated relative deviations extracted from the FRF spectra, comparing the reference hammer measurement with the four exciters. Excitation is applied at point L1, as shown in Figure 4.1.

4.1.2 Coherence assessment

Before further investigation of the coupling between the exciter and the board, the capability of the ESS method via the exciters was compared against the benchmark measurements

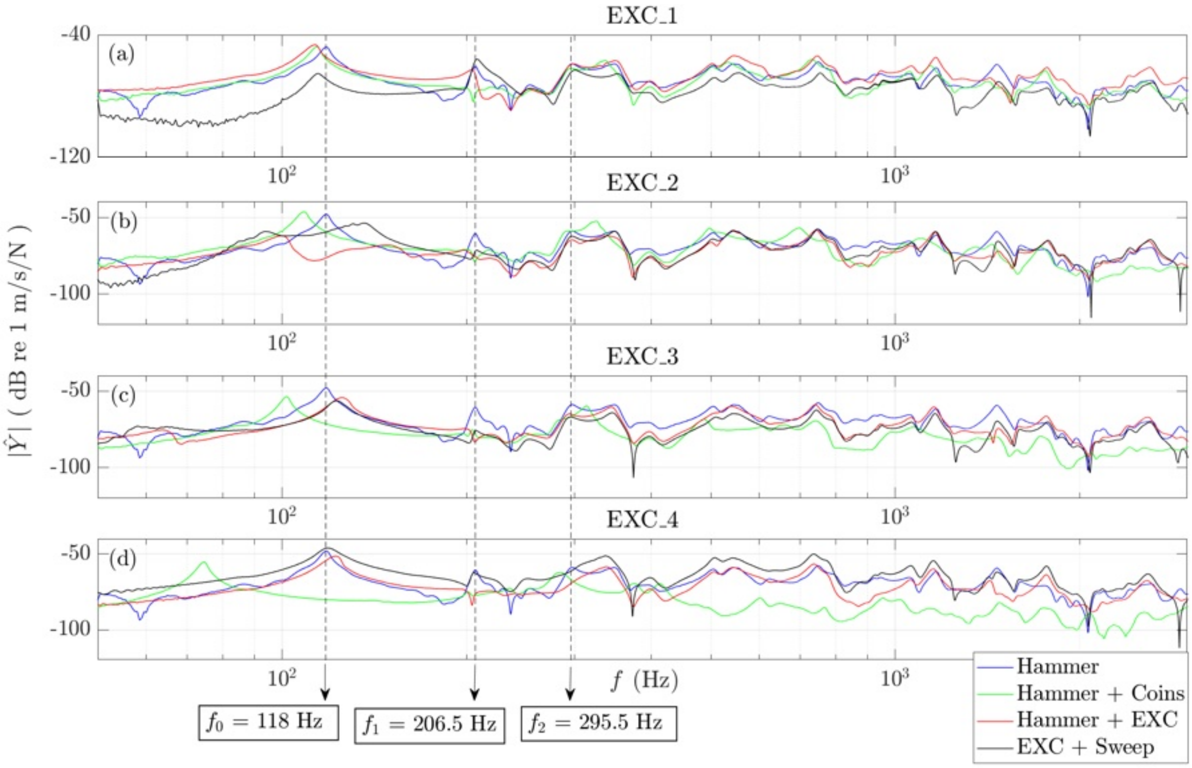

Fig. 4.5 Exciter validation. Same configuration as in Figure 4.4, but with excitation applied at point C.

from the impact hammer through a coherence evaluation between input and output signals resulting from the two setups. Specifically, for the measurements using the ESS method via the exciter, the coherence is here evaluated between the ideal IR obtained when convolving the input test signal with its inverse filter [103] against the measured IR obtained using the output response captured by the accelerometer, thus allowing an assessment of the linear correlation between the input and output signals. Figure 4.6 shows representative results for the different exciters. Overall, both hammer and exciter-driven sine sweeps delivered comparable coherence values up to about 200 Hz. At very low frequencies, the hammer achieved slightly higher coherence than the smallest exciter (i.e. Exciter 1), reflecting its limited driving power. However, beyond 3 kHz the performance reversed: the hammer coherence progressively degraded, whereas the ESS method maintained stable values up to the maximum test frequency of 8 kHz. This extended bandwidth is especially relevant when wide-band excitation is required, for instance, in experimental studies of bridges, bracings, or complete soundboards.

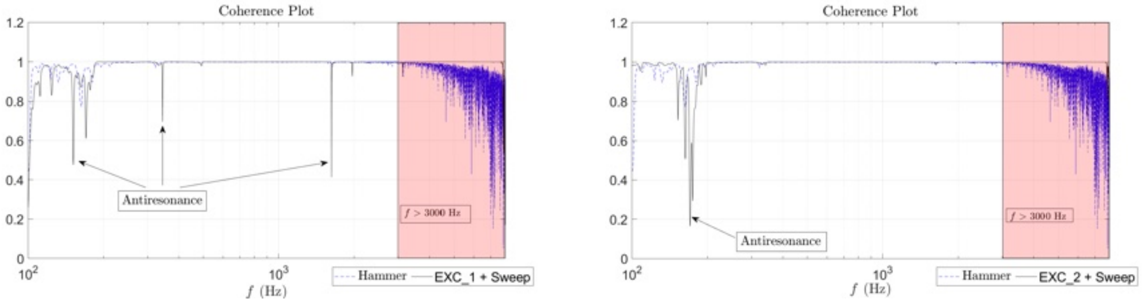

(a) Hammer against Exciter 1.

(b) Hammer against Exciter 2.

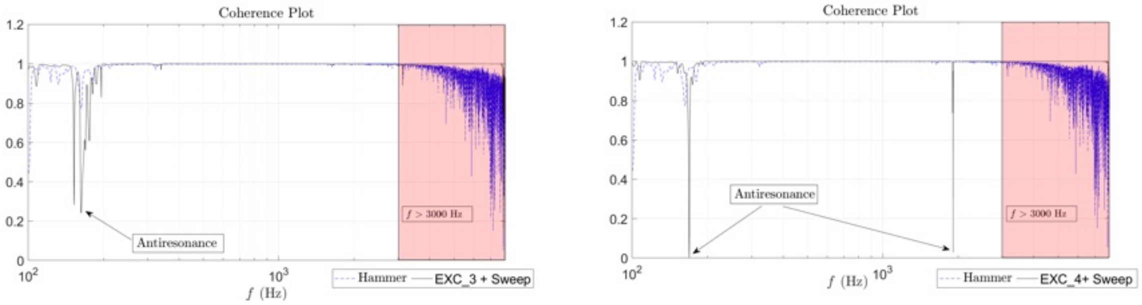

(c) Hammer against Exciter 3.

(d) Hammer against Exciter 4.

Fig. 4.6 Coherence comparison between the impact hammer method and the different exciters.

4.1.3 Impedance measurements

To better understand the coupling between the board under test and the exciter, electrical impedance measurements were conducted, as they represent a common practice for analysing the resonance behavior of the loudspeaker's mass-spring system [244, 152, 76]. Measurements were carried out with a calibrated Clio Pocket system by Audiomatica [8], which directly provides absolute impedance values later processed in Matlab. The exciters were connected using lightweight wiring fixed to the supporting frame to avoid parasitic vibration effects. The unit consists of one input and one output channel. In this setup, the output was operated in closed-loop mode so that the impedance magnitude $|Z|$ could be determined by applying a known voltage and simultaneously measuring the current across an internal reference resistor and the exciter under test [215]. The connections were made using cables terminated with crocodile clips, whose internal resistance was verified as $0.1\Omega \pm 0.05\Omega$. Each exciter was wired with lightweight, flexible leads, secured to the plexiglass frame with putty to prevent mechanical interference. A small arc of slack was intentionally left in the wire between the frame and the transducer to reduce constraint forces. To examine repeatability, Exciter 3 was mounted at location L1 and measured 32 times. For each measurement, the actuator was detached and repositioned with fresh wax, introducing minor changes in orientation and placement to simulate practical variability. Across all trials, the main impedance peak occurred at 75.6 Hz with a mean amplitude of 3.76 Ω. The three-sigma spread was ±2.7 Hz in frequency and ±0.57Ω in amplitude, demonstrating a high level of consistency in the electrical measurements, as shown in Figure 4.7.

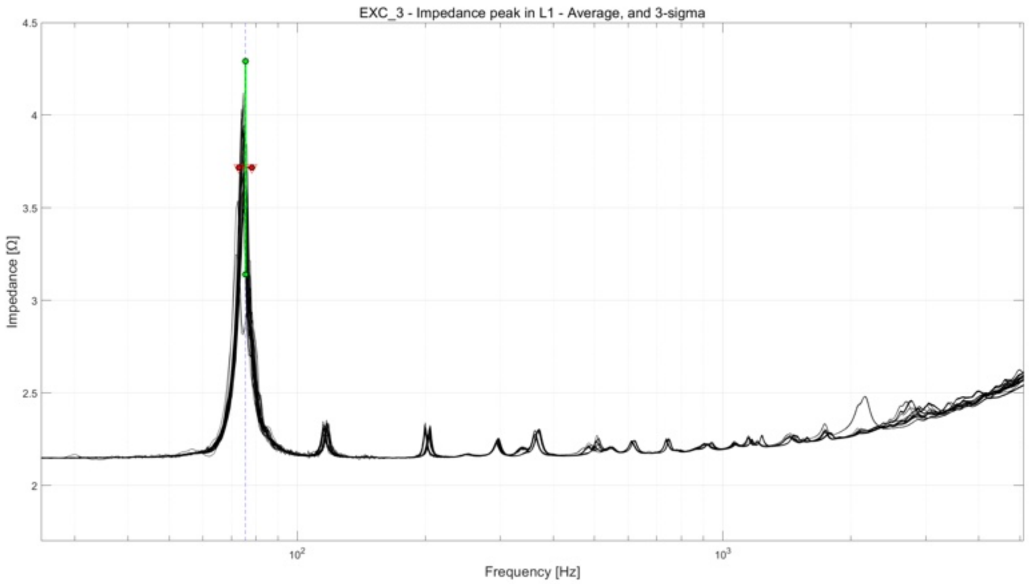

Fig. 4.7 Statistical evaluation of the electrical impedance for Exciter 3 measured at L1, based on 32 samples. The dashed blue line indicates the mean peak frequency of 75.6 Hz. The green line represents the $\pm 3\sigma$ range of the amplitude (± 0.57 Ω), while the red line denotes the $\pm 3\sigma$ interval for the peak frequency (± 2.7 Hz).

Given its limited driving capacity, Exciter 1 was excluded from subsequent tests. The other three exciters were then evaluated in both L1 and C positions, reproducing the conditions used for the impulse response experiments. Figure 4.8 compares the resulting impedance curves: when placed at L1, all devices exhibited a single dominant resonance peak with only minor secondary maxima, while at C, two large resonances appeared together with several additional local maxima, reflecting the different modal conditions at that point. A complementary experiment was performed using Exciter 3 to explore the effect of additional mass. Results are shown in Figure 4.9. Incrementally loading the transducer with rigid weights shifted the combined resonance f_{md} downward, as expected for a mass–spring system. The position of the higher-frequency local maxima remained essentially unchanged. The dashed lines indicate the resonance frequencies of the spruce plate itself, including the (0,0) mode at 118 Hz. At position L1, this mode appeared near the first local maximum, whereas at position C it was located between the "low" and "high" resonances (f_l, f_h). These

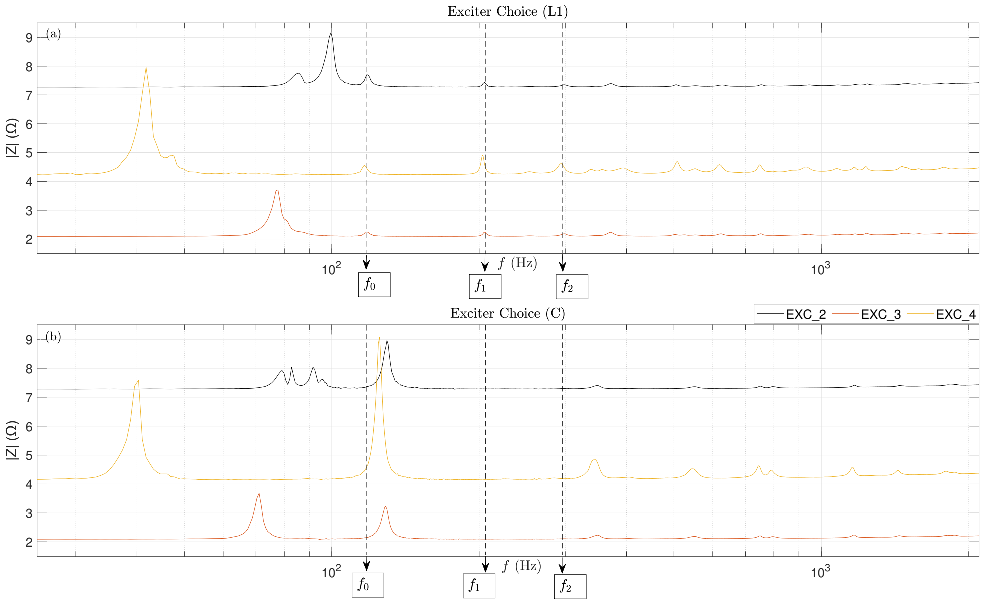

Fig. 4.8 Electrical impedance plots for Exciters 2,3 and 4 positioned at L1 (top) and C (bottom). Dashed lines indicate the first resonance frequencies of the board. At L1, each exciter exhibits a single dominant peak followed by smaller local maxima. In contrast, measurements at C show two prominent peaks and a distinct pattern of secondary maxima.

results highlight how both mounting position and additional mass influence the electrical response of the coupled system.

4.1.4 Model-Based Interpretation of the Coupled Exciter–Board System

To better understand the influence of the exciters on the board, a reduced-order electromechanical model (ROM) of the coupled system was used. This is illustrated in detail in [11] and reported in Appendix A. In the ROM, the soundboard and the exciter are modeled as two mass-spring-damper systems that are mechanically connected at the contact point as well as electrically coupled via the voice coil. The ROM uses experimentally measured exciter parameters together with the modal properties of the board under test. From these input values, it estimates both the mechanical response of the board (restricted here to its fundamental resonance mode) and the electrical impedance observed at the exciter terminals. For this purpose, Exciter 3 is considered as an example and its Thiele & Small parameters measured when attached to the board are reported in Table 4.3 . The modeled data is presented in Figure 4.10. Comparisons between model and experiment show good agreement. When the exciter is placed at the plate centre (C), the model reproduces the observed stiffening

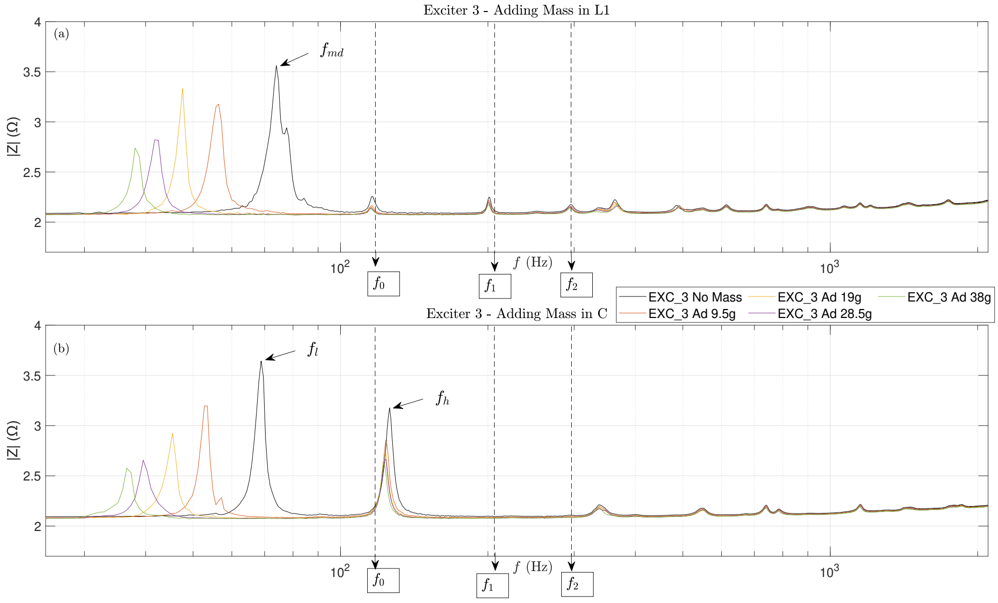

Fig. 4.9 Electrical impedance of Exciter 3 mounted at L1 (top) and C (bottom), with progressively added rigid masses to modify the mechanical resonance f_{md}. Dashed lines mark the first modal frequencies of the board; the fundamental mode (0,0), with $f_0 = 118\,\text{Hz}$, appears near the first small peak in panel (a) and between the two main peaks f_l and f_h in panel (b). An effective excitation point, as in panel (a), is characterized by a single dominant resonance f_{md}, corresponding to the coupled dynamics of the device under test and the transducer. As added mass increases, f_{md} shifts to lower frequencies, while secondary maxima remain unchanged.

effect: the fundamental resonance shifts upward in frequency, and the electrical impedance curve develops a two-peak structure, analogous to a loudspeaker coupled to a resonant cavity. Conversely, when the exciter is positioned at L1, the system behaves more like a free-air driver, with a single impedance peak and negligible disturbance to the plate resonance. Overall, the ROM confirms that the exciter does not simply act as an added mass: depending on placement, it can significantly interact with the structure. This provides a principal explanation for the experimental results shown in the previous paragraphs and underlines the importance of selecting excitation points away from modal maxima in order to obtain reliable frequency response measurements. From a practical perspective, the soundboard-exciter coupling behavior can be interpreted using loudspeaker analogies, as detailed in [11]. At L1 the behavior is equivalent to a driver in free air, giving a single impedance peak at f_{md}, while at C it resembles a vented box, producing two peaks (f_l, f_h) separated by a minimum at the

	f_{md} (Hz)	R_e (Ω)	C_{ms} (mm N^{-1})	M_{ms} (g)	Bl (N A^{-1})	L_e (mH)
EXC_3	73.9	2.1	0.35	13.18	1.01	0.06

Table 4.3 Thiele and Small (T&S) parameters of Exciter 3 measured at position L1. This setup can be interpreted as a free-air driver configuration, consistent with the frameworks proposed by Thiele, Lazar and Kubota, and Magalotti [254, 255, 164, 170]. Notably, the moving mass M_{ms} exhibits a significant variation compared to typical values.

board resonance f_0. These frequencies are linked by [255]:

$$f_{md} = \frac{f_l \cdot f_h}{f_0}. \tag{4.2}$$

As an example, for Exciter 3 in C, $f_l = 69$ Hz, $f_h = 126$ Hz, and $f_0 = 117$ Hz give $f_{md} = 74.3$ Hz, consistent with measurement. This confirms that placement in C alters the resonance (stiffening effect), whereas placement in L1 leaves the response essentially unaffected, ensuring more reliable measurements. From a practical standpoint, when the measured impedance curves show only small local maxima close to the board's eigenmodes, the exciter can be considered to operate safely above its own resonance, hence ensuring reliable measurements [182, 266].

4.2 Cost-effective measurement chain validation

In this section, two experimental measurement chains are tested to evaluate the consistency of the estimation routine presented in Chapter 3 and to systematically validate a simplified and more accessible measurement chain, following the advantages given from cost-effective solutions, as suggested from Section 4.1. To do this, a modal identification and estimation process is conducted for two measurement setups on a single small tonewood sample left from a guitar making process. As for the Kantele small rectangular sample in Section 3.6, the specimen is set under cantilever BCs using the same clamping system, as shown in Figure 4.11. The trivial properties of the plate are reported in Table 4.4.

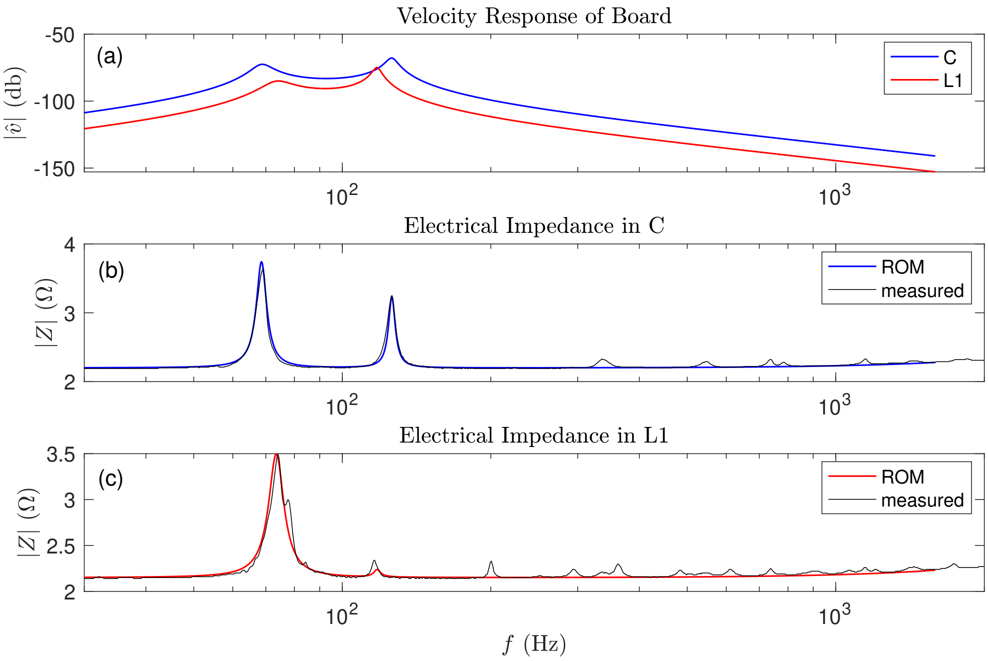

Fig. 4.10 Modeled response of the plate–exciter system for Exciter 3. When positioned at point C, the system exhibits increased stiffness, as indicated by the rightward shift of the board's resonance peak. This shift is also visible in the electrical impedance plot, reflecting the enhanced mobility of the exciter once coupled to the board.

L_x $[m]$	L_y $[m]$	h $[m]$	ρ $[Kg/m^3]$
≈ 0.077	≈ 0.093	≈ 0.0033	≈ 390

Table 4.4 Trivial physical properties of the tonewood sample from the guitar top plate.

4.2.1 High-end experimental setup

For the first experimental setup, representing the reference configuration, the signals from a PCB 086E80 miniature impact hammer and the acceleration signal from a PCB 352A21 uniaxial accelerometer are recorded using a dedicated National Instruments Compact Device Acquisition platforms (DAQs) through the Matlab Data Acquisition Toolbox. For this measurement setup, the accelerometer roves across eleven different measurements locations on the specimen surface. Once acquired, the measured data was then processed using the commercially available *B&K Connect* software, serving as a benchmark for the current evaluation. This allows the computation of all the FRFs per each point as well as a reconstruction

Fig. 4.11 Tonewood sample used in guitar making, here set under cantilever BCs.

of the experimental modal shapes via an industry standard measurement chain. A visual illustration of the measurement chain is given in Figure 4.12.

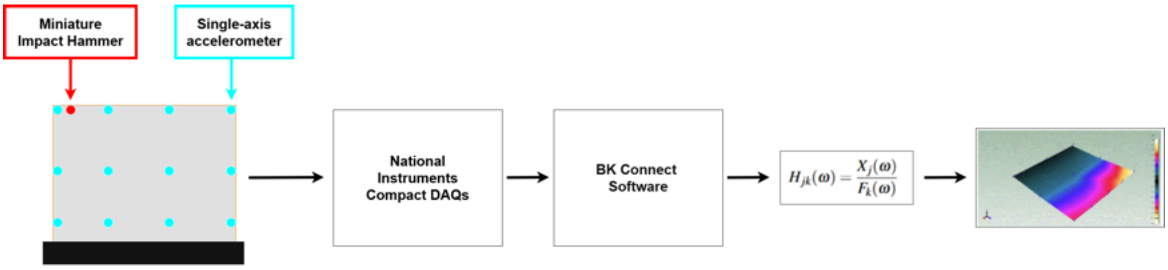

Fig. 4.12 Experimental Setup 1 for the tonewood sample from the guitar top plate. From left to right: schematic of the test configuration used to extract modal parameters via BK Connect software. Eleven accelerometer positions (light blue) and one impact location (red) are marked on the plate surface.

Cost-effective experimental setup

For the second experimental setup, a lower cost experimental measurement chain is adopted. The National Instruments DAQs are here replaced by the ZOOM F8 Audio interface, which, besides being a more accessible device, also represents a common interface used in many different audio related contexts, hence providing a more user-friendly tool. The matlab toolbox is also replaced by the free Audacity audio editor software [252]. On the other hand, concerning the post-processing side, the Chladni Patterns setup from Section 3.6 is used over the *B&K Connect* software to identify the deflection patterns on the plate surface. This was done using an electrodynamical exciter, following the validation offered in Section 4.1. A free and accessible dedicated patch in PureData, offering several excitation test signals, was implemented and used in this experimental setup. It specifically allows to generate and reproduce four different test signals:

- *Frequency oscillator.* This enables precise adjustment of the excitation frequency, which can be set using two horizontal sliders: the upper slider controls the coarse frequency, while the lower slider allows fine-tuning within a restricted range. Alternatively, the oscillator may also be operated via an external MIDI controller.

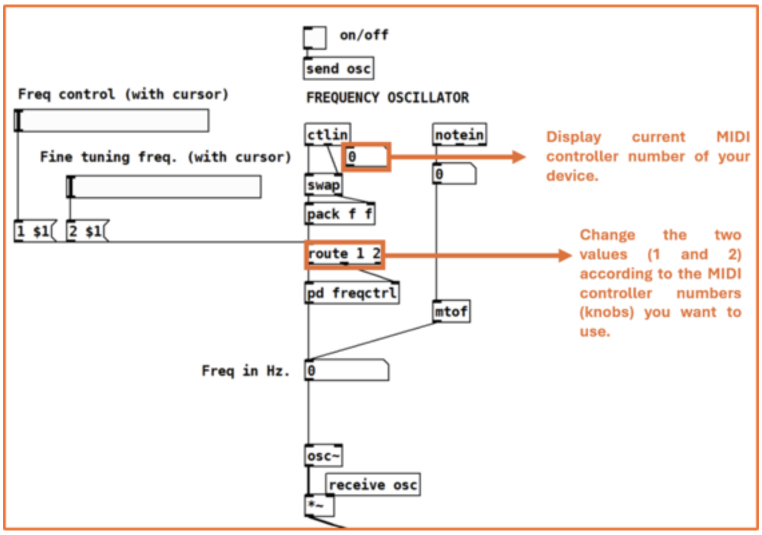

Display current MIDI controller number of your device.

Change the two values (1 and 2) according to the MIDI controller numbers (knobs) you want to use.

Fig. 4.13 Zoomed in view of the frequency oscillator section of the PD patch.

- *Noise generator.* This feature outputs a white noise signal which can be filtered by tweaking the cutoff frequency slider controlling a low-pass filter.

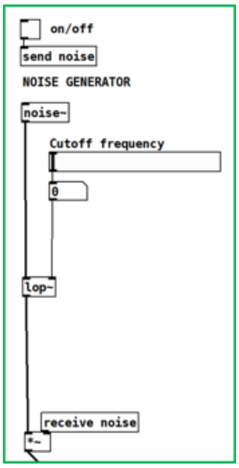

Fig. 4.14 Zoomed in view of the noise generator section of the PD patch.

- *Exponential sine sweep.* The exponential sine sweep module provides a customizable excitation signal, allowing the use of tailored frequency sweeps as input for the measurements.

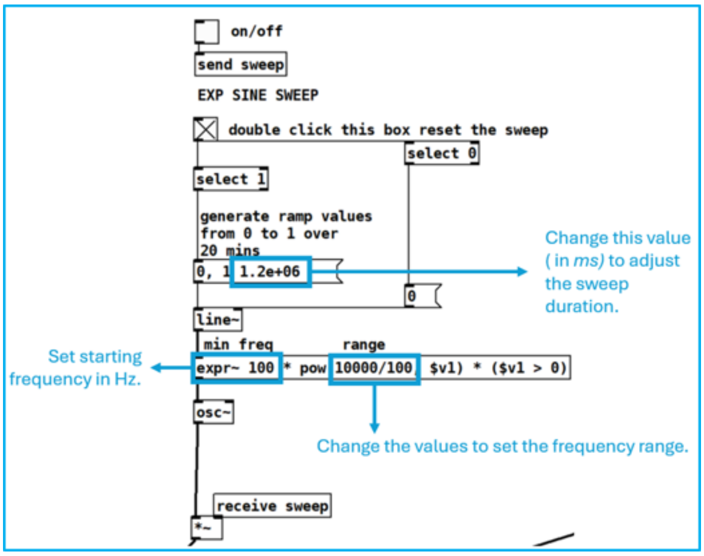

Fig. 4.15 Zoomed in view of the exponential sine sweep section of the PD patch.

- *External audio file.* This allows the user to upload and playback a personal audio file which can be used to excite the musical instrument plate.

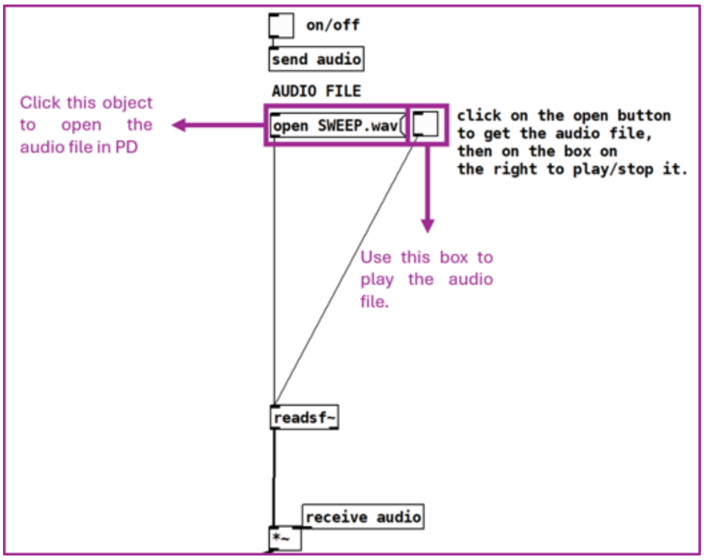

Fig. 4.16 Zoomed in view of the external audio file section of the PD patch.

The patch is available online at: https://github.com/Nemus-Project/pd-utilities/tree/main/signals_2_soundboards and its GUI is shown in Figure 4.17 . For this specific measurement

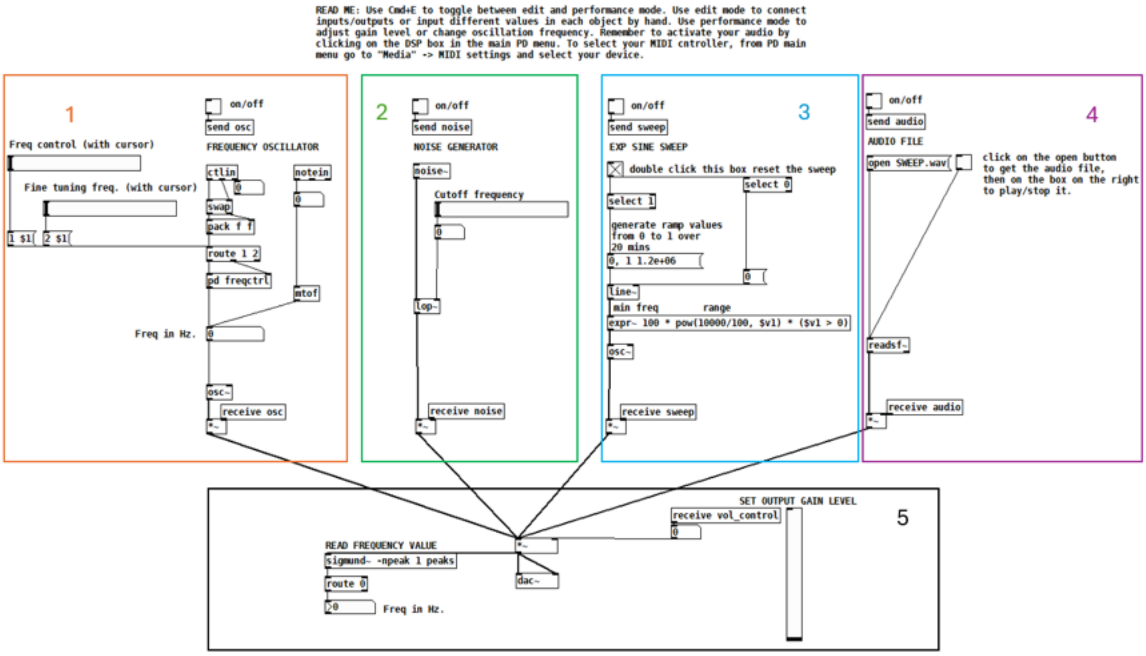

READ ME: Use Cmd+E to toggle between edit and performance mode. Use edit mode to connect inputs/outputs or input different values in each object by hand. Use performance mode to adjust gain level or change oscillation frequency. Remember to activate your audio by clicking on the DSP box in the main PD menu. To select your MIDI cntroller, from PD main menu go to "Media" -> MIDI settings and select your device.

Fig. 4.17 Implementation of the PD patch used to generate excitation signals for the cost-effective measurement chain. Colors and numbers correspond to different excitation paths. In the present work, pure sine waves were produced via the patch's frequency oscillator.

setup, the patch *Frequency oscillator* is used to easily swap across excitation frequencies, allowing for a more user friendly and practical solution when carrying out Chladni patterns tests. The PCB 086E80 miniature impact hammer is used to impact the plate. Nonetheless, for this setup a simple visual peak identification was performed from the spectrum computed through the Audacity own Fast Fourier Transform (FFT) algorithm. As a result, the full FRF is not calculated here and the acquisition of forcing input signal can be skipped, suggesting the use of alternative impulsive excitation techniques. Therefore, any kind of short impulsive forcing signal would assure a broad frequency range [98]. From preliminary investigations, the use of a small piano hammer yielded promising results as the same frequency peaks could be identified from the analyzed output spectrum. Also, alternative and simpler excitation techniques were suggested for similar measurement scenarios, demonstrating how a reliable excitation signal can be easily obtained with more accessible solutions [147]. However, such evaluation is not presented here in order to exclusively focus on the full measurement chain and the different signal processing stages. Finally, an accelerometer was used here instead of a microphone, as the acoustics environment did not allow for an adequate signal-to-noise ratio. Also, the use of an accelerometer is of interest as in many workshops scenarios the acoustics environment might not be suitable for the use of a pressure microphone. Although a low-cost accelerometer was tested in a preliminary study, it was discarded as significant differences were observed when comparing its response signal to that of a reference model. Therefore, the same accelerometer used in Section 4.2.1 was again used here to provide accurate acquisition data. Further research will investigate on the efficiency of lower cost solutions. As per the previous setup, an visual illustration of the measurement chain is

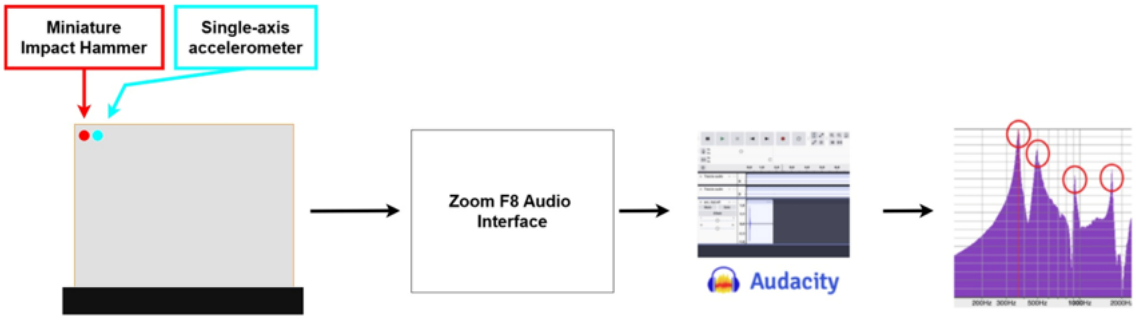

(a) Step 1: From left to right: schematic of the measurement chain showing one accelerometer (light blue) and one impact point (red), both positioned at the top-left corner of the sample.

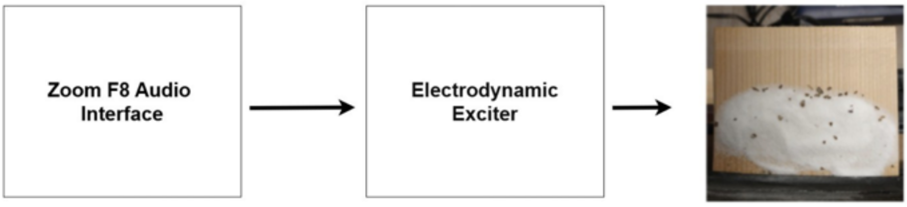

(b) Step 2: From left to right: schematic of the measurement chain used for identifying ODSs via Chladni patterns tests.

Fig. 4.18 Experimental Setup 2 for the Guitar leftover.

Results

Figure 4.19 shows the first four modes that were successfully detected from the two measurements campaigns. While the same deformation patterns can be visually identified, differences in the frequency peaks are $\leq 4.4\,\%$, indicating good agreement between the two setups.

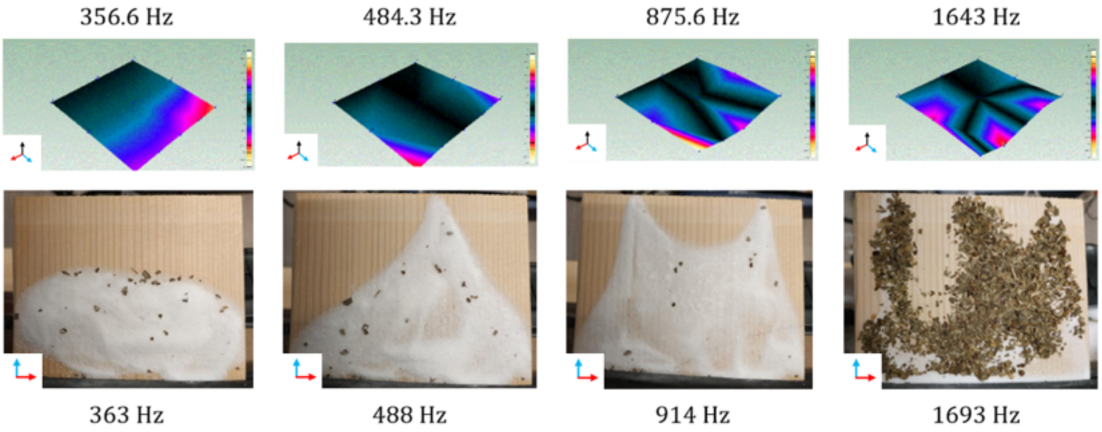

Fig. 4.19 Comparison of mode detection across the two experimental setups. Top row: identified experimental mode shapes. Bottom row: corresponding ODSs observed on the leftover plate sample.

Successively, the method from Section 3 is conducted to estimate the plate elastic constants. Table 4.5 reports the estimated mean values and standard deviations for the two cases, while Figure 4.25 visually illustrates the results.

		$\tilde{E}_x$ (GPa)	$\tilde{E}_y$ (MPa)	$\tilde{G}_{xy}$ (MPa)
Cost-effective experimental setup	mean	6.3	788	563
	rel. std	1.22%	2.55%	3.57%
High-end experimental setup	mean	6.2	763	507
	rel. std	2.12%	4.5%	6.79%

Table 4.5 Estimated mean values and relative standard deviations of the elastic constants obtained from the two experimental setups.

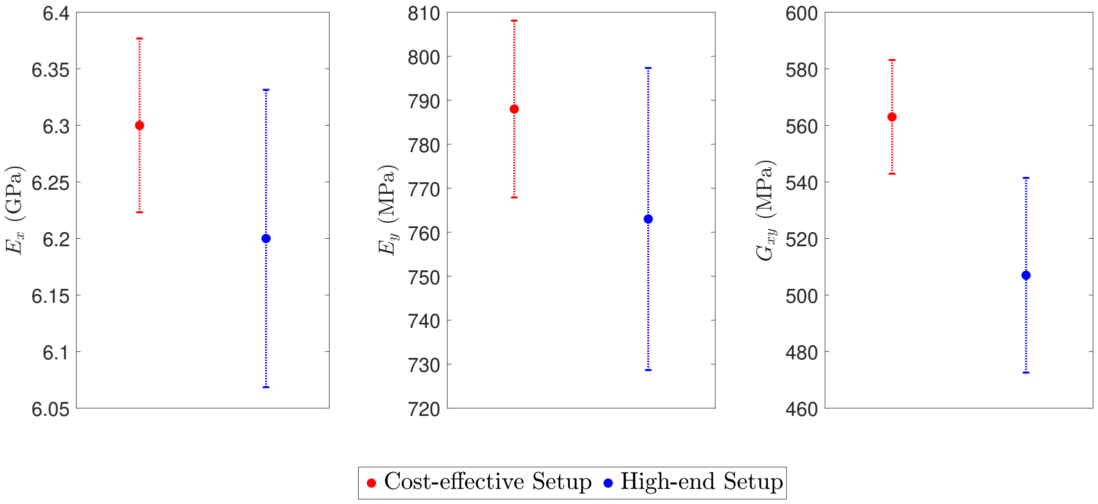

Fig. 4.20 Visual representation of the mean values and relative standard deviations for the estimations in Table 4.5

To assess the impact of the different estimates on the plate modal behavior, a FEM model of a guitar top plate is implemented in COMSOL and two eigenfrequency studies are run using the two sets of elastic constants. The model is built based on a real guitar plate, which will be discussed and assessed in a second case study presented in Section 4.5. The value of ρ used in the model is taken from Table 4.4. The Plate component is used to perform the studies, and a homogeneous h is assumed. An *extremely fine* predefined mesh grid is used to ensure reliable results. A visual representation of the modeled geometry and of the mesh grid is given in Figure 4.22.

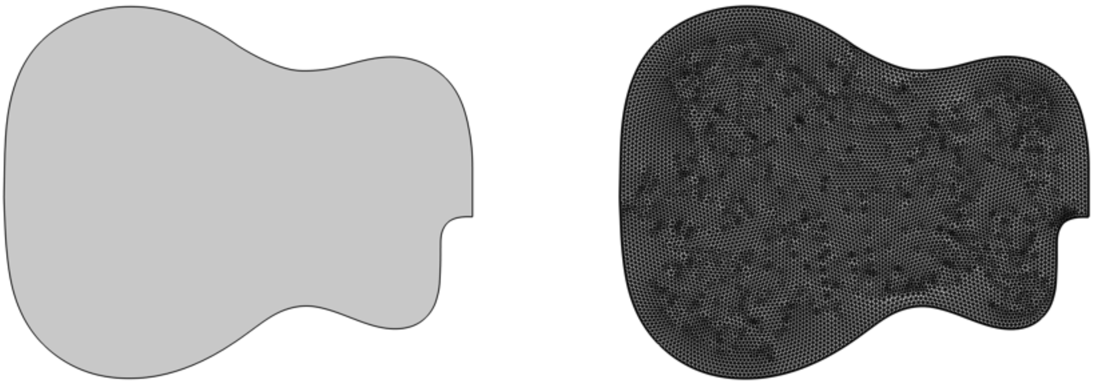

(a) Modelled CAD geometry.

(b) COMSOL mesh grid.

Fig. 4.21 COMSOL model of the reference guitar top plate. The soundhole is omitted to match the actual guitar plate analyzed in Section 4.5.

A comparison of the two sets of resulting eigenfrequencies and eigenshapes is given through Figure 4.22. Specifically, Figure 4.22a compares the first seven eigenfrequencies obtained from the high-end experimental setup (in blue solid line) and the cost-effective measurement chain assessed in this section (appearing as dashed red line). The discrepancies are also reported in Table 4.6.

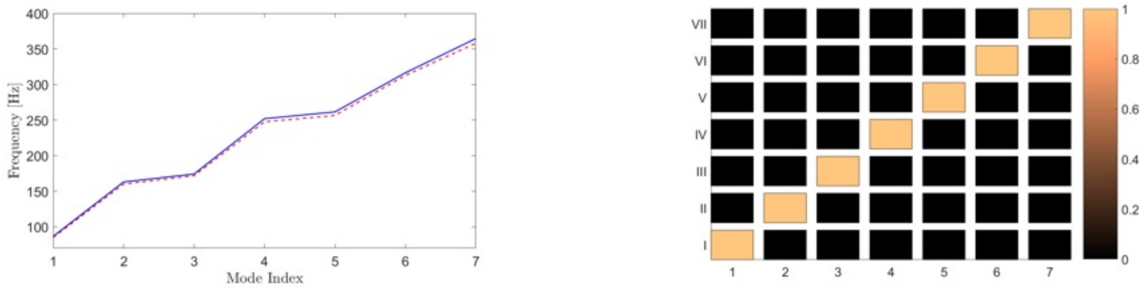

(a) Eigenfrequencies comparison.

(b) Eigenshapes comparison.

Fig. 4.22 Comparison of modal results obtained using the two sets of estimated elastic constants from different experimental setups. The first seven modes are considered. (a) Simulated eigenfrequencies: solid blue line for Setup 1, dashed red line for Setup 2. (b) MAC analysis comparing the corresponding simulated sets of modal shapes.

Mode Index	1	2	3	4	5	6	7
$2\frac{\lvert f_1-f_2\rvert}{f_1+f_2}$ [%]	≈ 1.7	≈ 1.8	≈ 1.3	≈ 1.8	≈ 1.9	≈ 1.2	≈ 1.8

Table 4.6 Discrepancies in the simulated eigenfrequencies obtained from the two sets of estimated elastic constants.

On the other hand, Figure 4.22b presents a MAC analysis comparing the respective first seven eigenshapes from the two sets of data. Overall, as it can be clearly observed from the numerical results, an high consistency is confirmed, validating the use of a more accessible experimental setup when performing the estimation routine introduced in Chapter 3 under practical workshop settings.

4.3 Elastic constants estimation of a guitar board via a cost-effective experimental setup

A second experimental validation for the method described in Section 3 is given by taking advantage of the experimental outcomes achieved from Sections 4.1 and 4.2. Specifically, the use of exciters is exploited for the estimation of elastic constants for a full rectangular guitar plate for which a higher force amplitude is required to excite all the interested experimental modes. In addition to the need for stronger wideband excitation, the size and weight of the plate also require the plate to be horizontally constrained on all sides, thus making the use of exciters. The specimen consists of two quarter-sawn spruce billets joined in a traditional *book-matched* configuration, a classic technique in instrument making in which two mirrored pieces are glued together to form the full board [223]. The material was purchased from the Fiemme Valley supplier Ciresa [94] , renowned for high-quality red spruce used in luthiery. To reproduce conditions similar to those encountered once the board is assembled into an instrument [118], the sample was tested under fully clamped edges. For this purpose, a plexiglass frame weighing 8 kg was prepared, fitted with uniformly spaced clamps. A second plexiglass counter-frame was pressed against the specimen, ensuring distributed pressure along the entire perimeter. The configuration is shown in Figure 4.23. The effective geometry of the clamped plate is $L_x = 60$ cm, $L_y = 41.2$ cm, thickness $h = 3$ mm, with density $\rho = 399$ kg $\cdot$ m^{-3}. The aspect ratio is therefore $\sigma = 105/103$, and the corresponding modal coefficients $a_{m,n}$, $b_{m,n}$, and $c_{m,n}$ are taken from Table 3.7. A custom-built electro-dynamic driver (48 g moving mass, 25 mm diameter voice coil, 8 Ω nominal impedance) was used. This ensured both sufficient force amplitude and ease of operation when working on the horizontal test configuration. An ESS test signal ranging from 45 Hz to 8 kHz was used to excite the board. Measurements were carried out by repositioning the exciter across four selected points on the plate surface. As a sufficient signal-to-noise ratio was achieved and room surfaces were covered using absorbing materials, reducing the sound reflection energy, an Earthworks MD30 class-1 microphone positioned at a short distance from the board (125 mm) was used to capture the response acoustics signal. The recorded data was processed with the Aurora software suite [56] to obtain impulse responses. The identified experimental frequencies used to perform the estimation process are collected in Table 4.7. To visualize the corresponding mode shapes, classical Chladni figures were generated. Differently from the chladni figures obtained in the previous sections, dry small tea leaves are now used to perform this test. Compared to the fine sand used previously, the coarser particles allow for a simpler and clearer visualization of the ODS on the plate, as they adhere less strongly to

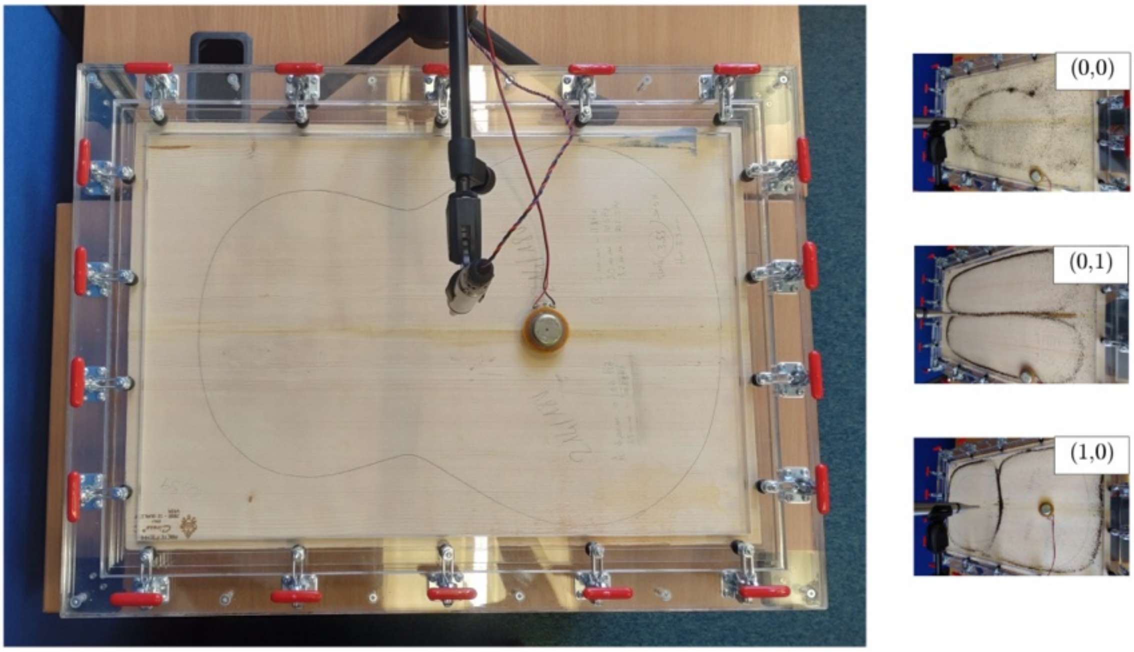

Fig. 4.23 Experimental setup and corresponding Chladni patterns for the spruce guitar board. The measurement used an Earthworks MD30 class-1 microphone and a custom-built electrodynamic exciter with a 8 Ω nominal impedance, a 48 g moving mass and a 25 mm voice coil diameter.

	(0,0)	(0,1)	(1,0)	(1,1)	(0,2)	(1,2)
Measured freqs. (Hz)	57	99	130	162	170	224

Table 4.7 Measured modal frequencies of the fully clamped spruce guitar plate.

the wooden board. The board was driven at the measured resonance frequencies with pure sine tones while dried tea leaves were spread over its surface. The leaves accumulated along nodal lines, revealing the modal patterns, which are displayed in Figure 4.23.

4.3.1 Results

The mean estimated elastic constants values and the associated standard deviations are reported in Table 4.8 As per the previous preliminary validation in Section 3.6, a comparison between the numerical eigenfreuquencies obtained by inputting the estimated values in COMSOL and the experimental peaks is presented in Table 4.9. Again, errors fall below 2%, hence confirming the accuracy of the method introduced in Section 3 when applied to a full guitar soundboard in a realistic instrument-making context. This result was obtained using

		$\tilde{E}_x$ (GPa)	$\tilde{E}_y$ (MPa)	$\tilde{G}_{xy}$ (MPa)
Finnish spruce (cantilever)	mean	10.4	994	526
	rel. std	0.9%	3.1%	14%

Table 4.8 Elastic constants mean values and corresponding standard deviations for the guitar rectangular plate. Values are in line with available literature values for spruce, as in [47, p.96].

	Meas. (Hz)	Num. (Hz)	Δf_n (Hz)	$\frac{\Delta f_n}{f_n}$ (%)	Δf_n (cent)
(0,0)	57	56	-1	-1.8	-31
(0,1)	99	98	-1	-1	-17
(1,0)	130	130	0	0	0
(1,1)	162	161	-1	-0.6	-11
(0,2)	170	168	-2	-1.2	-20
(1,2)	224	221	-3	-1.3	-23

Table 4.9 Errors between experimental and numerical eigenfrequencies, for the spruce guitar plate, under fully clamped BCs. Numerical eigenfrequencies were computed in COMSOL using the mean elastic constant values from Table 4.8.

an accessible experimental setup, further demonstrating the applicability of the measurement framework validated in Sections 4.1 and 4.2.

4.4 Validation of an open source toolbox for material characterization

In the previous sections, a commercial software (i.e. COMSOL) was used to compute the necessary training data needed for the calculation of the modal coefficient in the estimation routine described. In order to move towards a complete open source framework for the estimation of tonewoods elastic constants, the use of the MagPie open source toolbbox is here validated.

4.4.1 Introduction to MagPie

MagPie represents a free Matlab toolbox for modeling the dynamical behavior of thin rectangular plates, based on a series of Matlab scripts available at: https://github.com/

Nemus-Project/magpie-matlab. MagPie is based on an FD-based solution to the KL plate equation given in 2.32 as comprehensively described in [80, 132]. One of the main features of the toolbox is the implementation of arbitrary BCs which are enforced in the modeling as elastic forces. Accordingly, the expressions of force and moment from 4.4 are here expressed as:

$$F_n(0,y,t) = K^{(x0)}\, w(0,y,t), \qquad M_{nn}(0,y,t) = R^{(x0)}\, \frac{\partial w(0,y,t)}{\partial x}, \tag{4.3}$$

where $K^{(x0)}$ and $R^{(x0)}$ are the translational and rotational spring constants applied at the boundary $x = 0$. Analogous expressions apply at the other edges ($x = L_x$, $y = 0$, $y = L_y$) with the corresponding constants $K^{(\circ)}$ and $R^{(\circ)}$, where $\circ$ denotes either x or y direction. BCs are then set as:

$$\begin{aligned} \text{Free} : K^{\circ} &= R^{\circ} = 0, \\ \text{Simply-Supported} : K^{\circ} &\to \infty, R^{\circ} = 0 \\ \text{Clamped} : K^{\circ} &\to \infty, R^{\circ} \to \infty. \end{aligned} \tag{4.4}$$

The translational and rotational springs acting at the boundaries are illustrated in Figure 4.24. The governing Kirchhoff-Love PDE is discretized using a two-dimensional central finite-difference scheme where the displacement field $w(x,y,t)$ is discretized on a rectangular grid of step sizes Δ_x, Δ_y, yielding nodal values $w_{l,m}(t)$ at (x_l, y_m). The nodal spacings in the x and y directions are set from two user-defined parameters: the maximum frequency $f_{\max}$ to

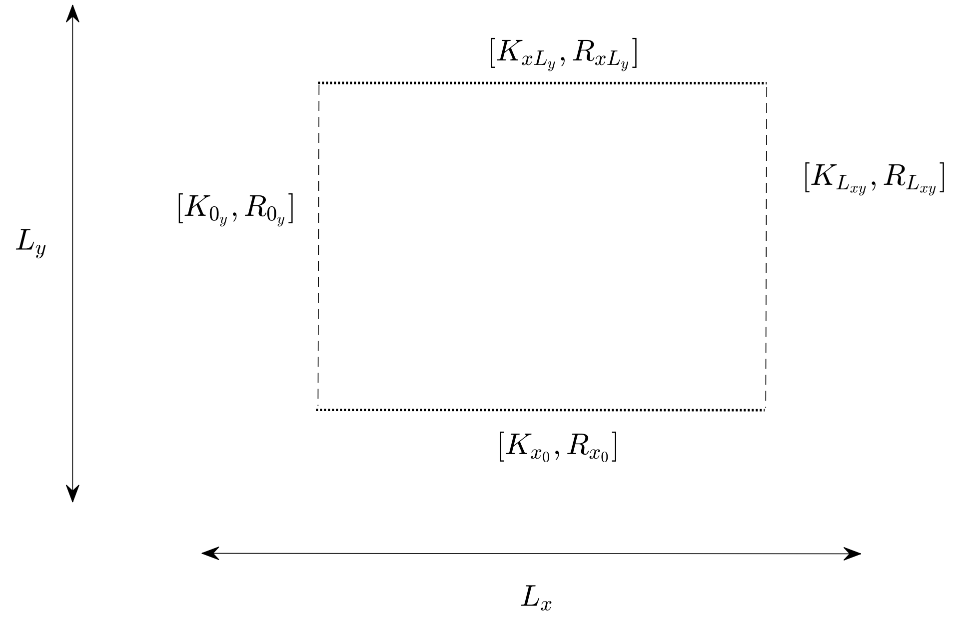

Fig. 4.24 Illustration of translational and rotational spring constants along plate edges

be resolved and the number of points per wavelength (ppw). The relationship between the mesh size and ppw is obtained as:

$$\Delta_\circ = \frac{c_\circ^\phi(f_{\max})}{f_{\max}\cdot \mathrm{ppw}} \tag{4.5}$$

Where $c_\circ^\phi(f)$ is the frequency-dependent phase velocity of bending waves (dispersive in nature). The number of grid points along each direction is then given by

$$N_\circ = \frac{L_\circ}{\Delta_\circ} \tag{4.6}$$

with $L_\circ$ the plate dimension in the chosen direction. This ensures that all bending waves up to $f_{\max}$ are sampled with the required spatial resolution, thereby avoiding numerical dispersion and guaranteeing accurate modal reproduction. The toolbox allow for both direct and inverse modeling. The former enables to predict the modal behavior for a given plate by inputting known values for the elastic parameters in the model while the latter permits to retrieve an estimate of E_x, E_y and G_{xy}, based on the estimation method introduced in Chapter 3 and by effectively substituting the need of COMSOL and integrating the whole estimation routine within a set of Matlab scripts.

For the purpose of this research, the toolbox is here firstly benchmarked against COMSOL considering a numerical rectangular orthotropic plate. Successively, the inverse modeling capabilities are validated by comparing the estimated elastic constants for the tonewood sample considered in Section 3.6 against the reference estimated values in Table 3.14.

4.4.2 Numerical benchmarking

First, a numerical orthotropic rectangular plate is modeled in COMSOL and in MagPie under different sets of BCs, namely fully constrained, free and cantilever BCs. The values used in the MagPie toolbox for the different BCs are given in Table 4.10 and the plate parameters are reported in Table 4.11.

	$K^{(x0)}$	$R^{(x0)}$	$K^{(0y)}$	$R^{(0y)}$	$K^{(xL)}$	$R^{(xL)}$	$K^{(Lx)}$	$R^{(Ly)}$
$C-C-C-C$	1e10	1e10	1e10	1e10	1e10	1e10	1e10	1e10
$C-F-F-F$	0	0	1e10	1e10	0	0	0	0
$F-F-F-F$	0	0	0	0	0	0	0	0

Table 4.10 Translational and rotational spring constants for the different sets of BCs defined along the numerical plate edges.The large values are used to represent clamping.

Kirchhoff plate parameters

ρ	L_x	L_y	h	E_x^0	E_y^0	G_{xy}	ν_{xy}
390	60	20	1	10.9	640	580	0.39
$\mathrm{kg} \cdot \mathrm{m}^{-3}$	mm	mm	mm	GPa	MPa	MPa	

Table 4.11 Input constants for the COMSOL simulations, inspired from the table in [47] (page 96).

The mesh resolution is increased in both modeling approaches to improve the accuracy of the computed eigenfrequencies. This is achieved in COMSOL by setting a fixed number of nodes in the mapped mesh. In MagPie, the same is achieved increasing the value of points per wavelength by directly changing the ppw value in the toolbox. The relative errors on the computed eigenfrequencies at increasing ppw are shown in Table 4.12, 4.13, 4.14. Overall, a very good agreement is found comparing the two methods, proving the accuracy of the MagPie toolbox.

	Error [%]							
	ppw=3	*ppw*=4	*ppw*=5	*ppw*=6	*ppw*=7	*ppw*=8	*ppw*=9	*ppw*=10
(0,0)	1.12	0.59	0.33	0.07	0.07	0.07	0.07	0.00
(0,1)	1.40	0.70	0.35	0.18	0.18	0.18	0.01	0.00
(0,2)	2.39	1.30	0.76	0.44	0.33	0.23	0.12	0.00
(1,0)	2.09	1.22	0.68	0.36	0.15	0.04	0.06	0.00
(1,1)	2.18	1.24	0.32	0.32	0.32	0.32	0.32	0.00
(1,2)	2.39	1.64	0.91	0.19	0.19	0.19	0.19	0.00

Table 4.12 Errors between COMSOL and MagPie eigenfrequency study for a fully clamped rectuangular plate.

	Error [%]							
	ppw=3	*ppw*=4	*ppw*=5	*ppw*=6	*ppw*=7	*ppw*=8	*ppw*=9	*ppw*=10
(0,0)	0.07	0.07	0.07	0.07	0.07	0.07	0.07	0.07
(0,1)	0.31	0.14	0.13	0.03	0.04	0.05	0.06	0.06
(0,2)	0.62	0.62	0.06	0.06	0.06	0.06	0.06	0.06
(1,0)	0.74	0.29	0.28	0.17	0.18	0.19	0.20	0.20
(1,1)	1.16	0.58	0.30	0.29	0.29	0.00	0.00	0.00
(1,2)	1.36	0.64	0.40	0.40	0.16	0.16	0.16	0.16

Table 4.13 Errors between COMSOL and MagPie eigenfrequency study for a rectuangular plate under cantilever BCs.

	Error [%]							
	ppw=3	*ppw*=4	*ppw*=5	*ppw*=6	*ppw*=7	*ppw*=8	*ppw*=9	*ppw*=10
(0,0)	0.30	0.11	0.01	0.05	0.10	0.12	0.14	0.17
(0,1)	0.62	0.41	0.23	0.00	0.11	0.08	0.06	0.05
(0,2)	0.55	0.22	0.07	0.00	0.09	0.12	0.16	0.18
(1,0)	1.24	0.74	0.45	0.62	0.21	0.14	0.08	0.08
(1,1)	1.17	0.67	0.36	0.43	0.12	0.09	0.04	0.02
(1,2)	1.32	0.94	0.51	1.69	0.29	0.16	0.11	0.09

Table 4.14 Errors between COMSOL and MagPie eigenfrequency study for a rectuangular plate under free1 BCs.

4.4.3 Inverse modelling validation

To validate the accuracy of the toolbox in the estimation of the thin plate elastic constants, the same tonewood sample assessed in the preliminary validation illustrated in Section 3.6 is considered here. For this purpose, the necessary initial elastic constants to generate the training set of numerical plates, as well as the required measured experimental frequencies, are inputted into the Matlab script. The toolbox then automates the estimation of the modal fitting parameters and encompasses the least squares process to provide the final estimate for E_x, E_y, and G_{xy}. The comparison between the two sets of estimations is reported in Table 4.15.

		$\tilde{E}_x$ (GPa)	$\tilde{E}_y$ (MPa)	$\tilde{G}_{xy}$ (MPa)
Reference estimation	mean	13	700	668
	rel. std	4%	2.2%	6.5%
MagPie based inverse modeling	mean	13	704	643
	rel. std	3.3%	1.23%	5.96%

Table 4.15 Estimated elastic constant mean values and relative standard deviations for the two sets of estimated elastic constants. The reference estimation is peformed using COMSOL as discussed in Section 3.6.

The results show an excellent agreement between the reference estimation and the values obtained from the MagPie-based inverse modeling. The mean values of E_x, E_y, and G_{xy} are nearly identical in the two cases, and the small discrepancies observed are fully encompassed within the relative standard deviations of the respective estimates, as it can be clearly seen from the illustration in Figure 4.25.

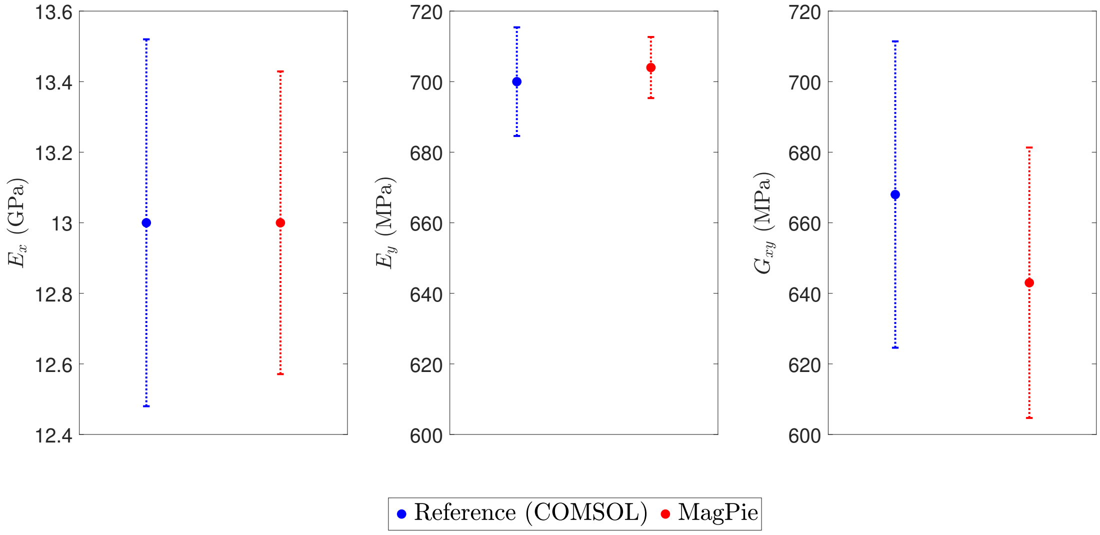

Fig. 4.25 Visual representation of the mean values and relative standard deviations for the estimations in Table 4.15

This confirms both the accuracy and the reliability of the open-source implementation with respect to the reference methodology. Therefore, the free framework can effectively be integrated within the cost-effective measurement chain validated in Section 4.2 and the use of small exciters introduced in Section 4.1 to provide a more accessible and resource-effective measurement ecosystem to perform modal analysis on musical instrument plates.

4.5 Case study 2: Material Characterization of musical instruments plates using tonewood Leftovers

After a comprehensive experimental validation of the estimation routine, a case study is presented in this section. Particularly, the aim here is to investigate the effectiveness of predicting the global behavior of a complete instrument plate by estimating its elastic constant from wood leftovers remaining from its manufacturing process. This matter is of interest not only to luthiers and instrument makers, since early material characterization based on small specimens can support quality control and design optimization during manufacturing, but also for assessing the reliability of estimation methods when access to the original soundboard is restricted or denied, for example due to conservation requirements or limited instrument availability. Analogously, this investigation aims to assess the natural uncertainty caused by quarter-sawn wooden plates. To this end, two case scenarios are considered. FEM models are developed for both a guitar top plate and a kantele top plate, using elastic and physical parameters obtained from their leftover samples. The numerical predictions are then validated by comparison with experimental data measured on the actual instrument plates, allowing us to assess how well the estimated properties reproduce the observed modal behavior.

4.5.1 Guitar top plate

The guitar top plate was constructed by joining two book-matched rectangular halves. After assembly, the board was planed down to the target thickness of approximately 3.3 mm. Once the plate was shaped, an appropriate leftover sample was selected for material testing, as illustrated in Figure 4.26. Note that this is the same leftover considered in Section 4.2 so the elastic properties are taken from Table 4.4. The basic physical characteristics of the shaped guitar plate are summarized in Table 4.16.

A $[m^2]$	h $[m]$	ρ $[Kg/m^3]$
≈ 0.16	≈ 0.0033	≈ 385

Table 4.16 Trivial physical properties of the guitar top plate.

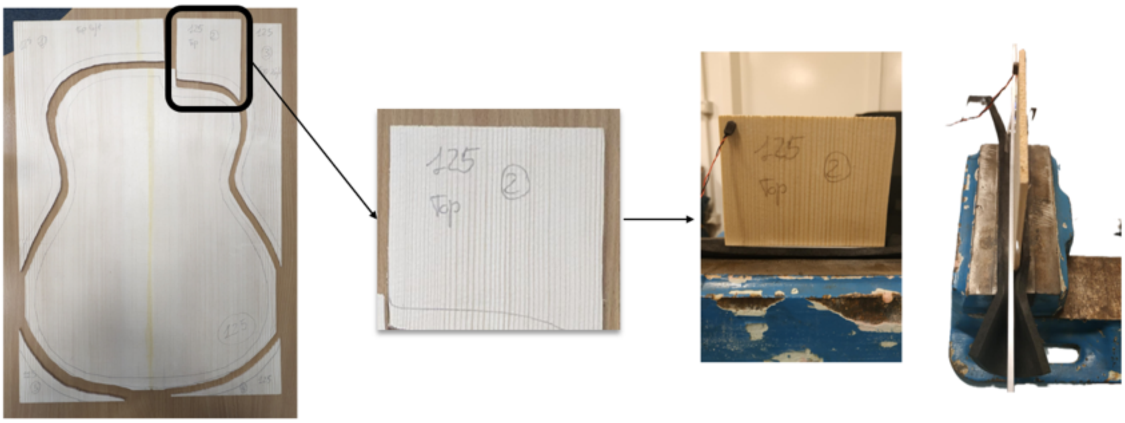

Fig. 4.26 Selection of the guitar plate leftover

Here, it is important to note that density fluctuations are known to occur even among boards cut from the same tonewood source [275]. Additional variability may arise from differences in fibre alignment, growth ring orientation, or moisture content, all of which can influence local material density [187, 270]. For the purposes of the present work, however, such uncertainties were not explicitly accounted for. As an elastic properties characterization of the sample was already conducted in Section 4.2, the estimated elastic constants obtained from the validated cost-effective setup are here used to collect the simulated data.

EMA measurements on the guitar top plate

EMA measurements are performed on the top plate to assess the accuracy of the FEM simulations. A dedicated clamping system is used to fully constrain the board, and a similar measurement setup to the one validated in Section 4.1 and Section 4.3 is here implemented. Two impulse response measurements on the guitar plate were obtained by using ESS test signals via an exciter while recording the response through an uniaxial PCB 352A21 accelerometer. The exciter was placed sequentially at two positions, located on the left and right waist of the board (red circles in Figure 4.27), while the response was captured by a lightweight uniaxial accelerometer fixed on the upper-right portion of the plate (light blue circle in Figure 4.27).

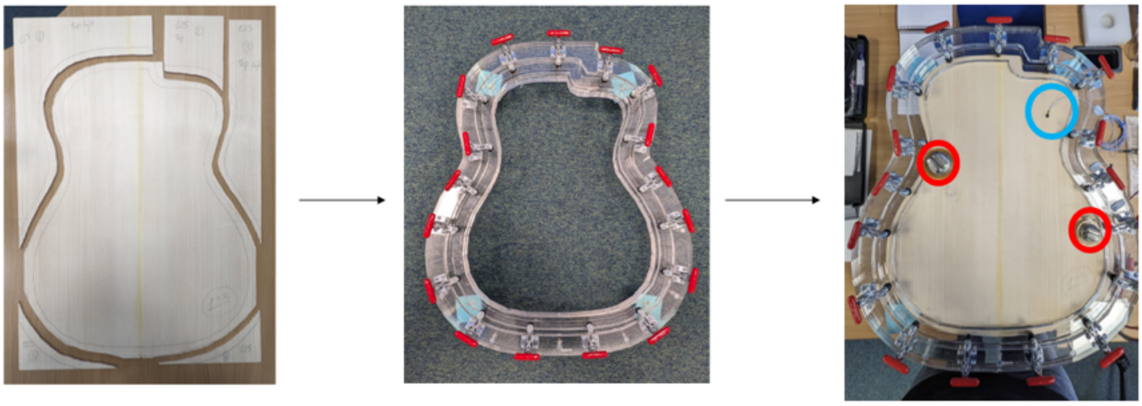

Fig. 4.27 EMA setup on the guitar top plate. Two exciter positions are shown in red on the right, and the accelerometer measurement location is indicated in light blue.

Chladni pattern experiments were also performed on the guitar plate, after identifying the resonance peaks from the frequency response spectra.

Estimated and Observed modal behavior

Figure 4.28 shows a side-by-side comparison between the predicted and experimentally observed deflection patterns of the guitar soundboard. Overall, the agreement is strong for most of the extracted mode shapes and ODSs. The discrepancy between the computed eigenfrequencies and the measured natural frequency peaks ranges from about 0.5% to 9%, with a standard deviation of 3.1%.

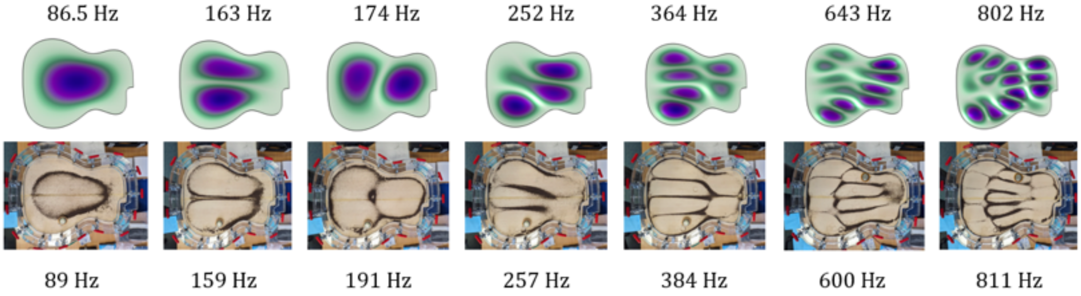

Fig. 4.28 Comparison between the modal behavior predicted by the FEM model of the guitar top plate and that observed experimentally through Chladni patterns on the physical board.

4.5.2 Kantele top plate

In the second case study, the focus shifts to a concert kantele top plate. The instrument's soundboard was produced by joining multiple spruce planks and subsequently shaping them into the required geometry. From one of the remaining planks, a small rectangular offcut was selected and mounted with the same BCs used for the guitar leftover. An illustration is given in Figure 4.29.

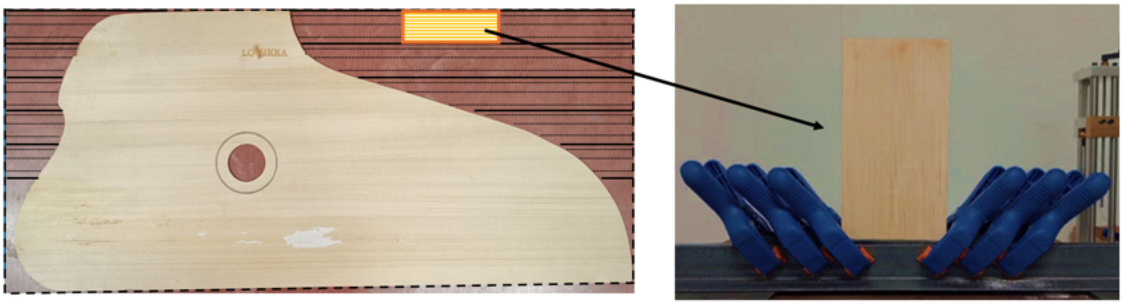

Fig. 4.29 Selected kantele plate leftover under cantilever BCs. Black solid lines sketch the geometry of the original planks from which the smaller sample (denoted in orange on the left) was taken.

The leftover piece is the same used in Section 3.6. The basic physical properties of the complete kantele top plate are listed in Table 4.17. The leftover properties are recalled and summarized in Table 4.18.

A $[m^2]$	h $[m]$	ρ $[Kg/m^3]$
≈ 0.35	≈ 0.0039	≈ 464.4

Table 4.17 Trivial physical properties of the kantele top plate

L_x $[m]$	L_y $[m]$	h $[m]$	ρ $[Kg/m^3]$
≈ 0.223	≈ 0.114	≈ 0.003	≈ 473.9

Table 4.18 Trivial physical properties of the kantele leftover sample.

Accordingly, the estimated elastic constants from Table 3.14, are used to inform the FEM simulations.

EMA measurements on the kantele top plate

For the EMA tests, a different experimental setup was considered. The kantele soundboard was supported on three small foam pads to approximate free-edge BCs. The structure was excited at a single location using an impact hammer, while its response was captured over the entire surface through a scanning LDV. The modal characteristics were then extracted using the Complex Mode Indicator Function (CMIF) approach [42], which enabled the reconstruction of the mode shapes. Figure 4.30 reports the experimental configuration.

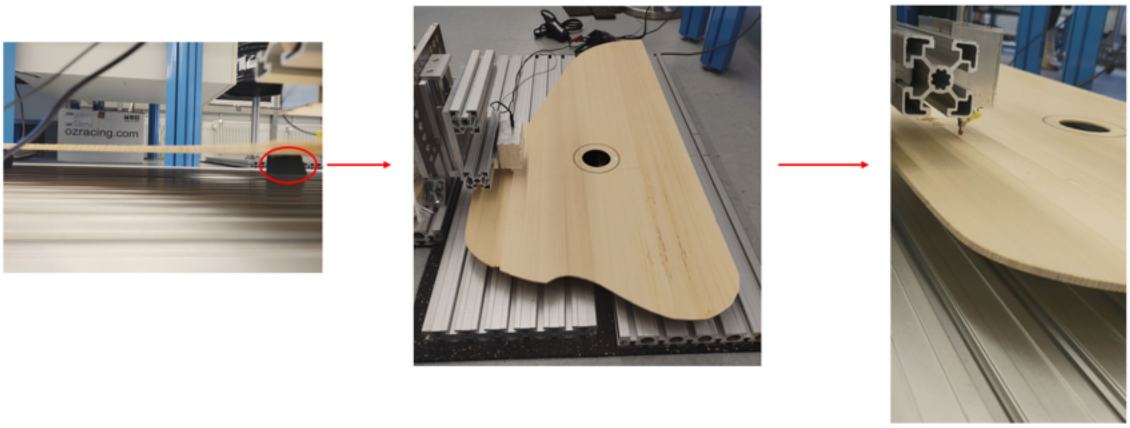

Fig. 4.30 EMA set-up for the kantele top plate under fully free BCs.

Estimated and Observed modal behavior

Figure 4.31 compares the predicted and experimentally identified mode shapes for the kantele plate. While certain correspondences can be seen, the discrepancies are noticeably larger than in the guitar plate case, with frequency deviations ranging from 5.6% up to 30% (SD = ±8.4%). Several factors may account for these differences. A first source of uncertainty lies in the experimental setup, as achieving ideal free BCs is inherently challenging and may introduce deviations between measured and simulated results. In addition, the elastic constants were derived from a relatively small leftover sample originating from one of several planks used in the instrument’s construction, meaning the estimated properties may not fully represent the average behavior of the complete soundboard.

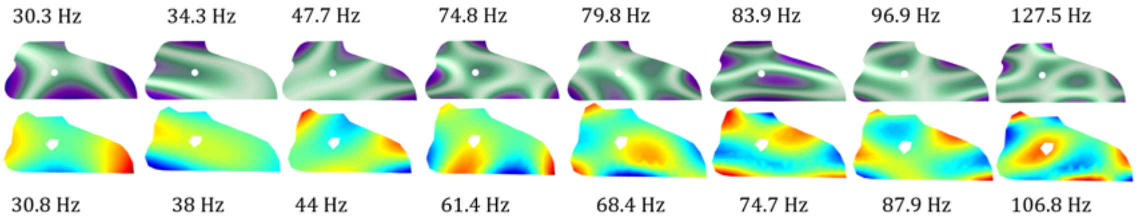

Fig. 4.31 Comparison between the modal behavior predicted by the FEM model of the kantele plate and the experimentally measured mode shapes and identified eigenfrequencies.

Research considerations

For the guitar plate, the estimated modal responses showed good agreement with experiments, with discrepancies across the first identified modes remaining below 9%. In contrast, the kantele plate exhibited considerably larger deviations. Overall, these are likely linked to the inherent difficulty of reproducing ideal free BCs in practice. Furthermore, it should be stressed how deriving elastic constants from a single leftover piece taken from one plank may not adequately represent the overall properties of the assembled soundboard. Variations in fiber orientation, annual ring distribution, and other natural heterogeneities can lead to significant differences across the instrument. Moreover, while the effect of moisture content is not explicitly assessed within this thesis, it is expected to further contribute to uncertainty given its impact on material properties, as discussed in Section 2.2.4. Future research investigations will also account for this parameter. Within the scope of this study, the discrepancies observed between simulated and measured data play a key role in assessing the reliability of using small specimens to characterize the material properties of full soundboards. This aspect is of practical importance not only for luthiers, who rely on accurate material assessments during instrument making, but also for addressing uncertainties in numerical modeling and for informing conservation practices on historical instruments, as will be further explored in Chapter 6.

4.6 Summary

This chapter introduced the validation of electro-dynamic actuators (i.e., exciters) for wide-band experimental modal analysis (EMA) measurements on musical instrument plates. In particular, reliable results were achieved up to 8 kHz. Impedance measurements were employed to efficiently identify the most suitable excitation point on the plate, thereby providing a valuable diagnostic tool for selecting the correct measurement configuration. Following the exciter validation, a cost-effective measurement chain was also proposed after comparison with a reference-standard EMA setup, which showed good agreement in the identification of modal parameters between the two configurations.

The validated exciters were then combined with the low-cost measurement chain to perform a further experimental validation of the estimation method introduced in Chapter 3. As in the first validation described in Section 3.6, low discrepancies were again observed between the experimentally measured eigenfrequencies and the numerical predictions obtained in COMSOL using the average estimated elastic constants, thereby confirming the reliability of the proposed cost-effective measurement setup.

A further comparison between the free MATLAB toolbox MagPie and COMSOL was also carried out to assess the suitability of an open-source numerical tool for modelling the modal behaviour of thin rectangular plates under different boundary conditions. The low numerical deviations observed between COMSOL and MagPie successfully validated the latter. As a result, a fully cost-effective analysis ecosystem can be proposed for performing modal analysis measurements and accurately estimating the elastic constants of thin orthotropic plates, thus satisfying the second and third research objectives stated in Section 1.5.

Finally, an application case study was presented, investigating the use of tonewood leftovers for estimating the elastic properties of musical instrument top plates. This study provided insights into potential sources of uncertainty in the accurate estimation of rigidity constants for full plates, mainly attributable to the use of multiple wood planks in the construction of certain musical instruments and to the practical difficulty of implementing ideal experimental boundary conditions in laboratory or workshop environments.

Chapter 5

FEM-based validation of thin-plate assumptions in musical instruments plates

The method introduced in Chapter 3 as well as many of the estimation routines mentioned in the literature review provided in Section 1.2 are based on thin-plate modeling assumptions. Overall, when it comes to musical instruments plates modeling, the KL equation in (2.32) represents a standard choice thanks to its efficiency and simplicity [258, 74, 120, 30, 132]. Nonetheless, these assumptions become less reliable as the area-to-thickness ratio of the plate under test increases, introducing more complex deformation effects due to the transverse shear deformation and rotary inertia phenomena [62] which are better described by the thicker plate MR model layed out in 2.37. It is then crucial to verify the validity of the in-plate assumptions of a given plate or soundboard in order to assess the accuracy of the estimated elastic properties. Dispersion analysis offers a valuable tool to validate these criteria [38, 89, 238]. An example of this approach is given in Figure 5.1. The graph compares the dispersion relations obtained from the KL and MR theories. The MR model produces three dispersion branches, here named as ω_1, ω_2 and ω_3, which appear as planar surfaces when expressed in terms of the wave vector components. At small wavenumbers ($\|\mathbf{k}\| \to 0$), the lowest branch approaches the KL curve, showing that the two models coincide in the long-wavelength limit. A distinctive property of the MR description is that two of its branches do not extend to zero, but instead they are bounded by cutoff frequency values. These are analogous to the cutoff frequencies observed in the Timoshenko beam model [77, 78]. Below these thresholds, shear deformation effects are usually regarded as negligible. The cutoff frequencies are obtained

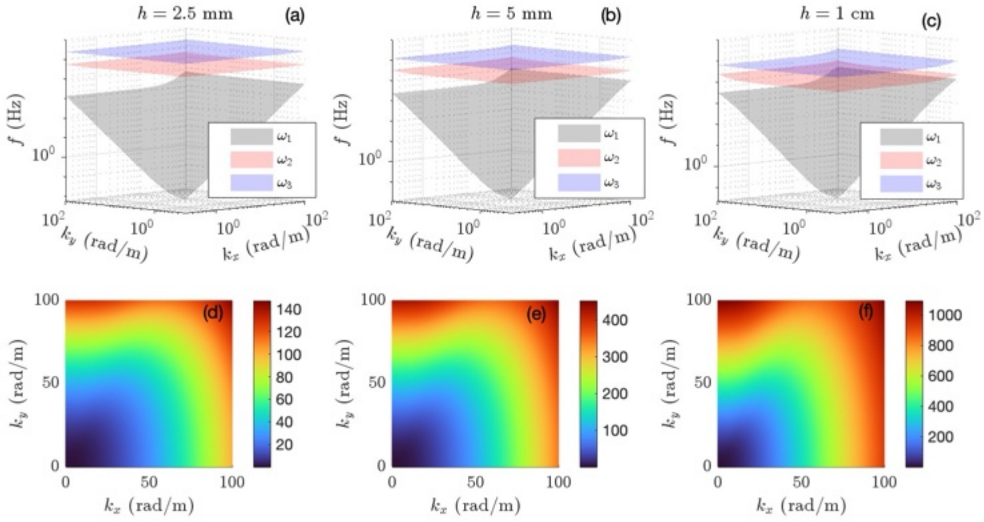

Fig. 5.1 Top row: the three branches of the Mindlin–Reissner dispersion relation, derived from (2.40) and here referred to as ω_1, ω_2, ω_3. Bottom row: frequency deviations, between the lower branch of the MR model and the KL dispersion relation, plotted as a function of the wavenumbers k_x, k_y. The deviation is defined as $\Delta_{\text{cent}}\omega := 1200\log_2(\omega_{KL}/\omega_{MR})$, where a difference of 100 cents equals one semitone. Plate parameters correspond to typical spruce, as reported in [47, page 96].

by evaluating the dispersion relation in the limit $k_x, k_y \to 0$, leading to:

$$\omega_{0x} = \frac{1}{h}\sqrt{\frac{12\kappa^2 G_{xz}}{\rho}}, \qquad \omega_{0y} = \frac{1}{h}\sqrt{\frac{12\kappa^2 G_{yz}}{\rho}}. \tag{5.1}$$

Since they scale with $1/h$, these cutoff values decrease for increasing plate thickness, meaning that shear-related corrections can emerge at progressively lower frequencies as h grows. For example, with a thickness of $h = 5$ mm and material parameters typical of tonewood, the cutoff values still lie well above 10 kHz. The bottom row of Figure 5.1 shows deviations, expressed in cents, between the lowest MR branch and the KL dispersion curve, clearly revealing a thickness dependence. However, this dispersion analysis is conducted over unbounded domains, neglecting the impact of BCs and finite geometries. Thus, this section aims to introduce an alternative analysis framework to validate thin-plate assumption in the modal domain. Particularly, the framework of analysis is here numerically conducted exploiting the use of FEM based models and by taking advantage of the non-dimensionalisation introduced in Chapter 3 to generalize the methodology across different geometries and material properties. As test cases, three geometries are assessed including both rectangular shapes boards as well as geometries inspired from real musical instruments soundboards.

5.1 A non-dimensional framework

The scaling law introduced Equation 3.1 provides a useful framework for interpreting the results. If the material parameters (density and elastic constants) and BCs are kept fixed, the scaling depends exclusively on h and A. This makes it possible to describe how deviations in modal frequencies and shapes from a reference *baseline* can be understood in terms of changes in h and A. To this end, a non-dimensional parameter is here defined as:

$$\iota := \frac{\sqrt{A}}{h}. \tag{5.2}$$

The square root of the area can be regarded as a representative length scale, consistent with earlier formulations [158]. In this chapter, this non-dimensional parameter is used to analyse the modal data obtained from COMSOL using the MR plate model. In particular, it provides a convenient means to track deviations between thin- and thick-plate models by monitoring different scaling trends of the non-dimensional frequencies, as it will be discussed in Section 5.6.

Although the derivation of the non-dimensional equations was carried out for a rectangular geometry, the parameter definition in (5.2) will be applied to plates of arbitrary shape in the following. It is important to recall that the dimensional angular frequencies ω are obtained from the non-dimensional ones $\bar{\omega}$ by rescaling with the time constant in (3.1):

$$\omega^2 = \frac{D_s}{\rho h A^2}\,\bar{\omega}^2. \tag{5.3}$$

This relationship provides a direct link between dimensional and non-dimensional quantities and will be used throughout the subsequent analysis.

5.2 Plates geometries

The three plate geometries are shown in Figure 5.2. The first is a rectangular plate with aspect ratio $\alpha = 3$, a geometry commonly encountered in book-matched soundboards [118]. The remaining two shapes correspond to real instruments: a classical guitar and a concert kantele. These have been modeled without any bracing or additional structural components.

The kantele outline was extracted in COMSOL with the *Image to Curve Add-In* from a high-resolution photograph of the board considered in 4.5.2, while the guitar shape was defined by a fourth-order B-spline interpolating manually selected boundary points. As the purpose of this investigation is not an accurate reconstruction of specific musical instruments, these geometries serve as representative examples of realistic soundboard plates used to test the methodology in different scenarios.

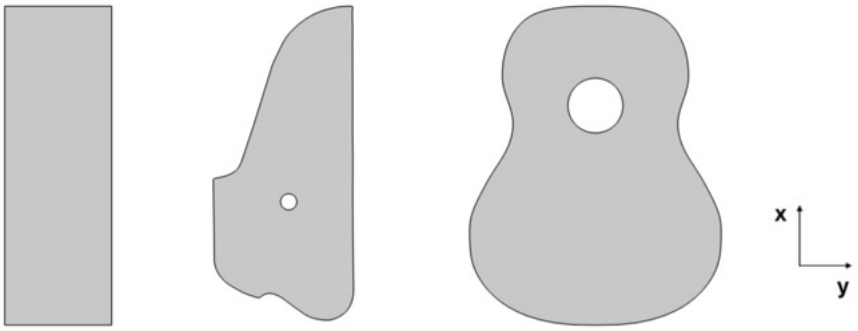

Fig. 5.2 Plate geometries considered in this study: rectangular, kantele, and guitar-inspired plates. The figure is for illustrative purposes only; dimensions are not to scale. The x-axis (longitudinal direction) is oriented vertically.

Table 5.1 summarizes the surface areas of the three geometries. For each type, **Plate 2** represents the reference area, while Plates 1 and 3 correspond to additional variants which are obtained by scaling the plates by a factor of four. The material properties employed for all geometries are listed in Table 5.2, based on values reported for spruce in [47, p. 96]. While COMSOL requires E_z, ν_{xz}, and ν_{yz} as input parameters, these do not explicitly appear in 2.37. Previous studies have indeed indicated that, for thin plates, the eigenfrequencies show low sensitivity to variations in these out-of-plane constants, particularly in the context

	R.Plates (m^2)	K.Plates (m^2)	G.Plates (m^2)
Plate 1	1.92	1.39	0.55
Plate 2	0.48	0.34	0.13
Plate 3	0.12	0.08	0.03

Table 5.1 Surface areas of the rectangular (R.Plates), kantele (K.Plates), and guitar (G.Plates) geometries. Values are rounded to two decimal places for clarity. Bold entries indicate the reference configurations, representative of typical instrument soundboards. Smaller and larger variants are derived by scaling the linear dimensions by a factor of two.

of acoustical radiation [40, 269, 187]. To track changes occurring in the modal domain, the thickness for each geometry kind is increased at discrete steps. Thickness values of $h = 0.5, 0.75, 1, 2, 3, 4, 5, 10, 20, 30$ mm are considered for the rectangular and kantele plates while $h = 0.1, 0.5, 0.75, 1, 2, 3, 4, 5, 10, 20, 30$ mm are used for the guitar plates, resulting in a total of 30 modeled plates for the rectangular and kantele shapes and 33 for the guitar top plates.

ρ	E_x	E_y	E_z	G_{xy}	G_{xz}	G_{yz}	ν_{xy}	ν_{xz}	ν_{yz}
390 kg m^{-3}	10.9 GPa	0.64 GPa	0.42 GPa	0.58 GPa	0.59 GPa	0.026 GPa	0.39	0.49	0.64

Table 5.2 Material input properties for all the plate geometries, derived from spruce data in [47, p. 96].

5.3 Reference modal baseline

Eigenfrequencies and corresponding mode shapes for the three plate families were computed in COMSOL Multiphysics using the *Plate* module. This module is based on the MR formulation, which accounts for transverse shear deformation and rotary inertia effects [66]. Each geometry is modeled as a two-dimensional surface with uniform thickness. To define a modal baseline set of modal shapes and eigenfrequencies under thin plate assumptions, low thickness values were used: $h = 0.1\,mm$ for the rectangular and kantele boards and $h = 0.05\,mm$ for the guitar plate. This arbitrary low values guarantee that the first six mode shapes exhibit thin plate modal behavior. Because the COMSOL *Plate* module does not include membrane dynamics, such reduced thicknesses do not lead to a change of physical regime. Instead, they allow the definition of baseline modes against which deviations from thin-plate behavior can later be evaluated. this also permits arbitrarily large values of the non-dimensional parameter ι. The analysis was carried out for the surface areas listed in Table 5.1. Within each plate family, scaled modal shapes and frequencies were identical, in agreement with the non-dimensional assumptions from Section 3.2. These sets of modes form the *baseline* and are used as reference throughout the study. Baseline modes are denoted by Roman numerals (from I to VI). A sufficiently fine mesh was employed to guarantee numerical convergence, with non-dimensional frequencies $\bar{f} := \bar{\omega}/2\pi$ converging up to four significant digits.

5.4 Analysis method

After the validation, the thickness of the different plates was then increased. The obtained sets of modal shapes and eigenfrequencies obtained at each increased h step are compared against the reference baseline. The discrepancies in the modal shapes are investigated through a MAC analysis. This enables to spot modal crossing and modal distortion effects in the evolution of the modal shapes compared to the original baseline. At each h step, the numerical modal shapes and frequencies are reordered relatively to the baseline, preserving the original baseline sequence. If the MAC analysis reveals no links between a mode to the baseline counterpart, the search extends beyond the first six computed modes. In case no satisfactory match is found, the corresponding frequency is omitted from the analysis, causing a loss in the evaluated data analysis. Frequency departures from the baseline are evaluated on the non-dimensional frequencies $\bar{f} = \bar{\omega}/(2\pi)$ and reported in cents:

$$\Delta\bar{f} := 1200 \log_2 \left(\frac{\bar{f}_{\text{baseline}}}{\bar{f}} \right). \tag{5.4}$$

The dependence on thickness is characterized by fitting a power law,

$$\Delta\bar{f} \approx a h^b \quad \Longleftrightarrow \quad \log(\Delta\bar{f}) \approx \log(a) + b \log(h), \tag{5.5}$$

with a and b estimated by linear regression in MATLAB.

5.5 Results

5.5.1 Rectangular plates

Figure 5.3 shows the MAC analysis for the rectangular plates while Figure 5.4 reports the modal shape baseline as well as a visual representation of the modal crossing occurring at increased h for the smallest rectangular plate. As it can be observed, the analysis reveals how modal crossings become increasingly significant for smaller plates, most notably for Plate 3 ($A = 0.12$ m^2). By contrast, the largest plate (Plate 1, $A = 1.92$ m^2) maintains MAC values close to one across all tested thicknesses, with crossings limited to modes 3 and 4 for $h \geq 10$ mm. In the case of Plate 2 ($A = 0.48$ m^2), the sixth mode at $h = 30$ mm no longer correlates with the baseline, as the associated shape is recovered further up the sequence. A similar effect is observed for Plate 3, where the sixth mode at $h = 20$ mm and $h = 30$ mm is also shifted to higher positions.

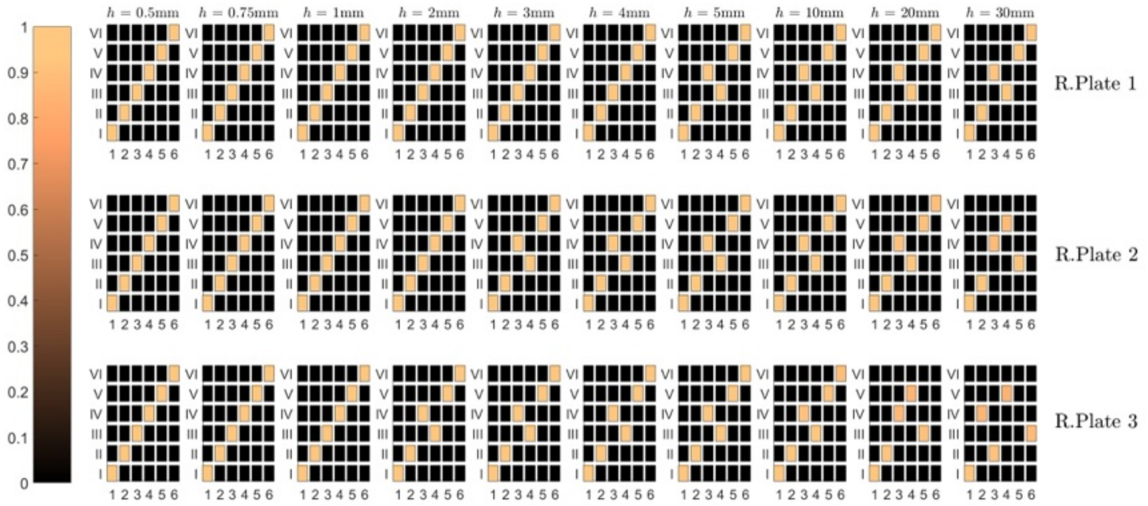

Fig. 5.3 MAC plots for rectangular plates (R.Plates) compared against the baseline configuration. Each column corresponds to a different plate thickness, while each row represents an increasing surface area: Plate 1 ($A = 1.92\,\mathrm{m}^2$), Plate 2 ($A = 0.48\,\mathrm{m}^2$), and Plate 3 ($A = 0.12\,\mathrm{m}^2$), from top to bottom.

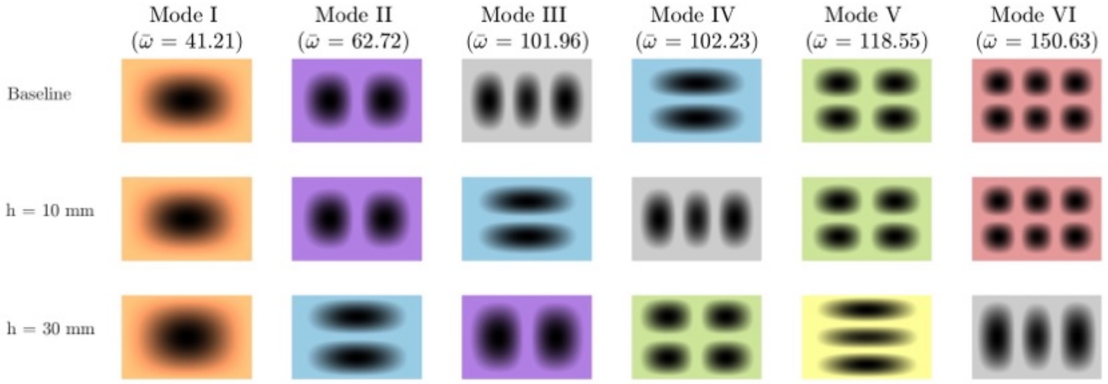

Fig. 5.4 Illustration of modal crossing happening within the first six mode shapes of the simulated smallest rectangular plate, (Plate 3, $A = 0.12$ m^2). Each row corresponds to a different h value. The first row shows the baseline modal shapes and the respective non-dimensional eigenfrequencies for the modeled plate.

Cent deviations from the thin-plate baseline are reported in Figure 5.5. Deviations increase systematically with thickness for all plates, with smaller surface areas showing the largest discrepancies. Higher modes are particularly affected: for modes IV–VI, differences $\geq$ 1000 cents appear at $h = 30$ mm.

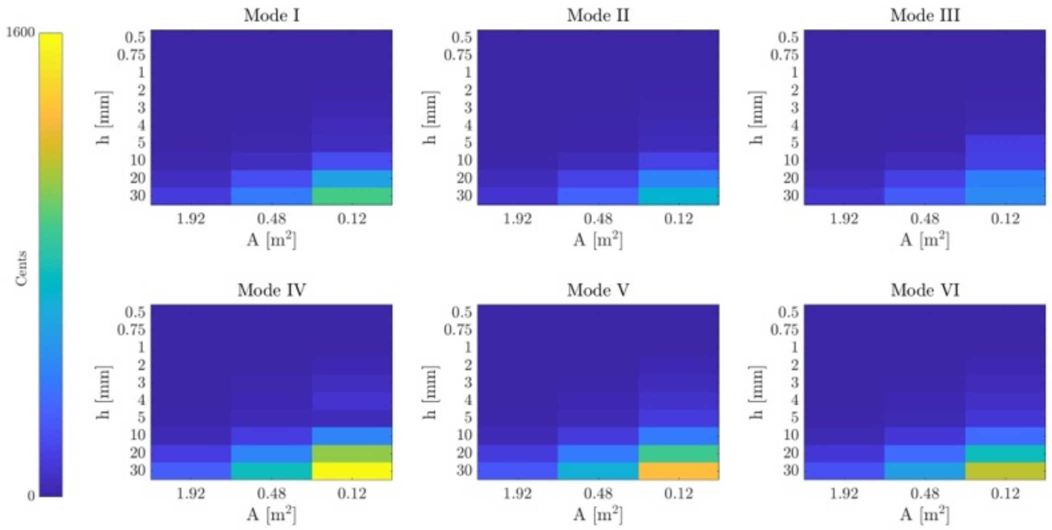

Fig. 5.5 Cent frequency deviations from the reference baseline (at h = 0.1 mm) for the rectangular plates.

The best-fit curves are presented in Figure 5.6 together with their exponents in Table 5.3.

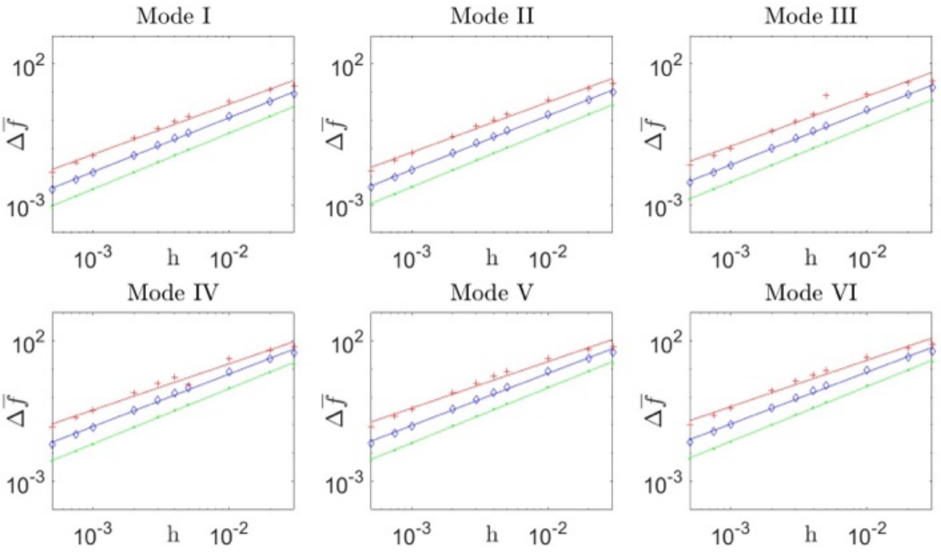

Fig. 5.6 Frequency deviations, computed using (5.5), as a function of thickness h for the six considered non-dimensional frequencies of the rectangular plates. Plate 3 ($A = 0.12\,\mathrm{m}^2$): red line with plus markers; Plate 2 ($A = 0.48\,\mathrm{m}^2$): blue line with diamond markers; Plate 1 ($A = 1.92\,\mathrm{m}^2$): green line with dot markers. For reference, a deviation of $\Delta\bar{f} = 100$ corresponds to one semitone.

The results indicate that larger plates display an almost quadratic dependence on h, while the exponents gradually decrease as the surface area decreases.

	I	II	III	IV	V	VI
R.Plate 1	1.98	1.98	1.98	1.96	1.96	1.95
R.Plate 2	1.92	1.92	1.92	1.86	1.85	1.84
R.Plate 3	1.78	1.78	1.78	1.64	1.65	1.65

Table 5.3 Best-fit exponents b, obtained from (5.5), for the fitting curves shown in Figure 5.6.

5.5.2 Guitar plates

From the MAC analysis for the guitar plates given in Figure 5.7, modal crossings between modes IV and V are observed at $h = 20$ mm for Plate 1 ($A = 0.55$ m^2), at $h = 10$ mm for Plate 2 ($A = 0.13$ m^2), and at $h = 3$ mm for Plate 3 ($A = 0.03$ m^2). Modal distortion is also evident across all three guitar plates for $h \geq 10$ mm, and again these effects are more pronounced for smaller areas. Examples of baseline and thick-plate modes for Plate 3 are shown in Figure 5.8.

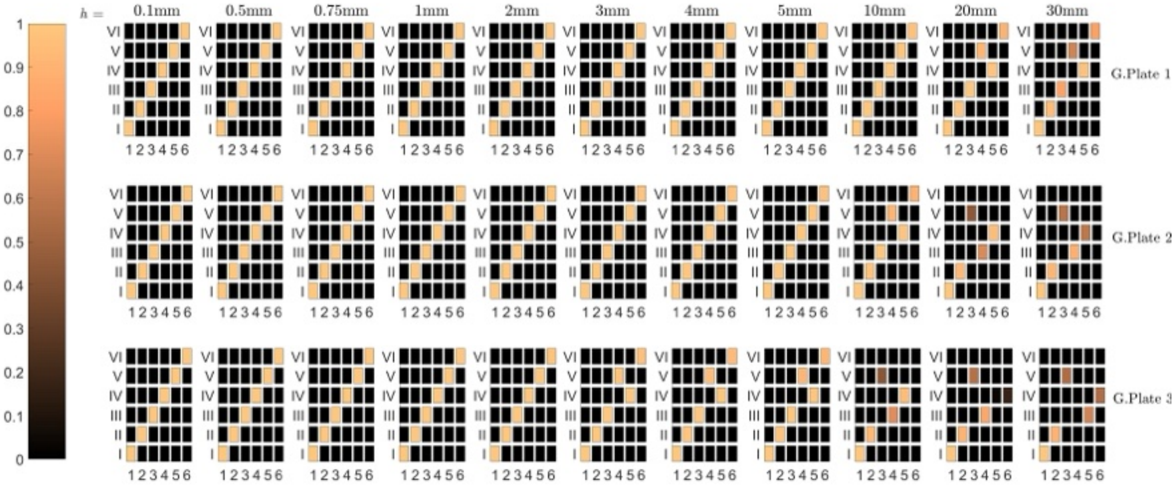

Fig. 5.7 The MAC plots for guitar plates (G.Plates) compared against the baseline configuration. Each column corresponds to a different plate thickness, while each row represents an increasing surface area: from top row to bottom row: Plate 1 ($A = 0.55\,\mathrm{m}^2$), Plate 2 ($A = 0.13\,\mathrm{m}^2$), and Plate 3 ($A = 0.03\,\mathrm{m}^2$), from top to bottom.

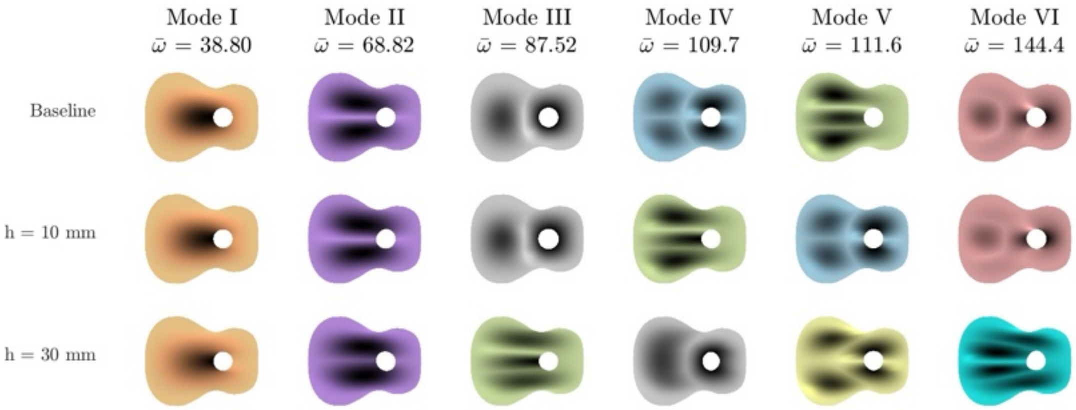

Fig. 5.8 Illustration of modal crossing happening within the first six mode shapes for the reference plate (Plate 2, $A = 0.13\ \mathrm{m}^2$). Each row corresponds to a different h value. The first row shows the baseline modal shapes and the respective non-dimensional eigenfrequencies for the modeled plate.

Cent deviations are displayed in Figure 5.9. As before, frequency shifts increase with h, but for the guitar plates deviations > 1000 cents also appear in the lower modes (I–III) of the smallest plate at $h = 30$ mm. The largest discrepancy is observed for Mode V of Plate 3 at this thickness. The sixth eigenfrequency of Plate 3 at $h = 30$ mm is excluded since the associated modal shape could not be identified in the sequence, as confirmed by the extended MAC plot in Figure 5.10.

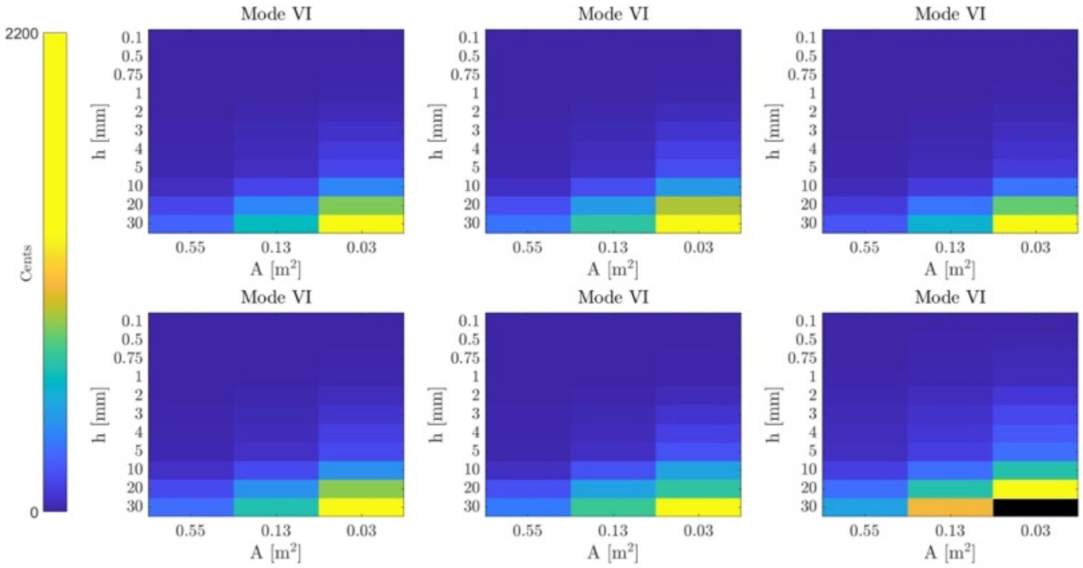

Fig. 5.9 Cent frequency deviations from the reference baseline (at h = 0.05 mm) for the guitar top plates. Note that due to the inability to identify a mode shape corresponding to the original baseline set at $h = 30\,\text{mm}$ for $A = 0.03\,\text{m}^2$, the corresponding data value is discarded from the plot and displayed in black.

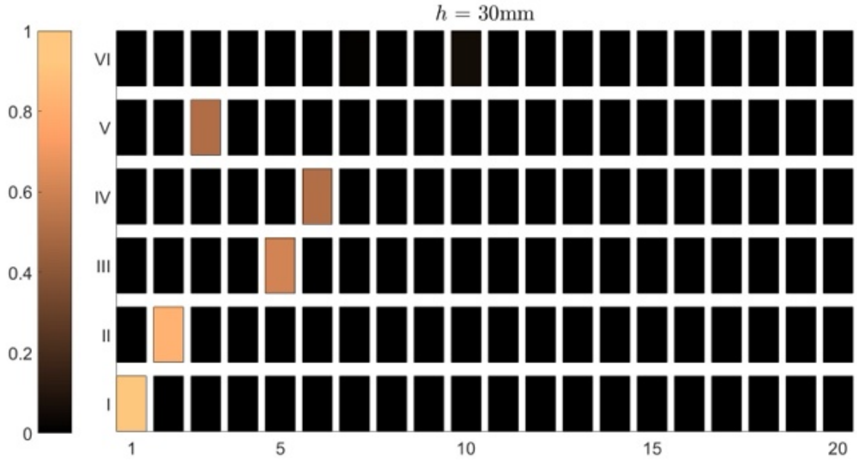

Fig. 5.10 MAC analysis example between the guitar plates reference baseline and the first twenty simulated modal shapes at $h = 30$ mm for Plate 3 ($A = 0.03$ m^2). It is observed that the baseline modal shape VI could not be detected.

The best-fit results are summarized in Figure 5.11 and Table 5.4.

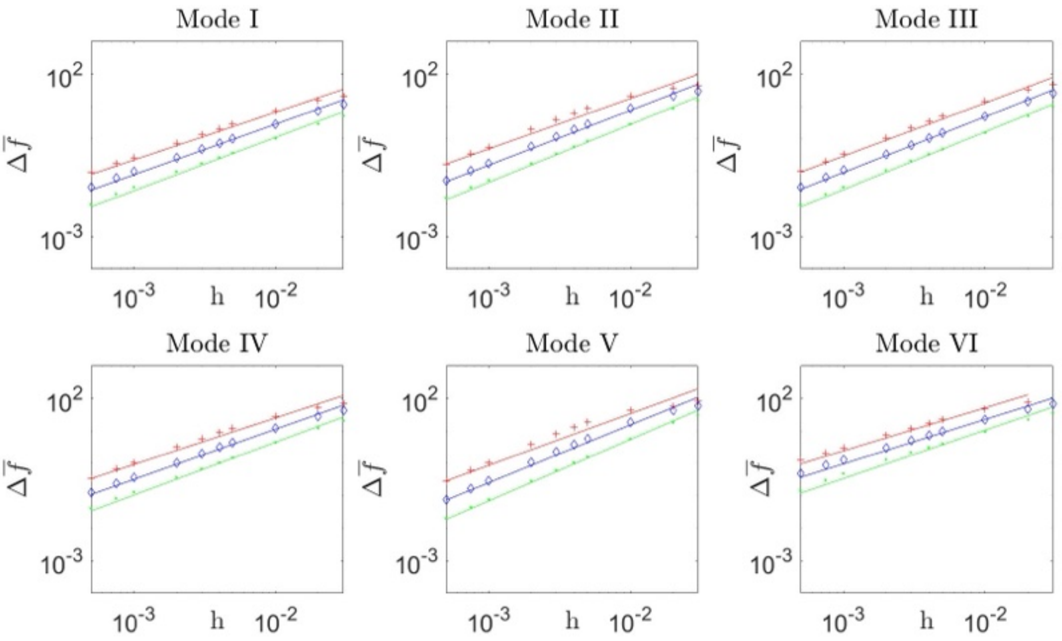

Fig. 5.11 Frequency deviations, computed using (5.5), as a function of thickness h for the six considered non-dimensional frequencies of the G.Plates. Plate 3 ($A = 0.03$ m^2): red line / plus sign marker. Plate 2 ($A = 0.13$ m^2): blue line / diamond sign marker. Plate 1 ($A = 0.55$ m^2): green line / dot sign marker. Note that for Plate 3, values of non-dimensional frequencies for Mode VI are not available for h = 30 mm.

	I	II	III	IV	V	VI
G.Plate 1	1.64	1.78	1.78	1.63	1.89	1.49
G.Plate 2	1.56	1.69	1.72	1.54	1.78	1.37
G.Plate 3	1.47	1.55	1.64	1.44	1.59	1.33*

Table 5.4 Best-fit exponents b, obtained from (5.5), for the fitting curves shown in Figure 5.11 for the guitar plates. *Note that for this case, frequency data associated with mode shapes showing no correlation in Figure 5.7 were excluded from the curve fitting analysis.

Unlike the rectangular case, the exponents tend to decrease with increasing plate area, and the largest guitar plate (G.Plate 1) shows a weaker quadratic dependence when compared with the rectangular plate of similar size (R.Plate 2).

5.5.3 Kantele plates

For the kantele plates, the MAC analysis in Figure 5.12 highlights a somewhat different behavior. Modal crossings are rare, limited to modes 5 and 6 of Plate 2 at $h = 30$ mm, modes 5 and 6 of Plate 3 at $h = 20$ mm, and mode 3 of Plate 3 at $h = 30$ mm, where a low correlation is observed. Modal distortion, however, emerges earlier as thickness increases. For Plate 1 ($A = 1.39$ m^2), distortion appears at $h = 20$ mm, for Plate 2 at $h = 10$ mm, and for Plate 3 already at $h = 5$ mm. Representative mode shapes are reported in Figure 5.13.

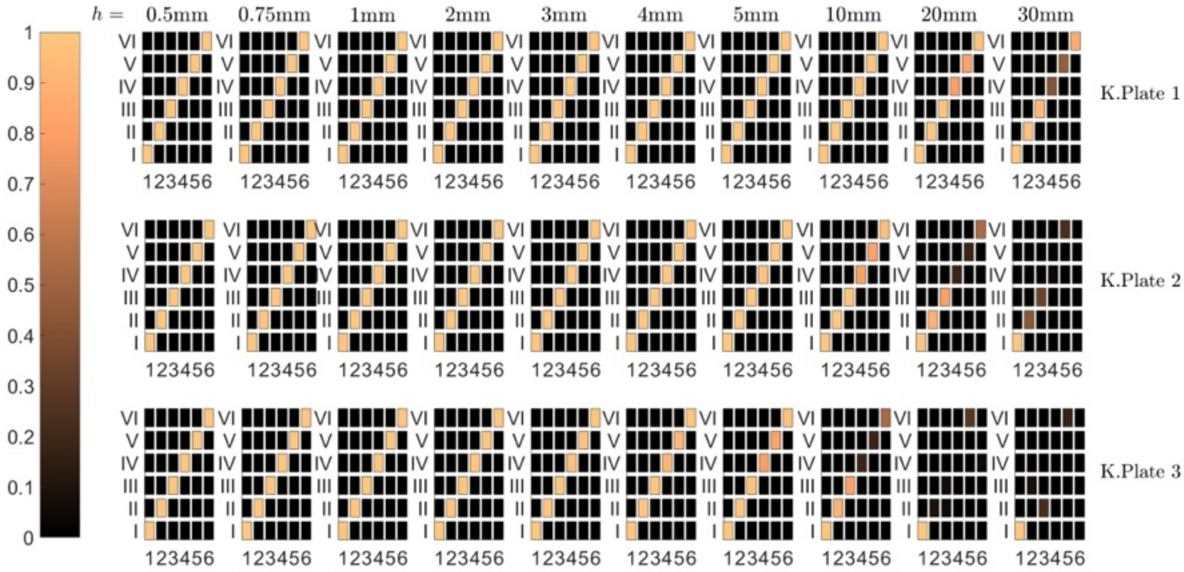

Fig. 5.12 MAC plots for kantele plates (K.Plates) compared against the baseline configuration. Each column corresponds to a different plate thickness, while each row represents an increasing surface area: Plate 1 ($A = 1.39\,\mathrm{m}^2$): red line with plus markers; Plate 2 ($A = 0.34\,\mathrm{m}^2$): blue line with diamond markers; Plate 3 ($A = 0.08\,\mathrm{m}^2$): green line with dot markers, from top row to bottom.

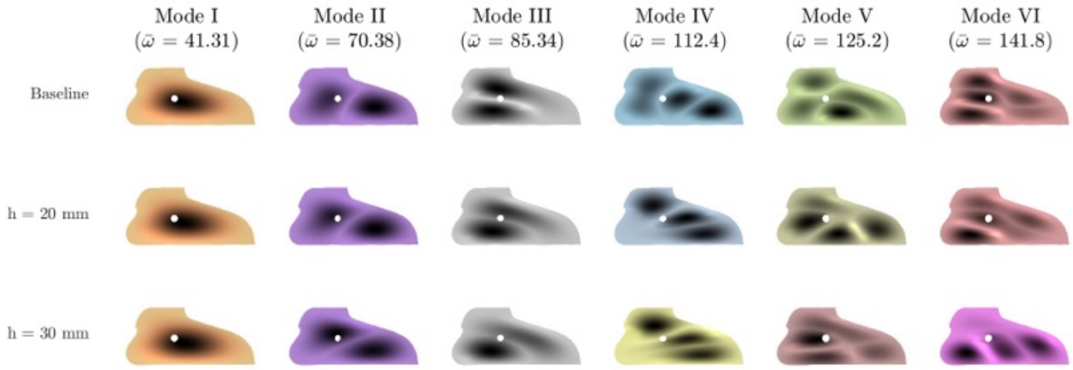

Fig. 5.13 Illustration of modal crossing happening within the first six mode shapes for the reference kantele top plate (Plate 2, $A = 0.34$ m^2). Each row corresponds to a different h value. The first row shows the baseline modal shapes and the respective non-dimensional eigenfrequencies for the modeled plate.

Cent deviations from the baseline are plotted in Figure 5.14. While several data points are discarded due to poor correlation, deviations above 1000 cents are found only for the smallest plate at $h = 30$ mm. The fitted scaling curves in Figure 5.15 and the exponents in Table 5.5 suggest a closer-to-quadratic dependence than in the guitar case, though still weaker than that of the rectangular plates.

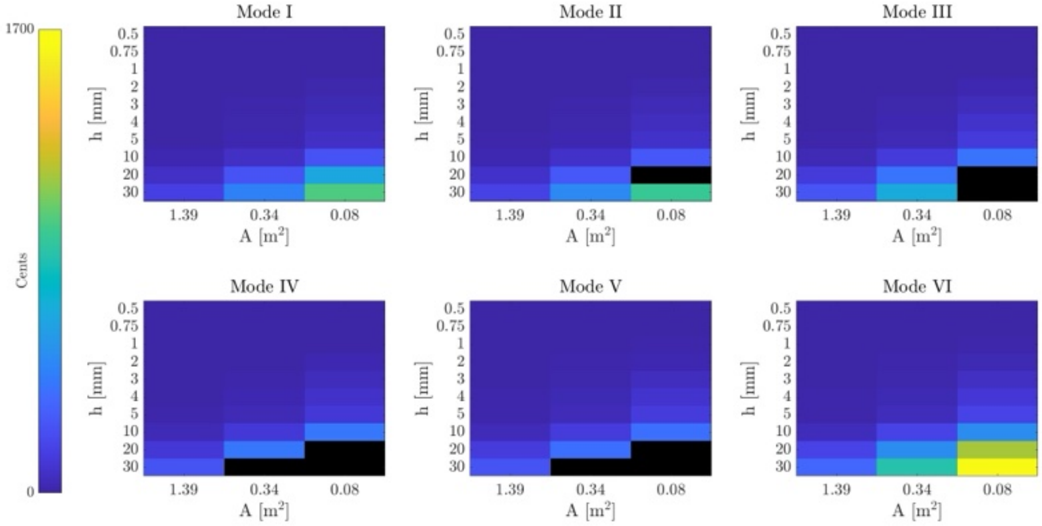

Fig. 5.14 Cent frequency deviations from the reference baseline (at $h = 0.1$ mm) for the kantele top plates. Note that, due to the inability to retrieve certain mode shapes corresponding to the baseline set (notably for Plate 2 and Plate 3), the affected data points are omitted and shown in black.

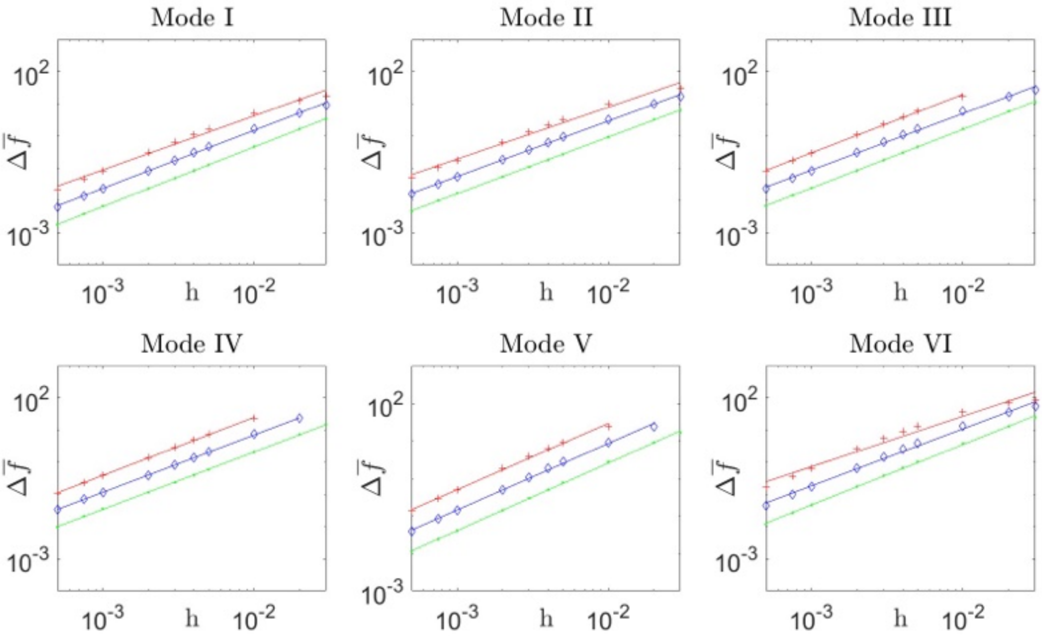

Fig. 5.15 Frequency deviations, computed using (5.5), as a function of thickness h for the six considered non-dimensional frequencies of the guitar top plates. Plate 1 ($A = 1.39\,\mathrm{m}^2$): red line with plus markers; Plate 2 ($A = 0.34\,\mathrm{m}^2$): blue line with diamond markers; Plate 3 ($A = 0.08\,\mathrm{m}^2$): green line with dot markers. Note that for Plate 3, values of non-dimensional frequencies for the 3rd, 4th, and 5th modes are not available for h = 20, 30 mm. Also, for Plate 3, the value of the non-dimensional frequency for the 2nd mode is not available for h = 20 mm. For Plate 2 values of non-dimensional frequencies for the 4th and 5th modes are not available for h = 30 mm.

	I	II	III	IV	V	VI
K.Plate 1	1.85	1.76	1.83	1.78	1.80	1.88
K.Plate 2	1.80	1.73	1.76	1.78*	1.78*	1.77
K.Plate 3	1.68	1.61*	1.82*	1.80*	1.77*	1.57

Table 5.5 Best fit exponents b obtained from (5.5), for the fitting curves shown in Figure 5.15 for the kantele top plates. *Note that for this case, differences in scaled frequencies corresponding to modal shapes with no correlation to baseline from Figure 5.13 were discarded in the curve fitting analysis.

5.6 A non-dimensional scaling law

The results above clarify how thickness h influences the dynamics of the three plate families. Departures from the thin-plate baseline appear as (i) distortions of modal shapes, (ii) modal crossings, and (iii) shifts in the non-dimensional frequency. The latter is modeled with the power law in (5.5). While that law quantifies within-mode deviations for plates of fixed area A, it is natural to question whether the dependence on A can be removed so that departures from the baseline collapse across sizes within each plate family (i.e. sharing same BCs and aspect ratio). To investigate this, a different power law is tested by expressing the deviations in terms of the non-dimensional parameter ι from 5.2, defined as:

$$\Delta\bar{f} \approx \alpha\,\iota^{-\beta}, \tag{5.6}$$

For this purpose, the modal frequencies from the different plate sizes for each geometry kind are collected and reported in Figure 5.16.

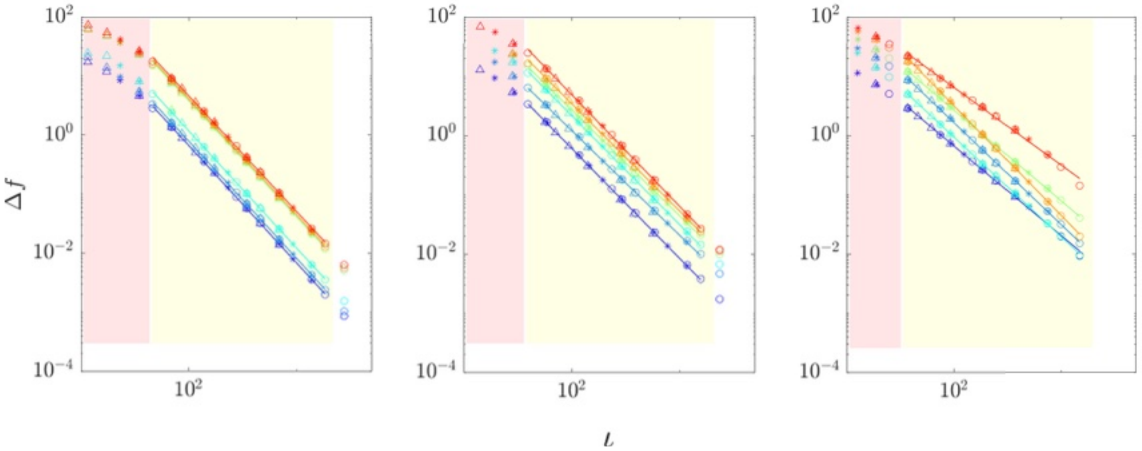

Fig. 5.16 Dimensionless frequency deviations plotted against ι for the three plate families (left to right: rectangular, kantele, guitar). In the yellow region—representing thin-plate behavior—the data follow straight lines in the log–log plot, consistent with the model in (5.6). In the red region, deviations from linearity begin to appear, indicating a breakdown of the model in 5.6.

From the different subplots, two main observations emerge. First, when plotted against ι, the data for a given family collapse onto a single line for each mode, provided ι is sufficiently large. This indicates an invariant pattern of frequency deviations for plates that share the same dimensionless baseline. Second, the plots reveal two regimes separated by a transition: in the yellow region, $\Delta\bar{f}$ varies as a straight line in log–log scale and is well described by the power law in (5.6). In the red region, the curves bend, suggesting how the model is not well suited anymore to accurately describe the behavior of $\Delta\bar{f}$. The boundary between these regions hence provides an empirical indicator for selecting an appropriate plate theory.

	I	II	III	IV	V	VI
R.Plates	1.99	1.98	1.98	1.96	1.96	1.96
K.Plates	1.85	1.77	1.84	1.79	1.81	1.88
G.Plates	1.51	1.71	1.69	1.52	1.83	1.31

Table 5.6 Best-fit exponents β obtained from (5.6) for the curves shown in Figure 5.16.

Despite it might be convenient to propose universal ι thresholds distinguishing thin, thick and membrane regimes as per previous research [158], the present data is best interpreted on a case-by-case basis. Table 5.7 gives the identified boundary values for the first six modes per each geometry kind. Overall, from Figure 5.16, the thin–to-thick transition for the first six modes lies near $\iota \approx 40$. Given that ι spans roughly four orders of magnitude (10^{-1} to 10^{3}), these values are broadly consistent with [158]. However, an upper ι bound separating plate-like from membrane-like behavior is not identified here, since the COMSOL *Plate* interface does not model membrane dynamics. Quantitatively, Table 5.6 shows that rectangular plates exhibit an almost quadratic trend across modes, whereas non-rectangular shapes deviate from this pattern; the smallest exponents occur for the guitar plates. Appendix B includes a full tabulated comparison between the dimensional and non-dimensional modal frequencies and the corresponding theoretical cutoff predictions for each geometry included in this study. Although such cutoff frequencies are often referenced in dispersion analyses, their predictive reliability diminishes in thick-plate regimes, and they should therefore be interpreted with caution.

$\iota_{\min}$		
R.Plates	G.Plates	K.Plates
46	37	39

Table 5.7 Estimated lower bounds on ι indicating the transition from thin-plate to thick-plate behavior, as inferred from Figure 5.16.

5.7 Reliable elastic characterization of a kantele top plate

To illustrate the practical use of the presented analysis framework, a case study is presented on the estimation of elastic constants for a kantele soundboard. Inferring material properties from a limited set of modal data is common in musical acoustics, typically under the thin-plate assumption [53, 183, 140]. When this assumption is violated, however, thick-plate effects can introduce systematic errors in the estimates. The analysis focuses on K.Plate 2 ($A = 0.34m^2$), which is representative of the concert kantele plate investigated experimentally in Secion 4.5.2. “Experimental” modal frequencies are produced via FEM simulation using the thin-plate elastic constants in Table 5.2. The estimation procedure introduced in Section 3 is here used to perform multiple estimates of Ex, Ey and Gxy for thickness values ranging from 0.1 to $20mm$. As shown in Figure 5.17, estimation errors remain below 5% up to $h = 5$mm ($\iota \approx 117$). Beyond this, the accuracy deteriorates rapidly, exceeding 20% at $h = 20$mm ($\iota \approx 29$). This behaviour mirrors the loss of modal shape correlation seen in Figure5.12 above 5 mm, and coincides with the red-shaded region in Figure 5.16, where deviations from thin-plate behaviour become dominant. Since concert kantele soundboards may reach thicknesses of around 5mm, the estimation method remains valid in this range. Smaller designs, with $\iota \approx 30$, enter a regime where thick-plate effects prevail and thin-plate inverse methods lose reliability. The same limitation applies to other large instruments with low ι, such as upright pianos [38, 63], for which the present framework provides a diagnostic tool to assess whether thin-plate models remain appropriate for a given modal sequence.

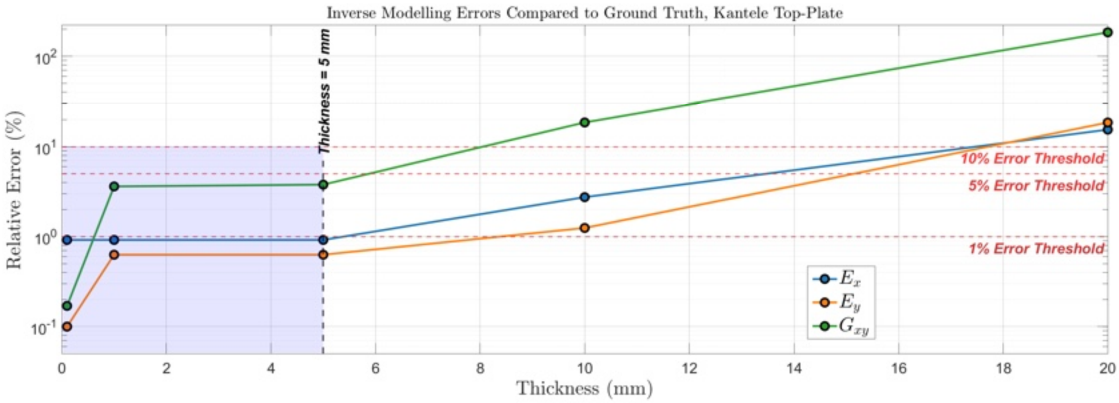

Fig. 5.17 Errors in the estimated elastic constants relative to the reference values for the “experimental” kantele plate, shown as a function of plate thickness h.

Chapter 6

On the impact of materials uncertainty in historical musical instruments: A pilot study

As anticipated in Section 4.5, one of the crucial aspects to take into account when dealing with the modeling of musical instruments, particularly when dealing with ancient and fragile artefacts, is the assessment of materials' properties uncertainty. In the following chapter, the impact of material uncertainty is considered through the case study of an ancient string-based musical instrument. This is done by considering two different approaches: a deterministic analysis and an info-gap approach. The latter aims to inform model-based decision-making under severe uncertainty [26], and it was recently introduced to assess the influence of materials properties uncertainty on the structural integrity of a historical cello [271]. This analysis requires the definition of an uncertainty set describing how little is known about the interested values (see Section 6.5.2). Then, a system model is required to predict how the outcomes behave under the defined uncertainty. Here, COMSOL is used to implement the physical model of the system (see Section 6.4). Finally, a performance requirement is set to determine an acceptable outcome, and the robustness function is evaluated to quantify how much uncertainty the decision-making can tolerate while still providing satisfactory results (see Section 6.5.2). The role of this analysis is twofold. First, it represents a second applied case scenario for the use of info-gap theory and uncertainty analysis in the context of digital restoration of historical musical instruments. Second, and above all, within the NEMUS project, it aims to lay the foundations for a broader reverse-engineering restoration protocol by introducing the use of CT scans for virtual prototyping. While in the presented pilot study, CT scans are only used as reference data, a discussion on the need for future research towards a full reverse-engineering framework is presented in Section 6.7. It is therefore important to note that the following study serves as a pilot case. The results should not yet be regarded as directly applicable by restorers, and the current limitations and recommendations for further research are discussed in Section 6.6.

6.1 The Antegnati Arpicordo (1552)

The historical musical instrument considered here is an Antegnati arpicordo (i.e., an Italian term to denote a poligonal spinet) from 1552. The instrument is shown in Figure 6.1. The instrument, several centuries old, exhibits clear signs of mechanical degradation, including multiple visible cracks in its wooden structure, among which the largest one is of the main interest here. The fracture is mainly attributed to cleavage failure (i.e., a splitting fracture), presumably developed during shrinkage, which reduced the soundboard's tensile capacity perpendicular to the grain, hence promoting the crack's expansion [233, 153]. These cracks, combined with the natural effects of material aging and environmental exposure, have raised concerns regarding its structural stability and safety during future playability. Throughout this

Fig. 6.1 Arpicordo Antegnati from 1552

chapter, the impact of uncertainty in the material properties on the soundboard static response will be taken into account and discussed via two approaches: a deterministic analysis and an info-gap approach. In the first case, different assumptions regarding the elastic properties of the soundboard are introduced in the FEM model to assess their influence on the predicted structural response. In particular, material parameters taken from literature values or available databases are compared against an elastic material characterization of the soundboard's main plate based on direct measurements on wood specimens of the same kind. This analysis is performed to demonstrate the impact of material uncertainty on the static assessment of the soundboard. On the other hand, the info-gap approach allows an exploration of how much uncertainty can be tolerated while still ensuring that the structure remains safe under typical loading conditions [25, 27, 28]. This method has proven effective in recent studies on historical musical instruments, notably in the assessment of an 18th-century cello with cracks, which inspired the present work [271]. That study demonstrated the particular suitability of Info-Gap theory combined with FEM analysis for evaluating the structural behavior of historical wooden instruments, by accounting for uncertainties in different material elastic properties which could not be directly measured because of conservation purposes. In this work, this approach is exploited to assess the robustness of the instruments with and without the presence of the main fracture.

6.1.1 The Hill Criterion

To evaluate the static response of the instrument's soundboard, a suitable metric is required. Among different criteria, the Hill Criterion is here used in accordance with similar research [271]. This is defined as:

$$\mathscr{H} = F(\sigma_{yy} - \sigma_{zz})^2 + G(\sigma_{zz} - \sigma_{xx})^2 + H(\sigma_{xx} - \sigma_{yy})^2 + 2L\sigma_{yz}^2 + 2M\sigma_{zx}^2 + 2N\sigma_{xy}^2 \quad (6.1)$$

Where σ_{ij} being the stress values in the i, j directions, the functions F, G, H, L, M, and N are defined as:

$$
\begin{aligned}
F &= \frac{1}{2}\left[\frac{1}{(\sigma_y^y)^2} + \frac{1}{(\sigma_z^y)^2} - \frac{1}{(\sigma_x^y)^2}\right] \\
G &= \frac{1}{2}\left[\frac{1}{(\sigma_z^y)^2} + \frac{1}{(\sigma_1^y)^2} - \frac{1}{(\sigma_y^y)^2}\right] \\
H &= \frac{1}{2}\left[\frac{1}{(\sigma_x^y)^2} + \frac{1}{(\sigma_2^y)^2} - \frac{1}{(\sigma_z^y)^2}\right] \\
L &= \frac{1}{2(\sigma_{yz}^y)^2} \\
M &= \frac{1}{2(\sigma_{zx}^y)^2} \\
N &= \frac{1}{2(\sigma_{xy}^y)^2}
\end{aligned}
\tag{6.2}
$$

Where σ_i^y is the yield stress in direction i, σ_{ij}^y represents the yield shear stress in the plane ij. The Hill criterion expresses the material's proximity to yielding as a quadratic function of the stress components, producing a scalar value $\mathscr{H}$. Accordingly, when $\mathscr{H} \geq 1$, the material reaches the onset of yielding, indicating the beginning of plastic deformation and an increased risk of crack initiation or propagation.

6.2 Soundboard material properties estimation strategies

The soundboard assembly of the Arpicordo consists of several distinct components, constructed from different wood species, as listed in Table 6.1. A visualization of the different components from the implemented CAD model of the soundboard is shown in Section 6.4. A fundamental step in this assessment is the estimation of the mechanical properties of the arpicordo's materials. Published databases for wood properties typically report values for modern or commercially available materials, which are not representative of cypress and pear wood that have formed part of a musical instrument for several centuries. Additionally,

COMPONENT	WOOD TYPE
Main plate	Cypress
Bridges (x2)	Maple
Braces (x2)	Spruce
Jacks Guide	Pear wood

Table 6.1 Components of the arpicordo soundboard and corresponding materials.

individual pieces of wood exhibit great variability in their mechanical behavior, influenced by factors such as age, grain orientation and moisture history [275, 270, 187].

6.2.1 Literature- based material characterization

To characterize the material elastic properties of the soundboard, a literature review was first conducted to gather available data on the mechanical properties of cypress and pear wood [233, 24, 47, 271]. However, given the lack of elastic constants data, particularly for cypress and pear wood, assumptions are needed when characterizing the soundboard materials. Specifically, while data from spruce and maple wood were entirely based on literature values [47], data for cypress and pear wood were estimated starting from available E_x values of Mediterranean cypress which has been attributed to the construction of similar historical soundboards [230]. This data was then used to approximate the remaining Young's moduli and shear moduli based on materials constants ratios for similar wood types [233]. Poisson ratios were also obtained from similar available wood types, namely bald cypress and birch wood [233]. Table 6.2 reports the material characterization based on available literature values and online databases.

Property	**Cypress**	**Pear**	**Spruce**	**Maple**
E_x (MPa)	5280	7800	10700	10000
E_y (MPa)	440	1537	710	1520
E_z (MPa)	206	671	430	870
ν_{xy}	0.338	0.392	0.38	0.46
ν_{yz}	0.411	0.695	0.51	0.82
ν_{zx}	0.326	0.428	0.51	0.50
G_{xy} (MPa)	332	1537	500	1220
G_{yz} (MPa)	37	133	23	290
G_{zx} (MPa)	285	757	620	1100
ρ (Kg/m^3)	535	690	390	590

Table 6.2 Orthotropic material properties used for FEM modelling of the arpicordo soundboard components.

Analogously, the yield stress and yield shear stress components needed for the computation of $\mathscr{H}$ are reported in Table 6.3 . These were based on both both literature findings [24, 233] and online databases [180]. However, as not enough data were collected, these initial values are characterized by high intrinsic uncertainty.

Stress field component	Yield stress values [MPa]
σ_x	46
σ_y	3
σ_z	3
σ_{xy}	6
σ_{yz}	6
σ_{zx}	6

Table 6.3 Yield stress and yield shear stress values for each stress field component.

6.2.2 Experimental material characterization

To reduce the uncertainty in the material properties of cypress and pear, destructive mechanical tests were performed on small samples of cypress and pear wood, which could be used without compromising valuable artifacts. The ASTM D198 standard procedure was followed to carry out the measurements [253]. Precisely, a total of 35 specimens were employed across both pear and cypress, distributed according to material and testing direction. For the yield stress, six pear specimens and six cypress specimens for each of the three anatomical directions (longitudinal, radial, and tangential) were tested in compression. ASTM D198 prescribes that the proportional limit stress, corresponding to the point marking the end of linear elastic behavior, is to be taken as the yield stress. Operationally, the corresponding force F at this transition was identified, and the yield stress was computed as:

$$\sigma_i = \frac{F}{A_c} \tag{6.3}$$

Where A_c is the cross-sectional area of the specimen and i corresponds to the tested fiber direction. For the value of E_x, seven pear specimens and ten cypress specimens were tested in flexure. Note that, while the main fracture considered in this study is mainly due to the tension acting perpendicular to the grain, for the presented case study measured compression yield stress values can be considered as comparable to measured tension yield stresses, as demonstrated by similar values reported in Table 3 in [271]. According to ASTM D198, E_x is defined as the slope of the straight-line portion of the load–deformation curve. In this work, the slope was extracted through linear regression applied to the initial linear region of the stress–strain data, thereby ensuring objectivity and reproducibility. Figure 6.2a shows the setup used for the three points bending test and the compression test performed on the samples in accordance with the ASTM D198 standard. Here, the experimentally obtained values of E_x for both cypress and pear were employed to rescale the full set

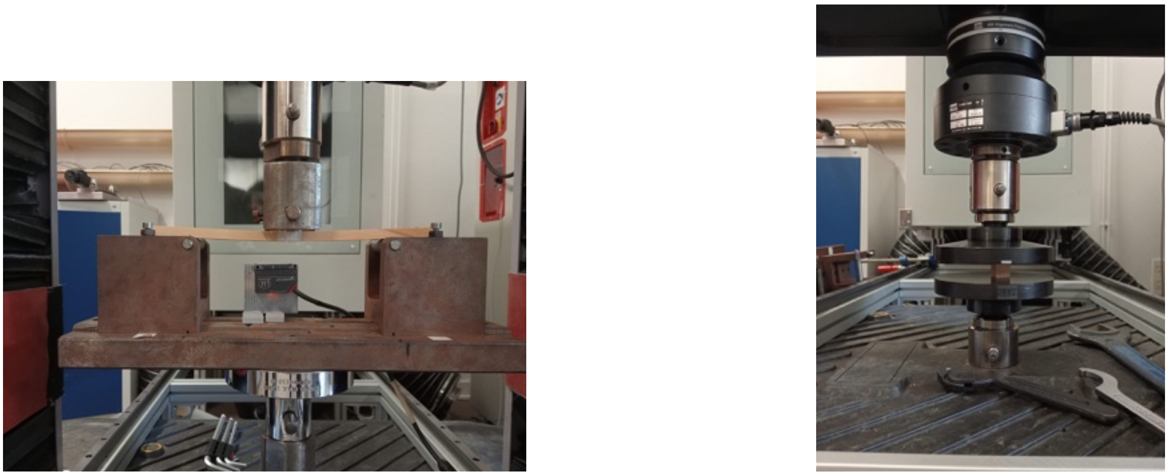

(a) Three points bending tests.

(b) Compression tests.

Fig. 6.2 Destructive measurements on cypress and pear wood tonewoods samples.

of elastic constants. The same literature orthotropic ratios for wood used to estimate the remaining elastic constants in Section 6.2.1 were applied. The experimentally-driven material characterization for cypress and pear wood is presented in Table 6.4 and Table 6.5. Despite the reduction of material uncertainty achieved through experimental testing, the limited number of available specimens and the specific preservation state of the historical instrument imply that significant uncertainty remains in the characterization of the soundboard properties.

	Experimentally driven		*Literature based*		*Difference[%]*	
Property	**Cypress**	**Pear**	**Cypress**	**Pear**	**Cypress**	**Pear**
E_L (MPa)	7100	9000	5280	7800	29.4	14.3
E_R (MPa)	596	1773	440	1537	30.1	14.3
E_T (MPa)	277	774	206	671	29.4	14.3
G_{LR} (MPa)	447	1323	1220	1537	29.5	15.0
G_{RT} (MPa)	50	153	290	133	29.9	14.0
G_{TL} (MPa)	383	873	1100	757	29.3	14.2
ρ (Kg/m^3)	632.4	707.6	535	690	16.7	2.5

Table 6.4 Comparison of experimentally and literature-driven material properties for cypress and pear wood used for FEM modeling of the arpicordo soundboard components.

	Yield stress values [MPa]		
Stress field component	*Experimentally driven*	*Literature based*	*Difference[%]*
σ_x	39.1	46	16.2
σ_y	11.8	3	118.9
σ_z	11.7	3	118.4

Table 6.5 Comparison of experimentally and literature-driven yield stress values for each stress field component.

This will be explicitly taken into account through the Info-gap analysis presented in Section 6.5.2.

6.3 Estimation of String Tension and Applied Loads

The forces applied to the soundboard by the strings were estimated based on each string's frequency, length, and linear mass density [136]:

$$f = \frac{1}{2L}\sqrt{\frac{\mathscr{T}}{\mu}} \quad \Rightarrow \quad \mathscr{T} = 4L^2 f^2 \mu \tag{6.4}$$

where f is the string frequency (Hz), L is the vibrating length of the string (m), $\mathscr{T}$ is the string tension (N), and μ is the linear mass density of the string (kg/m). The tuning, number of strings, and their material characteristics were estimated based on organological research on similar historical instruments and available relevant insights [197, 47]. As an example, the reference tuning was assumed from a similar instrument attributed to the same maker, illustrated in Figure 6.3. Similarly, string materials and dimensions were inspired by available data of a virginal replica shown in Figure 6.4. The string lengths and break angles (angles between the strings and the horizontal at the bridges) were estimated from the 3D CAD model of the arpicordo. The resulting string tensions were decomposed into components along the vertical (z) and longitudinal (x) directions. The vertical component for each string was calculated as $T \cdot \sin(\theta)$, and the longitudinal component as $T \cdot \cos(\theta)$, where θ is the angle of the string relative to the horizontal plane. The total vertical force on the soundboard was obtained by summing the z-components of all strings, and the total longitudinal force was obtained by summing the x-components. The strings assumed material

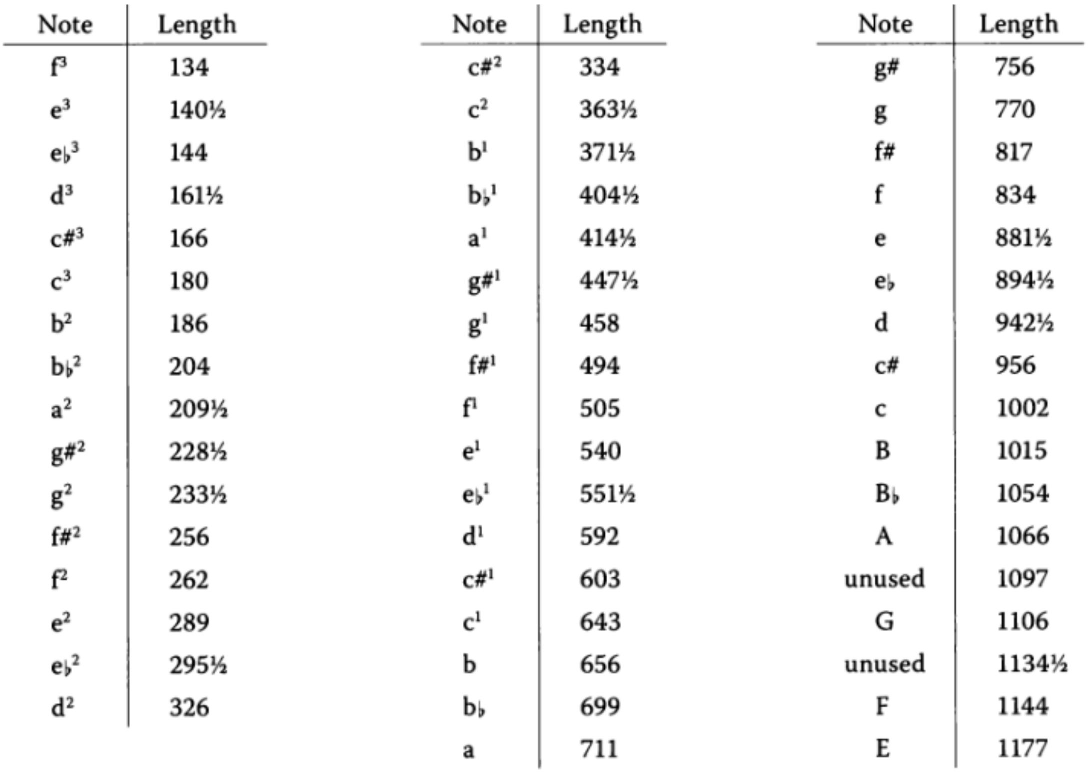

Note	Length	Note	Length	Note	Length
f^3	134	$c\#^2$	334	g#	756
e^3	140½	c^2	363½	g	770
$e\flat^3$	144	b^1	371½	f#	817
d^3	161½	$b\flat^1$	404½	f	834
$c\#^3$	166	a^1	414½	e	881½
c^3	180	$g\#^1$	447½	e♭	894½
b^2	186	g^1	458	d	942½
$b\flat^2$	204	$f\#^1$	494	c#	956
a^2	209½	f^1	505	c	1002
$g\#^2$	228½	e^1	540	B	1015
g^2	233½	$e\flat^1$	551½	B♭	1054
$f\#^2$	256	d^1	592	A	1066
f^2	262	$c\#^1$	603	unused	1097
e^2	289	c^1	643	G	1106
$e\flat^2$	295½	b	656	unused	1134½
d^2	326	b♭	699	F	1144
		a	711	E	1177

Fig. 6.3 Reference tuning and strings lengths (in mm) from [197] for the Nuremberg Virginal attributed to Gianfrancesco Antegnati.

properties and the resulting total force values used in the FEM model are summarized in Table 6.6.

Total force in Bridge 1		**Total force in Bridge 2**	
- *z direction*	- *x direction*	- *z direction*	+ *x direction*
40	456	44	456

Table 6.6 Total forces (in N) applied to each bridge in the FEM model.

The assumed properties of the strings are summarized in Table 6.7, following recommendations from Bucur [47].

Fig. 6.4 Three types of wire used in a virginal replica, namely iron, yellow brass and red brass with strings diameters ranging from 0.2 mm to 0.7 mm [47].

String type	**Radius [m]**	**μ [kg/m]**
Red brass (strings 1–3)	3.5×10^{-4}	3.4×10^{-3}
Yellow brass (strings 4–7)	3.5×10^{-4}	3.3×10^{-3}
Iron (strings 8 and higher)	1×10^{-4}	2.5×10^{-4}

Table 6.7 Assumed string types, radii, and linear densities.

6.4 FEM-based modeling of the Soundboard

A 3D FEM model of the Antegnati arpicordo soundboard was developed in COMSOL to analyze the mechanical behavior of the instrument under typical loading conditions and to evaluate its structural robustness. The geometry of the model was based on precise dimensional measurements conducted by an experienced restorer directly on the original instrument. In addition, high-resolution CT scans were performed, providing further geometrical insights into the internal structure of the soundboard. These data were used to complement and refine the CAD geometry, ensuring that the model implementation reflected both external measurements and internal features. Together, the restorer's measurements and the tomography scans provided accurate reference dimensions for the soundboard plate, the attached components, and the observed fracture geometry. Within this study, only the largest observable crack was taken into account. Examples of the high resolution CT scans are showed in Figure 6.5. As seen from the full view of the soundboard, the instrument displays a non-homogeneous profile, partly due to shrinkage effects from centuries of wood aging. In addition, the thickness distribution is intentionally irregular, reflecting historical design practices of the makers. These aspects were not incorporated into the present model, as the focus here is on evaluating the impact of material property uncertainties in the virtual prototyping of historical musical instruments.

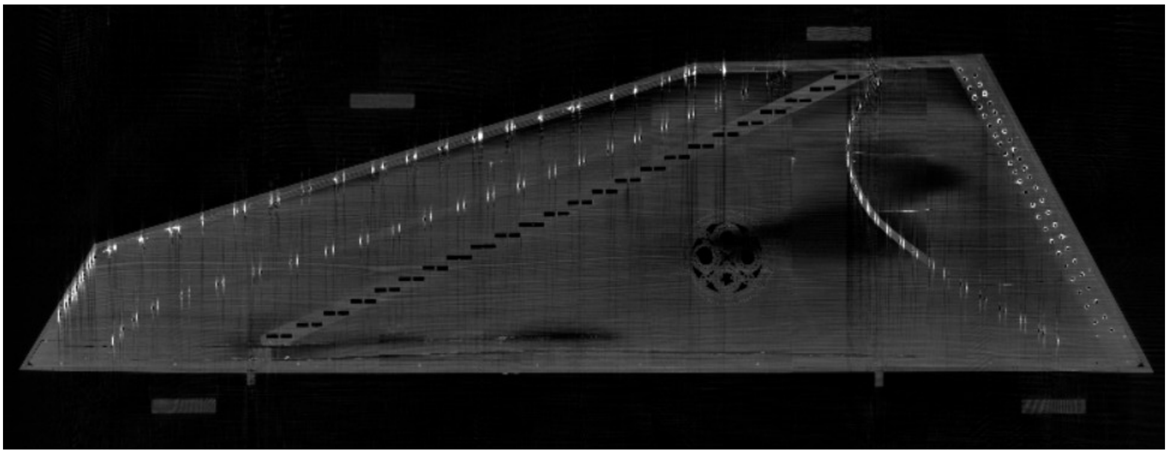

(a) Full soundboard view.

(b) Detailed soundboard fibers view.
(c) Detailed jacks guide fibers view.

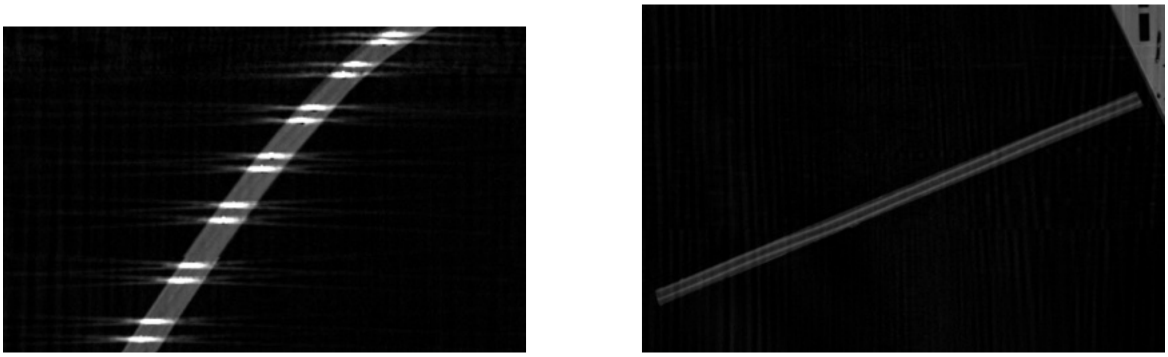

(d) Detailed bridge fibers view.
(e) Detailed brace fibers view.

Fig. 6.5 DICOM images obtained from CT scans on the instrument.

An initial 3D CAD model of the soundboard was created using Autodesk software. The main fracture was drawn into the model by superimposing a high-resolution photograph of the soundboard onto the CAD geometry and manually tracing its outline using splines. This process ensured that the FEM model could accurately reflect the actual crack paths observed in the instrument, rather than purely relying on theoretical or idealized assumptions. Two versions of the FEM model were developed: one representing the current cracked condition of the soundboard, and a second version representing an undamaged condition. This allowed for comparative analysis of the effects of the cracks on the structural behavior of the soundboard, and to assess the reduction in robustness caused by the observed damage. An illustration of the final CAD model of the instrument's soundboard is presented in Figure 6.6. Each component was individually modeled in COMSOL through the *Solid Mechanics* interface. The fiber orientation of each component was carefully defined based on visual inspection of the instrument and discussions with the restorer to accurately represent the orthotropic behavior of the materials. Examples of the different components coordinate systems are reported in figure 6.7.

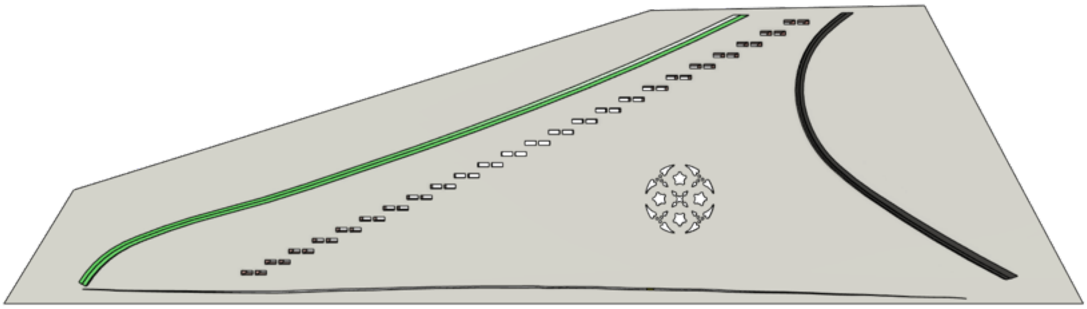

(a) Front view of the soundboard. In green: large bridge. In black: small bridge.

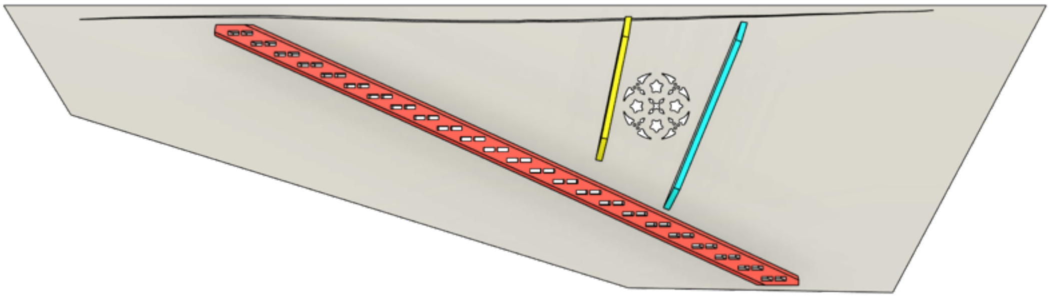

(b) Back view of the soundboard. In red: Jacks guide. In light blue: large brace. In yellow: small brace.

Fig. 6.6 Soundboard CAD model with the fracture imported in COMSOL.

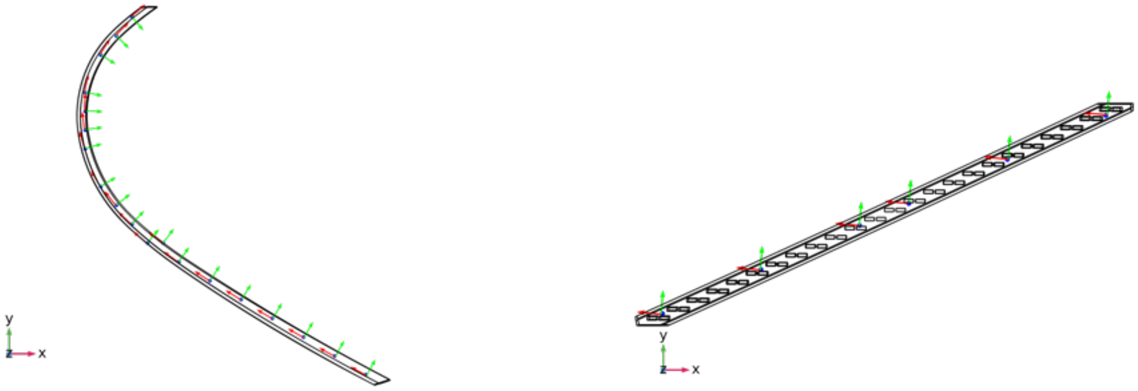

(a) Smaller bridge coordinate system.

(b) Jacks guide coordinate system.

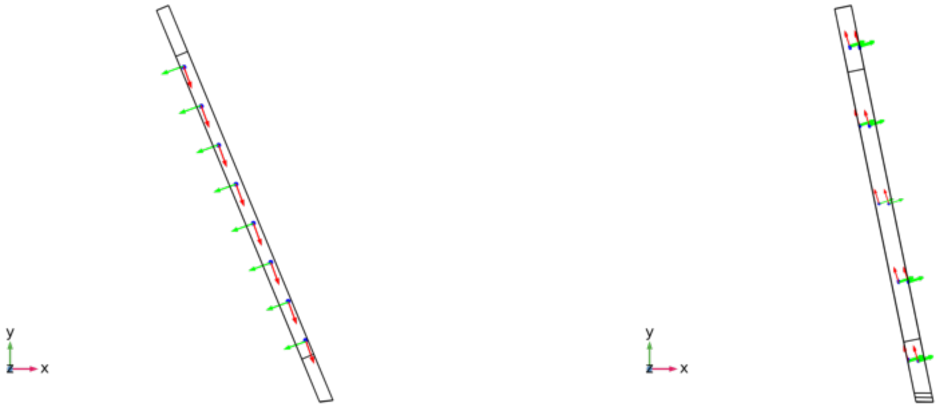

(c) Large brace coordinate system.

(d) Small brace coordinate system.

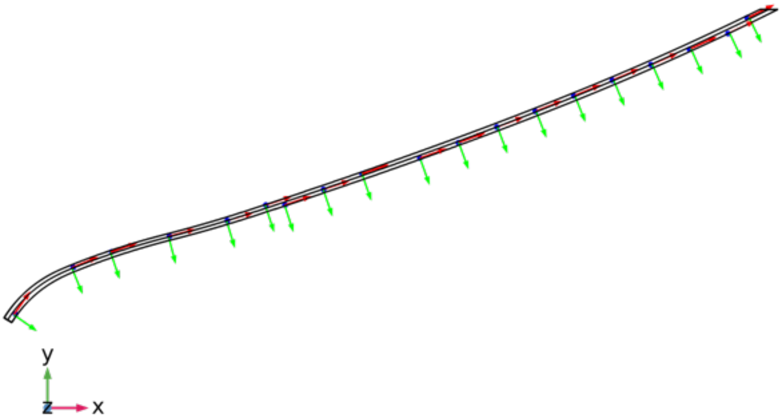

(e) Large bridge coordinate system.

Fig. 6.7 Illustration of the coordinate systems defined for the different soundboard components in COMSOL. The reference axis orientation shown in the bottom left corner indicates the global coordinate system of the model, which coincides with the main soundboard plate's coordinates.

Clamped boundary conditions were applied in the FEM model. The external edges of the soundboard plate were fully constrained, representing the rigid attachment of the soundboard to the instrument's frame. In addition, fixed constraints were applied at the interfaces between the soundboard plate and each attached component (bridges, braces, and jack guide), corresponding to the glued joints present in the actual instrument. The string tension data estimated in Table 6.6 was applied in the COMSOL model as boundary loads acting along the two bridges.

To reduce computational cost, a coarse free tetrahedral mesh was adopted in the FEM model. This is shown in Figure 6.8. This choice ensured efficiency but also introduced a limitation, as mesh density can influence the accuracy of stress and strain distributions, especially near cracks and material interfaces. Since the objective of this study was to evaluate the relative impact of material assumptions and associated uncertainties, the effect of mesh refinement was not investigated here. Nevertheless, its influence on result accuracy will be systematically addressed in future work through a dedicated mesh convergence study.

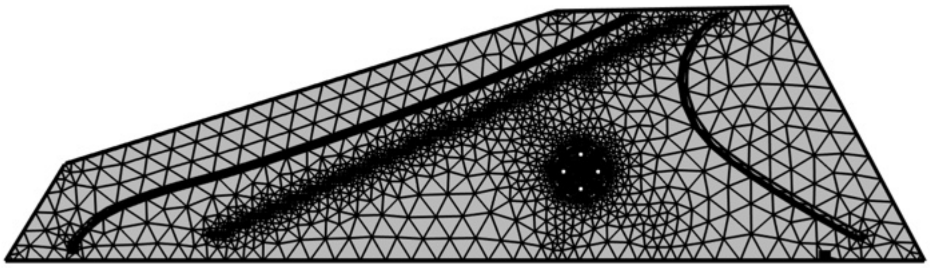

(a) Mesh in COMSOL without crack

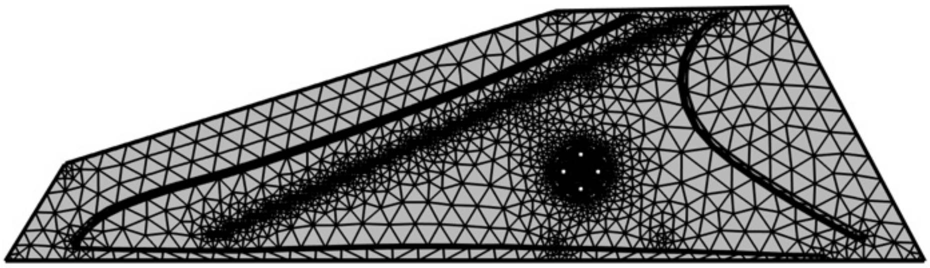

(b) Mesh in COMSOL with crack

Fig. 6.8 Finite element mesh of the arpicordo soundboard: (a) without crack; (b) with crack.

6.5 Uncertainty assessment

The results obtained from both a deterministic static analysis using initial values only as well as the results from the info-gap robustness analysis are presented in the following sections.

6.5.1 Deterministic results

In this section, deterministic results using both the literature based materials characterization as well as the estimated values from the experimental data are presented. For the cracked model, $\mathscr{H}$ was evaluated at specific points located at the tips of the fracture, where stress concentrations are expected and critical behavior is most likely to initiate. In contrast, for the undamaged model, $\mathscr{H}$ was computed as the maximum surface value over the entire soundboard. This approach ensured that, in the absence of pre-existing defects, the most critical location for potential failure was automatically identified. Thus, the choice between point evaluation and surface maximum was made according to the structural condition of the model: localized evaluation in the presence of cracks, and global maximum search for the intact case.

Results

The $\mathscr{H}$ values computed for both the intact and the damaged soundboard model are reported in Table 6.8. Besides, a visualization of the stress distribution for the damaged case scenario in the x and y directions as well as the shear stress distribution in the x, y is given in Figure 6.9. From the analysis, a significant difference is observed between the two estimation approaches.

Literature values		Experimental values	
$\mathscr{H}_{intact}$	$\mathscr{H}_{fracture}$	$\mathscr{H}_{intact}$	$\mathscr{H}_{fracture}$
≈ 0.75	≈ 2.12	≈ 0.15	≈ 0.39

Table 6.8 Hill criterion values obtained from the deterministic simulations using literature-based and experimental-based material characterizations.

Specifically, the $\mathscr{H}_{intact}$ value obtained using literature-based material properties is five times greater than the value based on the model informed by experimental data. Similarly, the $\mathscr{H}_{fracture}$ value predicted with literature-based properties is more than five times higher than the corresponding value obtained with experimental-based characterization. This suggests that relying solely on literature values might overestimate the structural demand in both intact and fractured configurations, while the use of experimentally informed properties results in consistently lower Hill criterion values, indicating a less critical structural state. Furthermore, the results highlight the limitations of a purely deterministic approach. In the case of historical musical instruments, additional uncertainty arises not only from the unknown long-term impact of environmental factors, but also from the fact that the material samples used for characterization can not always be taken from the original soundboard, as for the current case scenario. Accordingly, the findings show that the conclusions about structural safety or failure risk are highly sensitive to the choice of input parameters. Relying on a single set of initial values leaves too much uncertainty. This observation underlines the necessity of a robustness-oriented framework, such as Info-Gap analysis, to properly account for uncertainty and to evaluate the sensitivity of the conclusions to variability in the input data.

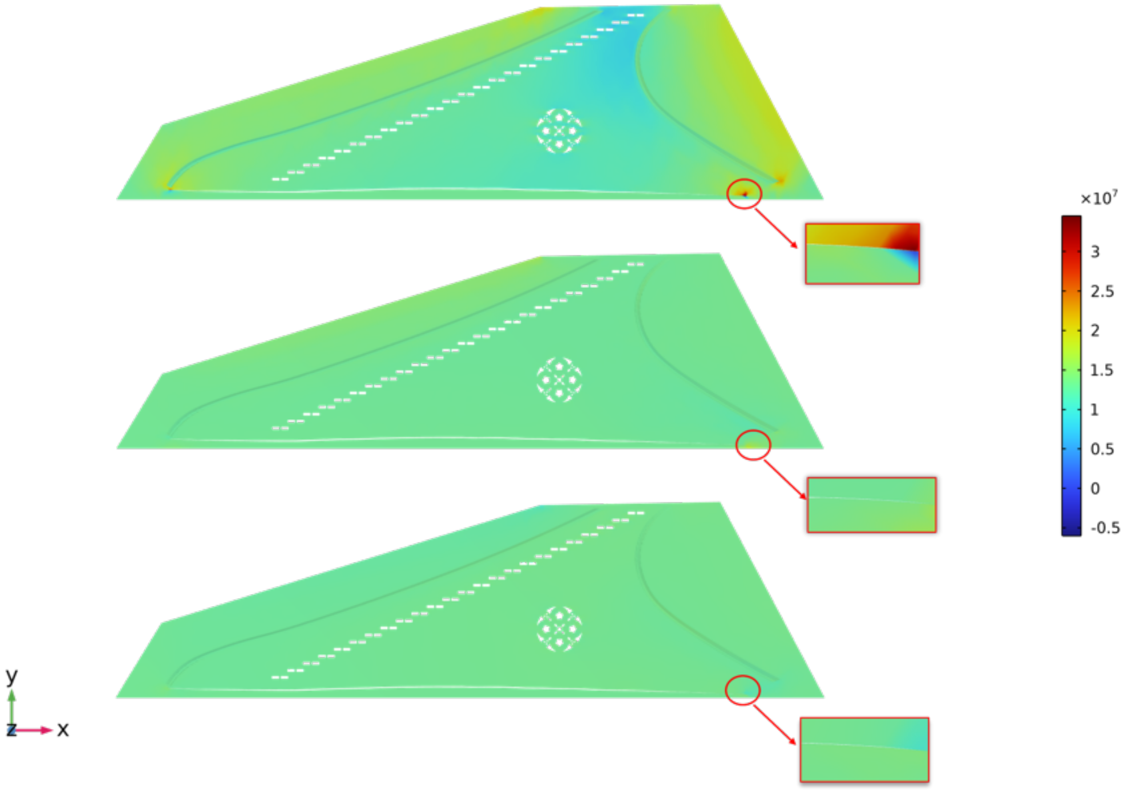

Fig. 6.9 Stress distribution in the x (top) and y (middle) directions and shear stress distribution in the x, y plane (bottom).

6.5.2 Info-gap Robustness analysis

The uncertainties in the experimentally driven material properties of the cypress soundboard are now modeled using an Info-Gap approach, following the formulation implemented in [271]. The Info-Gap uncertainty analysis was carried out using the SIMBAD platform, which was coupled with COMSOL Multiphysics through the LiveLink component for MATLAB [2]. This integration enabled COMSOL to be driven directly by MATLAB scripts, allowing SIMBAD to access the full range of MATLAB's preprocessing, model manipulation, and post-processing capabilities while operating on the FEM models built in COMSOL. In this way, SIMBAD could efficiently manage the uncertainty analysis by automating simulations and handling the iterative evaluations required by the Info-Gap framework [192, 283].

Uncertainity set

As per similar research [271], no probabilistic assumptions were made; instead, uncertainties were expressed through a fractional-error info-gap model describing the uncertainty around the initial values for the soundboard's plate elastic constants and yield stresses. The resulting uncertainty set was defined as:

$$W_q(h) = \left\{ \mathscr{Q} : \left| \frac{\mathscr{Q}_i - \hat{\mathscr{Q}}_i}{s_{\mathscr{Q}_j}} \right| \leq \mathfrak{h},\ \forall i \right\}, \quad \mathfrak{h} \geq 0 \tag{4}$$

where $\hat{\mathscr{Q}}_i$ are the nominal values of the material parameters that here vary by ± $s_{\mathscr{Q}_j}$ while $\mathfrak{h}$ represents the horizon of uncertainty. As in [271], Hill's quadratic yield criterion $\mathscr{H}$ was computed per each value of h, allowing the robustness function $\hat{\mathfrak{h}}(H_c)$ to be established. The resulting robustness horizon provides a quantitative measure of how large the parameter uncertainties can become before compromising structural safety, and thus offers direct guidance for assessing the playability of the instrument. For this preliminary case study, a common estimated relative error of 30 % was assigned to all the material properties and yield stress components related to the main cypress board. This error was intentionally set to be larger than reported literature variability [275] in the woods material properties to account also for the uncertainty caused by the aging of the instruments, the unknown environmental factors to which it has been exposed over several centuries, and the limitations inherent in the estimation of material properties from small test samples. A visual representation of the uncertainty horizon in the info-gap analysis conducted in this Section is given in Figure 6.10.

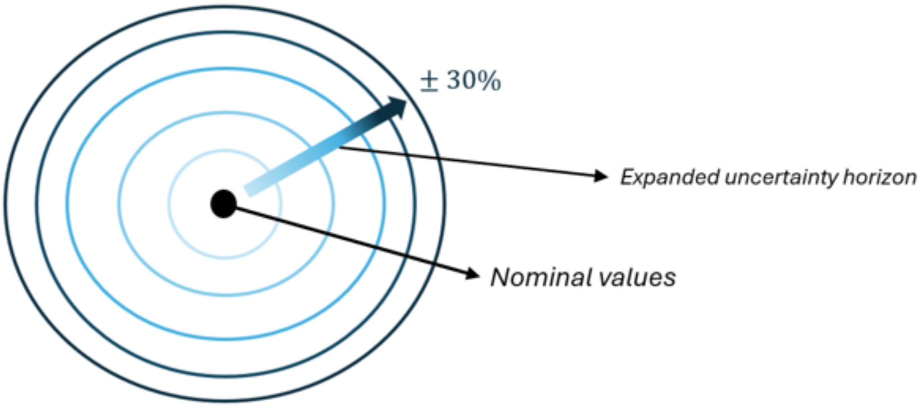

Fig. 6.10 Illustration of the uncertainty horizon in the info-gap robustness analysis of this study. The black dot represents the nominal material properties (here based on the gathered experimental data). Expanding circles represent the five successive sampled horizons of uncertainty h, within which parameter values may deviate from nominal. In this study, the maximum horizon corresponds to ±30% variation in the cypress wood material properties.

Performance requirement and Robustness function

The decision as to whether the instrument is considered playable, or not, depends on the computed value of Hill's quadratic failure function $\mathscr{H}$. A safety factor was chosen to be the same as in [271], leading to a critical threshold $\mathscr{H}_c = 1/3$ for the Hill criterion. Although this criterion can be arbitrarily chosen based on the conservation policies, it helps prevent the instrument from structurally failing under unexpected environmental factors or human errors. The instrument may be expected to remain structurally safe under potential playing conditions if $\mathscr{H}$ does not exceed this threshold.

The robustness function is defined as the largest uncertainty horizon $\mathfrak{h}$ such that Hill's criterion remains below the critical value for all combinations of parameters within the uncertainty set. It is expressed as:

$$\hat{\mathfrak{h}}(H_c) = \max\left\{\mathfrak{h} : \max_{\mathbf{q}\in W_q(\mathfrak{h})} (\mathscr{H}(\mathbf{q})) \leq \mathscr{H}_c\right\} \tag{6.5}$$

The robustness $\hat{\mathfrak{h}}(\mathscr{H}_c)$ therefore quantifies the maximum level of uncertainty on the material parameters that can be tolerated while ensuring that the soundboard remains structurally safe. In other words, it provides a measure of how sensitive the instrument's structural integrity is to the lack of precise knowledge about the mechanical properties of the aged cypress soundboard.

Results

In Info-gap theory, robustness is formally defined as a function of the performance requirement $\mathscr{H}_c$ in 6.5. While the admissible safety threshold is fixed at $\mathscr{H}_c = 1/3$, robustness can be evaluated for a range of requirements. This produces a robustness curve $\hat{\mathfrak{h}}(\mathscr{H}_c)$, which illustrates the trade-off between performance and robustness. In practice, this means that strict performance requirements (low $\mathscr{H}_c$) are associated with low robustness, whereas more relaxed requirements correspond to larger robustness margins [271]. The resulting robustness functions $\hat{\mathfrak{h}}(\mathscr{H}_c)$ are shown in Figure 6.11 for the two versions of the soundboard FEM model: with and without the crack profile. The curves display the evolution of robustness as a function of the Hill criterion threshold $\mathscr{H}_c$. In the plot, the robustness $\hat{h}$ is expressed as the allowed percentage variation assumed in the analysis. As expected, the undamaged model exhibits greater robustness across the entire range of performance requirements. At the target safety threshold $\mathscr{H}_c = 0.33$, the intact soundboard tolerates uncertainty up to $\hat{h} \approx 18\%$. On the other hand, it is worth to notice how for the fractured model, the $\hat{h}$ exceeds the maximum $\mathscr{H} = 1$ threshold at $\approx 18\%$.

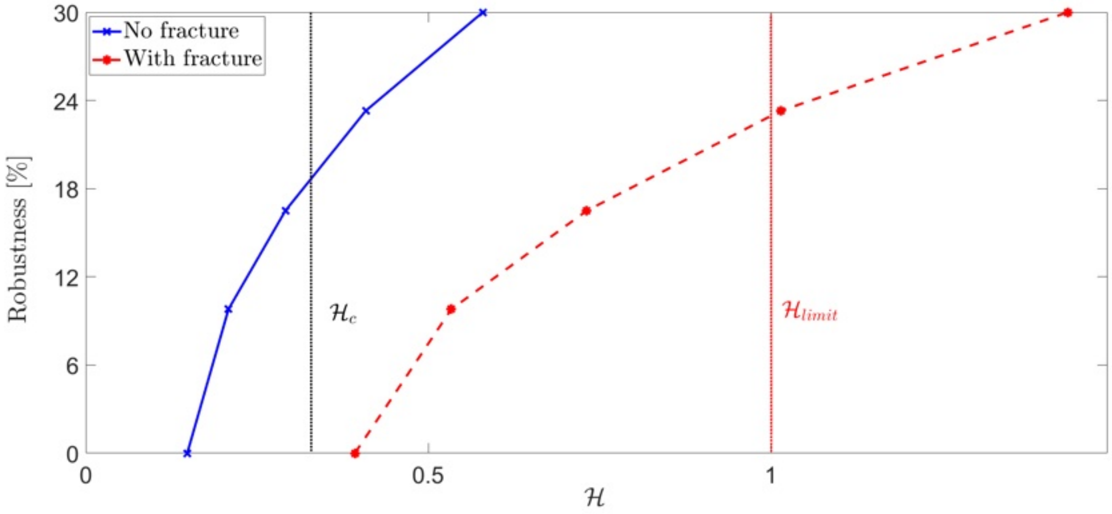

Fig. 6.11 Info-Gap Robustness analysis results. In solid blue line: Soundboard with no fracture. In red dashed line: Soundboard with fracture. Black and red dotted vertical lines denote the safety threshold $\mathscr{H}_c = 0.33$ and the $\mathscr{H}$ limit value = 1.

6.6 Implication for conservation strategies

While the presented analysis only served as a pilot study aiming to assess the impact of materials uncertainty on the structural integrity of historical musical instruments, the results offer valuable trends that can inform conservation practices. At first, the difficulty in accessing reliable data for certain woods used in musical instruments highlights the need to conduct further research and standardize experimental procedures to collect more data of tonewoods elastic properties. A useful trend from the numerical evaluation of the Hill Criterion can be taken from the deterministic investigation. The results stressed how sensitive the structural safety evaluation can be to the chosen input values for the different wood types. In fact, for the presented case study, a restorer exclusively relying on literature data would conclude that the arpicordo in its current state is critically unsafe from a structural integrity point of view. On the other hand, using experimental data to drive the material characterization of the more uncertain material properties of the instruments would lead to a relatively safe judgment of the same board, since the $\mathscr{H}_{fracture}$ value would remain quite below the maximum Hill Criterion threshold (i.e. $\mathscr{H} = 1$) while only slightly exceeding the safety threshold of $\mathscr{H} = 0.33$. This significant discrepancy demonstrates the risk of overconfidence in a deterministic analysis approach. Therefore, if decision making were based uniquely on this strategy, the outcomes could span from very conservative decisions which would prevent any further intervention aiming at bringing the instrument back to playable conditions to an underestimation of structural hazards that could expose the antique instrument to permanent and irreversible damage. Instead, an info-gap robustness analysis approach clearly helps overcoming this limitation by quantifying the maximum uncertainty that can be tolerated by the numerical model before the safety criterion is compromised. This offers a more reliable framework to be adopted in conservation policies, confirming its application to the conservation of historical musical instruments, as suggested by recent research [271]. With specific regard to the case study considered here, the info-gap analysis provides valuable insights which can support the restorer interventions. The results suggest how the intact instrument could be safely stored within a museum scenario in its current state and limited playability could be guaranteed under the considered assumptions, hence exploiting the intangible cultural heritage inherent to the instrument. However, it is shown how the dramatic loss in robustness caused by the presence of a fracture like the one evaluated in this study leads to very low values of tolerable uncertainty. For museum curators and conservators this underscores the relevance of monitoring structural artifacts by quantifying the change in the structural capability of the soundboard due to the presence of defects. More broadly, the FEM-based analysis confirmed to represent a valuable diagnostic tool, stressing its applicability to identify useful trends which can be of interests within a museum context, as suggested in previous research [3].

Limitations

As this section reported an initial study conducted over a real case scenario, limitations have to be reported in order to inform and support future studies towards the development of a larger framework for the analysis of similar musical instruments. Despite the valuable insights concerning trends and relative discrepancies from an intact and a damaged model of the same soundboard, different source of uncertainty remain. First, the soundboard geometry was simplified in the modeling. For instance, the soundboard was assumed to have a homogeneous thickness, although in reality its profile varies. These variations are expected to affect both the modal and static responses of the instrument. Future work should therefore include a sensitivity analysis to assess how different levels of geometric detail influence the numerical results, including the occurrence of fractures.

Similarly, while only the largest of the fractures appearing on the damaged instrument was assessed to quantify its impact from the intact case, this was modeled by tracing the profile of the fracture from a high-quality CT scan directly in the CAD model through a spline function. Slight variations from the actual fracture profile might have led to different stress distributions along the fracture's edges, leading to different structural safety evaluations. Thus, the degree of detail in the material removal should be addressed in order to quantify its impact on the numerical results. Another significant source of uncertainty is given here by the mesh size. While a compromise was chosen here to preserve computational costs over accuracy, the geometrical discretization represents a further source of uncertainty in the correct representation of stress distributions, which can be even more critical closer to discontinuity locations, including sharp corners caused by the modeled crack profile. Further studies need to systematically address mesh convergence by progressively refining the mesh size and quantify the variations both in the modal domain as well as in the static response. Furthermore, efficient mesh sizing should be designed in order to guarantee a more refined mesh around critical points characterized by large stress gradients, while a coarser discretization should be allowed in less critical areas to minimize the computational cost. Overall, a systematic convergence mesh study would also help in distinguishing between numerical artifacts and actual variations caused by structural interventions. Another source of uncertainty in this kind of analysis concerns the evaluation of the Hill Criterion in the interested domain. In this case scenario, the parameter was evaluated for the damaged case model at two points located at the opposite vertex of the fracture, which are relevant locations where stress concentrations are expected. While this can represent a relevant and plausible way when the structural integrity has to be assessed at specific local coordinates of the structure, it presents important limitations. Evaluating only discrete points may underestimate the maximum Hill Criterion if slightly larger values occur in the immediate vicinity, particularly in regions affected by steep stress gradients or local mesh artifacts. In future work, a more systematic strategy should be adopted, for example, by evaluating the Hill Criterion over the entire surface or by extracting maximum values along the fracture edges. Such an approach would reduce the risk of overlooking critical zones and would provide a more robust picture of the instrument's structural safety. Finally, the Info-Gap robustness analysis modeled the uncertainty only on the elastic properties of cypress and pear wood, given the lack of reliable data for these materials. However, the structural behavior of the soundboard is arguably also influenced by the mechanical properties of the other wood species used in the instrument making, as well as by the assumed string tensions. The variability of these additional parameters was not involved here, but their effect should be explored in future work to achieve a more comprehensive uncertainty assessment. In the following section, a conceptual framework for a comprehensive reverse-engineering process is proposed, aiming to outline the future research needs towards heritage conservation workflows.

6.7 Towards a conservation framework: from CT scanning to virtual prototyping of historical musical instruments

When implementing accurate virtual prototypes of existing historical musical instruments via non-destructive image-based techniques historical and fragile instruments for FEM based analysis, each case scenario represents a specific challenge due to its structural state, limiting their accessibility and transportation. No protocol has yet been studied and validated to recommend common practices supporting conservation interventions. Nonetheless, different limitations still need to be addressed in order to validate a full reverse engineering protocol that can offer accurate numerical investigations, informing the decision-making process of restorers and museum curators by quantifying several uncertainty sources. A crucial aspect concerns the choice of the best suited imaged based non-destructive method to acquire the volumetric data of the musical instrument. Whilst many techniques exist, each of them might be better suited for a different application [218], as reported in Table 6.9. Specifically, techniques like photogrammetry, Laser Scanning (LIDAR), and Structured Light Scanning

Method	**Optimal applications**	**Advantages**	**Limitations**
Photogrammetry	When highly accurate renderings of color and texture are needed	High portability, cost-effective, captures color	Depends too much on camera quality
LIDAR	Surveying archaeological sites and scanning large objects	High data acquisition speed, semi-portable	Air molecules can interfere with the light pulses; cannot detect color without extensions
Structured Light	When high-precision, noncontact, and detailed surface mapping are needed	High-resolution, high-precision	Cannot capture texture and color; sensor is sensitive to ambient light
CT	Analysis of internal structure of artifacts and diagnostics	Non-invasive, surveys entire volume at once	Limited availability of specialized equipment

Table 6.9 Comparison of 3D image based scanning methods taken from [218].

(SLS) only allow for a 3D reconstruction of the external component's surfaces [126, 218, 213, 75]. Therefore, despite the specialized equipment required, CT represents the most promising approach when a detailed reconstruction of the internal instrument structure is needed. This is crucial to allow detecting potential internal damages in the different structural components, which might affect the structural integrity of the instrument and therefore influence restoration practices. Different examples exist on relatively small and medium-sized ancient instruments, particularly the violin. Figure 6.12 shows examples of damage and interior structural details observed in a violin and cello instruments by means of CT scans [241, 106].

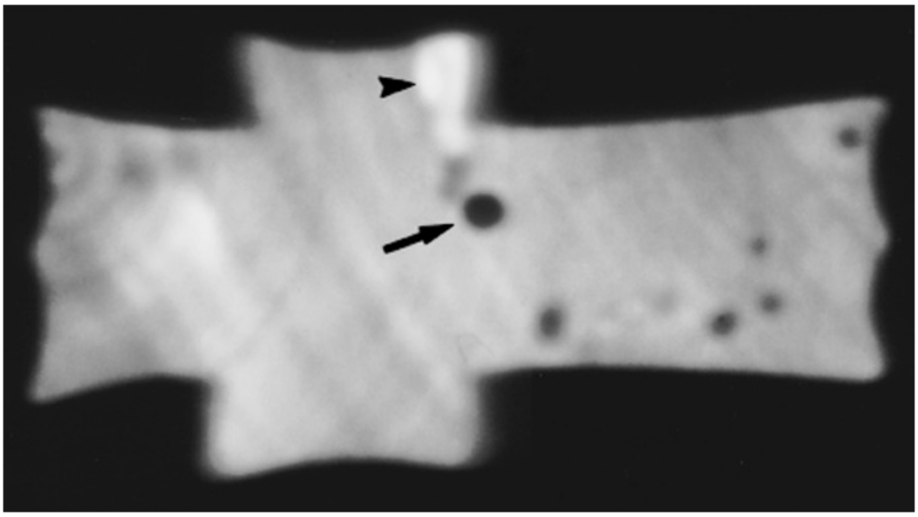

(a)

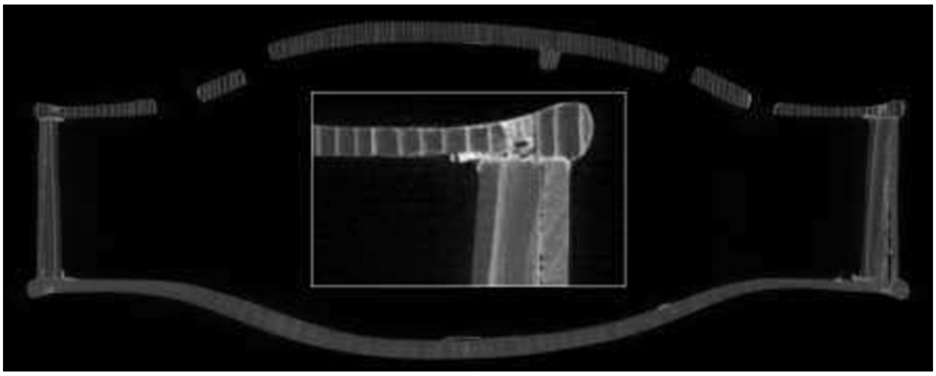

(b)

Fig. 6.12 Examples of damage and gap detection in the internal surfaces of historical musical instruments. **(a):** Wormhole detected in a peg box of a historical Venetian cello via CT scans from [241]. **(b):** Detailed view of a high-resolution CT scan obtained for a Hummel violin with a 50 μm resolution from [106].

Larger instruments may present additional challenges during digital acquisition. For example, the Antegnati Arpicordo examined in the previous sections underwent a CT scanning campaign to obtain more detailed information about its geometry and internal components. Figure 6.13 reports the mounting setup built specifically for the instrument.

(a) (b)

(c) (d)

Fig. 6.13 Different views of the setup used for CT scanning of the Antegnati Arpicordo.

In this case study, the images were primarily used to inform the reconstruction of the CAD model, with several finer details omitted. This was decided both to preserve simplicity in the pilot phase and also because of the additional challenges encountered in the reverse process required to obtain a CAD model of the instrument soundboard from the obtained point cloud (i.e. the digital representation of the volume reconstructed from the CT data). An example of identified internal damage which was not included in the CAD model in Section 6.4 is shown in Figure 6.14. Due to the instrument's relatively large size, multiple scans were required to capture its entire structure, which significantly increased the total acquisition time and post-processing effort. Several research initiatives have sought to establish guidelines for CT scanning of musical instruments. The MUSICES project, for instance, examined more than 100 historical instruments to produce detailed recommendations and practical instructions covering transportation, data acquisition, post-processing, and the optimization of scanning parameters. These efforts eventually culminated in a comprehensive set of guidelines for cultural heritage applications [106, 20]. Further studies are still required to develop standardized workflows that can reliably translate CT scan data into accurate and simulation-ready 3D CAD models. Some of the key challenges include surface segmentation, the generation of watertight geometries, and the implementation of meshes suitable for numerical analyses, such as FEM-based simulations. Addressing these steps systematically is essential to ensure that 3D reconstructions are not only geometrically faithful but also computationally efficient for mechanical and vibroacoustical modeling. Finally, future work should also focus on systematic numerical sensitivity analyses to quantify the influence of geometrical detail and mesh refinement on the simulation outcomes. Such studies would provide valuable

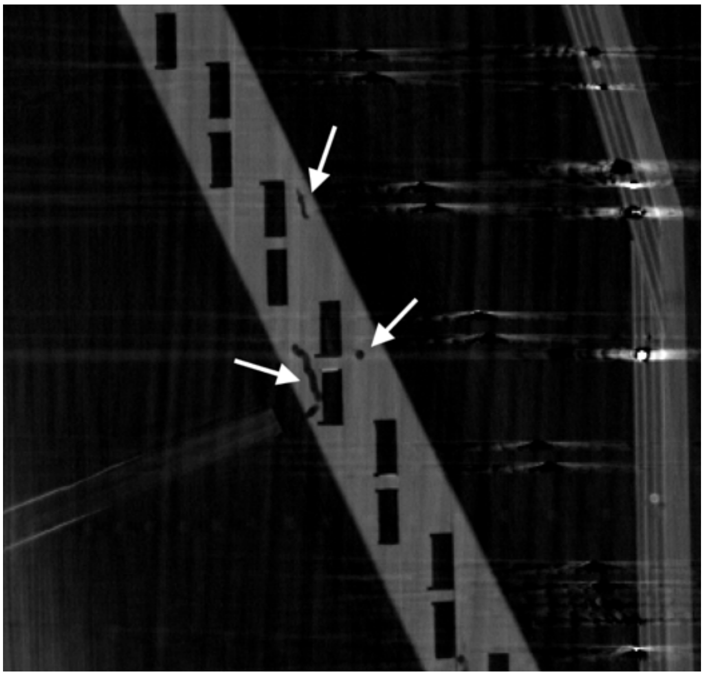

Fig. 6.14 Examples of internal material damage in the soundboard's jacks guide identified from the CT scans.

insights into how the level of model detail affects the accuracy and computational efficiency of the analyses, thereby enabling optimized CT scanning and post-processing protocols that could balance accuracy and efficiency.

Chapter 7

Conclusions

The presented thesis focused on the experimental vibroacoustic analysis of orthotropic plates, with specific application to string-based musical instruments. The literature review in Section 1 provided a comprehensive overview of both the historical development of methods for estimating material parameters and the state of the art in experimental and numerical approaches for analyzing the modal behavior of instrument plates. One of the main achievements of this work was the development of resource-efficient and cost-effective experimental methodologies for measuring and identifying the dynamic and elastic properties of wooden plates. These methods enable the collection of modal data and the estimation of the main elastic constants of orthotropic materials in a more accessible and practical way, aiming to support the activities of instrument makers and restorers.

A key contribution of this research was the validation of the inverse material parameter estimation method introduced in Section 3. This approach, based on a linear least-squares minimization, demonstrated the ability to accurately recover the elastic constants of thin orthotropic plates. The methodology was first numerically benchmarked, proving its efficiency under different boundary condition configurations. It was then experimentally validated on several sets of tonewood samples belonging to existing string-based musical instruments (see Sections 3.6, 4.3, and 3.7), confirming its efficiency under laboratory and workshop conditions. To enhance the accessibility of the approach, a low-cost measurement chain was also implemented and validated. This setup requires significantly less specialized equipment than standard laboratory EMA systems, allowing the method to be applied in workshop or instrument-making contexts. The non-dimensional analysis framework presented in Section 5 introduced diagnostic tools to assess whether a tested plate satisfies thin-plate assumptions, or whether its area-to-thickness ratio may compromise the accuracy of the estimated elastic constants. Although the procedures were demonstrated using a commercial FEM software, the numerical benchmarking and validation of the open-source MagPie platform (Section 4.4) highlight the potential for establishing a fully open and accessible analysis ecosystem. Finally, Chapter 6 extended the investigation by examining the impact of material property uncertainty on the structural response of a historical soundboard of an Antegnati arpicordo from 1552. A deterministic analysis was shown to be highly sensitive to input variability, emphasizing the need for uncertainty assessment in conservation modeling. To address this, an info-gap robustness analysis was carried out, introducing bounded variations in the nominal elastic properties of the main soundboard woods. Despite the simplifications in the modeling assumptions, the results revealed meaningful numerical trends and quantified the sensitivity of structural predictions to material uncertainties, thereby providing a more informed basis for restoration decision-making.

7.1 Future perspectives

A central ethos of the NEMUS project has been the open dissemination of knowledge and tools, ensuring that methods developed for musical acoustics can be shared, reproduced, and extended by the wider community. In this regard, the use of open-source computational approaches has been a cornerstone. The development of MagPie, for instance, has already demonstrated the feasibility of moving from commercial finite-element software such as COMSOL to an in-house, open-source numerical framework for rectangular soundboards. The continuation of this line of work will aim at expanding MagPie toward more complex geometries and boundary conditions, integrating it as part of the NEMUS ecosystem. Although numerical model development was not the main objective of this PhD, the results obtained here provide a foundation for coupling experimental findings with numerical prediction tools in a fully open-source environment. This integration will facilitate more comprehensive workflows in which the estimation of material parameters, uncertainty quantification, and model validation can occur within a single, transparent framework. Combining the numerical codes with the Info-Gap theory, previously applied to the restoration of the Antegnati arpicordo, will further allow the incorporation of robustness analysis into future modeling tools. This will enable the quantitative assessment of risk and uncertainty in virtual restoration, a topic that aligns closely with NEMUS's interdisciplinary vision.

With specific concern to historical musical instruments, as introduced in Section 6.7, future and ongoing research efforts will focus on integrating tomography scans into a framework for vibroacoustics and static analysis of such artefacts. While CT-based reconstruction provides a powerful, non-invasive means of accessing internal geometry, the reliability of

CAD models derived from scan data for numerical analyses remains an open question, particularly given the additional processing required to convert raw scan data into manifold geometries suitable for FE-based modeling. Ongoing work, therefore, includes a comparative assessment of CT-derived models against reference geometries obtained from direct measurements. To this end, pilot studies on small-sized instruments, such as a small kantele model shown in Figure 7.1 , will investigate the impact of CT scans-based reconstruction on the modal and static response of the instrument, with a long-term goal of establishing validation strategies and uncertainty bounds for CT-based finite-element models.

Fig. 7.1 Small kantele model used in an ongoing case study.

An illustration of the workflow used for the current ongoing study on the small kantele model is given in Figure 7.2 Beyond the numerical aspects, following the case study discussed in Section 4.5, future work will also attempt to establish tolerable error bounds and meaningful and standard JNDs in the modal domain when comparing two or more instruments to each other, which remains a relevant open question for repeatability purposes in musical instrument making.

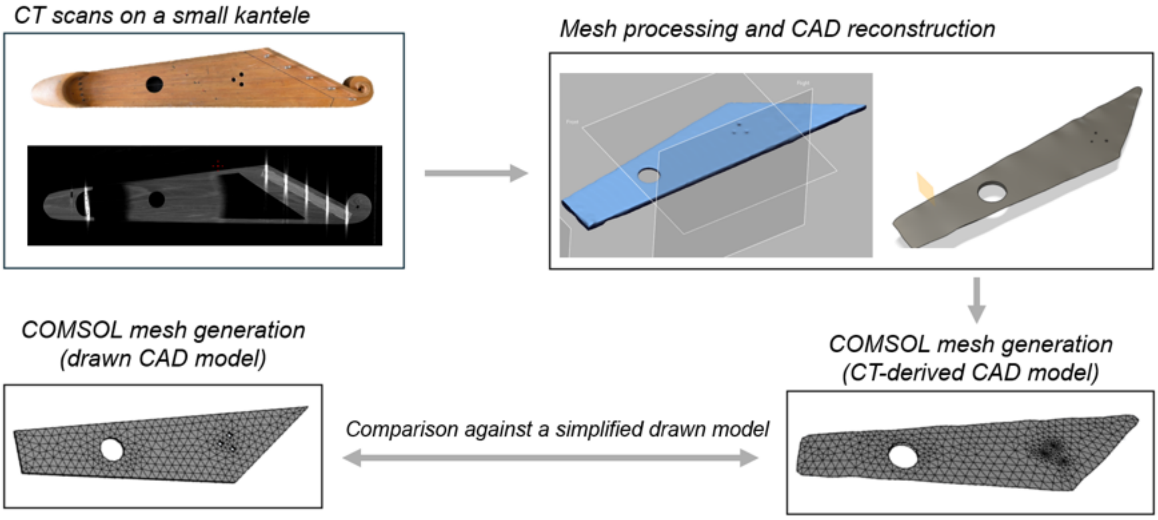

Fig. 7.2 Workflow for CT-Based CAD Reconstruction and Finite Element Modeling of a Kantele Soundboard.

In summary, this research lays the groundwork for an integrated open-source framework that combines:

- numerical simulation and modal analysis tools for orthotropic soundboards,
- uncertainty and robustness assessment via Info-Gap theory,
- post-processing and segmentation algorithms for experimental data,
- JND values for modal parameters linking numerical, experimental, and perceptual comparisons of musical instruments,
- and an ethos of accessibility, transparency, and knowledge sharing that continues to define the NEMUS project.

References

[1] AB, C. *COMSOL Multiphysics® – Simulation software for multiphysics modeling*. Accessed via official product website of COMSOL Multiphysics. 2025. URL: https://www.comsol.com/comsol-multiphysics (visited on 10/23/2025).

[2] AB, C. *LiveLink™ for MATLAB® – Run Multiphysics Simulations with MATLAB*. Add-on product for COMSOL Multiphysics® enabling MATLAB® integration. 2025. URL: https://www.comsol.com/livelink-for-matlab (visited on 10/23/2025).

[3] Almanza, V., Le Conte, S., Vaiedelich, S., Foltête, E., Viala, R., Mosquera, A. F. A., Martinez, L., Wilkie-Chancellier, N., Serfaty, S., Placet, V., et al. "Physics-based simulations for assessing the playability of heritage musical instruments: Impact of the soundboard assembly process on its low frequency behavior". In: *Applied Acoustics* 214 (2023), p. 109672.

[4] Arnold, D. N. and Falk, R. S. "Asymptotic analysis of the boundary layer for the Reissner–Mindlin plate model". In: *SIAM Journal on Mathematical Analysis* 27.2 (1996), pp. 486–514.

[5] Asakura, T., Ishizuka, T., Miyajima, T., Toyoda, M., and Sakamoto, S. "Vibration analysis for framed structures using the finite-difference time-domain method based on the Bernoulli-Euler beam theory". In: *Acoustical Science and Technology* 35.3 (2014), pp. 139–149.

[6] Ashby, M. F. and Gibson, L. J. "Cellular solids: structure and properties". In: *Press Syndicate of the University of Cambridge, Cambridge, UK* (1997), pp. 175–231.

[7] Ashory, M. R. "Assessment of the mass-loading effects of accelerometers in modal testing". In: *SPIE proceedings series*. 2002.

[8] Audiomatica Srl. *CLIO Pocket — Portable Measurement System*. Official product page, Audiomatica audio measurement systems. 2025. URL: https://www.audiomatica.com/wp/?page_id=3557 (visited on 10/18/2025).

[9] Ausiello, L. and Hockey, V. "Quantitative measurements to enhance performance of acoustic musical instruments and improve manufacturing". In: *Acoustic Bulletin* 47.2 (2021), pp. 47–2.

[10] Ausiello, L., Yule, L., Squicciarini, G., and Barlow, C. "Guitar soundboard measurements for repeatable acoustic performance manufacturing". In: *Reproduced Sound*. Institute of Acoustics. Bristol, UK, Nov. 2018.

[11] Ausiello, L., Ducceschi, M., Duran, S., and Morrison, B. "Affordable wide-band measurement ecosystem for musical acoustics based on electro-dynamic transducers". In: *Acta Acustica* 8 (2024), p. 53.

[12] Ausiello, L. and Hockey, V. "Advances in acoustics instruments measurements and system design". In: *Reproduced Sound 2020: Taking it up a level*. Institute of Acoustics. 2020.

[13] Ausiello, L. and Nicoletti, G. "FEM simulations and experimental validation of frequency response prediction for acoustic soundboards". In: *Reproduced Sound 2021: Institute of Acoustics Proceedings*. Vol. 43. Institute of Acoustics Proceedings 2. Bristol, United Kingdom: Institute of Acoustics, Nov. 2021, –. DOI: 10.25144/13793. URL: https://reproducedsound.co.uk/.

[14] Avitabile, P. *Modal testing: A practitioner's guide*. Hoboken, New Jersey: John Wiley & Sons, 2017.

[15] Ayorinde, E. "Elastic constants of thick orthotropic composite plates". In: *Journal of composite materials* 29.8 (1995), pp. 1025–1039.

[16] Ayorinde, E. and Gibson, R. F. "Elastic constants of orthotropic composite materials using plate resonance frequencies, classical lamination theory and an optimized three-mode Rayleigh formulation". In: *Composites Engineering* 3.5 (1993), pp. 395–407.

[17] Badiane, D. G., Gonzalez, S., Malvermi, R., Antonacci, F., and Sarti, A. "A neural network-based method for spruce tonewood characterization". In: *The Journal of the Acoustical Society of America* 154.2 (2023), pp. 730–738.

[18] Badiane, D. G., Malvermi, R., Gonzalez, S., Antonacci, F., and Sarti, A. "On the prediction of the frequency response of a wooden plate from its mechanical parameters". In: *ICASSP 2022-2022 IEEE International Conference on Acoustics, Speech and Signal Processing (ICASSP)*. IEEE. 2022, pp. 461–465.

[19] Bakarezos, M., Gymnopoulos, S., Brezas, S., Orfanos, Y., Maravelakis, E., Papadopoulos, C., Tatarakis, M., Antoniadis, A., and Papadogiannis, N. "Vibration analysis of the top plates of traditional greek string musical instruments". In: *Proceedings of the 13th International Congress on Sound and Vibration*. 2006, pp. 4939–4946.

[20] Bär, F. P., Fuchs, T., Wagner, R., Kirsch, S., Wolters, M., Fischeidl, K., Scholz, G., Kretzer, C., Raquet, M., Fichtner, M., Firsching, M., Wagner, S., Zepf, M., Schielein, R., Böhnel, M., Reims, N., Brennhäußer, G., and Weizel, V. *Recommendations for the Three-Dimensional Computed Tomography of Musical Instruments*. Technical Report. Germanisches Nationalmuseum, Nuremberg, 2018. URL: https://www.gnm.de/fileadmin/redakteure/Forschung/pdf/2018-10-11_MUSICES_Recommendations.pdf.

[21] Barbato, G., Barini, E., Genta, G., and Levi, R. "Features and performance of some outlier detection methods". In: *Journal of Applied Statistics* 38.10 (2011), pp. 2133–2149.

[22] Batahong, R. Y., Dayou, J., Wang, S., and Lee, J. "Vibrational Properties of sundatang soundboard". In: *Archives of Acoustics* 39 (2014).

[23] Bediz, B., Korkmaz, E., and Ozdoganlar, O. B. "An impact excitation system for repeatable, high-bandwidth modal testing of miniature structures". In: *Journal of Sound and Vibration* 333.13 (2014), pp. 2743–2761.

[24] Bektaş, İ. and Kurt, R. “Principal mechanical properties of cypress wood (Cupressus Sempervirens L.) naturally grown in (Kahramanmaraş) Eastern Mediterranean of Turkey”. In: *Gazi University Journal of Science* 23.3 (2010), pp. 357–362.

[25] Ben-Haim, Y. *Info-gap decision theory: decisions under severe uncertainty*. Elsevier, 2006.

[26] Ben-Haim, Y. *What is Info-Gap Theory?* Decision support methodology for model-based decisions under severe uncertainty. 2025. URL: https://info-gap.technion.ac.il/info-gap-theory/ (visited on 10/22/2025).

[27] Ben-Haim, Y. and Cogan, S. “Innovations and info-gaps: an overview”. In: *Model Validation and Uncertainty Quantification, Volume 3: Proceedings of the 35th IMAC, A Conference and Exposition on Structural Dynamics 2017*. Springer. 2017, pp. 263–271.

[28] Ben-Haim, Y. and Cogan, S. “Paradox of optimal learning: an info-gap perspective”. In: *ASCE-ASME Journal of Risk and Uncertainty in Engineering Systems, Part B: Mechanical Engineering* 9.3 (2023), p. 031203.

[29] Beurmann, A., Bader, R., and Schneider, A. “An acoustical study of a Kirkman harpsichord from 1766”. In: *The Galpin Society Journal* (2010), pp. 61–229.

[30] Bilbao, S. *Numerical sound synthesis: finite difference schemes and simulation in musical acoustics*. John Wiley & Sons, 2009.

[31] Bissinger, G. “Modal analysis of a violin octet”. In: *The Journal of the Acoustical Society of America* 113.4 (2003), pp. 2105–2113.

[32] Bissinger, G. “Structural acoustics of good and bad violins”. In: *The Journal of the Acoustical Society of America* 124.3 (2008), pp. 1764–1773.

[33] Bissinger, G. and Ye, K. “Automated hammer-impact modal analysis with a scanning laser vibrometer: working example-a violin”. In: *Proc. 18th Intern. Modal Analysis Conf.-Soc. Exp. Mechanics, Bethel, CT*. 2000, pp. 943–949.

[34] Blaschke, P., Schneider, S., Kamenzky, R., and Alarcón, D. J. “Non-linearity identification of composite materials by scalable impact modal testing”. In: *Sensors and Instrumentation, Volume 5: Proceedings of the 35th IMAC, A Conference and Exposition on Structural Dynamics 2017*. Springer. 2017, pp. 7–14.

[35] Bölke, O., Garcia, J., and Heimann, J. “Experimental Modal Analysis based on non-contact measurements with a commercial microphone array”. In: *ICSV26* (2019).

[36] Bonisoli, E., Casazza, M., Lisitano, D., and Dimauro, L. “Parametric experimental modal analysis of a modern violin based on a Guarneri del Gesù model”. In: *Rotating Machinery, Vibro-Acoustics & Laser Vibrometry, Volume 7: Proceedings of the 36th IMAC, A Conference and Exposition on Structural Dynamics 2018*. Springer. 2018, pp. 219–230.

[37] Borland, M. J. “The effect of humidity and moisture content on the tone of musical instruments”. PhD thesis. University of Waterloo Waterloo, 2014.

[38] Boutillon, X. and Ege, K. “Vibroacoustics of the piano soundboard: Reduced models, mobility synthesis, and acoustical radiation regime”. In: *Journal of Sound and Vibration* 332.18 (2013), pp. 4261–4279.

[39] Boyd, S. P. and Vandenberghe, L. *Convex optimization*. Cambridge university press, 2004.

[40] Brauchler, A., Hose, D., Ziegler, P., Hanss, M., and Eberhard, P. “Distinguishing geometrically identical instruments: Possibilistic identification of material parameters in a parametrically model order reduced finite element model of a classical guitar”. In: *Journal of Sound and Vibration* 535 (2022), p. 117071.

[41] Brauchler, A., Ziegler, P., and Eberhard, P. “Numerical models for classical guitars with updated parameters from experimental data”. In: *Forum Acusticum*. 2020, pp. 2155–2161.

[42] Brauchler, A., Ziegler, P., and Eberhard, P. “An entirely reverse-engineered finite element model of a classical guitar in comparison with experimental data”. In: *The Journal of the Acoustical Society of America* 149.6 (2021), pp. 4450–4462.

[43] Brémaud, I., El Kaım, Y., Guibal, D., Minato, K., Thibaut, B., and Gril, J. “Characterisation and categorisation of the diversity in viscoelastic vibrational properties between 98 wood types”. In: *Annals of Forest Science* 69.3 (2012), pp. 373–386.

[44] Brown, D., Allemang, R., and Phillips, A. “Forty Years of Use and Abuse of Impact Testing: A Practical Guide to Making Good FRF Measurements”. In: *Experimental Techniques, Rotating Machinery, and Acoustics, Volume 8*. Ed. by J. D. Clerck. Cham: Springer, 2015.

[45] Bucur, V. and Archer, R. “Elastic constants for wood by an ultrasonic method”. In: *Wood Science and Technology* 18.4 (1984), pp. 255–265.

[46] Bucur, V. *Acoustics of wood*. Springer Science & Business Media, 2006.

[47] Bucur, V. *Handbook of materials for string musical instruments*. Springer, 2016.

[48] Bucur, V. “Acoustics of Trees”. In: *Acoustics of Wood*. Springer, 2025, pp. 241–318.

[49] Buksnowitz, C., Teischinger, A., Müller, U., Pahler, A., and Evans, R. “Resonance wood [Picea abies (L.) Karst.]–evaluation and prediction of violin makers’ quality-grading”. In: *The journal of the acoustical society of America* 121.4 (2007), pp. 2384–2395.

[50] Burgos-Pintos, Á., Fernández-Zacarías, F., Mayuet, P. F., Hernández-Molina, R., and Rodríguez-Parada, L. “Influence of 3D Printing Direction in PLA Acoustic Guitars on Vibration Response”. In: *Polymers* 15.24 (2023), p. 4710.

[51] Burke, J. V. and Ferris, M. C. “A Gauss—Newton method for convex composite optimization”. In: *Mathematical Programming* 71.2 (1995), pp. 179–194.

[52] Cabaret, J. and Viala, R. “Exploring Modal Analysis for Characterizing Impact of Making Process on the Properties of Woods Used in Musical Instruments”. In: *IMAC, A Conference and Exposition on Structural Dynamics*. Springer. 2024, pp. 67–70.

[53] Caldersmith, G. and Freeman, E. “Wood properties from sample plate measurements I”. In: *Journal of the Catgut Acoustical Society* 1.series II (1990), pp. 8–12.

[54] Caldersmith, G. and Rossing, T. D. “Determination of modal coupling in vibrating rectangular plates”. In: *Applied Acoustics* 17.1 (1984), pp. 33–44.

[55] Caldersmith, G. W. “Vibrations of orthotropic rectangular plates”. In: *Acta Acustica united with Acustica* 56.2 (1984), pp. 144–152.

[56] Campanini, S., Farina, A., et al. *A new audicity feature: room objective acoustical parameters calculation module*. na, 2009.

[57] Carcagno, S., Bucknall, R., Woodhouse, J., Fritz, C., and Plack, C. J. "Effect of back wood choice on the perceived quality of steel-string acoustic guitars". In: *The Journal of the Acoustical Society of America* 144.6 (2018), pp. 3533–3547.

[58] Carlier, C., Alkadri, A., Gril, J., and Brémaud, I. "Revisiting the notion of" resonance wood" choice: a decompartementalised approach from violin makers' opinion and perception to characterization of material properties' variability". In: *arXiv preprint arXiv:1902.10977* (2019).

[59] Carvalho, M., Debut, V., and Antunes, J. "Physical modelling techniques for the dynamical characterization and sound synthesis of historical bells". In: *Heritage Science* 9.1 (2021), p. 157.

[60] Case Western Reserve University, CASLabs. *French/Flemish hpd (Baroque)*. Early Music Instrument Database, Baroque Instruments. 2025. URL: https://caslabs.case.edu/medren/baroque-instruments/frenchflemish-hpd-baroque/ (visited on 10/16/2025).

[61] Case Western Reserve University, CASLabs. *Italian/German hpd (Baroque)*. Early Music Instrument Database, Baroque Instruments. 2025. URL: https://caslabs.case.edu/medren/baroque-instruments/italiangerman-hpd-baroque/ (visited on 10/16/2025).

[62] Chabassier, J., Chaigne, A., and Joly, P. "Modeling and simulation of a grand piano". In: *The Journal of the Acoustical Society of America* 134.1 (2013), pp. 648–665.

[63] Chaigne, A., Cotté, B., and Viggiano, R. "Dynamical properties of piano soundboards". In: *The Journal of the Acoustical Society of America* 133.4 (2013), pp. 2456–2466.

[64] Chladni, E. F. F. *Treatise on Acoustics: The First Comprehensive English Translation of EFF Chladni's Traité d'Acoustique*. Springer, 2015.

[65] Coaldrake, A. K. "A finite element model of the Japanese koto constructed from computed tomography scans". In: *The Journal of the Acoustical Society of America* 148.5 (2020), pp. 3153–3170.

[66] COMSOL AB. *Structural Mechanics Module User's Guide*. 5.4. Electronic documentation (PDF). COMSOL Inc. Burlington, MA, USA, 2018. URL: https://doc.comsol.com/5.4/doc/com.comsol.help.sme/StructuralMechanicsModuleUsersGuide.pdf.

[67] Corradi, R., Fazioli, P., Marforio, S., Paluello, A., Ripamonti, F., and Squicciarini, G. "Modal analysis of a grand piano soundboard". In: *International conference on noise and vibration engineering (ISMA 2010)*. 2010.

[68] Corradi, R., Miccoli, S., Squicciarini, G., and Fazioli, P. "Modal analysis of a grand piano soundboard at successive manufacturing stages". In: *Applied Acoustics* 125 (2017), pp. 113–127.

[69] Curtin, J. "Measuring violin sound radiation using an impact hammer". In: *The Journal of the Acoustical Society of America VSA Papers* 22.1 (2009), pp. 186–209.

[70] Curtin, J., Jost, L., and Rogers, C. "A rig for measuring violin sound radiation". In: *The Journal of the Acoustical Society of America* 156.4_Supplement (2024), A92–A92.

[71] Damodaran, A., Lessard, L., and Suresh Babu, A. “An overview of fibre-reinforced composites for musical instrument soundboards”. In: *Acoustics Australia* 43.1 (2015), pp. 117–122.

[72] De Visscher, J., Sol, H., De Wilde, W., and Vantomme, J. “Identification of the damping properties of orthotropic composite materials using a mixed numerical experimental method”. In: *Applied Composite Materials* 4.1 (1997), pp. 13–33.

[73] Deobald, L. R. and Gibson, R. F. “Determination of elastic constants of orthotropic plates by a modal analysis/Rayleigh-Ritz technique”. In: *Journal of Sound and Vibration* 124.2 (1988), pp. 269–283.

[74] Derveaux, G., Chaigne, A., Joly, P., and Bécache, E. “Time-domain simulation of a guitar: Model and method”. In: *The Journal of the Acoustical Society of America* 114.6 (2003), pp. 3368–3383.

[75] Di Iorio, F., Fiocco, G., Angeloni, R., Es Sebar, L., Croci, S., Cacciatori, F., Malagodi, M., Pozzi, F., and Grassini, S. “Violins Unveiled: A Photogrammetric Framework Integrating Multiband and Spectroscopic Data for In-Depth Examination of Two Musical Instruments”. In: *Sensors* 25.11 (2025), p. 3278.

[76] Dodd, M., Klippel, W., and Oclee-Brown, J. “Voice coil impedance as a function of frequency and displacement”. In: *Audio Engineering Society Convention 117*. Audio Engineering Society. 2004.

[77] Ducceschi, M. and Bilbao, S. “Linear stiff string vibrations in musical acoustics: Assessment and comparison of models”. In: *The Journal of the Acoustical Society of America* 140.4 (2016), pp. 2445–2454.

[78] Ducceschi, M. and Bilbao, S. “Conservative finite difference time domain schemes for the prestressed Timoshenko, shear and Euler-Bernoulli beam equations”. In: *Wave Motion* 89 (2019), pp. 142–165.

[79] Ducceschi, M., Touzé, C., Bilbao, S., and Webb, C. J. “Nonlinear dynamics of rectangular plates: Investigation of modal interaction in free and forced vibrations”. In: *Acta Mechanica* 225.1 (2014), pp. 213–232.

[80] Ducceschi, M. “An open-source toolbox for direct and inverse modelling of orthotropic plates”. In: *Available at SSRN 5045108* (2024).

[81] Ducceschi, M. “Eigenvalue Problems and Modal Schemes in Musical Acoustics: A Tutorial”. In: ().

[82] Ducceschi, M. and Bilbao, S. “A Physical Model of the Prepared Piano”. In: *Proceedings of the 26th International Congress on Sound and Vibration*. Canadian Acoustical Association. 2019.

[83] Ducceschi, M., Duran, S., Tahvanainen, H., and Ausiello, L. “A method to estimate the rectangular orthotropic plate elastic constants using least-squares and Chladni patterns”. In: *Applied Acoustics* 220 (2024), p. 109949.

[84] Duerinck, T., Kersemans, M., Skrodzka, E., Leman, M., Verberkmoes, G., and Paepegem, W. V. “Experimental modal analysis of violins made from composites”. In: *Proceedings*. Vol. 2. 8. MDPI. 2018, p. 535.

[85] Duerinck, T., Segers, J., Skrodzka, E., Verberkmoes, G., Leman, M., Van Paepegem, W., and Kersemans, M. “Experimental comparison of various excitation and acquisition techniques for modal analysis of violins”. In: *Applied Acoustics* 177 (2021), p. 107942.

[86] Dumond, P. and Baddour, N. “Mechanical property relationships in sitka spruce soundboard wood”. In: *International Symposium on Musical Acoustics-Le Mans, France*. 2014.

[87] Duran, S., Ducceschi, M., Tahvanainen, H., and Ausiello, L. “Experimentally-tuned synthesis of a thin plate”. In: *Proceedings of the Institute of Acoustics*. Winchester, UK, Oct. 2023.

[88] Duran, S., Ducceschi, M., Tahvanainen, H., and Ausiello, L. “Fast estimation of wood elastic constants using least-squares”. In: *Forum Acusticum 2023: Acoustics for a green world*. 2023.

[89] Ege, K. “La table d’harmonie du piano – Études modales en basses et moyennes fréquences”. PhD thesis. ’École Polytechnique, Paris, France, 2009.

[90] Ege, K., Boutillon, X., and Rébillat, M. “Vibroacoustics of the piano soundboard:(Non) linearity and modal properties in the low-and mid-frequency ranges”. In: *Journal of Sound and Vibration* 332.5 (2013), pp. 1288–1305.

[91] Ege, K., Rébillat, M., and Boutillon, X. “Estimations of non-linearities in structural vibrations of string musical instruments”. In: *arXiv preprint arXiv:1210.4024* (2012).

[92] Elejabarrieta, M., Ezcurra, A., and Santamarıa, C. “Evolution of the vibrational behavior of a guitar soundboard along successive construction phases by means of the modal analysis technique”. In: *The Journal of the Acoustical Society of America* 108.1 (2000), pp. 369–378.

[93] Elie, B., Gautier, F., and David, B. “Acoustic signature of violins based on bridge transfer mobility measurements”. In: *The Journal of the Acoustical Society of America* 136.3 (2014), pp. 1385–1393.

[94] Enrico Ciresa S.r.l. *Tonewood and Soundboards – Ciresa, Val di Fiemme*. Official website – selection of tonewoods and musical instrument soundboards. 2025. URL: https://www.ciresafiemme.it/ (visited on 10/18/2025).

[95] Espinoz, C., Carreño, C., Chacra, E., and Gonzalez, S. “MetaWood: manipulation of the elastic properties of wood plates by periodic hole patterns”. In: *2022 Sixteenth International Congress on Artificial Materials for Novel Wave Phenomena (Metamaterials)*. IEEE. 2022, pp. 139–141.

[96] Esqueda, F., Kuznetsov, B., and Parker, J. D. “Differentiable white-box virtual analog modeling”. In: *24th International Conference on Digital Audio Effects (DAFx)*. Vienna, Austria, Sept. 2021, pp. 41–48.

[97] Eveno, P. and Le Conte, S. “An acoustical measurement used for the understanding of historical wind instruments”. In: *Journal of Cultural Heritage* 20 (2016), pp. 615–621.

[98] Ewins, D. *Modal testing: theory, practice and application*. John Wiley & Sons, 2009.

[99] Falaize, A. and Hélie, T. “Passive modelling of the electrodynamic loudspeaker: from the Thiele–Small model to nonlinear port-Hamiltonian systems”. In: *Acta Acustica* 4.1 (2020), p. 1.

[100] Fällström, K.-E. and Molin, N.-E. “A nondestructive method to determine material properties in orthotropic plates”. In: *Polymer composites* 8.2 (1987), pp. 103–108.

[101] Fällström, K.-E., Olofsson, K., Saldner, H. O., and Schedin, S. “Dynamic material parameters in an anisotropic plate estimated by phase-stepped holographic interferometry”. In: *Optics and Lasers in Engineering* 24.5-6 (1996), pp. 429–454.

[102] Farina, A. “Advancements in impulse response measurements by sine sweeps”. In: *Audio Engineering Society convention 122*. Audio Engineering Society. Vienna, Austria, May 2007.

[103] Farina, A. et al. “Simultaneous measurement of impulse response and distortion with a swept-sine technique”. In: *Preprints-Audio Engineering Society* (2000).

[104] Fletcher, N. H. and Rossing, T. D. *The Physics of Musical Instruments*. en. Google-Books-ID: gvDSBwAAQBAJ. Springer Science & Business Media, Dec. 2012. ISBN: 978-1-4612-2980-3.

[105] French, R. M. *Acoustic Guitar Design*. Springer, 2022.

[106] Fuchs, T., Wagner, R., Kretzer, C., Scholz, G., Bär, F., Kirsch, S., Wolters-Rosbach, M., and Fischeidl, K. “Musices-musical instrument computed tomography examination standard: results of the measurements and guidelines derived therefrom”. In: *Schweden: Gothenburg* (2018).

[107] Garai, M., Morandi, F., D’Orazio, D., Cesaris, S. D., and Loreti, L. “Acoustic measurements in eleven Italian opera houses: Correlations between room criteria and considerations on the local evolution of a typology”. In: *Buildings and Environment* 94 (2015), pp. 900–912.

[108] Gaul, L., Willner, K., and Hurlebaus, S. “Determination of Material Properties of Plates from Modal ESPI Measurements,# 5”. In: *PROCEEDINGS-SPIE THE INTERNATIONAL SOCIETY FOR OPTICAL ENGINEERING*. Vol. 2. SPIE INTERNATIONAL SOCIETY FOR OPTICAL. 1999, pp. 1756–1762.

[109] Gdoutos, E. and Konsta-Gdoutos, M. *Mechanical Testing of Materials*. Springer, 2024.

[110] Gétreau, F. “The conservation of acoustical specifications: a long ignorance in public collections of ancient instruments”. In: *17th International Congress on Acoustics Proceedings*. Brüel & Kjaer. 2001, pp. 391–396.

[111] Giordano, N. “Mechanical impedance of a piano soundboard”. In: *The Journal of the Acoustical Society of America* 103.4 (1998), pp. 2128–2133.

[112] Giordano, N. “Sound production by a vibrating piano soundboard: Experiment”. In: *The Journal of the Acoustical Society of America* 104.3 (1998), pp. 1648–1653.

[113] Giordano, N. and Chatziioannou, V. “Status and future of modeling of musical instruments: Introduction to the JASA special issue”. In: *The Journal of the Acoustical Society of America* 150.3 (2021), pp. 2294–2301.

[114] Göken, J., Fayed, S., Schäfer, H., and Enzenauer, J. “A study on the correlation between wood moisture and the damping behaviour of the tonewood spruce”. In: *Acta Physica Polonica A* 133.5 (2018), pp. 1241–1260.

[115] Golovin, Y. I., Gusev, A. A., Golovin, D. Y., Matveev, S. M., and Vasyukova, I. A. "Multiscale mechanical performance of wood: from nano-to macro-scale across structure hierarchy and size effects". In: *Nanomaterials* 12.7 (2022), p. 1139.

[116] Gonzalez, S., Chacra, E., Carreño, C., and Espinoza, C. "Wooden mechanical metamaterials: Towards tunable wood plates". In: *Materials & Design* 221 (2022), p. 110952.

[117] Gonzalez, S., Salvi, D., Antonacci, F., and Sarti, A. "Eigenfrequency optimisation of free violin plates". In: *The Journal of the Acoustical Society of America* 149.3 (2021), pp. 1400–1410.

[118] Gore, T. and Gilet, G. *Contemporary Acoustic Guitar Design and Build: Build*. Trevor Gore, 2011.

[119] Gore, T. "Wood for guitars". In: *Proceedings of Meetings on Acoustics*. Vol. 12. 1. Acoustical Society of America. 2011, p. 035001.

[120] Gough, C. "The violin: Chladni patterns, plates, shells and sounds". In: *The European Physical Journal Special Topics* 145.1 (2007), pp. 77–101.

[121] Gough, C. "Finite Element Analysis of Violin Shell Modes". In: *Proceedings of the Institute of Acoustics* 2 (2008), pp. 453–459.

[122] Gough, C. E. "A violin shell model: Vibrational modes and acoustics". In: *The Journal of the Acoustical Society of America* 137.3 (2015), pp. 1210–1225.

[123] Gough, C. "Musical acoustics". In: *Springer handbook of acoustics*. Springer, 2007, pp. 533–667.

[124] Graff, K. F. *Wave motion in elastic solids*. Courier Corporation, 2012.

[125] Gray, W. G. "Comparison of finite difference and finite element methods". In: *Fundamentals of transport phenomena in porous media*. Springer, 1984, pp. 899–952.

[126] Gröning, F. *Enhancing biomedical education: integrating digital visualization and 3D technologies*. Vol. 7. Springer Nature, 2025.

[127] Guidorzi, P., Barbaresi, L., D'Orazio, D., and Garai, M. "Impulse responses measured with MLS or Swept-Sine signals applied to architectural acoustics: an in-depth analysis of the two methods and some case studies of measurements inside theaters". In: *Energy Procedia* 78 (2015), pp. 1611–1616.

[128] Guitard, D. and El Amri, F. "Modèles prévisionnels de comportement élastique tridimensionnel pour les bois feuillus et les bois résineux". In: *Annales des sciences forestières*. Vol. 44. 3. EDP Sciences. 1987, pp. 335–358.

[129] Gurău, L., Timar, M. C., Coșereanu, C., Cosnita, M., and Stanciu, M. D. "Aging of wood for musical instruments: analysis of changes in color, surface morphology, chemical, and physical-acoustical properties during UV and thermal exposure". In: *Polymers* 15.7 (2023), p. 1794.

[130] Häggblad, B. and Bathe, K.-J. "Specifications of boundary conditions for Reissner/Mindlin plate bending finite elements". In: *International Journal for Numerical Methods in Engineering* 30.5 (1990), pp. 981–1011.

[131] Halvorsen, W. G. and Brown, D. L. "Impulse technique for structural frequency response testing". In: *Sound and Vibration* 63.1 (1978), S81.

[132] Hamilton, M., Ducceschi, M., Mousseau, A., and Duran, S. “MAGPIE: a web-based, open-source framework for plate vibration analysis”. In: *INTER-NOISE and NOISE-CON Congress and Conference Proceedings* 270.6 (2024), pp. 5918–5929.

[133] Harrington, J. J. “Hierarchical modelling of softwood hygro-elastic properties”. PhD thesis. University of Canterbury., 2002.

[134] HAUKAAS, T. *Kirchhoff and Mindlin Plates*. 2019.

[135] He, L., Liang, Y., Zhang, L., Zhou, J., Wang, R., and Liu, Z. “Measurement and Analysis of the Vibration Responses of Piano Soundboards with Different Structures”. In: *Materials* 17.5 (2024), p. 1004.

[136] Howard, D. and Angus, J. *Acoustics and psychoacoustics*. Routledge, 2013.

[137] Howard, K. “Musical instruments as tangible cultural heritage and as/for intangible cultural heritage”. In: *International Journal of Cultural Property* 29.1 (2022), pp. 23–44.

[138] Igea, F. and Cicirello, A. “A vibro-acoustic quality control approach for the elastic properties characterisation of thin orthotropic plates”. In: *Journal of Physics: Conference Series*. Vol. 1106. 1. IOP Publishing. 2018, p. 012031.

[139] Igea, F. and Cicirello, A. “Part-to-part variability assessment of material properties for flat thin orthotropic rectangular panels using Chladni patterns”. In: *Mech Sys Sig Proc* 139 (2020), p. 106559.

[140] Igea, F. and Cicirello, A. “Part-to-part variability assessment of material properties for flat thin orthotropic rectangular panels using Chladni patterns”. In: *Mechanical Systems and Signal Processing* 139 (2020), p. 106559.

[141] Inanli, S. and Altinsoy, E. “Vibroacoustics of Oud”. In: (2018).

[142] Inta, R. A. “The acoustics of the steel string guitar”. PhD thesis. UNSW Sydney, 2007.

[143] ISO, E. “3382-1, 2009,“acoustics—measurement of room acoustic parameters—part 1: Performance spaces,””. In: *International Organization for Standardization, Brussels, Belgium* 69 (2009).

[144] Jannifar, A., Zubir, M., and Kazi, S. “Development of a new driving impact system to be used in experimental modal analysis (EMA) under operational condition”. In: *Sensors and Actuators A: Physical* 263 (2017), pp. 398–414.

[145] Jin, Y. and Li, Z. “A new method for eliminating speckle noise from Laser Doppler Vibrometer signals”. In: *Journal of Physics: Conference Series*. Vol. 2041. 1. IOP Publishing. 2021, p. 012007.

[146] Jost, L. “Establishing and evaluating a procedure for measuring violin sound radiation in acoustically challenging spaces”. PhD thesis. Westsächsische Hochschule Zwickau, 2021.

[147] Jost, L. “Measuring speed of sound in the violin maker’s workshop through longitudinal standing waves: a simple alternative method”. In: *Proceedings of Meetings on Acoustics*. Vol. 49. 1. Acoustical Society of America. 2022, p. 035009.

[148] Kahle, E. and Woodhouse, J. “The influence of cell geometry on the elasticity of softwood”. In: *Journal of materials science* 29.5 (1994), pp. 1250–1259.

[149] Karami, E., Brémaud, I., Bardet, S., Almeras, T., Guibal, D., Langbour, P., Pourtahmasi, K., and Gril, J. “Reversible and irreversible effects of mild thermal treatment on the properties of wood used for making musical instruments: comparing mulberry to spruce”. In: *iForest: Biogeosciences and Forestry* 15 (2022), pp. 256–264.

[150] Kaselouris, E., Bakarezos, M., Tatarakis, M., Papadogiannis, N. A., and Dimitriou, V. “A review of finite element studies in string musical instruments”. In: *Acoustics*. Vol. 4. 1. MDPI. 2022, pp. 183–202.

[151] Kirsch, S. “Post-processing of musical instrument 3D-computed tomography data for conservational applications”. In: *Preservation of Wooden Musical Instruments-Ethics, Practice and Assessment* (2017).

[152] Klippel, W. “Assessment of voice coil peak displacement xmax”. In: *Proceedings of the AES 112 Convention*. Dresden, Germany, Oct. 2002, pp. 307–324.

[153] Kollman, F. “Principles of wood sciences and technology”. In: *I. Solid Wood* (1968), pp. 257–274.

[154] Konopka, D., Ehricht, S., and Kaliske, M. “Hygro-mechanical investigations of clavichord replica at cyclic climate load: experiments and simulations”. In: *Journal of Cultural Heritage* 36 (2019), pp. 210–221.

[155] Korkmaz, O. and Büyüksarı, Ü. “Effects of moisture content on mechanical properties of micro-size oak wood”. In: *BioResources* 14.4 (2019), pp. 7655–7663.

[156] Kottick, E. L., Marshall, K. D., and Hendrickson, T. J. “The acoustics of the harpsichord”. In: *Scientific American* 264.2 (1991), pp. 110–115.

[157] Kránitz, K., Sonderegger, W., Bues, C.-T., and Niemz, P. “Effects of aging on wood: a literature review”. In: *Wood Science and Technology* 50.1 (2016), pp. 7–22.

[158] Krauthammer, T. and Ventsel, E. *Thin plates and shells: theory, analysis and applications*. New York: Mercel Dekker Inc., 2001.

[159] Kucíková, L. “Micromechanical study of spruce wood”. PhD thesis. Master’s thesis, Czech Technical University in Prague, 2018.

[160] Ladevèze, P., Nedjar, D., and Reynier, M. “Updating of finite element models using vibration tests”. In: *AIAA journal* 32.7 (1994), pp. 1485–1491.

[161] Lai, T. and Lau, T. “Determination of elastic constants of a generally orthotropic plate by modal analysis”. In: *International Journal of Analytical and Experimental Modal Analysis* 8.1 (1993), pp. 15–33.

[162] Lanvermann, C., Hass, P., Wittel, F. K., and Niemz, P. “Mechanical properties of Norway spruce: intra-ring variation and generic behavior of earlywood and latewood until failure”. In: *arXiv preprint arXiv:1509.04012* (2015).

[163] Larsson, D. “Using modal analysis for estimation of anisotropic material constants”. In: *Journal of engineering mechanics* 123.3 (1997), pp. 222–229.

[164] Lazar, J. and Kubota, G. S. “Analysis of a Vented-Box Loudspeaker System via the Impedance Function”. In: *Proceedings of the AES 147th Convention, New York, USA*. Oct. 2019.

[165] Le Moyne, S., Le Conte, S., Ollivier, F., Frelat, J., Battault, J.-C., and Vaiedelich, S. “Restoration of a 17th-century harpsichord to playable condition: A numerical and experimental study”. In: *The Journal of the Acoustical Society of America* 131.1 (2012), pp. 888–896.

[166] Lehr, R. “Sixteen S-squared over D-squared: A relation for crude sample size estimates”. In: *Statistics in medicine* 11.8 (1992), pp. 1099–1102.

[167] Leissa, A. W. *Vibration of plates*. Vol. 160. Scientific and Technical Information Division, National Aeronautics and . . ., 1969.

[168] Limkar, B. and Chandekar, G. “Dynamic analysis of Sitar: A comparative study of operational and experimental modal analysis”. In: *Journal of Vibration and Control* 29.1-2 (2023), pp. 79–90.

[169] Madinier, N., Leclère, Q., Ege, K., and Berry, A. “Complex dynamic stiffness identification of panels using inverse methods based on optical deflectometry measurements”. In: *Journal of Sound and Vibration* (2025), p. 119373.

[170] Magalotti, R., Bugaj, K., and Said, A. “Assessing the acoustic load on a loudspeaker driver through electrical impedance measurements”. In: *Proceedings of the AES Conference, Le Mans, France*. Jan. 2024.

[171] Maierhofer, J., Mahmoudi, A. E., and Rixen, D. J. “Development of a low cost automatic modal hammer for applications in substructuring”. In: *Dynamic Substructures, Volume 4: Proceedings of the 37th IMAC, A Conference and Exposition on Structural Dynamics 2019*. Springer. 2019, pp. 77–86.

[172] Maloney, S., Traynor, R., and Photometric, L. “Modal testing of a soprano pan using a 3D laser Doppler vibrometer”. In: *Acoust. Bull.* 36 (2011), pp. 42–44.

[173] Malvermi, R., Albano, M., Gonzalez, S., Fiocco, G., Antonacci, F., Malagodi, M., and Sarti, A. “The impact of alkaline treatments on elasticity in spruce tonewood”. In: *Sci Rep-UK* 12.1 (2022), p. 13335.

[174] Mansour, H., Scavone, G., and Freour, V. “A comparison of vibration analysis techniques applied to the Persian setar”. In: *Proceedings of Acoustics*. Nantes, France, 2012, pp. 1743–1748.

[175] Mansour, H. “Modal analysis of the Setar: A numerical–experimental comparison”. In: *Journal of Vibration and Acoustics* 137.6 (2015), p. 061006.

[176] Mansour, H., Arzanpour, S., Alghassi, H., and Behzad, M. “Vibration Analysis of Setar for Extracting the Frequency Response Function (FRF)”. In: *ASME International Mechanical Engineering Congress and Exposition*. Vol. 43888. 2009, pp. 485–490.

[177] Manzo, G., Tippner, J., and Zatloukal, P. “Relationships between the macrostructure features and acoustic parameters of resonance Spruce for piano soundboards”. In: *Applied Sciences* 11.4 (2021), p. 1749.

[178] Martarelli, M. and Ewins, D. J. “Continuous scanning laser Doppler vibrometry and speckle noise occurrence”. In: *Mechanical Systems and Signal Processing* 20.8 (2006), pp. 2277–2289.

[179] Martínez, M. P., Poletti, P., and Espert, L. G. “Vibration testing for the evaluation of the effects of moisture content on the in-plane elastic constants of wood used in musical instruments”. In: *Vibration and structural acoustics analysis* (2011), pp. 21–57.

[180] MatWeb, L. *Spruce Wood — Material Property Data*. Material property database entry for spruce wood. 2025. URL: https://www.matweb.com/search/QuickText.aspx?SearchText=spruce (visited on 10/22/2025).

[181] Maynard, J. D., Williams, E. G., and Lee, Y. "Nearfield acoustic holography: I. Theory of generalized holography and the development of NAH". In: *The Journal of the Acoustical Society of America* 78.4 (1985), pp. 1395–1413.

[182] McConnell, K. G. *Vibration Testing: Theory and Practice*. John Wiley & Sons, 1995.

[183] McIntyre, M. and Woodhouse, J. "On measuring the elastic and damping constants of orthotropic sheet materials". In: *Acta Metallurgica* 36.6 (1988), pp. 1397–1416.

[184] Mclntyre, M. and Woodhouse, J. "On measuring wood properties, part 1–3". In: *J. Catgut Acoust. Soc* 42.11 (1984).

[185] Meincken, M., Roux, G., and Niesler, T. "An African violin-The feasibility of using indigenous wood from southern Africa as tonewood". In: *South African Journal of Science* 117.11-12 (2021), pp. 1–8.

[186] Meza-Perez, A., Gonzalez, S., Viala, R., and Fritz, C. "Developing a finite element model for the study of an experimental batch of violins". In: *Forum Acusticum 2023*. 2023, p. 752.

[187] Meza-Pérez, A., Stoppani, G., Viala, R., Gonzalez, S., Igartua, U., Rico, R. J., and Fritz, C. "Towards a finite element model of a batch of experimental violins: validation on sub-structural components". In: *Acta Acustica* 9 (2025), p. 2.

[188] Mihalcica, M., Stanciu, M., Gliga, V., Campean, M., Dinulică, F., and Nastac, S. "Experimental modal analysis of violin bodies with different structural patterns of resonance spruce". In: *IOP Conference Series: Materials Science and Engineering*. Vol. 1182. 1. IOP Publishing. 2021, p. 012048.

[189] Mindlin, R. "Influence of rotatory inertia and shear on flexural motions of isotropic, elastic plates". In: *Journal of Applied Mechanics* (1951).

[190] Miranda Valiente, P., Squicciarini, G., and Thompson, D. J. "Influence of soundboard modelling approaches on piano string vibration". In: *The Journal of the Acoustical Society of America* 155.5 (2024), pp. 3213–3232.

[191] Moosrainer, M. and Fleischer, H. "Application of BEM and FEM to musical instruments". In: *Boundary Elements in Acoustics* (2000), pp. 377–410.

[192] Nguyen, D. D. "Modeling a micro-mirror array and contribution to the development of a simulator of micro-system arrays". PhD thesis. Université Bourgogne Franche-Comté, 2017.

[193] Nieminen, R. "Thermally Aged Tonewood 2.7." en. In: *Thermally Aged Tonewood* (Jan. 2019). URL: https://www.academia.edu/126060101/Thermally_Aged_Tonewood_2_7 (visited on 09/12/2025).

[194] Niemz, P., Teischinger, A., and Sandberg, D. *Springer handbook of wood science and technology*. Vol. 1. Springer, 2023.

[195] Noguchi, T., Obataya, E., and Ando, K. "Effects of aging on the vibrational properties of wood". In: *Journal of Cultural Heritage* 13.3 (2012), S21–S25.

[196] Norman, P., Jung, G., Ratcliffe, C., Crane, R., and Davis, C. *Development of an automated impact hammer for modal analysis of structures*. Tech. rep. 2012.

[197] O'BRIEN, G. "A New Organological Approach Used in the Analysis of the Nuremberg Virginal Attributed to Gianfrancesco Antegnati, Brescia, c1558". In: *The Galpin Society Journal* (2019), pp. 23–139.

[198] Obataya, E., Ono, T., and Norimoto, M. "Vibrational properties of wood along the grain". In: *Journal of Materials Science* 35.12 (2000), pp. 2993–3001.

[199] Obataya, E. "Effects of natural and artificial ageing on the physical and acoustic properties of wood in musical instruments". In: *Journal of Cultural Heritage* 27 (2017), S63–S69.

[200] Oktav, A. "The variation in the acoustic response of the Karadeniz Kemenche depending on the thickness of the soundboard". In: *Acoustics Australia* (2024), pp. 1–15.

[201] Ollivier, F., Alais, P., and Karkaletsis, A. "Fast modal analysis by means of impulse acoustical holography". In: *Proceedings of the 11th ICSV* (2004), pp. 2395–2402.

[202] Ono, T. "Frequency responses of wood for musical instruments in relation to the vibrational properties". In: *Journal of the Acoustical Society of Japan (E)* 17.4 (1996), pp. 183–193.

[203] Ozturk, S. "Experimental and numerical modal analysis of the traditional percussion instrument" Erbane"". In: *International Journal of Engineering Science* 216 (2025), p. 104351.

[204] Palka, L. "Predicting the effect of specific gravity, moisture content, temperature and strain rate on the elastic properties of softwoods". In: *Wood Science and Technology* 7.2 (1973), pp. 127–141.

[205] Pastor, M., Binda, M., and Harčarik, T. "Modal assurance criterion". In: *Procedia Eng* 48 (2012), pp. 543–548.

[206] PCB Piezotronics, Inc. *Model 086E80 Miniature Instrumented Impulse Hammer, 0 to 50 lbf: Installation and Operating Manual*. Available: https://www.pcb.com. PCB Piezotronics, an Amphenol Company. Depew, NY, USA, 2023.

[207] Pedersen, P. and Frederiksen, P. "Identification of orthotropic material moduli by a combined experimental/numerical method". In: *Measurement* 10.3 (1992), pp. 113–118.

[208] Pedrammehr, S., Jafarzadeh Aghdam, N., Pakzad, S., Ettefagh, M. M., and Homayoun Sadeghi, M. "A study on vibration of Setar: stringed Persian musical instrument". In: *Journal of Vibroengineering* 20.7 (2018), pp. 2680–2689.

[209] Peters, R. *Acoustics and noise control*. Routledge, 2013.

[210] Peterson, D. "Hammered dulcimer". In: *The science of string instruments*. Springer, 2010, pp. 371–392.

[211] Pezzoli, M., De Lucia, R. R., Antonacci, F., Sarti, A., et al. *Predictive simulation of mechanical behavior from 3D laser scans of violin plates*. Universitätsbibliothek der RWTH Aachen, 2019.

[212] Pfeifle, F. and Bader, R. "Real-time finite difference physical models of musical instruments on a field programmable gate array (FPGA)". In: *Proc. of the 15th Int. Conference on Digital Audio Effects (DAFx-12)*. 2012, pp. 17–21.

[213] Plath, N. “3D imaging of musical instruments: methods and applications”. In: *Computational Phonogram Archiving*. Springer, 2019, pp. 321–334.

[214] Policardi, F. “MLS and Sine-Sweep technique comparison in room-acoustic measurements”. In: *Elektrotehniški Vestnik / Electrotechnical Review* 78.3 (2011), pp. 91–95.

[215] Ponteggia, D. “Loudspeaker Electrical Impedance Measurements Methods: A Brief Review”. In: *International Conference on Noise and Vibration Engineering*. Los Angeles, USA, 2006, pp. 1615–1626.

[216] Prato, A., Schiavi, A., Casassa, F., et al. “A modal approach for reverberation time measurements in non-diffuse sound field”. In: *ICSV23 Proceedings*. 2016.

[217] Pyrkosz, M. and Karsen, C. V. “Comparative modal tests of a violin”. In: *Experimental Techniques* 37 (2013), pp. 47–62.

[218] Qader, A. and Shwan, S. “An Overview of Various 3D Scanning Methods in the Context of Cultural Heritage Documentation”. In: *INFORMATIK 2024* (2024), pp. 963–972.

[219] Qiu, H., Cui, Y., Zhang, L., Ding, T., and Zhu, N. “The Influence of Different Moisture Contents on the Acoustic Vibration Characteristics of Wood”. In: *Forests* 16.4 (2025), p. 680.

[220] Quintavalla, M., Gabrielli, F., and Canevari, C. “Grading materials for stringed instruments soundboards: An approach considering the orthotropic elastic and damping properties”. In: *Appl Acoust* 187 (2022), p. 108521.

[221] Quintavalla, M., Gabrielli, F., and Canevari, C. “The acoustics of traditional Italian mandolins and their relation with soundboard wood properties”. In: *International Journal of Wood Culture* 2.1-3 (2022), pp. 1–18.

[222] Quintavalla, M., Gabrielli, F., and Canevari, C. “Acoustical survey and finite element analyses of late baroque mandolin”. In: *International Journal of Wood Culture* 4.1 (2024), pp. 39–57.

[223] Rau, M. “Measurements and analysis of acoustic guitars during various stages of their construction”. In: *The Journal of the Acoustical Society of America* 149.4 Supplement (2021), A25–A25.

[224] Rau, M., Smith, J. O., and Abel, J. S. “A comparison of modal parameter extraction methods when applied to measurements of stringed instruments”. In: *measurements* 1 (2023), p. 2.

[225] Rau, M. G. *Vibration and Acoustic Measurements of Guitars with Applications to Luthiery Synthesis and Audio Effects*. Stanford University, 2023.

[226] Ravina, E. “Violins characterization through vibro-acoustic experiments”. In: *Acoustics 2012 Nantes*. Ed. by S. F. d’Acoustique. Nantes, France, Apr. 2012. URL: https://hal.science/hal-00810566 (visited on 07/26/2025).

[227] Reddy, J. N. “An introduction to the finite element method”. In: *New York* 27.14 (1993).

[228] Reissner, E. “The effect of transverse shear deformation on the bending of elastic plates”. In: *Journal of Applied Mechanics* (1945).

[229] Ribeiro, R. and Inácio, O. “Experimental modal analysis of a fully assembled portuguese guitar”. In: *Actas del congreso EuroRegio 2016, Oporto, Portugal*. 2016, pp. 1–10.

[230] Rigali, F. “SOUNDING WOOD, Tonal differences of woods employed in historical soundboards”. MA thesis. University of Gothenburg, 2016.

[231] Roohnia, M., Hossein, M.-A., Alavi-Tabar, S.-E., Tajdini, A., Jahan-Latibari, A., and Manouchehri, N. “Acoustic properties in Arizona cypress logs: a tool to select wood for sounding board”. In: *BioResources* 6.1 (2011), pp. 386–399.

[232] Roohnia, M. “Tonewood: Treatment and Tuning”. In: *Properties and Treatment of Tonewood for String Instrument Construction: A Professional Guide*. Springer, 2025, pp. 225–291.

[233] Ross, R. J. et al. “Wood handbook: wood as an engineering material”. In: *USDA Forest Service, Forest Products Laboratory, General Technical Report FPL-GTR-190, 2010: 509 p. 1 v.* 190 (2010).

[234] Rossing, T. “Modal analysis”. In: *Springer Handbook of Acoustics*. Springer, 2007, pp. 1127–1138.

[235] Rossing, T. *Springer Handbook of Acoustics*. en. Springer Science & Business Media, 2007.

[236] Rossing, T. D. et al. *The science of string instruments*. Springer, 2010.

[237] Ruffinatto, F., Negro, F., and Crivellaro, A. “The macroscopic structure of wood”. In: *Forests* 14.3 (2023), p. 644.

[238] Santoni, A., Schoenwald, S., Van Damme, B., and Fausti, P. “Determination of the elastic and stiffness characteristics of cross-laminated timber plates from flexural wave velocity measurements”. In: *Journal of Sound and Vibration* 400 (2017), pp. 387–401.

[239] Schelleng, J. C. “The violin as a circuit”. In: *The Journal of the Acoustical Society of America* 35.3 (1963), pp. 326–338.

[240] Singh, A. and Moore, K. “An open-source, scalable, low-cost automatic modal hammer for studying nonlinear dynamical systems”. In: *Experimental Techniques* 46.5 (2022), pp. 775–792.

[241] Sirr, S. A. and Waddle, J. R. “Use of CT in detection of internal damage and repair and determination of authenticity in high-quality bowed stringed instruments”. In: *Radiographics* 19.3 (1999), pp. 639–646.

[242] Skrodzka, E., Łapa, A., Linde, B. B., and Rosenfeld, E. “Modal parameters of two incomplete and complete guitars differing in the bracing pattern of the soundboard”. In: *The Journal of the Acoustical Society of America* 130.4 (2011), pp. 2186–2194.

[243] Słupianek, A., Dolzblasz, A., and Sokołowska, K. “Xylem parenchyma—role and relevance in wood functioning in trees”. In: *Plants* 10.6 (2021), p. 1247.

[244] Small, R. H. “Vented-box loudspeaker systems–part 1: Small-signal analysis”. In: *Journal of the Audio Engineering Society* 21.5 (1973), pp. 363–372.

[245] Stoel, B. C. and Borman, T. M. “A comparison of wood density between classical Cremonese and modern violins”. In: *PLoS One* 3.7 (2008), e2554.

[246] Suzuki, H. “Vibration and sound radiation of a piano soundboard”. In: *The Journal of the Acoustical Society of America* 80.6 (1986), pp. 1573–1582.

[247] Tahvanainen, H. “On the acoustics of the concert kantele”. In: *Stockholm Music Acoustics Conference*. Stockholm, Sweden, June 2023.

[248] Tahvanainen, H. “Muunnellun kanteleen kopan värähtelyn ja äänisäteilyn mallintaminen”. In: (2012).

[249] Tahvanainen, H., Matsuda, H., and Shinoda, R. “Numerical simulation of the acoustic guitar for virtual prototyping”. In: *Proceedings of ISMA*. Vol. 2019. 2019, pp. 13–17.

[250] Tahvanainen, H., Pölkki, J., Penttinen, H., and Välimäki, V. “Finite element model of a kantele with improved sound radiation”. In: *Proceedings of the Stockholm Music Acoustic Conference, Stockholm, Sweden*. 2013, pp. 193–198.

[251] Tam, J. H., Ong, Z. C., Ismail, Z., Ang, B. C., and Khoo, S. Y. “Identification of material properties of composite materials using nondestructive vibrational evaluation approaches: A review”. In: *Mech Adv Mat Struct* 24.12 (2017), pp. 971–986.

[252] Team, A. *Audacity ® – Free Audio Editor, Recorder, Music More*. Official website of the Audacity open-source audio editor. 2025. URL: https://www.audacityteam.org/ (visited on 10/01/2025–10/31/2025).

[253] Testing Materials (ASTM) International, A. S. of. *ASTM D198-15, Standard Test Methods of Static Tests of Lumber in Structural Sizes*. 2015.

[254] Thiele, N. “Loudspeakers in Vented Boxes: Part 1”. In: *Journal of the Audio Engineering Society* 19.5 (1971), pp. 382–392.

[255] Thiele, N. “Loudspeakers in Vented Boxes: Part 2”. In: *Journal of the Audio Engineering Society* 19.6 (1971), pp. 471–483.

[256] Tognana, S., Salgueiro, W., Somoza, A., and Marzocca, A. “Measurement of the Young’s modulus in particulate epoxy composites using the impulse excitation technique”. In: *Materials Science and Engineering: A* 527.18-19 (2010), pp. 4619–4623.

[257] Topaloglu, E. “Effect of natural aging on selected properties of wooden facade elements made of scots pine and chestnut”. In: *Maderas. Ciencia y tecnología* 25 (2023).

[258] Trévisan, B., Ege, K., and Laulagnet, B. “A modal approach to piano soundboard vibroacoustic behavior”. In: *The Journal of the Acoustical Society of America* 141.2 (2017), pp. 690–709.

[259] Tronchin, L. “Modal analysis and intensity of acoustic radiation of the kettledrum”. In: *The Journal of The Acoustical Society of America* 117.2 (2005), pp. 926–933.

[260] Tronchin, L. et al. “Metodologie sperimentali applicate agli strumenti musicali”. In: *Acustica Musicale ed Architettonica*. De Agostini Ed, 2008, pp. 425–453.

[261] Tronchin, L. and Consani, C. “The acoustical behaviour of the soundboards of two Italian seventeenth-century harpsichords”. In: *Recercare* 13 (2001), pp. 275–297.

[262] Trujillo-Franco, L. G., Abundis-Fong, H. F., and Marin-Soriano, J. C. “An open-source data acquisition platform for teaching vibration analysis”. In: *Computer Applications in Engineering Education* 32.5 (2024), e22753.

[263] Urgela, S. “VibroColorTest: equipment for nondestructive testing of wood for musical instruments”. In: *Practical Holography XV and Holographic Materials VII*. Vol. 4296. SPIE. 2001, pp. 83–91.

[264] Urgela, S. and Saldner, H. O. “Determination of material properties of violin tone wood using electronic holography”. In: *Interferometry’94: Photomechanics*. Vol. 2342. SPIE. 1994, pp. 166–172.

[265] Vaiedelich, S. and Fritz, C. “Perception of old musical instruments”. In: *Journal of cultural heritage* 27 (2017), S2–S7.

[266] Varoto, P. and Oliveira, L. de. “Interaction between a vibration exciter and the structure under test”. In: *Sound and Vibration* 36 (2002), pp. 20–26.

[267] Veronesi, W. and Maynard, J. D. “Nearfield acoustic holography (NAH) II. Holographic reconstruction algorithms and computer implementation”. In: *The Journal of the Acoustical Society of America* 81.5 (1987), pp. 1307–1322.

[268] Viala, R., Placet, V., and Cogan, S. “Identification of the anisotropic elastic and damping properties of complex shape composite parts using an inverse method based on finite element model updating and 3D velocity fields measurements (FEMU-3DVF): Application to bio-based composite violin soundboards”. In: *Compos Part A-Appl S* 106 (2018), pp. 91–103.

[269] Viala, R., Placet, V., and Cogan, S. “Model-based evidence of the dominance of the guitar brace design over material and climatic variability for dynamic behaviours”. In: *Applied Acoustics* 182.108275 (2021).

[270] Viala, R. “Towards a model-based decision support tool for stringed musical instruments making”. PhD thesis. Université Bourgogne Franche-Comté, 2018.

[271] Viala, R., Ben-Haim, Y., Vaiedelich, S., and Cogan, S. “Value of information in the conservation of a heritage cello: An info-gap decision theory approach”. In: *Journal of Cultural Heritage* 71 (2025), pp. 165–174.

[272] Viala, R., Pérez, M. A., Placet, V., Manjón, A., Foltête, E., and Cogan, S. “Towards model-based approaches for musical instruments making: validation of the model of a Spanish guitar soundboard and characterization features proposal”. In: *Applied Acoustics* 172 (Jan. 2021), p. 107591. ISSN: 0003-682X. DOI: 10.1016/j.apacoust.2020.107591. URL: https://www.sciencedirect.com/science/article/pii/S0003682X20306952 (visited on 07/26/2025).

[273] Viala, R., Placet, V., and Cogan, S. “Virtual prototyping: a potential tool for wooden cultural heritage studies”. In: *Symposium: Analysis and characterization of wooden cultural heritage by scientific engineering methods*. 2016.

[274] Viala, R., Placet, V., and Cogan, S. “Identification of the anisotropic elastic and damping properties of complex shape composite parts using an inverse method based on finite element model updating and 3D velocity fields measurements (FEMU-3DVF): Application to bio-based composite violin soundboards”. In: *Composites Part A: Applied Science and Manufacturing* 106 (2018), pp. 91–103.

[275] Viala, R., Placet, V., and Cogan, S. “Simultaneous non-destructive identification of multiple elastic and damping properties of spruce tonewood to improve grading”. In: *Journal of Cultural Heritage* 42 (2020), pp. 108–116.

[276] Waltham, C. and Yoshikawa, S. “Construction of wooden musical instruments”. In: *Springer Handbook of Systematic Musicology*. Springer, 2018, pp. 63–79.

[277] Wegst, U. G. “Wood for sound”. In: *American Journal of Botany* 93.10 (2006), pp. 1439–1448.

[278] Willemsen, S. “The emulated ensemble: Real-time simulation of musical instruments using finite-difference time-domain methods”. In: (2021).

[279] Willemsen, S., Bilbao, S., Ducceschi, M., and Serafin, S. “A physical model of the trombone using dynamic grids for finite-difference schemes”. In: *2021 24th International Conference on Digital Audio Effects (DAFx)*. IEEE. 2021, pp. 152–159.

[280] Williams, E. G. *Fourier acoustics: sound radiation and nearfield acoustical holography*. Elsevier, 1999.

[281] Williams, E. G., Maynard, J. D., and Skudrzyk, E. “Sound source reconstructions using a microphone array”. In: *The Journal of the Acoustical Society of America* 68.1 (1980), pp. 340–344.

[282] Woodhouse, J. “The acoustics of a plucked harp string”. In: *Journal of Sound and Vibration* 523 (2022), p. 116669.

[283] Yang, B., Lenczner, M., Cogan, S., Menges, F., Riel, H., Gotsmann, B., Janus, P., and Boetch, G. “Modelling, simulation and optimization for a SThm nanoprobe”. In: *2014 15th International Conference on Thermal, Mechanical and Mulit-Physics Simulation and Experiments in Microelectronics and Microsystems (EuroSimE)*. IEEE. 2014, pp. 1–6.

[284] Yano, H., Kajita, H., and Minato, K. “Chemical treatment of wood for musical instruments”. In: *The Journal of the Acoustical Society of America* 96.6 (Dec. 1994), pp. 3380–3391. DOI: 10.1121/1.414894.

[285] Yokoyama, M., Lucia, R. R. D., Antonacci, F., and Sarti, A. “Influence of orthotropic properties on vibration of violin top plates”. In: *Proceedings of the 23rd International Congress on Acoustics*. Aachen, Germany: International Congress on Acoustics, Sept. 2019, unknown.

[286] Yoshihara, H. “Off-axis Young’s modulus and off-axis shear modulus of wood measured by flexural vibration tests”. In: *Holzforschung* 66 (2012), pp. 207–213.

[287] Yoshihara, H. and Maruta, M. “Determining the Young’s modulus of solid wood by considering the fundamental frequency under the free-free flexural vibration mode”. In: *Wood Science and Technology* 55.4 (2021), pp. 919–936.

[288] Yoshikawa, S. “Acoustical classification of woods for string instruments”. In: *The Journal of the Acoustical Society of America* 122.1 (2007), pp. 568–573.

[289] Zhang, A. and Woodhouse, J. “Reliability of the input admittance of bowed-string instruments measured by the hammer method”. In: *The Journal of the Acoustical Society of America* 136.6 (2014), pp. 3371–3381.

[290] Zhou, J., Chui, Y. H., Gong, M., and Hu, L. “Comparative study on measurement of elastic constants of wood-based panels using modal testing: choice of boundary conditions and calculation methods”. In: *Journal of Wood Science* 63.5 (2017), pp. 523–538.

Appendix A

ROM of the electromechanical coupling

The exciter-board coupled system is defined as:

$$\rho h \frac{\partial^2 u(\mathbf{x},t)}{\partial t^2} = \mathscr{L}(u(\mathbf{x},t)) - 2\tau\rho h \frac{\partial u(\mathbf{x},t)}{\partial t} + \mathscr{D}(\mathbf{x}-\mathbf{x}_{md}) C_{ms}\left(w(t) - u(\mathbf{x}_{md},t)\right) - \mathscr{D}(\mathbf{x}-\mathbf{x}_{md}) BlI(t) \tag{A.1a}$$

$$M_{ms}\frac{d^2 w(t)}{dt^2} = -2M_{ms}\,\xi\,\frac{dw(t)}{dt} - C_{ms}\left(w(t) - u(\mathbf{x}_{md},t)\right) + BlI(t) \tag{A.1b}$$

$$V(t) = L_e \frac{dI(t)}{dt} + R_e I(t) + K\left(\frac{dw(t)}{dt} - \frac{\partial u(\mathbf{x}_{md},t)}{\partial t}\right) \tag{A.1c}$$

The displacement of the board is denoted $u(\mathbf{x},t)$, with $\mathbf{x} \in (0,L_x) \times (0,L_y)$, and the exciter's motion is described by $w(t)$. The electrical variables include the current $I(t)$ through the exciter and the applied voltage $V(t)$. The operator $\mathscr{L}(u)$, governing the plate's internal dynamics, follows the standard orthotropic formulation (see [83] for details). The exciter contact point $\mathbf{x}_{md}$ is defined either centrally or off-center, depending on the mounting configuration.

The density of the board is ρ = 390 kg/m^3, and its thickness is $h = 4\,\text{mm}$. The parameters M_{ms}, C_{ms}, R_e, L_e, and Bl represent the Thiele & Small parameters of the exciter as mounted on the plate, with values listed in Table 4.1. Additional parameters include τ, ξ, and K, which represent, respectively, the exponential decay rate of the board, the loss coefficient of the exciter, and the back-electromechanical coupling constant.

To reduce model complexity while retaining physical relevance, a reduced-order model (ROM) capturing only the dynamics of the first mode of the board is used. This is justified by the fact that this mode is most affected by the position of the exciter $\mathbf{x}_{md}$. One can assume that the displacement field $u(\mathbf{x},t)$ can be approximated by the modal expansion:

$$u(\mathbf{x},t) \approx \sin\frac{\pi x}{L_x}\sin\frac{\pi y}{L_y}r(t), \tag{A.2}$$

where $r(t)$ is the time-dependent modal coordinate. The chosen shape function corresponds to the fundamental mode of a simply-supported rectangular plate, which is qualitatively similar to that of a clamped plate, as both exhibit a maximum at the center and decay toward the boundaries.

By substituting the modal approximation (A.2) into the full coupled system and applying a standard Galerkin projection (see [79]), one arrives at the following set of reduced-order equations governing the coupled electromechanical dynamics:

$$\frac{d^2r(t)}{dt^2} = -\omega_0^2 q(t) - 2\tau\frac{dq(t)}{dt} + bM_{ms}M^{-1}\omega_{md}^2\left(w(t)-br(t)\right) - bM^{-1}BI(t) \tag{A.3a}$$

$$\frac{d^2w(t)}{dt^2} = -2\eta\frac{dw(t)}{dt} - \omega_{md}^2\left(w(t)-br(t)\right) + M_{ms}^{-1}BI(t) \tag{A.3b}$$

$$V(t) = L_e\frac{dI(t)}{dt} + R_eI(t) + K\left(\frac{dw(t)}{dt} - b\frac{dr(t)}{dt}\right) \tag{A.3c}$$

where the coefficient

$$b := \sin\left(\frac{\pi x_{md}}{L_x}\right)\sin\left(\frac{\pi y_{md}}{L_y}\right) \tag{A.4}$$

quantifies the contribution of the modal shape at the location of the exciter $\mathbf{x}_{md}$. All parameters appearing in this model are either known from measurements or can be reasonably estimated. The fundamental frequency is given by $f_0 = 117\,\mathrm{Hz}$, leading to $\omega_0 = 2\pi f_0$. The damping of the board is computed via $\tau = 3\log(10)/t_{60} \approx 14\,\mathrm{s}^{-1}$, based on an energy decay time $\tau_{60} \approx 0.5\,\mathrm{s}$ for a $60\,\mathrm{dB}$ reduction [216]. The modal mass of the board for the (0,0) mode is obtained via projection as $M = 0.25\rho hL_xL_y \approx 50\,\mathrm{g}$. The coordinate $\mathbf{x}_{md} = (x_e, y_e)$ corresponds to the exciter's mounting location, taken from Fig. 4.1. In this study, two possible locations are considered: for position C, $\mathbf{x}_{md} = (0.5L_x, 0.5L_y)$; for position L1, $\mathbf{x}_{md} = (0.7L_x, 0.9L_y)$. The exciter's resonance is expressed as $\omega_{md} = 2\pi f_{md}$, with $f_{md} = \sqrt{C_{ms}/M_{ms}}/(2\pi) = 73.9\,\mathrm{Hz}$, as reported in Table 4.3. The parameters $\xi \approx 15\,\mathrm{s}^{-1}$ and $K \approx 0.6\,\mathrm{V}\cdot\mathrm{s}\cdot\mathrm{m}^{-1}$ are estimated heuristically.

Assuming a harmonic excitation of the form $V(t) = \hat{V}e^{j\omega t}$, the system can be recast in the frequency domain as:

$$\mathbf{Z}(\omega)\hat{\mathbf{I}} = \hat{\mathbf{V}} \tag{A.5}$$

Here, the response vector is defined as $\hat{\mathbf{I}} = \left(j\omega\hat{r} := \hat{v},\, j\omega\hat{w},\, \hat{I}\right)^T$, representing the frequency-domain velocities and current, while the input vector is $\hat{\mathbf{V}} = (0,\, 0,\, 1)^T$. The matrix $\mathbf{Z}(\omega) \in \mathbb{C}^{3\times 3}$ denotes the system's impedance and is omitted here for brevity. Once known, this matrix allows for direct computation of both the plate's velocity response $\hat{v}$ and the input electrical impedance, defined as $Z := \hat{V}/\hat{I}$.

Appendix B

Cutoff Frequency Tables

The following tables present both dimensional and non-dimensional modal frequencies for rectangular, guitar-shaped, and kantele plates across a range of thicknesses. Theoretical cutoff frequencies derived from the MR plate model are also included for reference. Although these cutoff values are widely cited in plate theory, they do not serve as reliable indicators of the transition to thick-plate behavior. In compiling the data, modal frequencies have been reordered at each thickness increment to maintain alignment with the baseline modal sequence. Frequencies that could not be identified are marked as ‘n/a’.

For smaller h values, all plates—independent of their surface area—display modal patterns and non-dimensional frequencies that closely align with the thin-plate reference case. However, as h increases, notable divergences appear. These deviations become increasingly significant with greater thickness and are especially pronounced in plates with smaller surface areas. This trend reflects the expected scaling behavior governed by the parameter $\iota = h^{-1}\sqrt{A}$.

Table B.1 Dimensional and non-dimensional modal frequencies for modal shapes I-VI for the rectangular plates across three thicknesses. Reference cutoff frequencies f_{0x}, f_{0y} are reported for each case. Values in Hz. The non-dimensional values are shown in parentheses using a smaller font.

Plate Thickness: $h = 0.1$mm, $f_{0x} = 6.10 \cdot 10^6$ Hz, $f_{0y} = 1.28 \cdot 10^6$ Hz

Plate	**Area [m^2]**	Mode I (41.21)	Mode II (62.72)	Mode III (101.9)	Mode IV (102.2)	Mode V (118.5)	Mode VI (150.6)
Rectangular	1.92	0.24 (41.21)	0.37 (62.72)	0.60 (101.9)	0.69 (102.2)	0.69 (118.5)	0.88 (150.6)
Rectangular	0.48	0.96 (41.21)	1.46 (62.72)	2.38 (101.9)	2.39 (102.2)	2.77 (118.5)	3.52 (150.6)
Rectangular	0.12	3.85 (41.21)	5.86 (62.72)	9.52 (101.9)	9.55 (102.2)	11.1 (118.5)	14.1 (150.6)

Plate Thickness: $h = 3$ mm, $f_{0x} = 2.03 \cdot 10^5$ Hz, $f_{0y} = 4.27 \cdot 10^4$ Hz

Plate	**Area [m^2]**	Mode I (41.21)	Mode II (62.72)	Mode III (101.9)	Mode IV (102.2)	Mode V (118.5)	Mode VI (150.6)
Rectangular	1.92	7.21 (41.19)	11.0 (62.70)	17.8 (101.9)	17.9 (102.1)	20.7 (118.4)	26.3 (150.5)
Rectangular	0.48	28.8 (41.08)	43.8 (62.57)	71.3 (101.7)	71.1 (101.4)	82.4 (117.7)	105 (149.6)
Rectangular	0.12	114 (40.70)	174 (62.11)	283 (101.1)	278 (99.26)	323 (115.4)	412 (147.0)

Plate Thickness: $h = 30$ mm, $f_{0x} = 2.03 \cdot 10^4$ Hz, $f_{0y} = 4.27 \cdot 10^3$ Hz

Plate	**Area [m^2]**	Mode I (41.21)	Mode II (62.72)	Mode III (101.9)	Mode IV (102.2)	Mode V (118.5)	Mode VI (150.6)
Rectangular	1.92	67.2 (39.85)	104 (61.11)	170 (99.57)	153 (94.58)	180 (110.4)	233 (141.5)
Rectangular	0.48	230 (32.79)	317 (52.99)	610 (87.04)	457 (65.35)	563 (80.37)	761 (108.7)
Rectangular	0.12	674 (24.04)	1170 (41.85)	1900 (67.65)	1160 (41.27)	1550 (55.26)	2180 (77.65)

Table B.2 Dimensional and non-dimensional modal frequencies for modal shapes I-VI for the guitar top plates across three thicknesses. Reference cutoff frequencies f_{0x}, f_{0y} are reported for each case. Values in Hz. The non-dimensional values are shown in parentheses using a smaller font.

Plate Thickness: $h = 0.05$ mm, $f_{0x} = 6.10 \cdot 10^6$ Hz, $f_{0y} = 1.28 \cdot 10^6$ Hz

Plate	**Area [m^2]**	Mode I (38.8)	Mode II (68.82)	Mode III (87.52)	Mode IV (109.7)	Mode V (111.6)	Mode VI (144.4)
Guitar	0.55	0.40 (38.8)	0.70 (68.82)	0.90 (87.52)	1.13 (109.7)	1.15 (111.6)	1.48 (144.4)
Guitar	0.13	1.59 (38.8)	2.83 (68.82)	3.59 (87.52)	4.51 (109.7)	4.58 (111.6)	5.93 (144.4)
Guitar	0.03	6.37 (38.8)	11.3 (68.82)	14.4 (87.52)	18.0 (109.7)	18.3 (111.6)	23.7 (144.4)

Plate Thickness: $h = 3$ mm, $f_{0x} = 2.03 \cdot 10^5$ Hz, $f_{0y} = 4.27 \cdot 10^4$ Hz

Plate	**Area [m^2]**	Mode I (38.8)	Mode II (68.82)	Mode III (87.52)	Mode IV (109.7)	Mode V (111.6)	Mode VI (144.4)
Guitar	0.55	23.8 (38.63)	42.2 (68.48)	53.8 (87.32)	67.2 (109.0)	68.4 (111.0)	87.7 (142.3)
Guitar	0.13	94.4 (38.32)	167 (67.67)	214 (86.87)	266 (107.8)	270 (109.4)	344 (139.6)
Guitar	0.03	369 (37.45)	640 (64.99)	842 (85.42)	1030 (104.1)	1020 (103.9)	1310 (132.9)

Plate Thickness: $h = 30$ mm, $f_{0x} = 2.03 \cdot 10^4$ Hz, $f_{0y} = 4.27 \cdot 10^3$ Hz

Plate	**Area [m^2]**	Mode I (38.8)	Mode II (68.82)	Mode III (87.52)	Mode IV (109.7)	Mode V (111.6)	Mode VI (144.4)
Guitar	0.55	208 (33.77)	333 (54.03)	480 (77.89)	552 (89.67)	501 (81.4)	676 (109.8)
Guitar	0.13	678 (27.51)	979 (39.74)	1550 (63.11)	1670 (67.88)	1340 (54.5)	1950 (79.07)
Guitar	0.03	1870 (18.98)	2490 (25.26)	4070 (41.28)	4300 (43.69)	3150 (31.96)	(n/a)

Table B.3 Dimensional and non-dimensional modal frequencies for modal shapes I-VI for the kantele top plates across three thicknesses. Reference cutoff frequencies f_{0x}, f_{0y} are reported for each case. Values in Hz. The non-dimensional values are shown in parentheses using a smaller font.

Plate Thickness: $h = 0.05$ mm, $f_{0x} = 6.10 \cdot 10^6$ Hz, $f_{0y} = 1.28 \cdot 10^6$ Hz

Plate	**Area [m^2]**	Mode I (41.31)	Mode II (70.38)	Mode III (85.34)	Mode IV (112.4)	Mode V (125.2)	Mode VI (141.8)
Kantele	1.39	0.33 (41.31)	0.56 (70.38)	0.68 (85.34)	0.90 (112.4)	1.00 (125.2)	1.14 (141.8)
Kantele	0.34	1.33 (41.31)	2.26 (70.38)	2.74 (85.34)	3.61 (112.4)	4.02 (125.2)	4.55 (141.8)
Kantele	0.08	5.30 (41.31)	9.04 (70.38)	11.0 (85.34)	14.4 (112.4)	16.1 (125.2)	18.2 (141.8)

Plate Thickness: $h = 3$ mm, $f_{0x} = 2.03 \cdot 10^5$ Hz, $f_{0y} = 4.27 \cdot 10^4$ Hz

Plate	**Area [m^2]**	Mode I (41.31)	Mode II (70.38)	Mode III (85.34)	Mode IV (112.4)	Mode V (125.2)	Mode VI (141.8)
Kantele	1.39	9.93 (41.27)	16.9 (70.28)	20.5 (85.18)	27.0 (112.2)	30.1 (124.9)	34.1 (141.5)
Kantele	0.34	39.6 (41.31)	67.4 (70.38)	81.0 (85.34)	108 (112.4)	120 (125.2)	135 (141.8)
Kantele	0.08	157 (40.71)	266 (69.19)	320 (83.16)	423 (109.9)	468 (121.5)	527 (136.8)

Plate Thickness: $h = 30$ mm, $f_{0x} = 2.03 \cdot 10^4$ Hz, $f_{0y} = 4.27 \cdot 10^3$ Hz

Plate	**Area [m^2]**	Mode I (41.31)	Mode II (70.38)	Mode III (85.34)	Mode IV (112.4)	Mode V (125.2)	Mode VI (141.8)
Kantele	1.39	91.8 (38.17)	155 (64.50)	180 (74.70)	240 (99.39)	262 (109.2)	286 (118.7)
Kantele	0.34	313 (32.51)	525 (54.50)	571 (59.31)	(n/a)	(n/a)	847 (88)
Kantele	0.08	917 (23.82)	1630 (42.29)	(n/a)	(n/a)	(n/a)	2200 (57.07)